
博士論文

Study on strain-induced enhancement of plasma dispersion effect and free-carrier absorption for SiGe optical modulators/attenuators

(SiGe 光変調器/減衰器に向けた歪誘起によるプラズマ分散効果及び自由キャリア吸収増大に関する研究)

A DISSERTATION
SUBMITTED TO THE DEPARTMENT OF ELECTRICAL
ENGINEERING AND INFORMATION SYSTEMS OF
THE UNIVERSITY OF TOKYO
FOR THE DEGREE OF DOCTOR OF ENGINEERING

December 1st 2014

Younghyun Kim (金栄現)

Supervisor Mitsuru Takenaka

Abstract

The plasma dispersion effect and free-carrier absorption are well-known physical phenomena that change optical constants, the refractive index (n) and absorption coefficient (α), of semiconductors, and are the most promising effects for silicon (Si) to build-up optical modulators, as previously shown in the study by Soref and Bennett. Currently most Si optical modulators, which are one of the fundamental building blocks of Si-based electronic-photonic integrated circuits (EPICs) for off-chip and on-chip optical interconnects, have been demonstrated using these free-carrier effects.

However, the weak plasma dispersion and free-carrier absorption in Si cause low modulation efficiency, resulting in large device footprints and power consumption. Thus, enhancement of the plasma dispersion and free-carrier absorption will be fundamentally important to improve the modulation efficiency of Si-based optical modulators for small device footprints and low power consumption. The plasma dispersion effect and free-carrier absorption are expressed by the Drude model, which describes the changes in the refractive index and absorption coefficient upon a change in the plasma frequency of free carriers, which is dependent on the number of free carriers and their conductivity effective masses. Since the effects are inversely proportional to the conductivity effective masses of electrons and holes, lighter conductivity masses result in a larger plasma dispersion effect and free-carrier absorption.

In the dissertation, we have theoretically and experimentally investigated the enhancement of plasma dispersion and free-carrier absorption by strain-induced mass modulation in silicon-germanium (SiGe). The introduction of compressive strain to SiGe reduces the conductivity hole mass, resulting in enhanced plasma dispersion and free-carrier absorption. We expect that compressively strained $\text{Si}_{0.7}\text{Ge}_{0.3}$, which can be coherently grown on Si, will exhibit approximately two times higher plasma dispersion and three times higher free-carrier absorption than Si. The enhancement of the plasma dispersion effect and free-carrier absorption in SiGe is experimentally examined using a Si/SiGe/Si double-heterostructure optical waveguide with a lateral *pin* junction for carrier injection in the near-infrared wavelength range from 1.3 to 1.6 μm , which is the most important range of wavelengths for optical communication.

We have experimentally proved that the effective mass modulation by using strain to SiGe is an effective way to enhance the plasma dispersion effect and free-carrier absorption. We have invented a novel strained SiGe optical modulator, which consists of Si/SiGe/Si

heterostructure in waveguide core and successfully demonstrated the enhancement in the plasma dispersion effect and free-carrier absorption for the first time. We have experimentally demonstrated that the modulation efficiency can be enhanced twice by introducing strained SiGe in the telecommunication wavelength range from 1.3 to 1.6 μm .

Finally, we have also demonstrated the high-speed optical modulator and variable optical attenuator, taking advantage of the strain-induced mass modulation which is effective to improve the plasma dispersion effect and free-carrier absorption. The introduction of compressively strained SiGe is a promising method of boosting the modulation efficiency of Si-based optical modulators. As is well known, technology for enhancing mobility by strain has been widely used in most Si metal-oxide-semiconductor (MOS) transistors to enhance the transistor performance since the first mass production of strained Si MOS transistors by Intel. In a similar manner, the strain-induced enhancement of the free-carrier effects can soon be applied to Si-based optical modulators to improve their performances owing to the compatibility of SiGe with the standard complementary metal-oxide-semiconductor (CMOS) process.

Acknowledgements

Since I moved to Tokyo for a graduate course in The University of Tokyo, I have started research on SiGe optical modulators/VOAs in Takagi-Takenaka group in electrical engineering and information systems. At the first time, we needed substrates for device fabrication to realize our goal. I still remember that I was operating MBE in room 100 to prepare SiGe substrates, but now many co-workers provide high-quality SiGe wafers, which make us focus on device fabrication and analysis thanks to our promising research results on SiGe technology for applications of optical modulators/VOAs. During this course in Takagi-Takenaka group, I could learn many things, not only knowledge for research on SiGe optical modulators/VOAs but also ability to systemically progress research. Also, I would like to mention that this successful research experience will be my one of the greatest properties in my life. Above all, I would like to express my gratitude to all who I owe many obligations, direct and indirect.

I especially wish to express my gratitude to my academic advisor, Assoc. Prof. Mitsuru Takenaka, and, who from the outset, encouraged me in my work, provided me with many details and suggestions for all of my research and carefully read the manuscript. For five years, I could learn how to progress the researches toward our goal from him.

I am also most grateful to Prof. Shinichi Takagi. His excellent insight and knowledge greatly gave me effects on my research life. Recently, I really enjoyed the discussions on electrical properties of the SiGe modulator and appreciate his advices and hospitality.

I greatly appreciate to Prof. Yoshiaki Nakano, Prof. Masaaki Tanaka, Assoc. Prof. Takashi Yatsui, and Assoc. Prof. Ishikawa Yasuhiko for their insightful and valuable comments. Thanks to those comments, this dissertation could be improved further.

I wish to record my appreciation to Dr. Masafumi Yokoyama and Dr. Ryosho Nakane who have given me help and encouragement over the period of PhD course. Especially, their empirical advices on process skills and maintenance of equipment have assisted my experiments.

I thank to our group members for giving me the opportunity to study with them. The constant discussions with them have been boosted motivation toward my tasks.

I would like to thank to Dr. Takenori Osada and Dr. Masahiko Hata, who provided high-quality SiGe epitaxial growth and its substrates. I could not make such great research accomplishments without their support.

I would like to appreciate to Dr. Junichi Fujikata and Dr. Shigeki Takahashi, who work together for SiGe optical modulators. Their advices on dynamic characterization of optical modulators were very helpful to accomplish this thesis.

I would like to express my thanks to the Japanese Government MEXT scholarship. It has financially supported my foreign life during five years.

Finally, I also want to take this opportunity to thank my parents, Kangtae Kim and Kangsoon Cho, and my sister, Youngeun Kim for having been there and providing all sorts of tangible and intangible support.

10th. Jan. 2015
Younghyun Kim

Contents

Abstract	i
Acknowledgements	iii
Contents	v

Chapter 1

Introduction

1.1	On-chip optical interconnects	1
1.2	Silicon photonics	4
1.3	Si optical modulators	6
1.4	Current issue in Si optical modulator	17
1.5	Research Objective	18
1.6	Outline of thesis	19
	References	22

Chapter 2

Theory of strain-induced enhancement of plasma dispersion effect and free-carrier absorption through mass modulation in SiGe

2.1	Introduction	26
2.2	Physical properties of SiliconGermanium	27
2.3	Plasma dispersion effect and free-carrier absorption SiGe	33
2.5	Conclusion	41
	References	42

Chapter 3

Numerical analysis of carrier-injection type SiGe optical modulator/attenuator

3.1	Introduction	44
3.2	Proposed device structure of carrier-injection type SiGe optical modulator	45
3.3	Simulation method	46
3.4	Device simulation result	47

3.5	Conclusion	56
	References	58

Chapter 4

Demonstration of SiGe rib waveguide for SiGe optical modulator/attenuator

4.1	Introduction	60
4.2	Device fabrication	61
4.3	Characterization of epitaxially grown Si/SiGe/Si-OI and device	62
4.4	Conclusion	69
	References	70

Chapter 5

Demonstration of enhanced free-carrier effect in carrier-injection type SiGe variable optical attenuator

5.1	Introduction	72
5.2	Experiment	74
5.3	Result and discussion	76
5.4	Conclusion	85
	References	86

Chapter 6

Low temperature Al₂O₃ surface passivation for high carrier-injection efficiency

6.1	Introduction	89
6.2	Evaluation of interface trap	91
6.3	Device fabrication and characterization	94
6.4	Conclusion	98
	References	99

Chapter 7

Optimization of distance between pin junctions for high carrier-injection efficiency

7.1	Introduction	102
-----	--------------	-----

7.2	Optimization of distance between highly doped p+ and n+ region	104
7.3	Device fabrication	105
7.4	Static characteristics	106
7.5	Dynamic characteristics	109
7.6	Conclusion	114
	References	115

Chapter 8

SiGe-based carrier-injection Mach-Zehnder modulator with enhanced plasma dispersion effect in strained SiGe

8.1	Introduction	117
8.2	Numerical analysis of strained SiGe MZ modulator	118
8.3	Fabrication of strained SiGe MZ modulator	120
8.4	Static characteristics of strained SiGe asymmetric MZ modulator	121
8.5	Dynamic characteristics of strained SiGe asymmetric MZI modulator	124
8.6	Power consumption of SiGe Mach-Zhender modulator	125
8.7	Conclusion	127
	References	128

Chapter 9

High Ge fraction SiGe optical modulator by considering Ge diffusion at high temperature process

9.1	Introduction	130
9.2	Design for SiGe layer of high Ge fraction with consideration of Ge diffusion	131
9.3	Numerical analysis on dependence of SiGe layer thickness in SiGe modulator	132
9.4	Estimation of higher Ge fraction SiGe layer in Si/SiGe/SOI	136
9.4	Conclusion	138
	References	139

Chapter 10

Numerical Analysis of Carrier-Depletion Strained SiGe Optical Modulators with Vertical P-N Junction

10.1	Introduction	140
10.2	Comparison of lateral and vertical pn junctions for carrier-depletion modulators	142
10.3	Carrier-depletion strained SiGe optical modulator with vertical pn junction	143
10.4	Conclusion	160
	References	161

Chapter 11

Conclusion

11.1	Conclusion	164
11.2	Future work and prospect	167
	References	169

List of Publications

171

Chapter 1

Introduction

Silicon photonics has attracted great attentions to solve the bottleneck of further increasing data transmission for internet data centers, high computing microprocessors and. To realize the brand new technology of Silicon photonics, the essential building blocks has been intensely researched in a decade. Among them, Si optical modulators based on the free-carrier effects have achieved dramatic development in terms of high-speed operation. However, the further improvement of modulation efficiency is required for small device footprint, well-suited for opto-electronic integrated circuits. In this chapter, the brief introductions of optical interconnect, Silicon photonics, and Si optical modulators will be shown. Then, we will make it clear what this thesis aims to.

1.1 On-chip optical interconnect

Burgeoning demand on data transmission has been issued in recent years due to tremendous growth of data traffic in internet data centers due to various applications such as massive storage and social networking. With regard to the further increasing data traffic, optical interconnect is expected to be a promising solution as it has been replaced the conventional copper interconnects from long-haul to short-haul communications with the advantage of its large bandwidth. The bottleneck of data transmission in high-computing microprocessors as well as internet data centers is one of the significant challenges in a decade, requiring the new technology for chip-to-chip and on-chip interconnects.

Si complementary metal-oxide-semiconductor (CMOS) technology has been dramatically developed by scaling law in last four decades. The numbers of transistors has been doubling per every 18 months for high computing microprocessors, which has had a negative impact on high resistivity of metal interconnects. There was one

improvement that the conventional copper interconnect in large scaled integrated circuits replaced the aluminum interconnect due to low resistivity and electromigration [1.1]. However, the copper interconnect couldn't resolve the further increasing resistivity as scaling. As technology node decreases, the resistivity increases due to grain boundary scattering and surface scattering [1.2], as shown in Fig. 1.1. As a result, power consumption in the copper interconnect has become the largest portion of power consumption in integrated circuit [1.3]. Also, the copper interconnect cannot keep pace with the transistor performance, meaning the propagation delay in global interconnect is a more dominant than gate delay [1.4]. Consequently, the replacement of the conventional copper interconnect is indispensable.

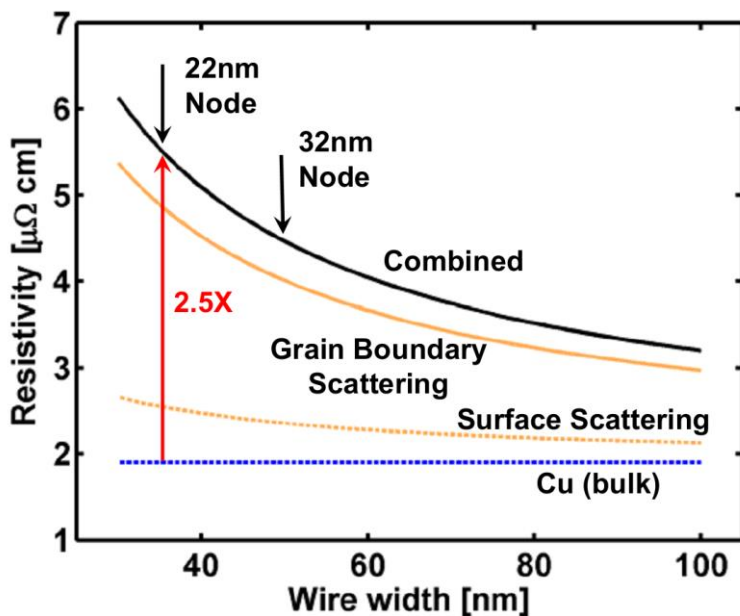


Figure 1.1 Resistivity as a function of wire width, corresponding to technology node^[1.5].

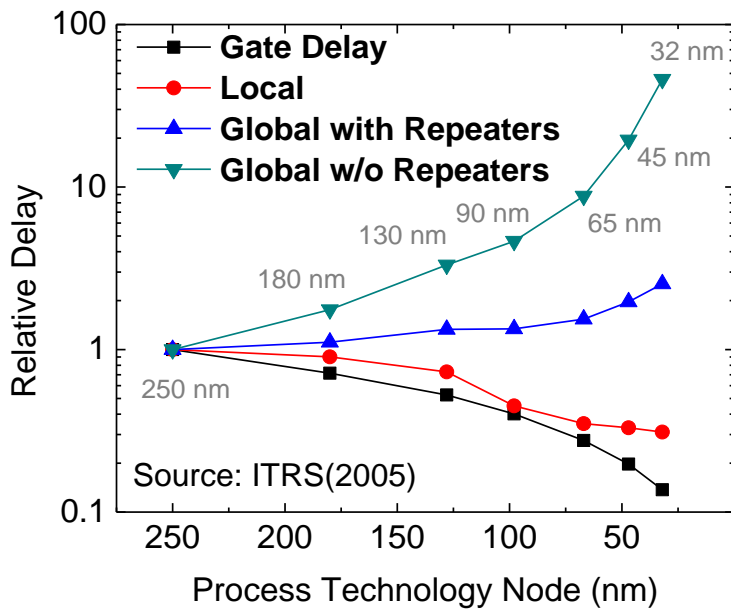


Figure 1.2 Relationship between relative delay and process technology node^[1.4].

As alternative candidates of copper replacements, various options have been reported by ITRS, which are nanowires, carbon nanotube and optical interconnect etc.^[1.4]. Among the applications, optical interconnect seems to be the most promising with the advantage of large bandwidth and low power consumption^[1.6]. As it has been seen in optical communication technology when the optical fibers replaced copper cables around globe and cities, the copper interconnect in a datacenter is now started to be replaced by optical fibers. Following this trend, optical interconnect can be competitive with the copper interconnect on-board and may even on-chip interconnect. The transition of electronics to optics for communications is well-depicted in Fig. 1.3. The demand on data transmission has been increasing in short distance communication. When the data transmission rate above approximately 10 Gb/s is required, it is important to transit to optical technology at a proper time. Therefore, it is necessary to develop the breakthrough technology which is high-performance as well as cost effective. In terms of that, Silicon photonics has been considered as one of the most promising candidate for short distance communication.

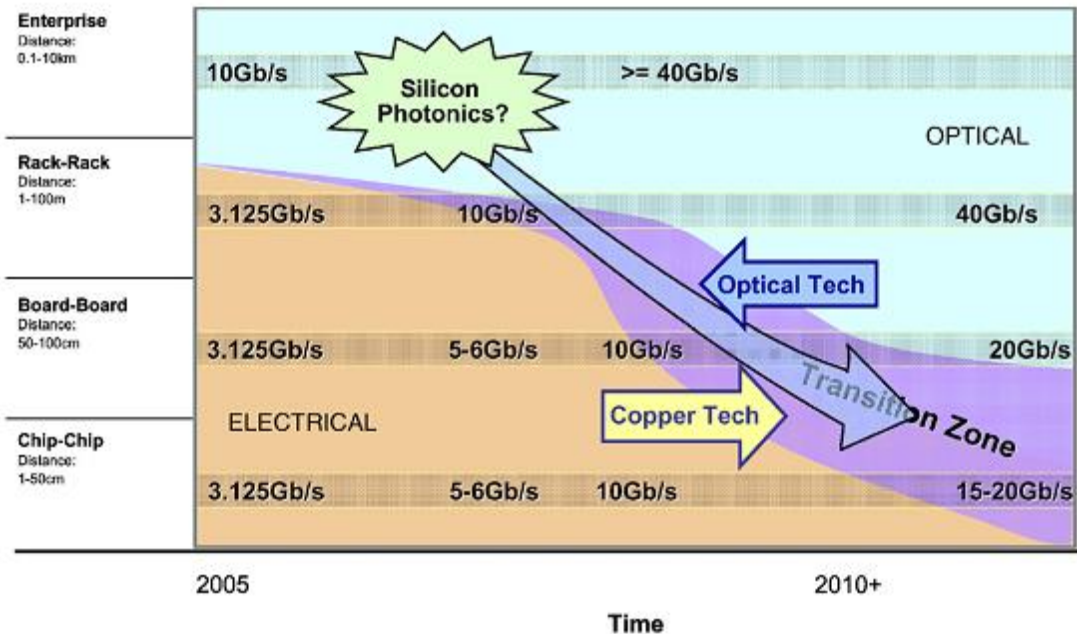


Figure 1.3 Schematic showing possible electrical-to-optical transition associated with various applications^[1.8].

1.2 Silicon Photonics

Silicon is an amazing material throughout the burgeoning development in electronics. However, in photonics, it is not a preferable material than III-V materials and Lithium Niobate (LiNbO_3) which have merits on optical properties for photonic devices even though Silicon has many advantages which are cost effective, well-understood, outstanding thermal and electrical properties for the semiconductor technology. The III-V materials are the relative ease of laser fabrication and prospect of optical amplification and electronic integration. The Lithium Niobate (LiNbO_3) has a large electro-optic coefficient, enabling optical modulation via the Pockels effect. In comparison of those materials, Silicon has the physical demerits for photonics such as the indirect bandgap which is unfavorable for light emission and a centro-symmetric crystal structure which cannot exhibit a linear electro-optic effect.

However, silicon has emerged as a key material for photonics, aiming to on-chip optical interconnects. The advantage of silicon for optical devices is that silicon is transparent at certain wavelength larger than $1.1 \mu\text{m}$, low cost, and well understood

material. In particular, with advent of SOI, silicon is not only an excellent material for electronics but also photonics because it provides strong optical confinement for telecommunication wavelengths, $1.31\text{ }\mu\text{m}$ and $1.55\text{ }\mu\text{m}$, which enables dramatic device scaling of the photonic devices. Furthermore, CMOS-compatible process of Silicon photonics results in further dense integration of optical and electrical circuitry, which results in the mass production of opto-electronic integrated circuits. Therefore, several researchers have been studying the possibility of silicon as a material for photonics to replace the conventional copper interconnects with the concept of Si photonics as shown in Fig. 1.4^[1.11].

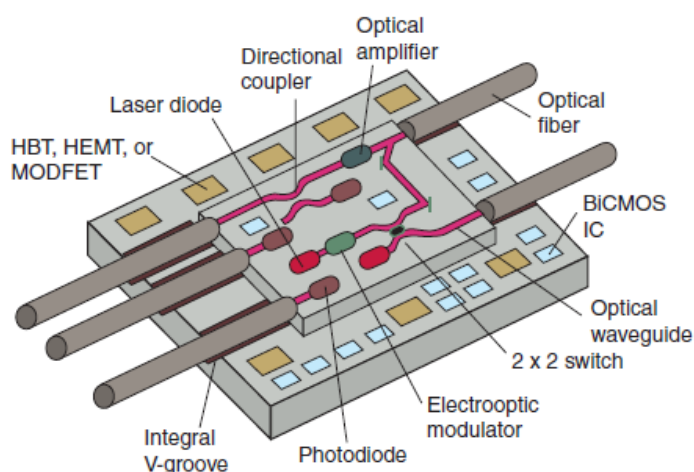


Figure 1.4 Silicon based optoelectronic integrated circuit “*Superchip*”^[1.11].

Silicon photonics means optical device or integrated photonic circuit technology which can be realized by CMOS-compatible process using Silicon-on-insulator (SOI) substrate. In recent years, the achievements in Silicon photonics technology make it possible to incorporate all of necessary components such as Silicon lasers, waveguides, modulators, and detectors with electronic devices on a chip, that is, monolithic integration with complementary metal-oxide-semiconductor (CMOS) technology. The building diagram shows the Si photonics system, mainly composed of transmitters and receivers including a laser, a modulator, a waveguide and a photodetector as shown in Fig. 1.5. Also, one of the pioneer companies in Si photonics, Luxtera has been demonstrated Si photonic integrated circuit as shown in Fig. 1.6^[1.12].

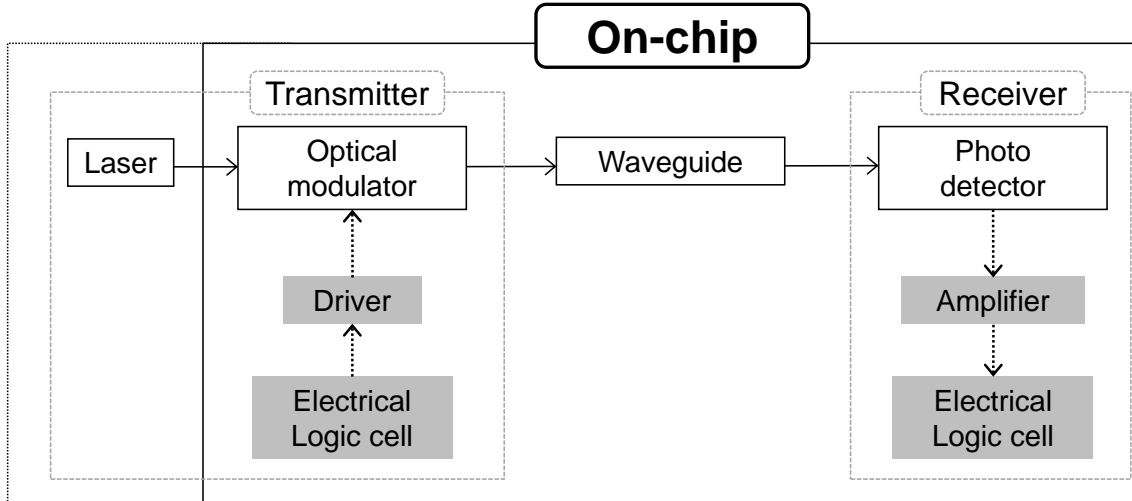


Figure 1.5 Diagram of essential building blocks for Silicon Photonics.

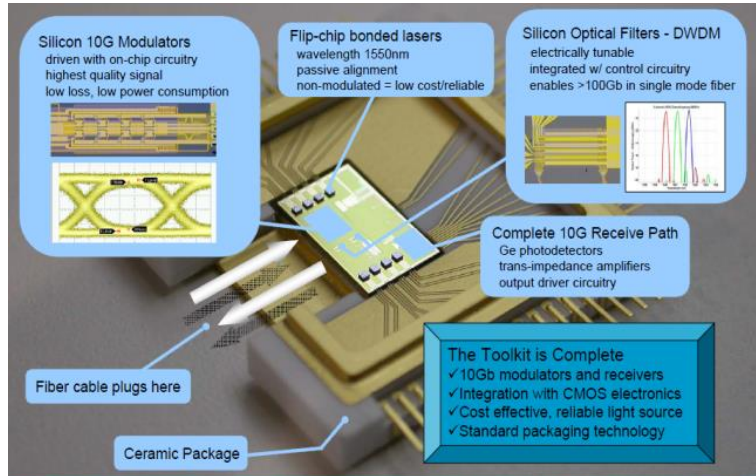


Figure 1.6 Overview of Si Photonics^[1,12].

1.3 Si optical modulator

The primary benefit of using light rather than an electrical signal over metallic wire is significantly greater capacitance. To encode the wealth of data, a modulator is the one of the most important components for OEIC (opto-electronic integrated circuit). Generally, an optical modulator is a device that modulates beam parameters such as intensity, phase, polarization, direction of propagation, and frequency (or wavelength) by method of external electric, magnetic, mechanic, and optic effect. For high speed and

controllability, electrical method is widely used to modulators to modulate phase and intensity of light, also in Si photonics.

The working principles of Si optical modulator are mainly classified by the free-carrier effects and the electric-field effects as shown in Fig. 1.7. The free-carrier effects are the plasma dispersion effect and free-carrier absorption which are the changes in refractive index and absorption coefficient by changes in carrier densities, respectively. In particular, the Si optical modulators based upon plasma dispersion effect have been mostly demonstrated using interferometers. In electric field effects, the pockels effect using strained Si, Franz-Keldish effect and quantum confinement stark effect (QCSE) using SiGe or Ge have been demonstrated on the SOI platform. We will describe the physical principle of each effects and show the remarkable demonstrations.

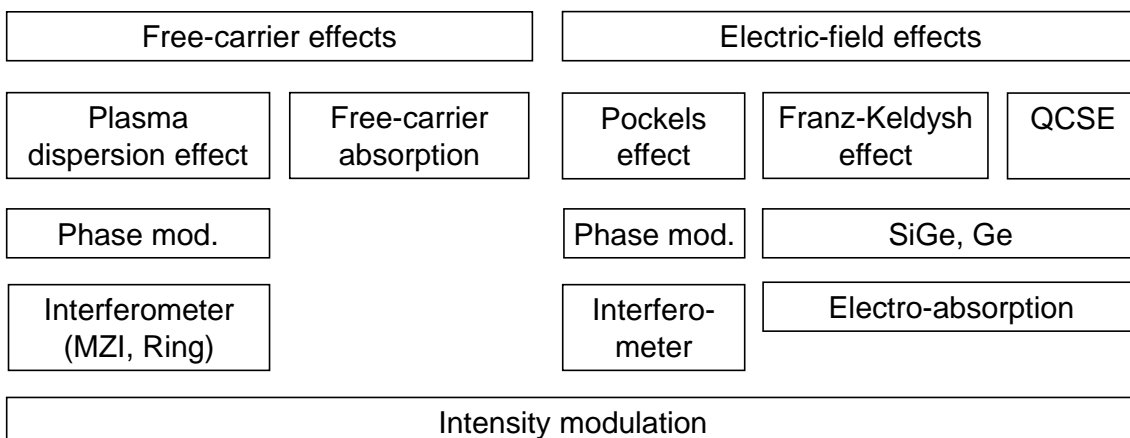


Figure 1.7 Classification of working principle of silicon optical modulators.

1.3.1 Free-carrier effects

The free-carrier effects are the physical phenomena by interaction between light and carriers, which are the plasma dispersion effect and free-carrier absorption. In particular, the plasma dispersion effect is the most common method to modulate the phase of light by changes in refractive index. Soref and Bennett published a paper performed to estimate the refractive index perturbations of Silicon produced by change in applied field and free-carrier densities. It showed that electric field based effects are extremely small but injected/depleted carriers has high potential as a modulation mechanism. The

change in refractive index and the absorption coefficient by variation of free-carrier densities can be expressed as the following equations, respectively:

$$\Delta n = -[8.8 \times 10^{-22} \times \Delta N_e + 8.5 \times 10^{-18} \times (\Delta N_h)^{0.8}] \quad (1.1)$$

$$\Delta \alpha = 8.5 \times 10^{-18} \times \Delta N_e + 6.0 \times 10^{-18} \times \Delta N_h \quad (1.2)$$

where ΔN_e , ΔN_h are the change of electron and hole concentrations in Silicon, respectively.

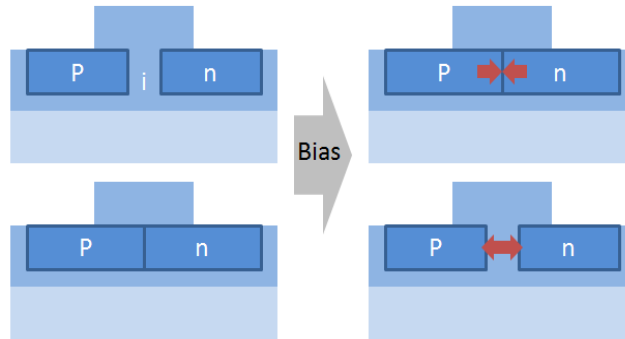


Figure 1.8 Carrier injection and depletion type modulators. Above figure is a *pin* diode in forward bias and below figure is a *pn* diode in reverse bias.

Using the two expressions above, it is easy to calculate both the changes, for instance, Δn of -1.67×10^{-3} and $\Delta \alpha$ of 7.25 cm^{-1} (31.5 dB/cm) at a wavelength of $1.55 \mu\text{m}$ in case of $5 \times 10^{17} \text{ cm}^{-3}$ of the both carrier densities. The value of $\Delta \alpha$ shows that the plasma dispersion has a significant potential as absorption based modulator. Figure 1.8 shows that carrier injection and depletion type modulators. Top part of the figure is a *pin* diode in forward bias and below part is a *pn* diode in reverse bias. While injection type of modulator has a strong effect with many carriers, slow modulation speed of $\sim 10 \text{ GHz}$ is a disadvantage due to minority carriers. However, the depletion type modulator has a fast modulation speed of $> 40 \text{ GHz}$ but weaker effect causes the length of the device longer.

The *pn*-depletion type modulator based on the plasma dispersion effect was proposed by Ling Lio et al. in 2007 [1,14]. The modulator composes an asymmetric Mach

Zehnder interferometer for intensity modulation as shown in Fig. 1.9(a). It has a data transmission speed of 40 Gbps and a 3-dB bandwidth of \sim 30 GHz. It is interesting to note two key points for device performance. First, the *pn*-junction and built-in depletion region are slightly above the center of the optical mode to optimize phase efficiency because the depletion region widens and sweeps to *p*-region for reverse biased as shown in Fig. 1.9(b). Secondly, a traveling wave electrode based on coplanar wave guide structure for RF signal is used to achieve high-speed performance, minimizing RC limitation. It is interesting to give a look at their further works, a silicon photonic integrated chip which is capable of total transmitting data of 200 Gbps with an array of eight modulators^[1,14].

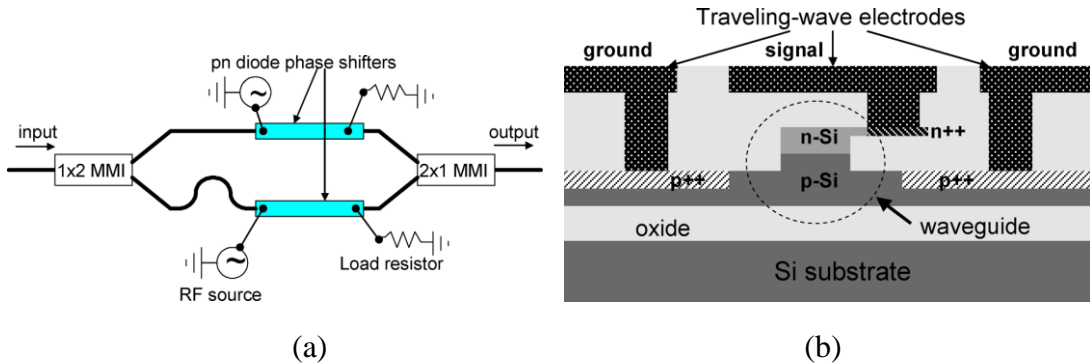


Figure 1.9 (a) Illustration of an asymmetric Mach-Zehnder interferometer modulator. (b) Cross-sectional view of a *pn* junction waveguide phase shifter^[1,14].

It is a challenge that the depletion type modulators based on the plasma dispersion effect are as large as several mm orders which are not favorable for OEIC. In terms of that, the injection type modulators have strong effect, resulting in small device footprint. However the bottleneck for injection type is hard to over transmission speed of 10 GHz owing to minority carrier lifetime. In this sense, it is interesting to note that the high-speed ring modulator first introduced by Cornell group, Q.Xu et al.^[1,16] has strong potential for high-speed operation using pre-emphasis method and monolithic integration with CMOS technology using ring resonator as a small device dimension of 12 μm . The device structure based a lateral *pin*-diode and transmission spectra of ring resonator are shown in Fig. 1.10(a). As shown in Fig. 1.10(b), the pre-emphasis driving method improved results of 16 Gbps at a modulation depth of 8 dB. However, the demerit of ring resonators is temperature dependent; therefore temperature stabilization

is necessary to be required. It is worthy to observe their further research on the dual ring resonator made of a simple integrated circuit connecting the two rings of fast modulation speed of > 40 Gbps, published in last year^[1.17].

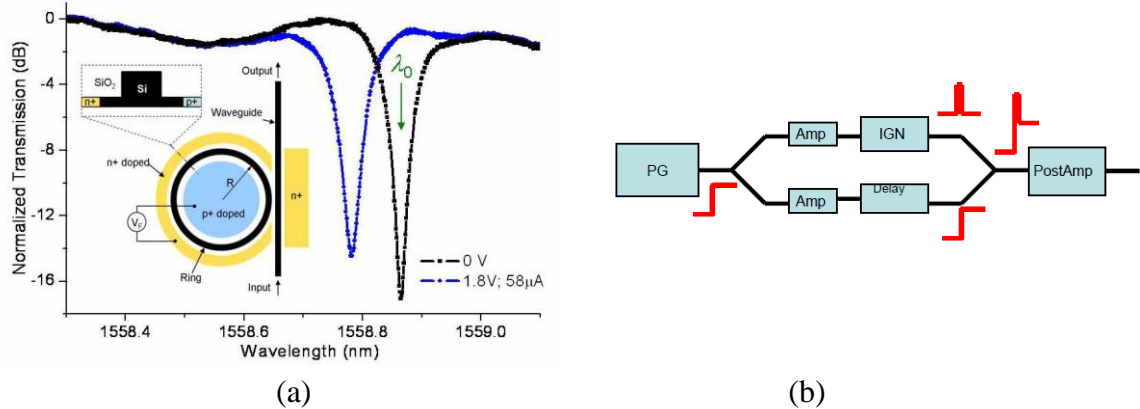


Figure 1.10 (a) Normalized transmission spectra of the modulator. Inset: schematic of the device structure. (b) Setup for generating pre-emphasized signals^[1.16].

Using a lateral pin junction based carrier injection type waveguide, the variable optical attenuator (VOA) as well as the modulator has been demonstrated using changes in absorption coefficient by free-carrier absorption. One of the research groups in Japan, NTT K. Yamada *et al.* has reported the integrated Si photonic components such as Si VOA, Ge photodetector on Si platform, and Array waveguide grating^[1.18]. Figure 1.11 shows the cross sectional schematic of Si VOA and its performance. 20 dB attenuation has been achieved 27.9 mA with a 0.5 mm-long device and the dynamic characteristics of 3 dB cut-off frequency is 100 MHz which is generally limited by minority carrier lifetime in *pin*-injection type modulator.

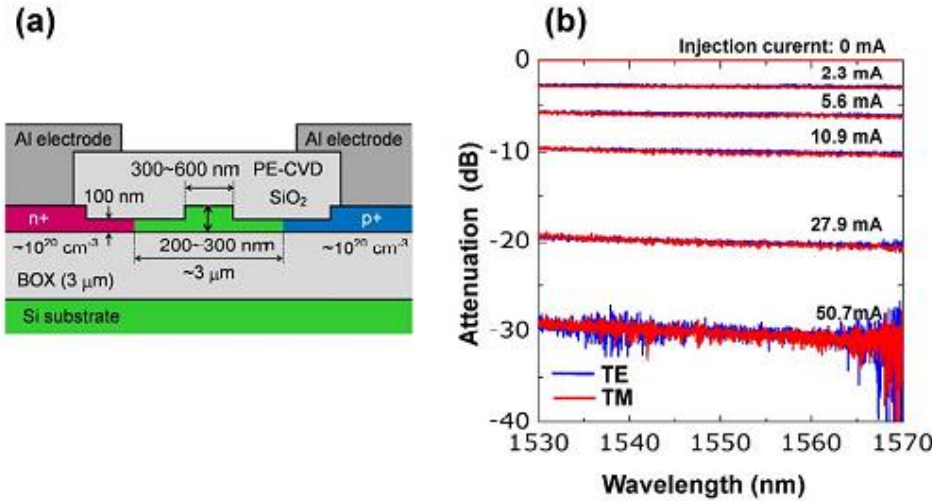


Figure 1.11 (a) Vertical structure and (b) VOA operation of silicon waveguide with lateral *pin* junction based carrier injection structure^[1,18].

1.3.2 Electro-field effects

The electro-filed effects have been used in the conventional modulators using several optical materials such as III-V compounds and Lithium Niobate (LiNbO₃). It is strong point that the modulation by electric field is much faster than that of carriers. As Soref showed that the electro-filed effect in pure Si is too small to apply, novel researches have been demonstrated the modulators using the electro-field effects in conjunction with the SOI platform, keeping CMOS compatibility of Si photonics. We will introduce the principle of the effects for modulator application and novel researches based on the electro-field effects.

For fast modulation speed and low power consumption, The Franz-Keldysh effect can be applied for an electro-absorption modulator (EAM). The Franz-Keldysh effect is a tunneling effect that external electric field allows tunneling of electrons and holes due to effectively decreased band gap as shown in Fig. 1.12. Thus, it causes the shift of the absorption band, in turn, modulated as shown Fig. 1.13.

J. Liu et al have a waveguide-integrated, gigahertz GeSi electro-absorption (EA) modulator as shown in Fig.1.14(a) on SOI for communication band applications with a ultra-small active device footprint of 30 μm², an ultra-low energy consumption of 50 fJ/bit, and an operational spectrum range of 1539-1553nm as shown in Fig.1.14(b)

^[1,19]. With an ultra-low energy consumption and a small device area, the device offers unique benefits for large scale electronic-photonic integration on Si. However, the 3-dB frequency of 1.2 GHz limited by the series resistance of the device as high as $\sim 15 \text{ k}\Omega$ is lower than those of the modulators which have usually faster than 10 GHz. The high series resistance is caused by the overetching of the n+ poly Si and p+ c-Si electrodes.

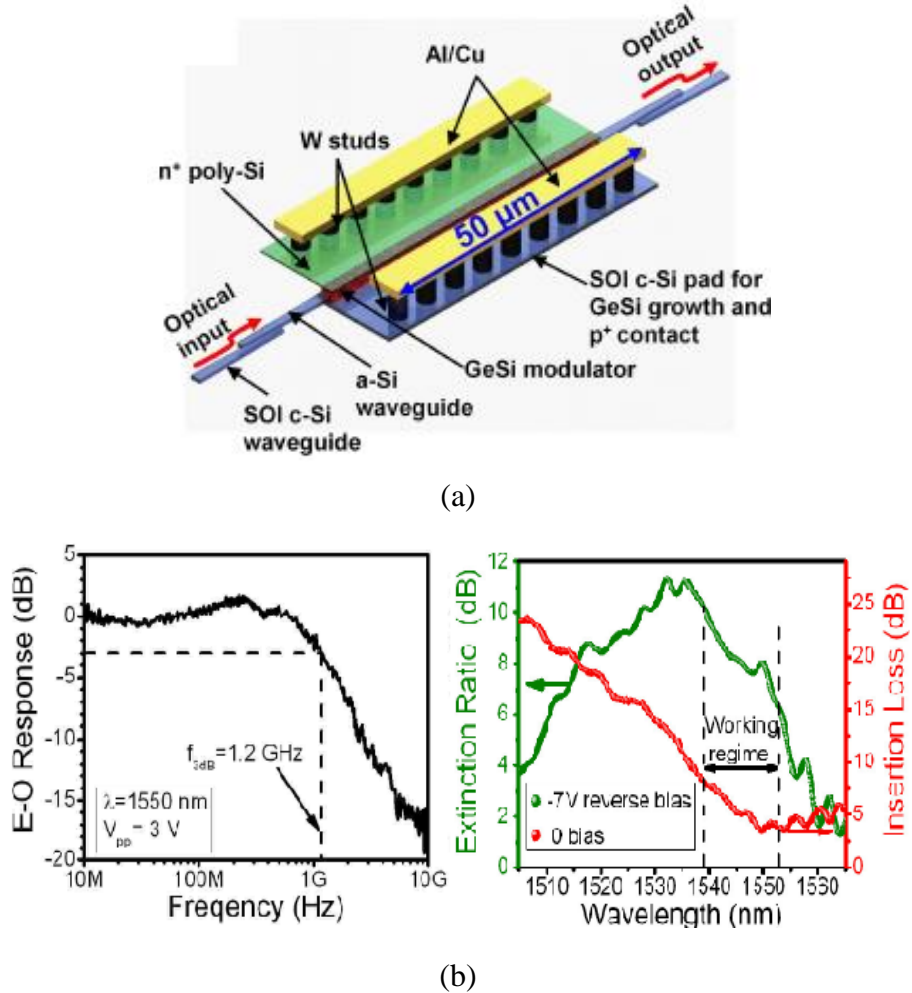


Figure 1.12 (a) Schematic diagram of a waveguide integrated GeSi EA modulator with c-Si to a-Si waveguide coupling (b) Dynamic electro-optical (E-O) response of the device in the frequency range of 10 MHz to 10 GHz, and extinction ratio at -7 V bias and insertion loss at 0 bias as a function of wavelength ^[1,19]

To understand Quantum Confinement Stark Effect deeply, it is necessary to understand the behavior of exciton in Multi Quantum Well (MQW). The exciton is a bound state of an electron and hole, generated by absorption, are attracted to each other

by the electrostatic Coulomb force. It doesn't exist in the crystal of bulk semiconductor because the binding energy of exciton is relatively smaller than thermal energy at room temperature [1.20]. However, in MQW structure, the exciton exists in quantum well structure owing to its confinement. For example, 10^4 V/m of electric field is applied to 10-nm-quantum well, it tilts 10 meV. The exciton in the quantum well does not dissociate at the electric field which is not enough to, and the absorption spectrum is observed to the peak structure that shifts to the low energy without dissociation. This phenomenon is called "Quantum Confinement Stark Effect". In comparison with the Franz-Keldysh effect, the absorption change is larger in QCSE because of taking advantage of the shift by the drastic exciton absorption spectrum. Overall, QCSE mechanism can be used today for high-speed, lower power telecommunication modulators with III-V materials as well as IV materials, Silicon and Germanium.

In case of next modulators, the QCSE may be the strongest and the most high-speed EA effect enabling modulators with only a few microns of optical path length even without the ring resonators. A surprising research on electroabsorption modulator is germanium quantum well structures, shown in Fig.1.16(a) on silicon based on the QCSE, reported by Yu-Hsuan Kuo et al^[1.21].

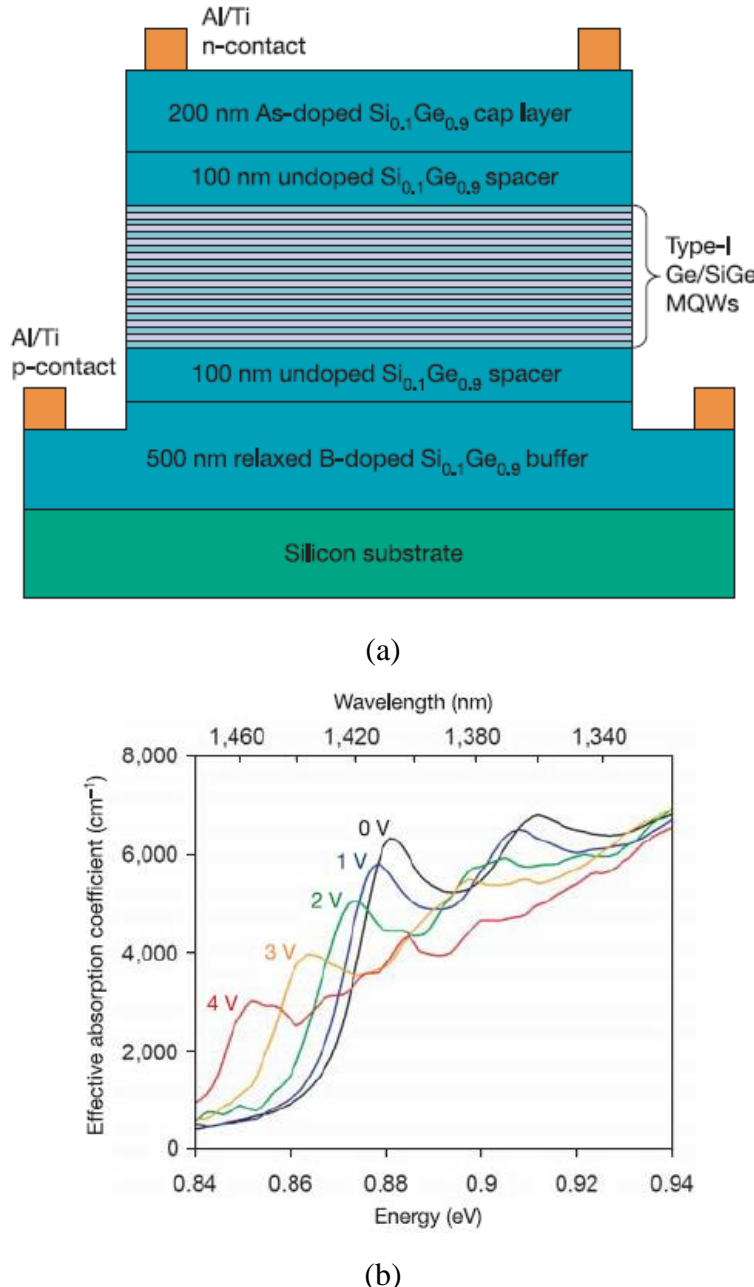


Figure 1.16 (a) A pin structure on silicon with Ge/SiGe quantum wells on relaxed SiGe buffer
(b) Effective absorption coefficient spectra. Strong QCSE is observed at room temperature with reverse bias from zero to 4V^[1,21].

Even though the structure has not a modulator with waveguide, it confirmed that the behavior of the exciton peaks, the band edge shift and the shift in absorption coefficient are comparable to those observed in III-V materials at similar wavelengths as shown in Fig.16(b), and this approach is very promising for silicon based

electroabsorption modulator at high speed, low power, low operating voltage with small device dimension. Their next research, their next research on fabrication of coplanar high-speed optical modulator based on the Ge/SiGe quantum well shows performances of the modulator, an eye diagram 3.125 GHz and small-signal optical modulation of up to 13 GHz^[1,22]. For further advancement, it should be considered to operate at 1.55 μm which is compatible with long-distance telecommunications.

One of the interesting modulator is strained silicon as a new electro-optic material reported by Rune S. Jacobsen et al^[1,23]. They have found that a significant linear optic effect, Pockels effect, is induced in silicon by isotropic crystal symmetry, and then, the induced nonlinear coefficient makes it possible to realize a silicon electro optic modulation. To achieve isotropic crystal symmetry of silicon, they used silicon nitride glass (Si_3N_4) as a straining layer as shown Fig. 1.17. It has the ability to induce a change in effective refractive index which can be applied to make an amplitude modulator using MZI.

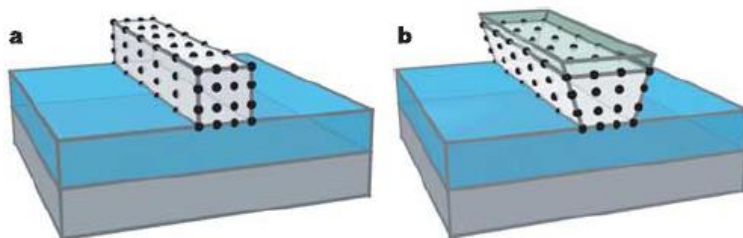


Figure 1.17 Applying strain to crystalline silicon. (a) Waveguide fabricated in the top layer of an SOI wafer. (b) The same waveguide with a straining layer deposited on top. The straining layer breaks the inversion symmetry and induces a linear electro-optic effect^[1,23].

1.3.3 Comparison of Si-based optical modulators

As discussed above, various Si-based optical modulators have been demonstrated with novel structures utilizing electro-optic effects in Si or SiGe. There are requirements for optical modulators for EPIC such as operating voltage, power consumption, footprint, CMOS compatibility, operating wavelength range, insertion loss, and modulation speed. It is difficult to perfectly satisfy the requirements; therefore, it is highly important to figure out their pros and cons. Table 1.1 shows the comparison of Si-based optical modulators of free-carrier effects-based carrier-injection, carrier-depletion, carrier-accumulation MZ modulators and QCSE-based intensity modulator. We

summarized the comparison of four types of modulators in terms of the requirements.

For the requirements of operating voltage, power consumption, and footprint related to the modulation efficiency, a QCSE-based modulator has the highest score due to its strong effect. For free-carrier effects, carrier-injection type modulator shows relatively higher performance due to large changes in carriers comparing to carrier-depletion and carrier accumulation types. However, QCSE-based modulators are low CMOS compatibility owing to the complex structure, and it has some other drawbacks on high insertion loss and limited wavelengths. In terms of that, carrier-injection MZ modulators are highly CMOS compatibility, and they shows large wavelength and low insertion loss. Even though the modulation speed is limited by minority carrier lifetime, the recent demonstration shows 50 Gbps data transmission^[1,24] by the pre-emphasis method. Therefore, it is promising for optical modulators in OEIC to utilize carrier-injection MZ modulators.

Table 1.1 Comparison of Si-based optical modulators

	Carrier-injection MZM (PIN)	Carrier-depletion MZM (PN)	Carrier-accumulation MZM (MOS)	QCSE
Operating voltage	◎	△	○	◎
Power consumption	○	△	△	◎
Footprint	○	×	△	◎
CMOS compatibility	◎	◎	◎	△
Operating wavelength	◎	◎	◎	×
Insertion loss	◎	○ or △	△	×
Modulation speed	×→△	○	○	◎

1.4 Current issue in Si optical modulators

As introduced above, the various Si optical modulators have been demonstrated from the remarkable demonstrations. Among the various effects, the plasma dispersion effect of the free-carrier effects and Franz-Keldysh effect and QCSE of the electro-optic effects have been widely used for state-of-the-art Si-based optical modulators. However, the optical modulators based on Franz-Keldysh effect and QCSE needs high Ge fraction in SiGe and relatively complex fabrication process, which make those low CMOS compatibility. Also, the modulation occurs the particular wavelength region because the change in the absorption coefficient is large at the edge of bandgap, which results in high loss and limited working wavelength range. Comparing to those electro-absorption modulators, the Si optical modulators based on the plasma dispersion effect and MZI are highly CMOS compatible with the conventional lateral *pn* or *pin* junctions and broad wavelengths for operation. Therefore, the Si optical modulators based upon the plasma dispersion effect have been mostly researched for OEIC.

The most of demonstrated modulators based on the plasma dispersion effect has several bottlenecks of a long phase shifter, high driving voltage and power consumption comparing to modulators of electro-optic effect, which is not preferable to the integrated circuits. This is because the weak free-carrier effects in Si cause the low modulation efficiency, resulting in the larger device footprint, higher driving voltage, and high power consumption^{[1.13], [1.25], [1.26]}. In particular, it is the most important to focus on device power consumption to replace conventional metal interconnect by optical interconnect. Considering the power consumption of the current electrical interconnect, the system of optical interconnect should be ~ 100 fJ/bit or lower for off-chip and 50 – 200 fJ/bit or lower to offer sufficient advantages of optical interconnect. In terms of that, optical modulators should operate with several tens of fJ/bit or lower^[1.27]. For example, the demonstrated carrier-injection type Si optical modulator^[1.13] shows the power consumption of 5 pJ/bit with 10-Gbps-speed operation, which is too high to compose of optical interconnect. Therefore, it is required to fundamentally enhance the plasma dispersion effect for small device footprint, low driving voltage, and low power consumption.

1.5 Research Objectives

To achieve small device footprint, it is important to fundamentally boost the free-carrier effects. SiGe technology is applied to enhance the effects, well-known technology for enhancing mobility by strain has been widely used in most Si metal-oxide-semiconductor (MOS) transistors to enhance the transistor performance since the first mass production of strained Si MOS transistors by Intel^[1.28].

The plasma dispersion effect and free-carrier absorption are expressed by the Drude model, which describes the changes in the refractive index (Δn) and absorption coefficient ($\Delta\alpha$) arising from a change in the plasma frequency of free carriers, which is dependent on not only the number of free carriers but also their conductivity effective masses. According to the model, the Δn induced by the plasma dispersion effect is inversely proportional to the conductivity effective masses of electrons and holes. Therefore, the lighter the conductivity masses become, the greater the plasma dispersion is^{[1.29], [1.30]}. It was also experimentally observed that the plasma dispersion effect and free-carrier absorption in Si at the far-infrared wavelength range from 5 to 20 μm were modified by uniaxial strain mechanically applied to Si through strain-induced mass modulation^{[1.31], [1.32], [1.33]}. However, there has not been experimental proof in near-infrared wavelength range, which is the most important range for optical communication.

In this thesis, the main research objective is to demonstrate the enhancement of free-carrier effects by strain-induced mass modulation in strained SiGe optical modulator/attenuator in near-infrared wavelengths. We have investigated the enhancement of plasma dispersion effect and free-carrier absorption by strain-induced mass modulation in Si/strained SiGe/Si double-heterostructure waveguide with a lateral *p*-*n*-junction for carrier injection at the near-infrared wavelength range from 1.3 to 1.6 μm , which are most important wavelengths for optical communications. Furthermore, we will demonstrate the development of SiGe optical modulator/ attenuator for high modulation efficiency, taking advantage of the enhanced free-carrier effects by strain-induced mass modulation in SiGe.

1.6 Outline of thesis

This thesis consists of 11 chapters which are different stories but ultimately same goal for advanced Si-based optical modulator by strain-induced enhancement of free-carrier effects in SiGe.

In chapter 2, it is introduced that strain effect on the plasma dispersion effect and free-carrier absorption in SiGe. The physical properties of SiGe and strained SiGe are briefly reviewed for the theory of strain-induced enhancement. Then, the enhancement are shown, which is quantitatively analyzed.

In chapter 3, we propose the carrier-injection type of SiGe optical modulator/attenuator to demonstrate strain-induced enhancement of the plasma dispersion effect and free-carrier absorption in SiGe. The working principle of carrier-injection type optical modulator will be introduced first. Strain effect on carrier-injection type SiGe optical modulators is numerically investigated.

In chapter 4, we demonstrate photonic-wire waveguides with Si/SiGe/Si heterostructure ribs for Si-based optical modulators. The Si (80 nm)/Si_{0.72}Ge_{0.28} (40 nm) layers grown on Si-on-insulator by molecular beam epitaxy for optical modulators were evaluated by *in-situ* reflection high-energy electron diffraction, atomic force microscope, X-ray diffraction and Raman spectroscopy, exhibiting that the fully-strained highly-crystalline SiGe layer was obtained.

In chapter 5, we have experimentally investigated the enhancement of the plasma dispersion effect and free-carrier absorption by strain-induced mass modulation in silicon-germanium (SiGe). The strained SiGe-based optical modulator exhibits more than twice modulation efficiency as large as that of the Si modulator. It is the first demonstration of the enhanced free-carrier effects in strained SiGe at the near-infrared telecommunication wavelength.

In chapter 6, we show that the surface passivation technique using Al₂O₃ deposited by atomic layer deposition (ALD) at 200 °C is examined to suppress surface recombination for carrier-injection SiGe optical modulators. We have investigated the interface trap densities at SiO₂/Si and Al₂O₃/Si interfaces formed by plasma enhanced chemical vapor deposition (PECVD) and ALD, respectively. By evaluating metal-oxide-semiconductor (MOS) capacitors formed on Si surfaces after dry etching,

we found that the interface trap density of Al_2O_3 passivated surface is more than one order of magnitude less than that of SiO_2 passivated one. As a result, the modulation efficiency is improved by 1.3 by inserting Al_2O_3 layer prior to SiO_2 deposition by PECVD owing to superior interface between Al_2O_3 and Si.

In chapter 7, We demonstrate a strained SiGe variable optical attenuator (VOA) with a lateral *pin* junction which has record-low injection-current by applying enhanced free-carrier absorption in compressively strained SiGe. We have optimized the distance between highly doped regions of p+ and n+ alongside a waveguide core to effectively inject electrons and holes, taking into account the attenuator loss. The strained SiGe VOA with optimized lateral *pin* junction represents 20-dB attenuation by 20-mA/mm injection current, which is 1.5 times lower current density than that of the Si VOA. For dynamic characteristics, the SiGe VOA shows the higher small-signal response than the Si VOA. Furthermore, 2-GHz switching and error-free transmission of 50-Gbps WDM signal have been also achieved.

In chapter 8, we demonstrate strained SiGe-based carrier-injection MZ optical modulator with low driving current of 1.47 mA owing to the enhanced plasma dispersion effect in SiGe. The 10 Gbps modulation with clear eye opening is also obtained.

In chapter 9, we propose a novel method to achieve high Ge fraction SiGe optical modulator taking into account Ge diffusion. The thickness dependence of $\text{Si}_{0.7}\text{Ge}_{0.3}$ optical modulator is estimated. Sub-mA for π -phase shift can be achieved even 20-nm-thick $\text{Si}_{0.7}\text{Ge}_{0.3}$ with 2-times enhancement factor. Higher Ge fraction SiGe wafers are prepared for high Ge fraction SiGe optical modulator. 20- and 15-nm-thick $\text{Si}_{0.4}\text{Ge}_{0.6}$ show cracks, indicating strain relaxation. 10-nm-thick $\text{Si}_{0.4}\text{Ge}_{0.6}$ is promising for 20-nm-thick $\text{Si}_{0.7}\text{Ge}_{0.3}$ optical modulator.

In chapter 10, the modulation characteristics of carrier-depletion strained SiGe optical modulators with a vertical *p-n* junction are numerically analyzed by technology computer-aided design (TCAD) simulation and finite-difference optical mode analysis. In addition to the strong optical confinement in vertical direction for the fundamental transverse electric field (TE) mode, the vertical *p-n* junction effectively depletes the strained SiGe layer where the plasma dispersion effect is enhanced owing to the mass

modulation of hole by strain. We predict that the $\text{Si}_{0.7}\text{Ge}_{0.3}$ optical modulator exhibits the $V_{\pi}L$ as small as 0.31 V-cm at a bias voltage of -2 V, which is approximately 1.8 times smaller than that of the Si optical modulator. The product of $V_{\pi}L$ and the phase-shifter loss ($\alpha V_{\pi}L$) is also expected to exhibit as low as -18.3 V-dB at -2 V, enabling the optical modulation with 5-dB extinction ratio in a symmetric Mach-Zehnder modulator.

In chapter 11, the most important thing in this thesis is that we have successfully demonstrated strain-induced enhancement free-carrier effects in SiGe and optical modulators and variable optical attenuators using strained SiGe with the enhancement. In this chapter, we conclude each chapter and we discuss the future works and prospect with regard to strained SiGe technology for optical modulators.

References

- [1.1] Tapan Gupta, "Copper interconnect technology", Springer, (2009).
- [1.2] W. Steinhogl, G. Schindler, G. Steinlesberger, and M. Engelhardt, "Size-dependent resistivity of metallic wires in the mesoscopic range," *Physical Review B*, vol. 66, Aug 15 2002.
- [1.3] N. Magen, A. Kolodny, U. Weiser, and N. Shamir, "Interconnect-power dissipation in a microprocessor," in Proceedings of the 2004 International Workshop on System Level Interconnect Prediction (ACM, 2004), pp. 7–13.
- [1.4] International Technology Roadmap for Semiconductors (ITRS), interconnect section, 2005.
- [1.5] K. Saraswat, H. Cho, Kapur, Pawan, K-H. Koo, "Performance comparison between copper, carbon nanotube, and optical interconnects," Circuits and Systems, 2008. ISCAS 2008. IEEE International Symposium on.
- [1.6] International Technology Roadmap for Semiconductors (ITRS), interconnect section, 2011.
- [1.7] K. H. Koo, H. Cho, P. Kapur, and K. C. Saraswat, "Performance comparisons between carbon nanotubes, optical, and Cu for future high-performance on-chip interconnect applications," *IEEE Transactions on Electron Devices*, vol. 54, pp. 3206-3215, Dec 2007.
- [1.8] P. Kapur and K. C. Saraswat, "Optical interconnects for future high performance integrated circuits," *Physica E-Low-Dimensional Systems & Nanostructures*, vol. 16, pp. 620-627, Mar 2003.
- [1.9] A. S. Liu and M. Paniccia, "Advances in silicon photonic devices for silicon-based optoelectronic applications," *Physica E-Low-Dimensional Systems & Nanostructures*, vol. 35, pp. 223-228, Dec 2006.
- [1.10] P. Kapur and K.C. Saraswat, "Comparisons between electrical and optical interconnects for on-chip signaling", Interconnect Technology Conference, 2002. Proceedings of the IEEE 2002 International, pp. 88-91, 2002.
- [1.11] G. Abstreiter, "Engineering the Future of Electronics," *Physics World*, vol. 5, pp. 36-39, Mar 1992.
- [1.12] C. Gunn, "CMOS photonics for high-speed interconnects," *IEEE Micro*, vol.

26, pp. 58-66, Mar-Apr 2006.

- [1.13] W. M. J. Green, M. J. Rooks, L. Sekaric, and Y. A. Vlasov, "Ultra-compact, low RF power, 10 gb/s silicon Mach-Zehnder modulator," *Optics Express*, vol. 15, pp. 17106-17113, Dec 10 2007.
- [1.14] L. Liao, A. Liu, D. Rubin, J. Basak, Y. Chetrit, H. Nguyen, R. Cohen, N. Izhaky, and M. Paniccia, "40 Gbit/s silicon optical modulator for high-speed applications," *Electron. Lett.* **43**, no. 22, (2007).
- [1.15] L. Liao, A. Liu, D. Rubin, J. Basak, Y. Chetrit, H. Nguyen, *et al.*, "40 Gbit/s silicon optical modulator for high-speed applications," *Electronics Letters*, pp. 51-52, Jun 2009.
- [1.16] Q. F. Xu, B. Schmidt, S. Pradhan, and M. Lipson, "Micrometre-scale silicon electro-optic modulator," *Nature*, vol. 435, pp. 325-327, May 19 2005.
- [1.17] Q. F. Xu, "Silicon dual-ring modulator," *Optics Express*, vol. 17, pp. 20783-20793, Nov 9 2009.
- [1.18] S. Park, K. Yamada, T. Tsuchizawa, T. Watanabe, H. Nishi, H. Shinojima, *et al.*, "All-silicon and in-line integration of variable optical attenuators and photodetectors based on submicrometer rib waveguides," *Opt Express*, vol. 18, pp. 15303-10, Jul 19 2010.
- [1.19] J. Liu, M. Beals, A. Pomerene, S. Bernardis, R. Sun, J. Cheng, *et al.*, "Waveguide-integrated, ultralow-energy GeSi electro-absorption modulators," *Nature Photonics*, vol. 2, pp. 433-437, Jul 2008.
- [1.20] D. A. B. Miller, D. S. Chemla, T. C. Damen, A. C. Gossard, W. Wiegmann, T. H. Wood, *et al.*, "Electric-Field Dependence of Optical-Absorption near the Band-Gap of Quantum-Well Structures," *Physical Review B*, vol. 32, pp. 1043-1060, 1985.
- [1.21] Y. H. Kuo, Y. K. Lee, Y. S. Ge, S. Ren, J. E. Roth, T. I. Kamins, *et al.*, "Strong quantum-confined Stark effect in germanium quantum-well structures on silicon," *Nature*, vol. 437, pp. 1334-1336, Oct 27 2005.
- [1.22] Y. W. Rong, Y. S. Ge, Y. J. Huo, M. Fiorentino, M. R. T. Tan, T. I. Kamins, *et al.*, "Quantum-Confining Stark Effect in Ge/SiGe Quantum Wells on Si," *IEEE Journal of Selected Topics in Quantum Electronics*, vol. 16, pp. 85-92, Jan-Feb

2010.

- [1.23] R. S. Jacobsen, K. N. Andersen, P. I. Borel, J. Fage-Pedersen, L. H. Frandsen, O. Hansen, *et al.*, "Strained silicon as a new electro-optic material," *Nature*, vol. 441, pp. 199-202, May 11 2006.
- [1.24] S. Akiyama, T. Baba, T. Akagawa, M. Noguchi, E. Saito, Y. Noguchi, N. Hirayama, T. Horikawa, T. Usuki "50-Gb/s Silicon Modulator Using 250- μ m-Long Phase Shifter Based-on Forward-Biased Pin Diodes" Group IV Photonics (GFP), 2012 IEEE 9th International Conference on, ThC2.
- [1.25] T. Baehr-Jones, R. Ding, Y. Liu, A. Ayazi, T. Pinguet, N. C. Harris, *et al.*, "Ultralow drive voltage silicon traveling-wave modulator," *Optics Express*, vol. 20, pp. 12014-12020, May 21 2012.
- [1.26] J. F. Ding, R. Q. Ji, L. Zhang, and L. Yang, "Electro-Optical Response Analysis of a 40 Gb/s Silicon Mach-Zehnder Optical Modulator," *Journal of Lightwave Technology*, vol. 31, pp. 2434-2440, Jul 15 2013.
- [1.27] D. A. B. Miller, "Device Requirements for Optical Interconnects to Silicon Chips," *Proceedings of the IEEE*, vol. 97, pp. 1166-1185, Jul 2009.
- [1.28] T. Ghani *et al.*, "A 90nm high volume manufacturing logic technology featuring novel 45nm gate length strained silicon CMOS transistors". *Tech. Dig. Int. Electron Devices Meeting*, (Washington, D.C., 2003).
- [1.29] M. Takenaka and S. Takagi, "Strain Engineering of Plasma Dispersion Effect for SiGe Optical Modulators," *IEEE Journal of Quantum Electronics*, vol. 48, pp. 8-16, Jan 2012.
- [1.30] Y. Kim, M. Yokoyama, N. Taoka, M. Takenaka, and S. Takagi, "Ge-rich SiGe-on-insulator for waveguide optical modulator application fabricated by Ge condensation and SiGe regrowth," *Opt Express*, vol. 21, pp. 19615-23, Aug 26 2013.
- [1.31] A. K. Walton, "Infrared Modulation and Energy Band Parameters in Multivalley Semiconductors through Uniaxial Stress Dependence of Free Carrier Contribution to Optical Constants," *Physica Status Solidi B-Basic Research*, vol. 43, pp. 379-&, 1971.
- [1.32] A. K. Walton and S. F. Metcalfe, "Free-Carrier Absorption at

Low-Temperatures in Uniaxially Stressed N-Type Ge, Si and Gaas," *Journal of Physics C-Solid State Physics*, vol. 9, pp. 3605-3625, 1976.

- [1.33] A. E. Belyaev, O. P. Gorodnichii, E. V. Pidlisny, Z. A. Demidenko, and P. M. Tomchuk, "Free Carrier Absorption in Uniaxially Stressed N-Si," *Solid State Communications*, vol. 42, pp. 441-445, 1982.

Chapter 2

Theory of strain-induced enhancement of plasma dispersion effect and free-carrier absorption through mass modulation in SiGe

Strain effect on the plasma dispersion effect and free-carrier absorption in SiGe will be introduced in this chapter. The SiGe which can be coherently grown on Si has lighter effective mass for holes with an increase in Ge fraction, resulting in larger free-carrier effects. The effective mass is calculated by the $k \cdot p$ method. Then, we estimate the enhancement of the plasma dispersion effect and free-carrier effect based on Drude model. The enhancement factors of changes in refractive index (Δn) and absorption coefficient ($\Delta \alpha$) increase with an increase in Ge fraction and are expected to be approximately 2 for Δn and 3 for $\Delta \alpha$ in compressively $\text{Si}_{0.7}\text{Ge}_{0.3}$ which are promising for carrier-injection type optical modulators/attenuators.

2.1 Introduction

Nowadays, the SiGe technology is one of the familiar technologies in semiconductor industry. In particular, it is the well-known technology to enhance mobility by strain, which has been widely used in most Si metal-oxide-semiconductor (MOS) transistors to enhance the transistor performance since the first mass production of strained Si MOS transistors by Intel^[2,1]. The CMOS compatibility of SiGe is one of the strong points for the application of strained SiGe optical modulator in this sturdy.

In this chapter, we will introduce physical properties of SiGe. Then, the theory on strain-induced enhancement of the free-carrier effects through mass modulation in

SiGe will be demonstrated as the most important concept.

2.2 Physical property of SiliconGermanium

Silicon-germanium (SiGe) is an alloy semiconductor consisting of Si and Ge with diamond structure. Both Si and Ge are the group IV materials. To understand the physical property of SiGe, it is necessary to start from the property of the each semiconductor of Si and Ge since the property of SiGe is originated from Si and Ge. They show indirect transition between the conduction band and the valence band that means an indirect bandgap. Both of materials have the valence band edge (maximum energy level) at Γ -valley consisting of degenerated LH (light hole) and HH (heavy hole) bands, and a SO (split off) band positioned at lower energy level than that of them. The conduction band edges (minimum energy level) are at Δ -valley and L -valley for Si and Ge respectively in E - k space.

Physical properties at room temperature of Si and Ge are shown in Table 2.1. The physical property of SiGe can be roughly estimated by interpolating of the properties of Si and Ge. However, the physical property cannot be estimated when the strain is applied in the alloy. As shown in Table 2.1, the lattice mismatch between Si and Ge is as large as 4%. Therefore, the SiGe in lattice-unmatched system has the different physical properties to lattice-matched system. The former is strained SiGe and the latter is relaxed SiGe. In particular, the effective mass of holes is important parameter when the strain is applied in this study.

Table. 2.1 Properties of Silicon and Germanium at 300K [2.2].

Property	Symbol (Unit)	Ge	Si
Atoms/cm ³	(cm ⁻³)	4.42×10^{22}	5.0×10^{22}
Atomic weight	(-)	72.60	28.09
Breakdown field	E_b (V/cm)	$\sim 10^5$	$\sim 3 \times 10^5$
Crystal structure	(-)	Diamond	Diamond
Density	d (g/cm ³)	5.3267	2.328
Dielectric constant	ϵ_s (-)	16.0	11.9
Effective DOS in CB	N_s (cm ⁻³)	1.04×10^{19}	2.8×10^{19}
Effective DOS in VB	N_v (cm ⁻³)	6.0×10^{18}	1.04×10^{19}
Effective mass	m^*/m_0		
Electrons (longitudinal)	m_l^*	1.64	0.98
Electrons (transverse)	m_t^*	0.082	0.19
Light holes	m_{lh}^*	0.044	0.16
Heavy holes	m_{hh}^*	0.28	0.49
Electron affinity	χ (eV)	4.0	4.05
Energy gap at 300K	E_g (eV)	0.66	1.12
Intrinsic carrier concentration	n_i (cm ⁻³)	2.4×10^{13}	9.65×10^{10}
Lattice constant	a (Å)	5.64613	5.43095
Melting point	(°C)	937	1415
Minority carrier lifetime	(s)	10^{-3}	2.5×10^{-3}
Thermal diffusivity	(cm ² /s)	0.36	0.9
Mobility (drift)			
Electron	μ_e (cm ² /Vs)	3900	1500
Hole	μ_h (cm ² /Vs)	1900	450

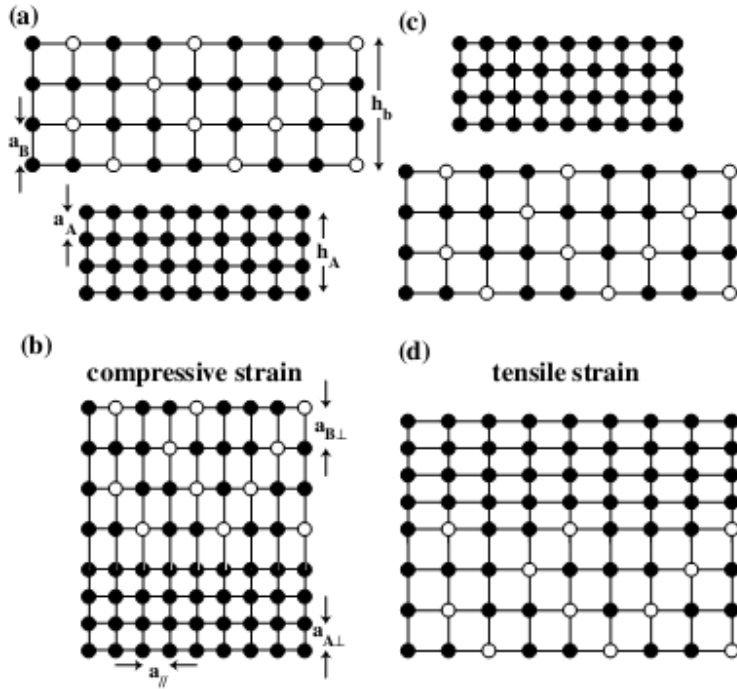


Figure 2.1 (a) A schematic diagram of the bulk lattice constant of a thin $\text{Si}_{1-x}\text{Ge}_x$ film to be grown on top of a thin bulk silicon layer. (b) A schematic diagram showing the tetragonal lattice distortion when the two films from (a) are placed together with the top $\text{Si}_{1-x}\text{Ge}_x$ film being compressively strained. (c) A schematic diagram of the bulk lattice constants of a bulk Si film to be grown on top of a bulk $\text{Si}_{1-y}\text{Ge}_y$ film. (d) A schematic diagram of the two films in (c) placed together with the top film being tensile strained^[2,3].

Figure 2.1 shows the illustration of compressive and tensile strain when the thin film is grown on a bulk material. As mentioned above, Ge has 4%-large lattice constant than that of Si. The lattice constant is almost linear as predicted by Vegard's law but more precise value was measured and given by the following equation^[2,4].

$$a_{\text{Si}1-x\text{Ge}x} = 0.5431 + 0.01992x + 0.0002733x^2 \quad (\text{nm}) \quad (2.1)$$

The lattice mismatch is able to apply compressive and tensile strain on purpose. For example, for compressive strain, a thin $\text{Si}_{1-x}\text{Ge}_x$ film of is grown on top of a thin bulk silicon layer and for tensile strain, a bulk Si film is grown on top of a bulk $\text{Si}_{1-y}\text{Ge}_y$ film as illustrated in Figure 2.1. The different physical properties of two materials such as 4% of lattice mismatch, energy level and direction of conduction band minima etc. can be useful for band and strain engineering for improvement of device performances.

Needless to say, it is the most important to note that the bandgap dependent on Ge fraction in SiGe alloy. The bandgap energy of (100)-oriented $\text{Si}_{1-x}\text{Ge}_x$ is shown in Figure 2.2. It is interesting to note that the bandgap energy is totally different between strained and unstrained cases. The bandgap for both LH and HH of strained $\text{Si}_{1-x}\text{Ge}_x$ alloy dramatically decreases with an increase in a Ge fraction. This phenomenon was interpreted by a simple and reliable model to predict the band lineups. The theory based on model-solid theory was given by Van de Walle and Martin Error! Reference source not found.[2,5]. Actually, the bandgap shrinkage is manly affected by the valence band offset because the conduction valence band offset is quite small comparing with the valence band offset. In terms of the bandgap shrinkage, it is important to know whether the SiGe can be transparent or lossy for optical modulator applications. For $1.55 \mu\text{m}$ corresponding to approximately 0.8-eV photon energy, the 30 to 40 % of Ge fraction in SiGe can be almost transparent.

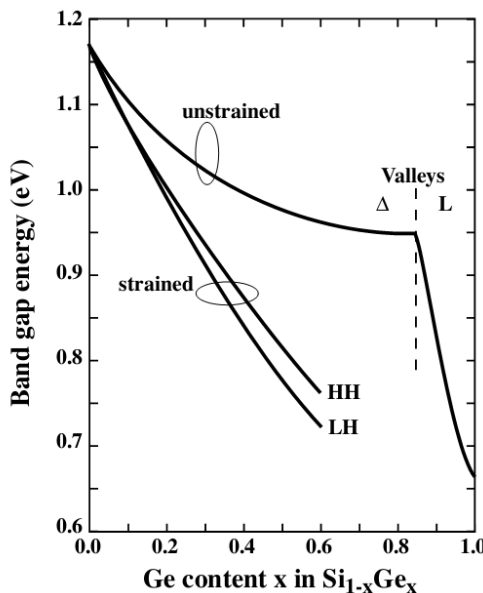


Figure 2.2 The band gap in eV for strained $\text{Si}_{1-x}\text{Ge}_x$ grown on bulk silicon substrates and for unstratind $\text{Si}_{1-x}\text{Ge}_x$ Error! Reference source not found.[2,6].

Figure 2.3 shows the critical thickness of $\text{Si}_{1-x}\text{Ge}_x$ on Si as a function of Ge fraction. The critical thickness decreases as increasing Ge fraction, and the defects are generated when the thickness is over than the critical thickness due to strain relaxation. The black squares show the stable and the red circles show the metastable state of the

SiGe film. The metastable is theoretically unstable but coherently grown state without defects for practical purposes. The experimental results of defect free SiGe films on Si are shown in star plots near the metastable. For the carrier-injection type of strained SiGe modulator, it is the most important to grow high-quality SiGe film without defects due to trap-assisted recombination. Furthermore, the high Ge fraction is required for high strain in SiGe alloy, but the thickness decreases resulting in a decrease in optical confinement factor of SiGe. Therefore, the Ge fraction and thickness of SiGe should be taken into account for device design, which are described in detail in the next chapter.

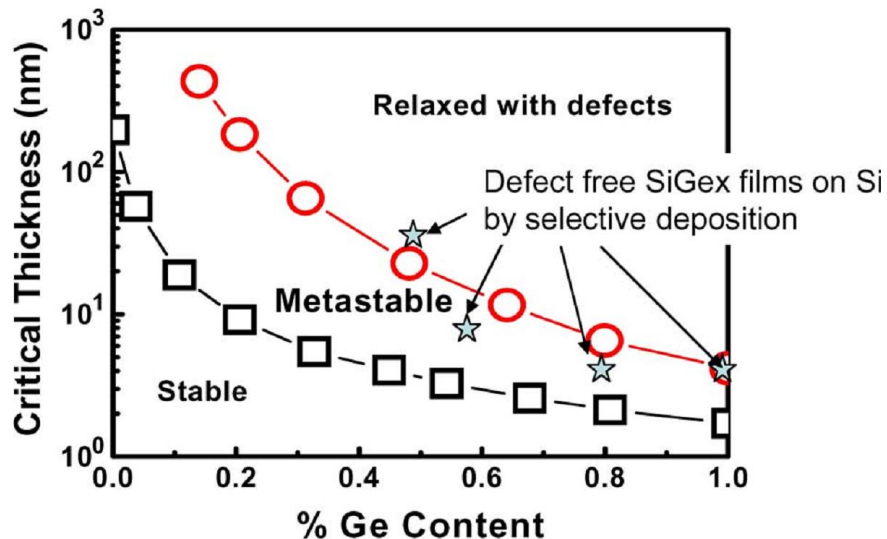


Figure 2.3 Critical thickness of strained SiGe as a function of Ge fraction^[2,7].

Unlike electron cases, the effective mass of holes has large changes with variable Ge fractions as shown in Figure 2.4. The left and right sides show strained SiGe on Si and strained Si on relaxed SiGe, respectively. The $v1$ and $v2$ is corresponding to LH and HH, respectively. The advantage of HH is that the valence band maxima and the larger change in hole mass is HH band. In the case of strained SiGe on Si, the hole mass of LH and HH decreases as increasing Ge fraction. In particular, it is interesting to note that the hole mass of HH shows dramatic decreases. Therefore, it is promising to introduce strain into SiGe by increasing Ge fraction for light effective mass of holes.

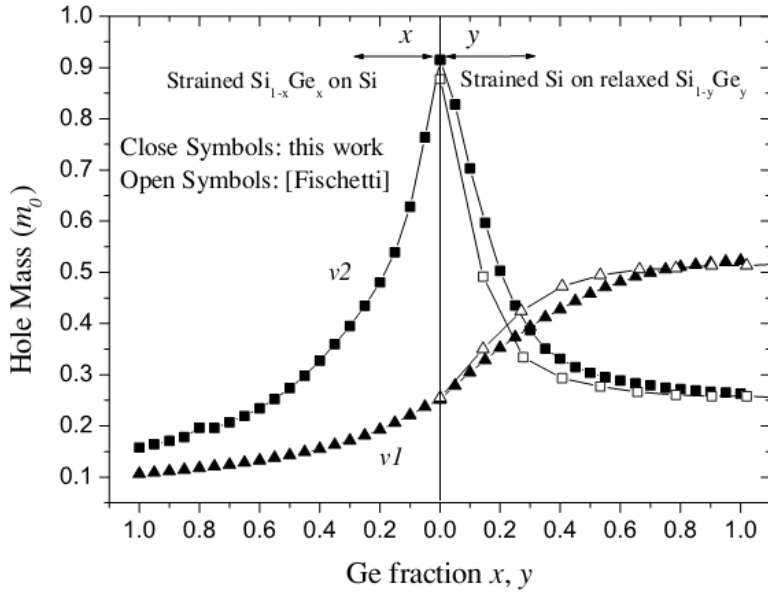


Figure 2.4 Ge fraction dependence of hole density-of-states masses at T=300 K for a strained SiGe layer on a Si substrate (left half) and a strained Si layer on a SiGe substrate (right half), $v1$ and $v2$ mean LH and HH respectively^[2,8].

The refractive index as a function of a Ge fraction is shown in Figure 2.5. As increasing Ge fraction, the refractive index increases. The refractive index as a function of Ge fraction can be expressed by the quadratic function in the inset of the following figure.

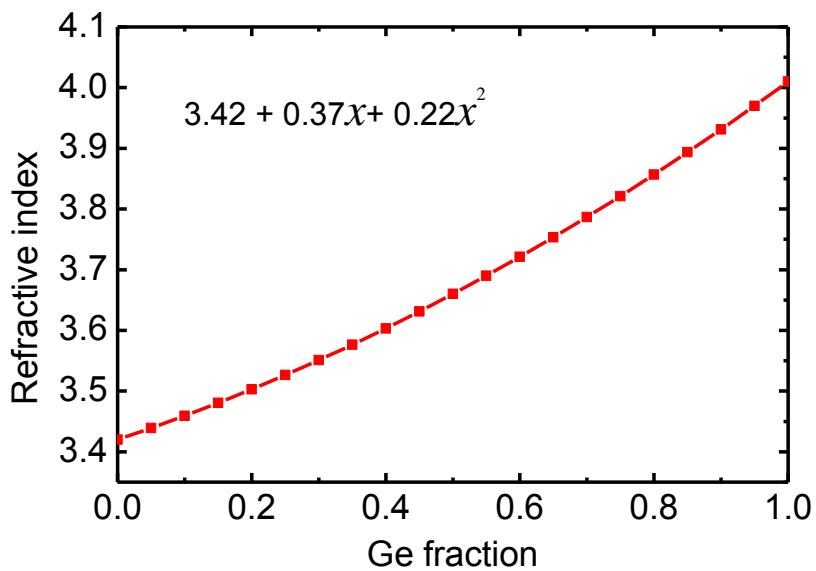


Figure 2.5 Refractive index as a function of Ge fraction^[2,9].

2.3 Plasma dispersion effect and free-carrier absorption for SiGe

The basic physical properties of strained SiGe has been described above. In this part, the plasma dispersion effect and free-carrier absorption in strained SiGe will theoretically introduced with the enhancement of free-carrier effects comparing to Si.

2.3.1 Drude model

The Drude model is the physical model describing the microscopic behavior of electrons in a solid is treated to be classically, and it can be used to explain frequency dependent response of light with regarding to a material. Therefore, in this thesis, the Drude model is used to analyze the change in optical constant of strained SiGe.

Let's assume the oscillator which is an electron bound to a restoring force in a solid. Then, the motion equation is expressed as follows:

$$m^* \frac{d^2x}{dt^2} + \frac{m^*}{\tau} \frac{dx}{dt} = -eE \quad (2.1)$$

, where m^* is electron mass, e is electron charge, τ is averaged scattering time, E is electric field of light which is proportion to $\exp(i\omega t)$, and x is displacement of an electron. The displacement of an electron can be obtained by solving the differential equation (2.1) as follows:

$$x = \frac{eE}{m(\omega^2 - i\omega/\tau)} \quad (2.2)$$

, where the ω is angular frequency. From the polarization and the displacement of an electron, the equations of $P = N_e(-e)x$ and $D = \epsilon_0 E + P = \epsilon\epsilon_0 E$, where P is the polarization, N_e is the number of electrons, D is the electric flux, ϵ is the permittivity, and ϵ_0 is the vacuum permittivity. Therefore, the permittivity is obtained as follow,

$$\varepsilon = 1 - \frac{N_e ex}{\varepsilon_0 E} \quad (2.3)$$

From the complex permittivity $\varepsilon = \varepsilon_1 - i\varepsilon_2$ and complex refractive index $N = n - ik$,

$$\varepsilon = \sqrt{N} \quad (2.4)$$

$$\varepsilon_1 = n^2 + k^2 \quad (2.5)$$

$$\varepsilon_2 = 2nk \quad (2.6)$$

, where n is refractive index, and k is extinction coefficient which has linear relationship to absorption coefficient $\alpha = 4\pi k / \lambda$. Therefore, ε_2 can be obtained by substituting (2.2) to (2.3) as follows:

$$\varepsilon_2 = \frac{ne^2}{\varepsilon_0} \cdot \frac{1/\omega\tau}{m\omega[1+1/(\omega\tau)^2]} \approx \frac{ne^2}{\varepsilon_0 m \omega^3 \tau} \quad (2.7)$$

Here, the square of $\omega\tau$ is small enough to be ignored. Using (2.6), the absorption coefficient can be obtained:

$$\alpha = \frac{e^3 \lambda^2}{4\pi^2 c^3 \varepsilon_0 n} \cdot \frac{N_e}{m^2 \mu_e} \quad (2.8)$$

Therefore, absorption may be modified with the relationship considering the changes in carrier concentrations [2.18]:

$$\Delta\alpha(w) = \alpha(w, \Delta N_e, \Delta N_p) - \alpha(w, 0, 0) \quad (2.9)$$

By (2.9), the change in absorption coefficient is shown, also taking into account both electrons and holes:

$$\therefore \Delta\alpha = \frac{e^3 \lambda^2}{4\pi^2 c^3 \epsilon_0 n} \left(\frac{\Delta N_e}{m_{ce}^{*2} \mu_e} + \frac{\Delta N_h}{m_{ch}^{*2} \mu_h} \right) \quad (2.10)$$

It is well known that n and k are related by the Kramers-Kronig relations. In a similar manner, Δn and $\Delta\alpha$ has the same relation which enables to calculate Δn as follows:

$$\Delta n(\omega) = \frac{c}{\pi} P \int_0^\infty \frac{\Delta\alpha(\omega)}{\omega_1^2 - \omega^2} d\omega_1 \quad (2.11)$$

, where P is Cauchy principal value. Finally, Δn is obtained by substituting (2.10) to (2.11) as follows:

$$\therefore \Delta n = -\frac{e^2 \lambda^2}{8\pi^2 c^2 \epsilon_0 n} \left(\frac{\Delta N_e}{m_{ce}^*} + \frac{\Delta N_h}{m_{ch}^*} \right) \quad (2.12)$$

where e is the elementary charge, ϵ_0 is the permittivity in vacuum, c is the speed of light in vacuum, λ is the wavelength, n is the unperturbed refractive index, m_{ce}^* and m_{ch}^* are the conductivity effective masses of electrons and holes, and μ_e and μ_h are the mobilities of electrons and holes, respectively.

2.3.2 Calculation of conductivity effective mass of holes in compressively strained SiGe using $k \cdot p$ method

To calculate the conductivity effective mass of holes in compressively strained SiGe, the valence band structure of SiGe coherently grown on (001) Si is calculated by the $k \cdot p$ method. The following 6×6 Hamiltonian is used to evaluate strain-induced coupling between the heavy-hole (HH) bands, light-hole (LH) bands, and spin-orbit split-off (SO) bands [2,10]:

$$H(\mathbf{k}) = \begin{bmatrix} P+Q & -S & R & 0 & -\frac{1}{\sqrt{2}}S & \sqrt{2}R \\ -S^\dagger & P-Q & 0 & R & -\sqrt{2}R & \sqrt{\frac{3}{2}}S \\ R^\dagger & 0 & P-Q & S & \sqrt{\frac{3}{2}}S^\dagger & \sqrt{2}Q \\ 0 & R^\dagger & S^\dagger & P+Q & -\sqrt{2}R^\dagger & -\frac{1}{\sqrt{2}}S^\dagger \\ -\frac{1}{\sqrt{2}}S^\dagger & -\sqrt{2}Q & \sqrt{\frac{3}{2}}S & -\sqrt{2}R & P+\Delta & 0 \\ \sqrt{2}R^\dagger & \sqrt{\frac{3}{2}}S^\dagger & \sqrt{2}Q & -\frac{1}{\sqrt{2}}S & 0 & P+\Delta \end{bmatrix} \quad (2.13)$$

with $P = P_k + P_\varepsilon$, $Q = Q_k + Q_\varepsilon$, $R = R_k + R_\varepsilon$, $S = S_k + S_\varepsilon$, and

$$\begin{aligned} P_k &= \frac{\hbar^2}{2m_0} \gamma_1 (k_x^2 + k_y^2 + k_z^2), \quad Q_k = \frac{\hbar^2}{2m_0} \gamma_2 (k_x^2 + k_y^2 + k_z^2), \\ R_k &= \frac{\hbar^2}{2m_0} \sqrt{3} [-\gamma_2 (k_x^2 - k_y^2) + 2i\gamma_3 k_x k_y], \quad S_k = \frac{\hbar^2}{2m_0} 2\sqrt{3} \gamma_3 (k_x - ik_y) k_z, \\ P_\varepsilon &= -a_V \text{Tr}(\varepsilon), \quad Q_\varepsilon = -\frac{b}{2} (\varepsilon_{xx} + \varepsilon_{yy} - 2\varepsilon_{zz}), \quad R_\varepsilon = \frac{\sqrt{3}}{2} b (\varepsilon_{xx} - \varepsilon_{yy}) - id\varepsilon_{xy}, \\ S_\varepsilon &= -d (\varepsilon_{xx} - \varepsilon_{yy}), \end{aligned}$$

where Δ is the spin-orbit splitting, γ_1 , γ_2 , and γ_3 are the Luttinger parameters, and b and d are the Bir-Pikus shear deformation potentials. Table S1 shows the material parameters of Si and Ge in this study. All values are from references [2.11], [2.12], except for the valence band parameters [2.13]. The unit of the valence band parameters is $\hbar/2m_0$, where \hbar is the Planck constant divided by 2π and m_0 is the electron mass. The values for SiGe are given by linear interpolation of the parameters for Si and Ge, with the exception of the lattice constant of $\text{Si}_{1-x}\text{Ge}_x$, which is approximately expressed as

$$a_{SiGe}(x) = a_{Si} + 0.200326 \cdot x (1 - x) + (a_{Ge} - a_{Si}) x^2 , \quad (2.14)$$

where x is the Ge mole fraction [2,14]. The three band-edge levels HH, LH, and SO are obtained by solving $\det[H(\mathbf{k}) - E] = 0$ and then, the in-plane conductivity effective mass of holes in SiGe is calculated.

Table 2.2 Material parameters of Si and Ge

Symbol	Quantity	Units	Si	Ge
a	Lattice constant	Å	5.43	5.65
C_{11}	Elastic constants	Mbar	1.658	1.285
C_{12}		Mbar	0.539	0.483
a_v	Hydrostatic deformation potential	eV	2.46	1.24
b	Bir-Pikus shear deformation	eV	-2.2	-2.3
d	potential	eV	-5.1	-5.0
Δ	Spin-orbit split-off energy	eV	0.044	0.295
L	Valence band parameters	$\hbar/2m_0$	-5.53	-30.53
M			-3.64	-4.64
N			-8.32	-33.64

Figure 2.7 shows the valance band structures of a light hole (LH) and heavy hole (HH) as a function of the wave vector in the k_x [100]- k_y [010] plane calculated by the $k \cdot p$ method when SiGe films with Ge fractions, x of 0, 0.15, and 0.3 are coherently grown on Si (001) [2,15], [2,16]. In the case of Si ($x = 0$), the HH and LH bands are degenerate at the Γ point. The compressive strain splits this degeneracy; thus, the HH band is shifted to above the LH band in the case of strained $Si_{1-x}Ge_x$ on Si ($x > 0$). The energy surfaces of the LH and HH bands become sharp at the minimum-energy Γ point, indicating that the biaxial compressive strain reduces the effective hole mass at the Γ point.

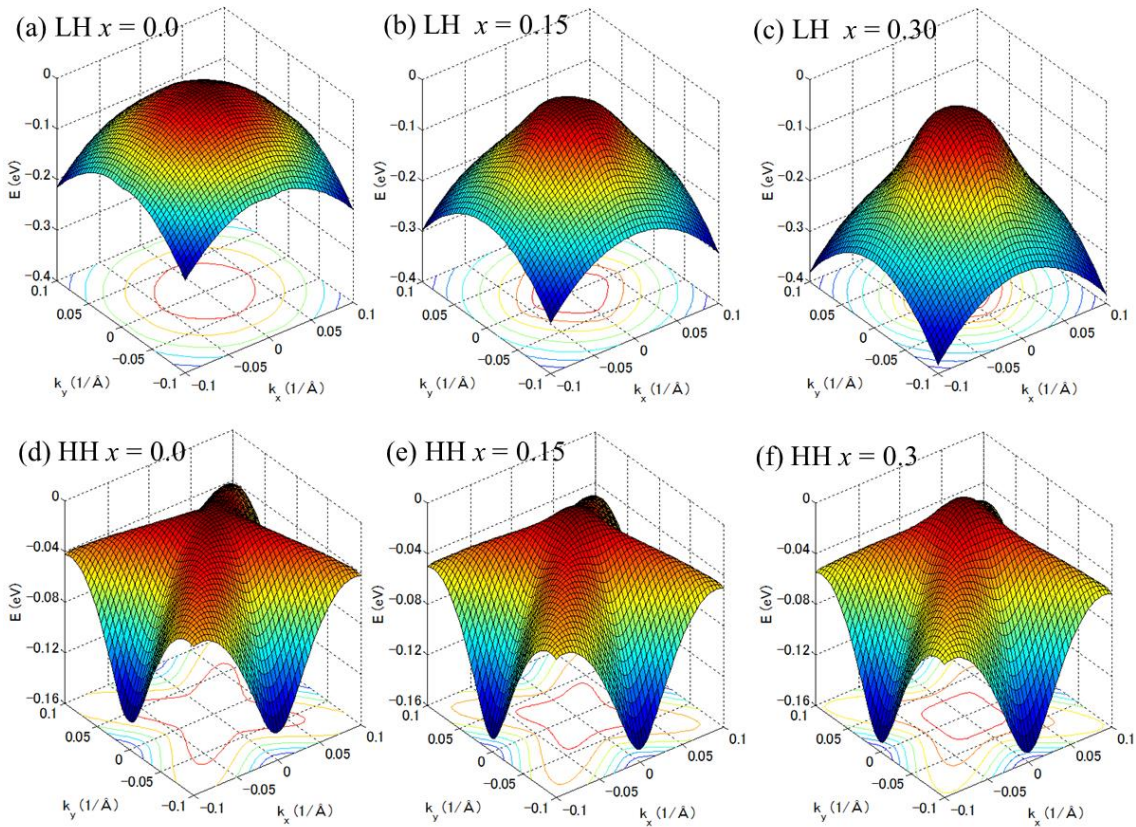


Figure 2.6 Valence band structures and constant-energy contours of $\text{Si}_{1-x}\text{Ge}_x$ grown on Si (001) as a function of wavevector in the k_x [100]- k_y [010] plane calculated by the six-band kp method. The top three figures (a), (b), and c are LH band structures and the bottom three figures (d), (e), and (f) are HH band structures of $\text{Si}_{1-x}\text{Ge}_x$ at $x = 0$ (Si), 0.15, and 0.3, respectively. The energy surfaces of the LH and HH bands become sharp at the minimum energy Γ point with increasing Ge fraction, indicating that biaxial compressive strain reduces the effective hole mass.

The conductivity effective masses of holes and electrons as a function of the Ge fraction are shown in Fig. 2.7. From the calculated valance band energies of LH and HH, the conductivity effective hole masses of strained and relaxed SiGe are obtained. The conductivity effective mass of electrons is taken from reference ^[2,12]. Compared with the mass of Si ($x = 0$), the conductivity hole mass of relaxed SiGe deceases with increasing Ge fraction. Moreover, the conductivity hole mass rapidly decreases owing to the compressive strain. On the other hand, the in-plane mass of electrons in Δ valleys remains almost constant regardless of the Ge fraction in the case of applying biaxial compressive strain.

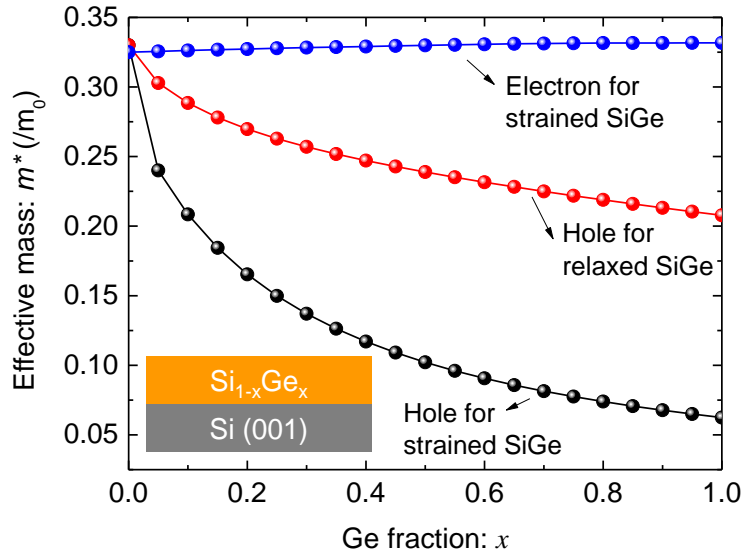


Figure 2.7 Calculated in-plane conductivity effective hole masses of compressively strained $\text{Si}_{1-x}\text{Ge}_x$ grown on Si (black) and relaxed $\text{Si}_{1-x}\text{Ge}_x$ (red), and electron masses for strained SiGe^[2,12] (blue). Comparing the hole masses of relaxed and strained SiGe, the compressive strain has a large effect on reducing the conductivity hole mass.

2.3.3 Estimation of enhancement factor of changes in refractive index and absorption coefficient

The plasma dispersion effect and free-carrier absorption are expressed by the Drude model, which shows that changes in the refractive index and absorption coefficient arise from a change in the plasma frequency of free carriers, which is dependent on the number of free carriers and their conductivity effective masses.

According to the Drude model expressed as equations (2.10) and (2.12), the changes in the optical constants are inversely proportional to the conductivity effective mass for Δn and the square of the conductivity effective mass multiplied by the mobility for $\Delta\alpha$. Therefore, the changes in the optical constants are expected to be enhanced by reducing the conductivity effective masses.

Figures 2.8(a) and 2.8(b) show the enhancement of changes in the refractive

index and absorption coefficient in compressively strained SiGe, respectively in which the mobilities of electrons^[2.12] and for holes^[2.19] were taken from the literatures. The refractive index of SiGe was taken from the reference^[2.20]. The changes in the optical constants caused by holes increase with an increase in the Ge fraction because the conductivity hole mass of SiGe is reduced by compressive strain as shown in Fig. 2.8. On the other hand, there is no enhancement of the change in the refractive index caused by electrons because there is almost no modulation of the electron mass by strain, as shown in Fig. 2.8. The reduction in the electron mobility with increasing Ge fraction slightly contributes to the enhancement of the change in the absorption coefficient by electrons, but this contribution is much smaller than that of holes. When we consider a SiGe optical modulator into which carriers are injected through a forward-biased *pin* junction, the same amounts of electrons and holes exist in the SiGe layer owing to the charge neutrality condition. Thus, the average changes in the optical constants caused by injected electrons and holes in the *pin* structure are reduced, as shown in Fig. 2.8. However, the average enhancement factors of Δn and $\Delta \alpha$ still increase with increasing Ge fraction and are expected to be approximately 1.6 for Δn and 2.1 for $\Delta \alpha$ in $\text{Si}_{0.7}\text{Ge}_{0.3}$.

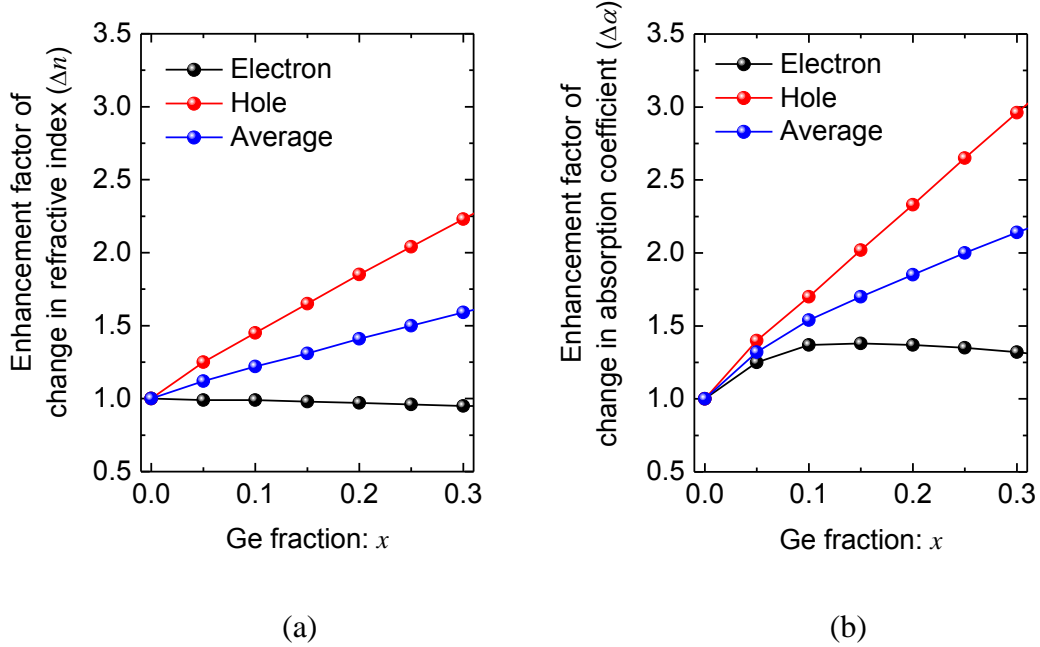


Figure 2.8 Enhancement factors for changes in optical constants. (a) Refractive index and (b) Absorption coefficient as functions of the Ge fraction. The changes in the optical constants increase with increasing Ge fraction, and Δn and $\Delta\alpha$ are expected to be enhanced by as much as 1.6 and 2.1, respectively, in compressively strained $\text{Si}_{0.7}\text{Ge}_{0.3}$.

2.4 Conclusion

The physical properties of SiGe were briefly introduced. In particular, the strain-induced mass modulation was analyzed for the theory of strain-induced enhancement of free-carrier effects in SiGe. We estimated the enhancement of the plasma dispersion effect and free-carrier effect based on Drude model. The enhancement factors of changes in refractive index (Δn) and absorption coefficient ($\Delta\alpha$) increase with an increase in Ge fraction. the average enhancement factors for carrier-injection type of Δn and $\Delta\alpha$ still increase with increasing Ge fraction and are expected to be approximately 1.6 for Δn and 2.1 for $\Delta\alpha$ in $\text{Si}_{0.7}\text{Ge}_{0.3}$.

References

- [2.1] Ghani, T. *et al.* A 90nm high volume manufacturing logic technology featuring novel 45nm gate length strained silicon CMOS transistors. *Tech. Dig. Int. Electron Devices Meet.*, (Washington, D.C., 2003).
- [2.2] Sze, S. M., Physics of Semiconductor Devices, 2nd edition, Wiley-Interscience, New York, (1981).
- [2.3] V. T. Bublik, S. S. Gorelik, A. A. Zaitsev, and A. Y. Polyakov, "Calculation of Binding-Energy of Ge-Si Solid-Solution," *Physica Status Solidi B-Basic Research*, vol. 65, pp. K79-K84, 1974.
- [2.4] D. J. Paul, "Si/SiGe heterostructures: from material and physics to devices and circuits," *Semiconductor Science and Technology*, vol. 19, pp. R75-R108, Oct 2004.
- [2.5] C. G. Van De Walle, "Band Lineups and Deformation Potentials in the Model-Solid Theory," *Physical Review B*, vol. 39, pp. 1871-1883, Jan 15 1989.
- [2.6] D. V. Lang, R. People, J. C. Bean, and A. M. Sergent, "Measurement of the Band-Gap of Gexsi1-X/Si Strained-Layer Heterostructures," *Applied Physics Letters*, vol. 47, pp. 1333-1335, 1985.
- [2.7] P. Majhi, P. Kalra, R. Harris, K. J. Choi, D. Heh, J. Oh, *et al.*, "Demonstration of high-performance PMOSFETs using Si-Si_xGe_{1-x}-Si quantum wells with high-kappa/metal-gate stacks," *IEEE Electron Device Letters*, vol. 29, pp. 99-101, Jan 2008.
- [2.8] L. F. Yang, J. R. Watling, R. C. W. Wilkins, M. Borici, J. R. Barker, A. Asenov, *et al.*, "Si/SiGe heterostructure parameters for device simulations," *Semiconductor Science and Technology*, vol. 19, pp. 1174-1182, Oct 2004.
- [2.9] Schaffler F., in *Properties of Advanced Semiconductor Materials GaN, AlN, InN, BN, SiC, SiGe*. Eds. Levenshtein M.E., Rumyantsev S.L., Shur M.S., John Wiley & Sons, Inc., New York, 2001, 149-188
- [2.10] C. Y. P. Chao and S. L. Chuang, "Spin-Orbit-Coupling Effects on the Valence-Band Structure of Strained Semiconductor Quantum-Wells," *Physical Review B*, vol. 46, pp. 4110-4122, Aug 15 1992. Yu, P. Y. and Cardona, M. *Fundamentals of Semiconductors*. (New York: Springer-Verlag, 1995).

- [2.11] Shiraki, Y. & Usami, N. *Silicon-Germanium (SiGe) Nanostructures*. (Cambridge, U.K.: Woodhead Publishing, 2011).
- [2.12] M. V. Fischetti and S. E. Laux, "Band structure, deformation potentials, and carrier mobility in strained Si, Ge, and SiGe alloys," *Journal of Applied Physics*, vol. 80, pp. 2234-2252, Aug 15 1996.
- [2.13] J. P. Dismukes, R. J. Paff, and L. Ekstrom, "Lattice Parameter and Density in Germanium-Silicon Alloys," *Journal of Physical Chemistry*, vol. 68, pp. 3021-&, 1964.
- [2.14] J. M. Luttinger and W. Kohn, "Motion of Electrons and Holes in Perturbed Periodic Fields," *Physical Review*, vol. 97, pp. 869-883, 1955.
- [2.15] J. M. Luttinger, "Quantum Theory of Cyclotron Resonance in Semiconductors - General Theory," *Physical Review*, vol. 102, pp. 1030-1041, 1956.
- [2.16] C. Y. P. Chao and S. L. Chuang, "Spin-Orbit-Coupling Effects on the Valence-Band Structure of Strained Semiconductor Quantum-Wells," *Physical Review B*, vol. 46, pp. 4110-4122, Aug 15 1992.
- [2.17] M. Rieger and P. Vogl, "Electronic-Band Parameters in Strained $\text{Si}_{1-x}\text{Ge}_x$ Alloys on $\text{Si}_{1-y}\text{Ge}_y$ Substrates," *Physical Review B*, vol. 48, pp. 14276-14287, Nov 15 1993.
- [2.18] R. A. Soref and B. R. Bennett, "Electrooptical Effects in Silicon," *IEEE Journal of Quantum Electronics*, vol. 23, pp. 123-129, Jan 1987.
- [2.19] N. D. Arora, J. R. Hauser, and D. J. Roulston, "Electron and Hole Mobilities in Silicon as a Function of Concentration and Temperature," *IEEE Transactions on Electron Devices*, vol. 29, pp. 292-295, 1982.
- [2.20] Schaffler, F. *Properties of Advanced Semiconductor Materials GaN, AlN, InN, BN, SiC, SiGe*. (New York: Wiley, 2001).

Chapter 3

Numerical analysis of carrier-injection type SiGe optical modulator/attenuator

In this chapter, we propose the carrier-injection type of SiGe optical modulator/attenuator to demonstrate strain-induced enhancement of the plasma dispersion effect and free-carrier absorption in SiGe. The working principle of carrier-injection type optical modulator will be introduced first. Strain effect on carrier-injection type SiGe optical modulators is numerically investigated. Owing to enhancement in free-carrier absorption of strained SiGe, SiGe optical device is predicted to exhibit the $3.6\times$ enhancement of free-carrier absorption and $3 \times$ enhancement of the plasma dispersion effect against Si.

3.1 Introduction

Si optical modulators based on a diode structure have attracted much attentions as the one of the critical building blocks for optical interconnect^[3.1]. The Si optical modulators based on plasma dispersion effect have been demonstrated by means of injection and depletion of free carriers where the light is confined and propagates^{[3.2], [3.3], [3.4]}.

However, the modulation efficiency of Si modulators with *pn*-junction is still low because plasma dispersion effect and free-carrier absorption is not strong enough in Si. Hence, enhancement of plasma dispersion effect and free-carrier absorption will be required to improve the modulation efficiency of Si-based optical modulators. For this purpose, we have proposed strain engineering of plasma dispersion effect and free-carrier absorption for enhancing the charge-carrier effects by means of using light

effective mass materials such as strained silicon- germanium (SiGe) ^[3.5] based on the Drude model ^[3.6].

In this chapter, we numerically study modulation characteristics of strained SiGe-based carrier-injection intensity optical modulators. Strained SiGe is predicted to exhibit enhancement in plasma dispersion effect and free-carrier absorption by reduction in the effective hole mass of SiGe ^[3.5]. We performed the technology computer aided design (TCAD) simulation in conjunction with the finite-difference optical mode analysis, which predicts that the free-carrier absorption in the strained SiGe optical modulators exhibits 3.6 \times enhancement in free-carrier absorption and 3 \times enhancement in the plasma dispersion effect against a Si-based modulator owing to the strain-induced mass modulation.

3.2 Proposed device structure of carrier-injection type SiGe optical modulator

First of all, we show the device structure of carrier-injection type SiGe optical modulator with a lateral *pin* junction. The carrier-injection type optical modulators have been demonstrated ^[3.7], taking advantage of large changes in effective refractive index due to large changes in carrier density. The electrons and holes from n+ and p+ regions respectively are injected toward a waveguide core by forward bias.

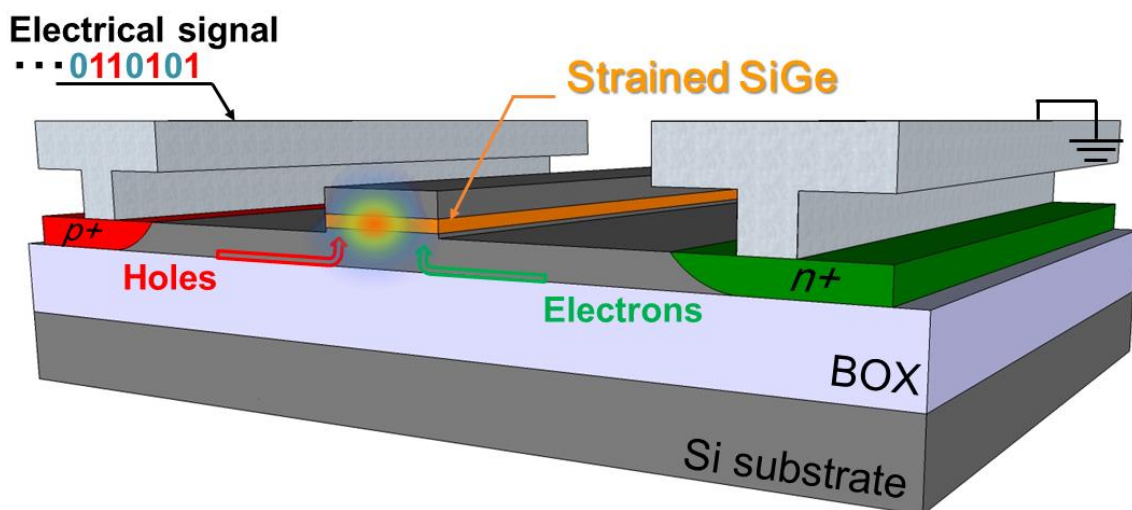


Figure 3.1 Proposed device structure of the *pin* injection-type SiGe optical modulator

Figure 3.1 shows the device structure of the carrier injection type SiGe optical modulator with a lateral pin junction, proposed in this thesis. As applying the forward bias through pin junction, the carriers are injected, and the optical constants are changed due to changes in carrier concentrations. The changes in refractive index and absorption coefficient are for VOA and optical modulator, respectively. In particular, the compressively strained SiGe is positioned to the center of the waveguide core to obtain the large optical confinement factor in SiGe. Furthermore, the narrowed bandgap of compressively strained SiGe contributes charge confinement effect so that the strain-induced enhancement effectively affects the device performance.

3.3 Simulation method

The modulation characteristics are simulated by Sentaurus in conjunction with a mode profiler pf SiGe optical waveguided-modulator.

Sentaurus is one of the powerful semiconductor device simulators, allowing numerical calculations of given device structure with various physical models. In this work, Sentaurus is used for the electrical properties of SiGe optical modulator with a lateral *pin* junction. The drift-diffusion model is used to simulate carrier transport by solving Poisson equation and continuity equation. It is important to note that the recombination models play an important role in *pin* diode such as Shockley-Read-Hall of surface and doping dependence and Auger recombination. Finite-difference optical mode analysis is used to calculate electric and magnetic field distribution mode. This simulator numerically calculates Maxwell's equations with boundary conditions given by designed structure with the finite difference methods. Finally, the carrier concentration and optical distribution are overlapped to calculate the changes in effective refractive index and absorption coefficient based on plasma dispersion effect and free carrier absorption.

The device structure of the strained SiGe-based optical modulator consists of a 115-nm-thick and 600-nm-wide waveguide mesa with boron doped at a constant doping level of 10^{16} cm^{-3} . A 30-nm-thick $\text{Si}_{1-x}\text{Ge}_x$ layer is embedded in the center of the waveguide mesa, which can be coherently grown on Si (001) when the Ge fraction is up to 0.3^[3,8]. p^+ and n^+ regions with a doping level of 10^{20} cm^{-3} are formed on both sides of

the waveguide mesa for carrier injection. The optical confinement factor of the SiGe layer is estimated to be 19% by finite-difference mode analysis. The carrier concentration is calculated by taking into account recombination processes such as Shockley-Read-Hall (SRH) and Auger recombination^{[3.9], [3.10], [3.11]} when electrons and holes are injected by applying a forward-bias voltage between the p^+ and n^+ regions. We assumed ohmic contacts in the p^+ and n^+ regions. After calculating the carrier concentration, the changes in the refractive index and absorption coefficient of SiGe and Si were calculated using the Drude model. Finally, the changes in the effective refractive index and absorption coefficient were obtained by calculating the overlap between the carrier distribution and the optical field distribution.

3.4 Device simulation result

We numerically analyzed the modulation characteristics of a carrier-injection waveguide optical modulator with a biaxial compressive strained SiGe well in the heterostructure by performing a technology computer aided design (TCAD) simulation in conjunction with finite-difference optical mode analysis as shown a schematic of the device structure with a lateral *pin* junction for carrier injection in Fig. 3.1.

First, we carry out the calculation of optical mode in Si/SiGe/Si waveguide core. Figure 3.2 shows the electric field distribution of fundamental transverse electric (TE) mode calculated by the finite-difference method. The optical confinement factor of the SiGe layer is estimated to be 19% by finite-difference mode analysis. Here, we ignore the difference between refractive indices of Si and SiGe since the latter is slightly higher, which doesn't affect optical confinement factor in SiGe.

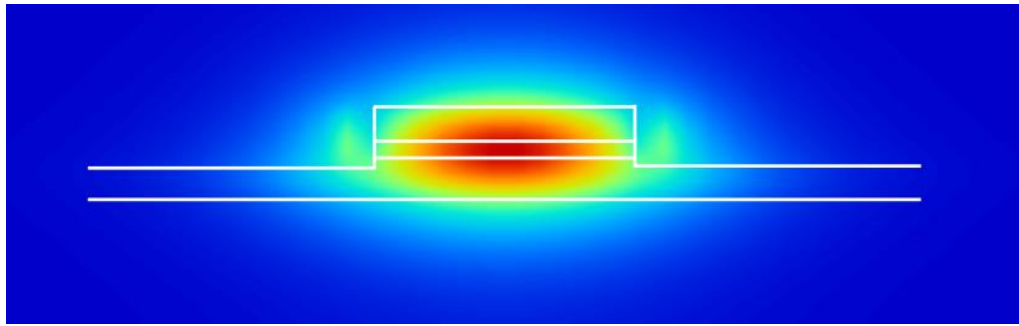


Figure 3.2 Electric field distribution of the fundamental TE mode of the SiGe optical modulator. The SiGe layer is placed at the center of the rib to obtain the maximum optical confinement factor.

As shown in Fig. 3.3, the electrical characteristics are calculated to obtain charge density at each forward bias point. The changes in carrier densities of electrons and holes at certain bias point are calculated by subtraction from a 0-V bias point. Then, the changes in refractive index and absorption coefficient can be obtained. Finally, the effective values are calculated by equations of (3.1) and (3.2).

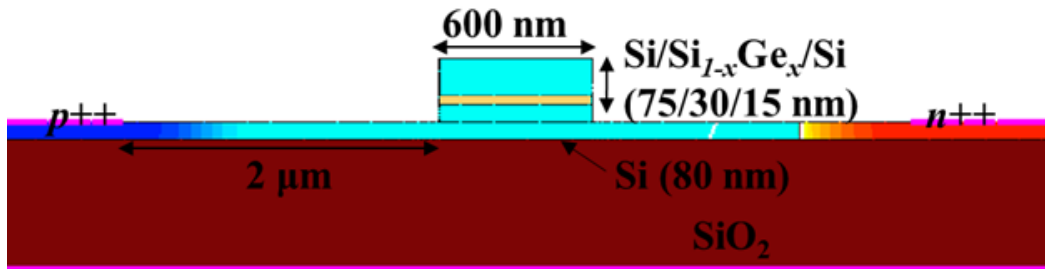


Figure 3.3 Device structure of SiGe optical modulator/attenuator for calculation of electrical characteristics by Sentaurus.

$$\Delta n_{eff} = \frac{\iint_S \Delta n(x, y) \times |E(x, y)|^2 dx dy}{\iint_S |E(x, y)|^2 dx dy} \quad (3.1)$$

$$\Delta\alpha_{eff} = \frac{\iint_S \Delta\alpha(x, y) \times |E(x, y)|^2 dx dy}{\iint_S |E(x, y)|^2 dx dy} \quad (3.2)$$

First we show the band diagram of carrier-injection optical modulators to clearly understand how carrier-injection is carried out and SiGe affects the device performance. As shown in Fig. 3.4(a), the pin junction is depicted based on quasi Fermi potential at 0.0 eV. With applying 1.1 V forward bias, the electron energies of the two bands of p+ and p- junctions move downside. Quasi Fermi potentials for electrons and holes are close to the conduction band edge and valence band edge, respectively, indicating that electrons and holes are injected to waveguide region.

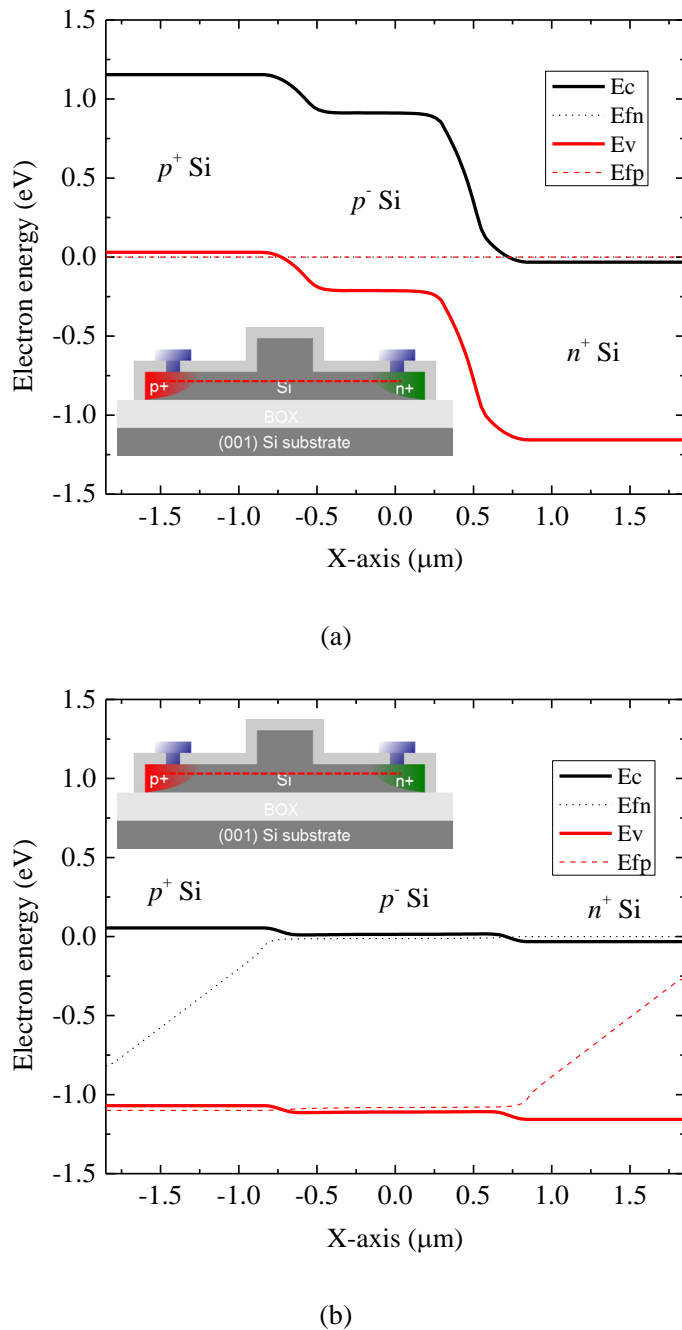


Figure 3.4. Band diagram of horizontal cross section of *pin* junction of Si modulator; (a) without forward bias and (b) with 1.1 V forward bias.

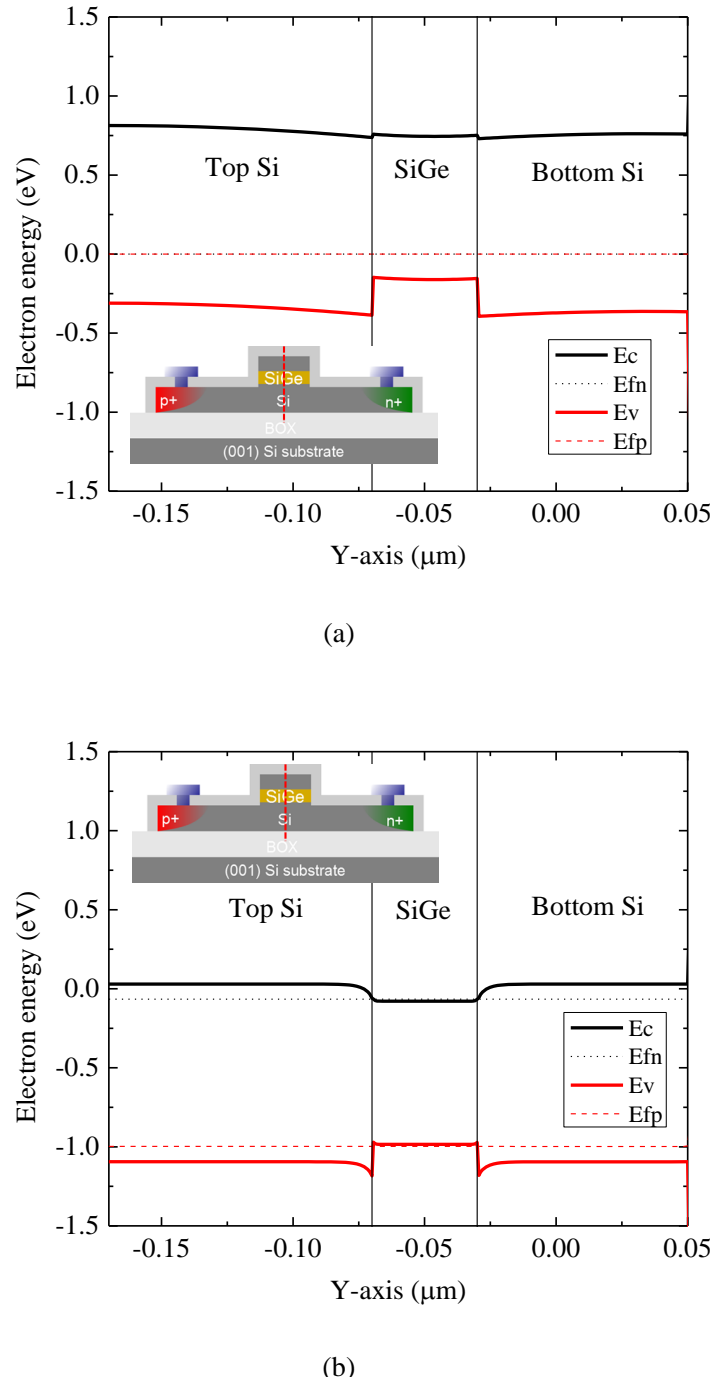
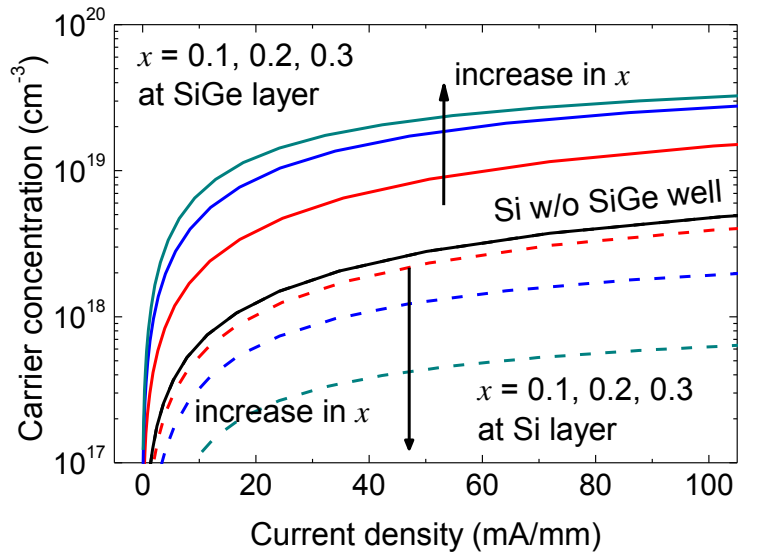


Figure 3.5. Band diagram of vertical cross section of *pin* junction of SiGe modulator; (a) without forward bias and (b) with 1.1 V forward bias.

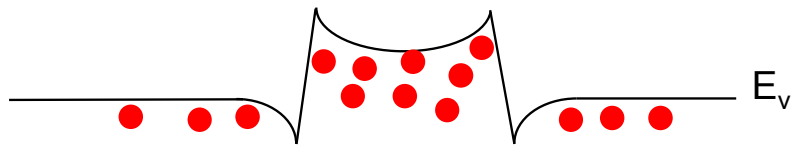
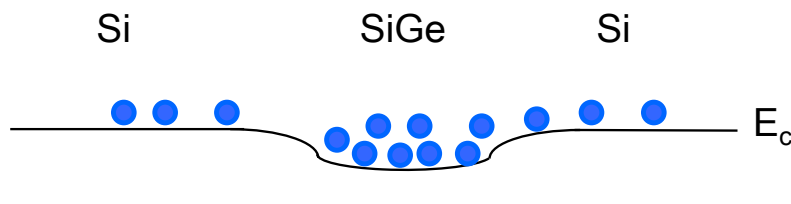
For the SiGe modulator, the horizontal cross section of band diagram of a pin junction with and without a forward bias is similar to the case of the Si modulator as shown in Fig. 3.4. However, the vertical cross section of band diagram of the SiGe

modulator has a big difference due to narrowed bandgap and its offset against Si of strained SiGe. It is shown that the band diagrams of conduction band edge, valence band edge, quasi Fermi potential for electrons, and quasi Fermi potential for holes with and without forward bias are in Fig. 3.5. In Fig.3.5(a), the large band offset between Si and SiGe in valance band edge are shown and the confinement for hole is expected even without bias, considering quasi Fermi potential. When the forward bias is applied, the bandstructure becomes Type I to satisfy charge neutrality condition. The both quasi Fermi potentials in SiGe are almost positioned at conduction and valence band sides, meaning the high densities of electrons and holes are confined into the SiGe layer.

We show the carrier concentrations calculated by TCAD simulation in Fig. 3.6(a) as a function of the current density injected into the Si/SiGe/Si heterostructure modulator. It is found that the carrier concentration in the SiGe layer is much larger than that in the Si layer because the injected carriers are confined in the SiGe layer owing to the band offset between Si and SiGe, as shown in Fig. 3.6(b), which also contributes to improving the modulation efficiency of Si-based optical modulators^[3,12]. The carrier concentration in the SiGe layer increases by an order of magnitude as the Ge fraction increases from 0 to 0.3 because the band offset between Si and SiGe increases. Thus, it is possible to synergistically enhance the changes in the effective refractive index and absorption coefficient by accumulating the injected carriers in the SiGe layer, where the plasma dispersion effect and free-carrier absorption are larger than those of Si.



(a)

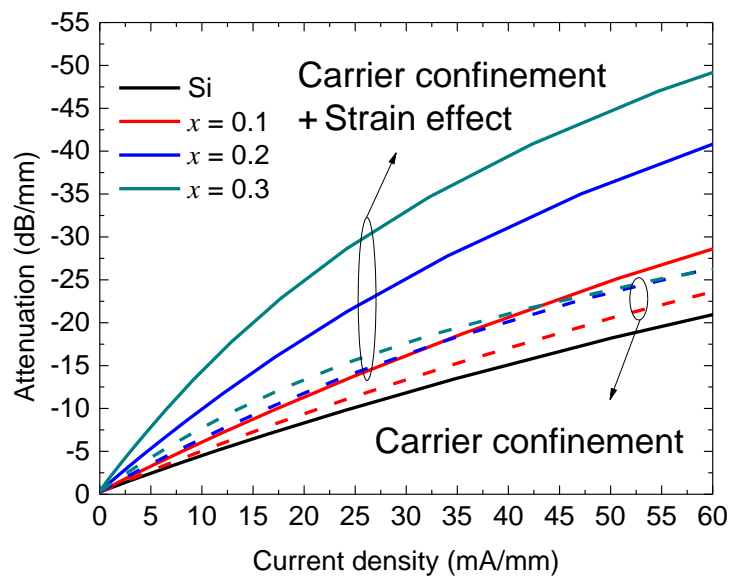


(b)

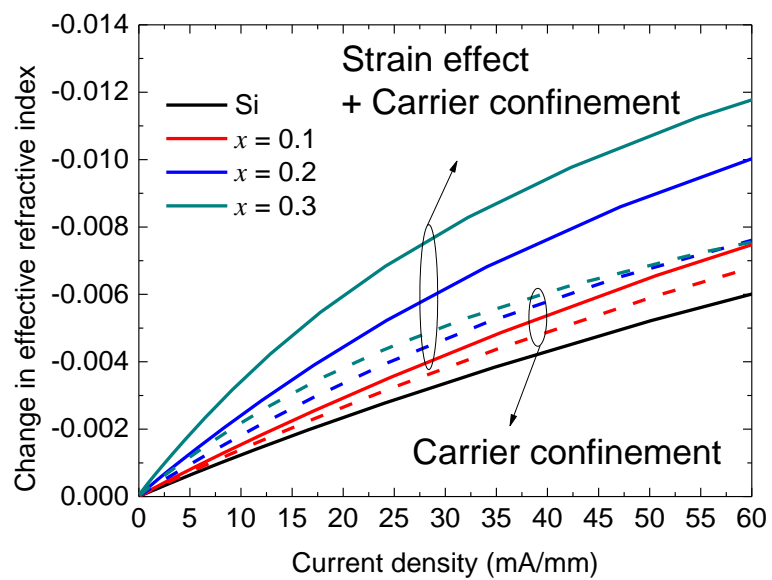
Figure 3.6. Carrier confinement in SiGe layer. (a) Carrier concentrations at Si and SiGe layers as a function of injected current density with the Ge fractions of 0.0 to 0.3. (b) Bandstructure of Si/SiGe/Si heterostructure illustrating carrier confinement in the SiGe layer.

The solid lines in Fig. 3.7(a) show the optical attenuation characteristics of the SiGe optical modulator with a Ge fraction from 0 to 0.3 as a function of injected current density. Owing to the enhanced free-carrier absorption and the carrier confinement^[3,12] by the band offset^[3,13] in the SiGe layer as shown in Fig. 3.6, the optical attenuation increases with the Ge fraction. Figure 3.7(b) shows the change in the refractive index

which has same trend as the attenuation characteristics. To identify the effect of carrier confinement on the modulation efficiency, the modulation characteristics considering only carrier confinement, in which the enhancement of the plasma dispersion effect and free-carrier absorption in SiGe are neglected, are calculated as shown by the broken lines in Figs. 3.7(a) and 3.7(b). Although the carrier confinement partly contributes to enhancing the device performance, the strain effect has the most important role in enhancing the modulation characteristics. Figure 3.7(d) shows the current density required for 20 dB attenuation and the enhancement factor of optical attenuation against Si as a function of the Ge fraction. The current density required for 20 dB attenuation significantly decreases from 57 mA for Si ($x = 0$) to 15 mA for $\text{Si}_{0.7}\text{Ge}_{0.3}$. Hence, the modulation efficiency of the $\text{Si}_{0.7}\text{Ge}_{0.3}$ -based in-line intensity modulator based on free-carrier absorption is predicted to be approximately 3.7 times as large as that of the Si-based modulator.



(a)



(b)

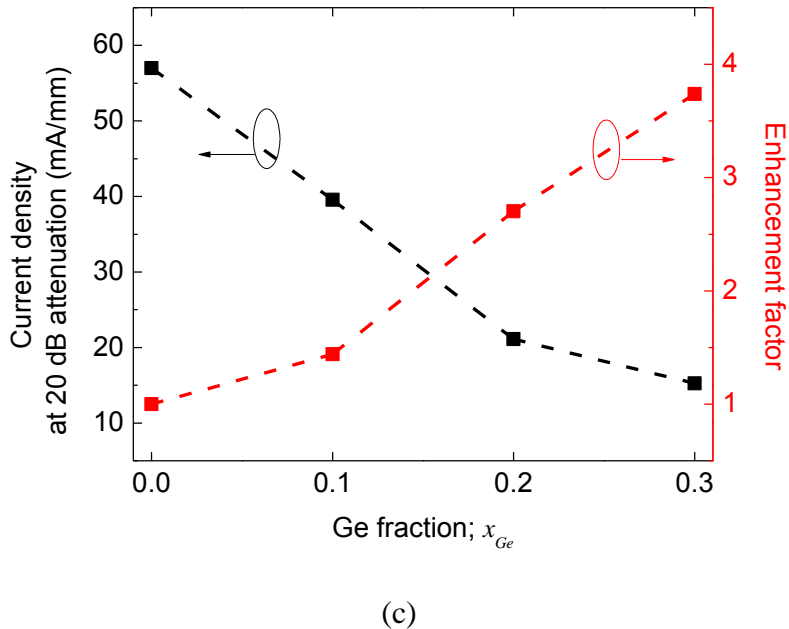


Figure 3.7 Simulation results of the pin injection-type strained SiGe optical modulator. (a) Attenuation characteristics as a function of injected current density to the in-line modulator with Ge fractions of 0.0 to 0.3. (b) Change in refractive index as a function of current density injected to in-line modulator with Ge fractions of 0.0 to 0.3. (c) Current density required for 20 dB attenuation (left-axis) and its enhancement factor (right axis) as a function of Ge fraction; the efficiency of the $\text{Si}_{0.7}\text{Ge}_{0.3}$ -based in-line intensity modulator is predicted to be approximately 3.7 times as large as that of the Si-based modulator.

3.5 Conclusion

The numerical analysis on SiGe-based modulator/attenuator comparing with the Si modulator has been carried out for obtaining the high modulation efficiency. By taking into account the enhancement in the plasma dispersion effect and free-carrier absorption in the SiGe layer, the modulation characteristics of SiGe-based optical modulators and variable optical attenuator were analyzed. The current-injection $\text{Si}_{0.7}\text{Ge}_{0.3}$ -based VOA exhibits the current density of approximately 15 mA/mm for 20 dB-attenuation, which is 3 times as small as that of the Si-based optical modulator. Also, the injection current for π -shift is expected to be reduced by 1/3 using strained $\text{Si}_{0.7}\text{Ge}_{0.3}$. As we have seen

the strain engineering in Si CMOS technology, it is also highly promising method to boost the performance of optical modulators through mass modulation by strain effect.

References

- [3.1] G. T. Reed, G. Mashanovich, F. Y. Gardes, and D. J. Thomson, "Silicon optical modulators," *Nature Photonics*, vol. 4, pp. 518-526, Aug 2010.
- [3.2] L. Liao, A. Liu, D. Rubin, J. Basak, Y. Chetrit, H. Nguyen, *et al.*, "40 Gbit/s silicon optical modulator for high-speed applications," *Electronics Letters*, pp. 51-52, Jun 2009.
- [3.3] Q. F. Xu, S. Manipatruni, B. Schmidt, J. Shakya, and M. Lipson, "12.5 Gbit/s carrier-injection-based silicon micro-ring silicon modulators," *Optics Express*, vol. 15, pp. 430-436, Jan 22 2007.
- [3.4] D. J. Thomson, F. Y. Gardes, Y. Hu, G. Mashanovich, M. Fournier, P. Grosse, *et al.*, "High contrast 40Gbit/s optical modulation in silicon," *Opt Express*, vol. 19, pp. 11507-16, Jun 6 2011.
- [3.5] M. Takenaka and S. Takagi, "Strain Engineering of Plasma Dispersion Effect for SiGe Optical Modulators," *IEEE Journal of Quantum Electronics*, vol. 48, pp. 8-16, Jan 2012.
- [3.6] R. A. Soref and B. R. Bennett, "Electrooptical Effects in Silicon," *IEEE Journal of Quantum Electronics*, vol. 23, pp. 123-129, Jan 1987.
- [3.7] W. M. J. Green, M. J. Rooks, L. Sekaric, and Y. A. Vlasov, "Ultra-compact, low RF power, 10 gb/s silicon Mach-Zehnder modulator," *Optics Express*, vol. 15, pp. 17106-17113, Dec 10 2007.
- [3.8] R. People and J. C. Bean, "Calculation of Critical Layer Thickness Versus Lattice Mismatch for Ge_xSi_{1-x}/Si Strained-Layer Heterostructures," *Applied Physics Letters*, vol. 47, pp. 322-324, 1985.
- [3.9] D. J. Roulston, N. D. Arora and S. G. Chamberlain, "Modeling and measurement of minority-carrier lifetime versus doping in diffused layers of n⁺-p silicon diodes," *IEEE Transaction Electron Devices* ED-29, 180–187 (1982).
- [3.10] G. R. Zhou, M. W. Geis, S. J. Spector, F. Gan, M. E. Grein, R. T. Schulein, *et al.*, "Effect of carrier lifetime on forward-biased silicon Mach-Zehnder modulators," *Opt Express*, vol. 16, pp. 5218-26, Apr 14 2008. .
- [3.11] S. Park, K. Yamada, T. Tsuchizawa, T. Watanabe, H. Shinojima, H. Nishi, *et al.*, "Influence of carrier lifetime on performance of silicon p-i-n variable optical attenuators fabricated on submicrometer rib waveguides," *Opt Express*, vol. 18, pp.

11282-91, May 24 2010.

- [3.12] S. Sekiguchi, T. Kurahashi, L. Zhu, K. Kawaguchi, and K. Morito, "Compact and low power operation optical switch using silicon-germanium/silicon hetero-structure waveguide," *Optics Express*, vol. 20, pp. 8949-8958, Apr 9 2012.
- [3.13] M. M. Rieger and P. Vogl, "Electronic-Band Parameters in Strained Si_{1-X}Ge_X Alloys on Si_{1-Y}Ge_Y (Vol 48, Pg 14276, 1993)," *Physical Review B*, vol. 50, pp. 8138-8138, Sep 15 1994.

Chapter 4

Demonstration of SiGe rib waveguide for SiGe optical modulator/attenuator

We have characterized photonic-wire waveguides with Si/SiGe/Si heterostructure ribs for Si-based optical modulators. The Si (80 nm)/Si_{0.72}Ge_{0.28} (40 nm) layers grown on Si-on-insulator by molecular beam epitaxy for optical modulators were evaluated by *in-situ* reflection high-energy electron diffraction, atomic force microscope, X-ray diffraction and Raman spectroscopy, exhibiting that the fully-strained highly-crystalline SiGe layer was obtained. We have evaluated the propagation loss of the Si/strained SiGe/Si photonic-wire waveguides. The wavelength dependence of the propagation loss exhibits the bandgap narrowing of the strained Si_{0.72}Ge_{0.28}, while the optical absorption of the strained Si_{0.72}Ge_{0.28} is not significant for the optical modulator application at 1.55- μm wavelength.

4.1 Introduction

Recently, silicon (Si) optical modulators have attracted much attention as the one of the fundamental building blocks for optoelectronic integrated circuits toward large-scaled integrated circuits with on-chip optical interconnects [4.1], [4.2], [4.3]. High speed optical modulators have recently been demonstrated so far by using a Mach-Zehnder interferometer (MZI) with phase-shifters in which the effective refractive index of the Si waveguide is modulated by the electrical signal. An MZI has been mostly used for getting optical modulation because of its wide wavelength bandwidth, while the large device length of several millimeters is considered as one of the most challenging problems for large scale integration [4.4], [4.5], [4.6].

To solve this problem, strained SiGe-based optical modulators have been proposed [4.7], [4.8]. The refractive index change from the plasma dispersion effect is inversely proportional to conductivity effective masses of electrons and holes [4.9]. Therefore, the lighter conductivity masses become, the larger plasma dispersion occurs. Compressively strained SiGe, which is one of the promising materials for future scaled p-channel metal-oxide-semiconductor (MOS) transistors [4.10], [4.11], [4.12] is well known to exhibit the light conductivity hole mass. Thus, the plasma dispersion effect is expected to be enhanced through effective mass modulation in strained SiGe, enabling small device footprint. In the previous our work [4.8], the strain effect on carrier-injection type optical modulators by using the Si/strained SiGe/ Si waveguide is numerically investigated. Owing to enhancement in free-carrier effects, the plasma dispersion effect and free-carrier absorption, of strained SiGe, the pin-junction Si/SiGe_{0.28}/Si optical modulator has approximately 4.5 times smaller switching power than that of the Si modulator. However, the bandgap energy decreases with an increase in the Ge fraction of SiGe, causing an increase in optical absorption at 1.55-μm wavelength [4.13], [4.14]. In this chapter, we have fabricated Si/strained Si_{0.72}Ge_{0.28}/Si heterostructures on a silicon-on-insulator (SOI) wafer by molecular beam epitaxy (MBE), and evaluated the propagation loss of the Si/SiGe/Si photonic-wire waveguides for optical modulator applications at 1.55-μm wavelength.

4.2 Device fabrication

We show the process flow of the Si/SiGe/Si photonic-wire waveguide in Fig. 1. The Si/SiGe/Si-OI substrate was prepared by using a (001) SOI wafer with a 2-μm-thick buried oxide layer (BOX). First, a 220-nm-thick SOI layer was thinned to be 100 nm by thermal oxidation at 1100 °C and BHF etching of a thermally grown SiO₂ layer as shown in Figs. 1(a) and (b). Then, a 40-nm-thick Si_{0.72}Ge_{0.28} layer and an 80-nm-thick Si layer were grown on the SOI by MBE under the base pressure of 3×10^{-8} Pa at 400 °C and 600 °C, respectively as shown in Fig. 1 (c). The thickness of the SiGe layer was kept below the critical thickness for avoiding strain relaxation [4.15]. Then, photonic-wire waveguides with a Si/SiGe mesa were fabricated by using the Si/SiGe/Si-OI wafer. After cleaning the substrate, the electron beam resist (ZEP520A) was coated on the

substrate with the spin condition of 3000 rpm for 30 s followed by the prebake at 160 °C for 10 min and deep ultraviolet (DUV) lithography. Then, waveguide patterns of variable waveguide widths were formed by reactive ion etching with CF₄ gas for approximately 11 min. The gas pressure of CF₄ and RF power were set to be 1 Pa and 20 W, respectively. Finally, a 500-nm-thick SiO₂ layer was deposited by plasma-enhanced chemical vapor deposition for device passivation as shown in Fig. (d). Si photonic-wire waveguides as a control sample were also fabricated by using the 220-nm-thick SOI substrate, which is corresponding to the total thickness of the 80-nm-thick Si/40-nm-thick SiGe/100-nm-thick Si waveguide.

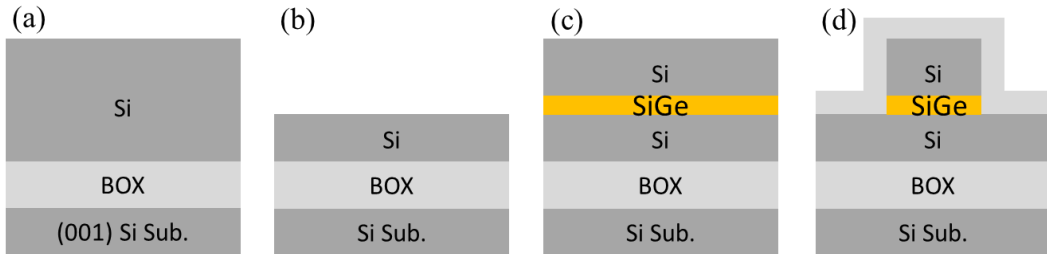


Figure 4.1 Process flow of Si/SiGe/Si photonic-wire waveguide. (a) initial 220-nm-thick SOI, (b) 100-nm-thick SOI thinned by thermal oxidation, (c) Si/SiGe/Si-OI grown by MBE, and (d) dry etching of waveguide mesa, followed by SiO₂ passivation.

4.3 Characterization of epitaxially grown Si/SiGe/Si-OI and device

Figures 4.2 show the *in-situ* reflection high-energy electron diffraction (RHEED) images during the crystal growth process of Si/SiGe on the SOI substrate. The as-installed sample shows the spotty 1×1 RHEED pattern due to hydrogen termination during BHF as shown in Fig. 4.2(a). Figure 4.2(b) shows the longish 2×1 RHEED pattern after thermal cleaning at 850 °C for 30 min, meaning that hydrogen was removed by high thermal energy. Figures 4.2(c) and (d) show the longish 2×1 RHEED patterns during the SiGe and Si growth, indicating the two dimensional island morphology.

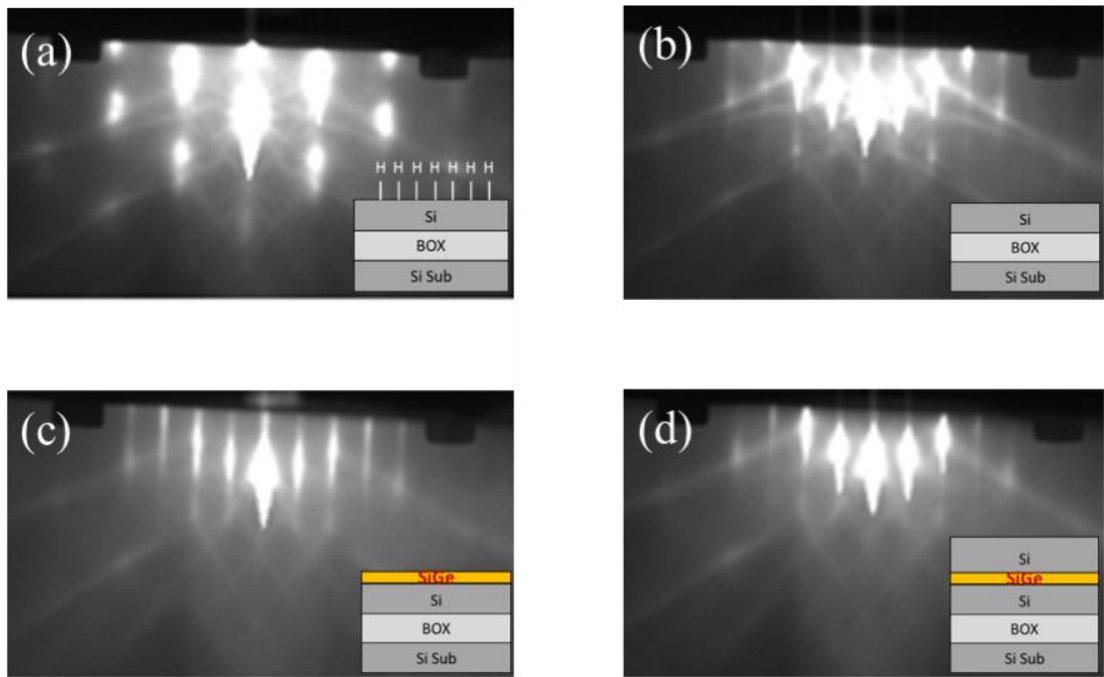


Figure 4.2. *in-situ* RHEED images during MBE growth procedures: after (a) SOI installation, (b) thermal cleaning, (c) SiGe growth, and (d) Si growth.

Figures 4.3 show the surface morphologies of the Si/SiGe/SOI substrate measured by atomic force microscope (AFM, Nanocute SS, Dynamic force mode). The root-mean-squares of the surface roughness with the scanning areas of (a) $500 \times 500 \text{ nm}^2$, (b) $5 \times 5 \mu\text{m}^2$, and (c) $10 \times 10 \mu\text{m}^2$ are less than 0.18 nm, indicating that the pseudomorphic strained SiGe layer is obtained.

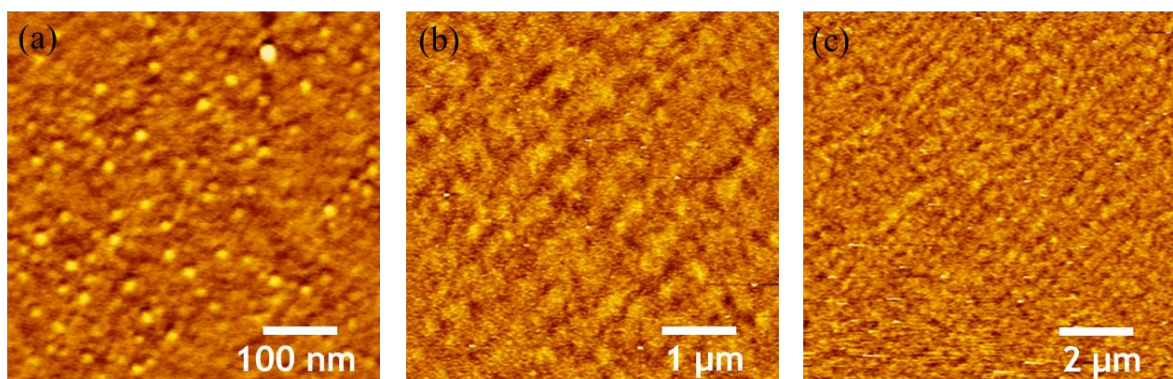


Figure 4.3 AFM evaluation of surface roughnesses of the Si/SiGe/SOI samples grown by MBE with the scanning areas of (a) $500 \times 500 \text{ nm}^2$, (b) $5 \times 5 \mu\text{m}^2$, and (c) $10 \times 10 \mu\text{m}^2$.

μm^2 (Color scale: 1.5 nm).

To investigate the crystal quality of the grown SiGe layer, we measured the ω - 2θ profile of Si/SiGe/SOI substrate by using x-ray diffraction (XRD, X'Pert PRO MRD, 1.8 kW, K α 1). The x-ray diffraction peak of the SiGe layer was clearly observed with the peak of the Si substrate (004) shown in Fig. 4.4. From the angle of diffraction, the lattice constant of SiGe normal to the surface was estimated to be 5.532 Å, much larger than that of a relaxed Si_{0.72}Ge_{0.28}, 5.489 Å. Thus, the compressive strain is estimated to be as large as 1.0% when the Ge fraction of the SiGe alloy is 28%.

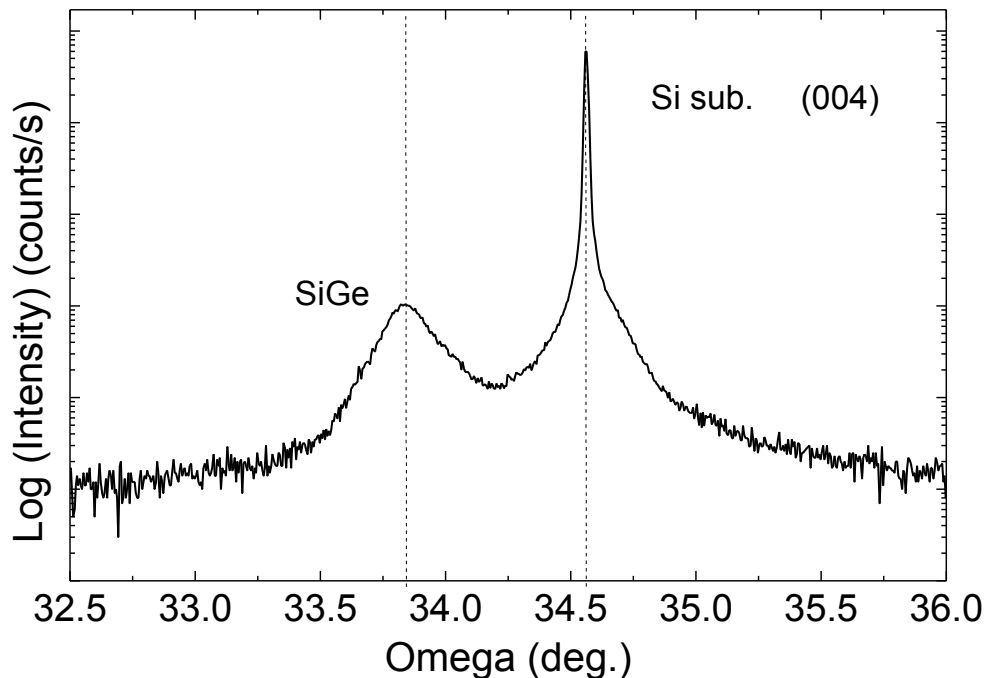


Figure 4.4 ω - 2θ profiles around the (004) x-ray diffraction of the Si/SiGe/SOI.

The Si/SiGe/Si-OI substrate was also evaluated by Raman spectroscopy (LabRAM HR, 488 nm) to precisely evaluate the Ge fraction and strain value in the SiGe layer by using the method depicted in the reference [4,16]. The Raman spectrum of the SiGe layer shown in Fig. 4.5 exhibits the three major phonon modes corresponding to the Si-Si, Si-Ge, and Ge-Ge bonds. It is found from Fig. 4.5 that the Ge fraction and the compressive strain value of the SiGe layer is approximately 28% and 1.1%

respectively, which means that the SiGe layer is almost fully strained as indicated in the inset of Fig. 4.5.

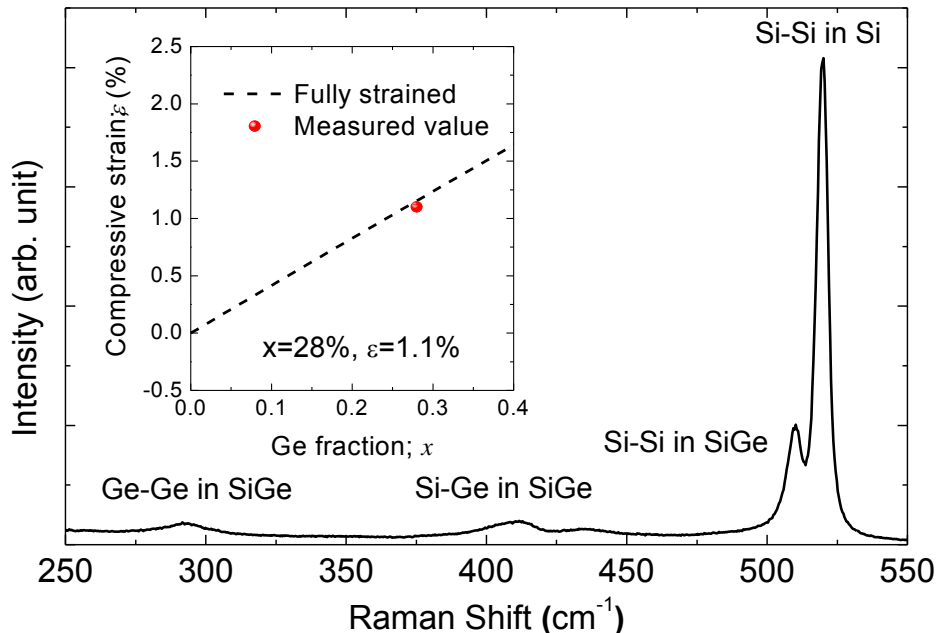


Figure 4.5 Raman spectrum of Si/SiGe/Si-OI. The inset is the measured compressive strain as a function of the Ge fraction.

Figures 4.6(a) and (b) show the cross-sectional and bird's-eye view scanning electron microscope (SEM, S-4700, 10 kV) images of the Si/SiGe/Si photonic-wire waveguide, clearly indicating a well-defined core without excessive lateral over-etching in the SiGe layer.

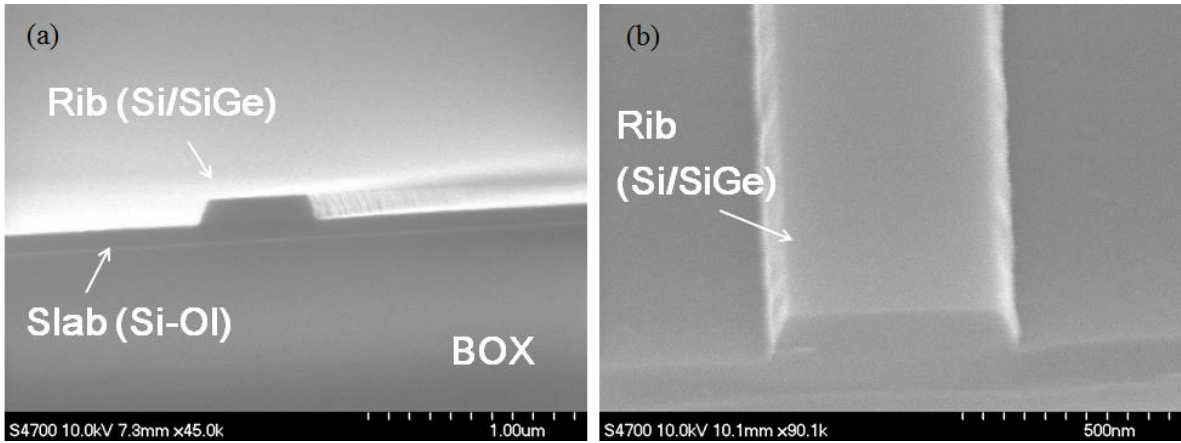


Figure 4.6 SEM images of the fabricated optical waveguide with Si/SiGe/Si core: (a) tilted-cross-sectional view and (b) tilted-bird's-eye view.

To investigate the absorption related to the bandgap of the strained SiGe, the wavelength dependence of the Si/SiGe/Si photonic-wire waveguide loss was measured from 1340 nm (0.761 eV) to 1630 nm (0.925 eV). A continuous-wave (CW) light from tunable laser sources was coupled the waveguide through a lensed fiber with a spot size of approximately 4 μm . The input light is adjusted to TE-polarized light by using an in-line polarizer. The output light from the waveguide was collected by an objective lens and coupled again to a single-mode optical fiber. The output power was monitored by an InGaAs photodetector. Here, it has been reported that SiGe waveguides has nonlinear optical properties, which is dependent on the power of laser [4.17]. However, in our experiment, the power of laser coupled to waveguides is small enough for suppressing such a nonlinear effect described in [4.17]. The power of laser coupled to waveguides is approximately -10 dBm (0.1 mW) by taking a coupling loss into account, which is smaller than that discussed in [4.17] by three orders of magnitude.

The device length was approximately 1 cm. Figure 4.7 shows that the absorption of the Si/SiGe/Si waveguide increases with an increase in the photon energy due to the indirect bandgap of $\text{Si}_{0.72}\text{Ge}_{0.28}$ near 0.88 eV [4.18]. The propagation loss at 1.55- μm wavelength, which is the most important wavelength for optical communications, was also measured by the cut-back method with variable waveguide width as shown in Fig. 8. The propagation loss dramatically increases in both SiGe and Si waveguides as the width decreases due to the sidewall roughness arising from DUV

lithography. The width dependence loss is known by the theoretical model in which the loss was expressed to be inversely proportional to the width squared [4.19]. The propagation loss based on the theoretical model can be expressed by

$$\text{propagation loss} = \frac{\sigma}{w^2} + \text{offset} \quad (4.1)$$

where, σ is the fitting parameter related to surface roughness, w is the width of a waveguide, and offset is additional loss from band-to-band absorption. The experimental results of the width dependence losses of the Si/SiGe_{0.28}/Si and Si waveguides were fitted by using the fitting parameters in Eq. (4.1) to the model in which the loss was expressed to be inversely proportional to the square of width.

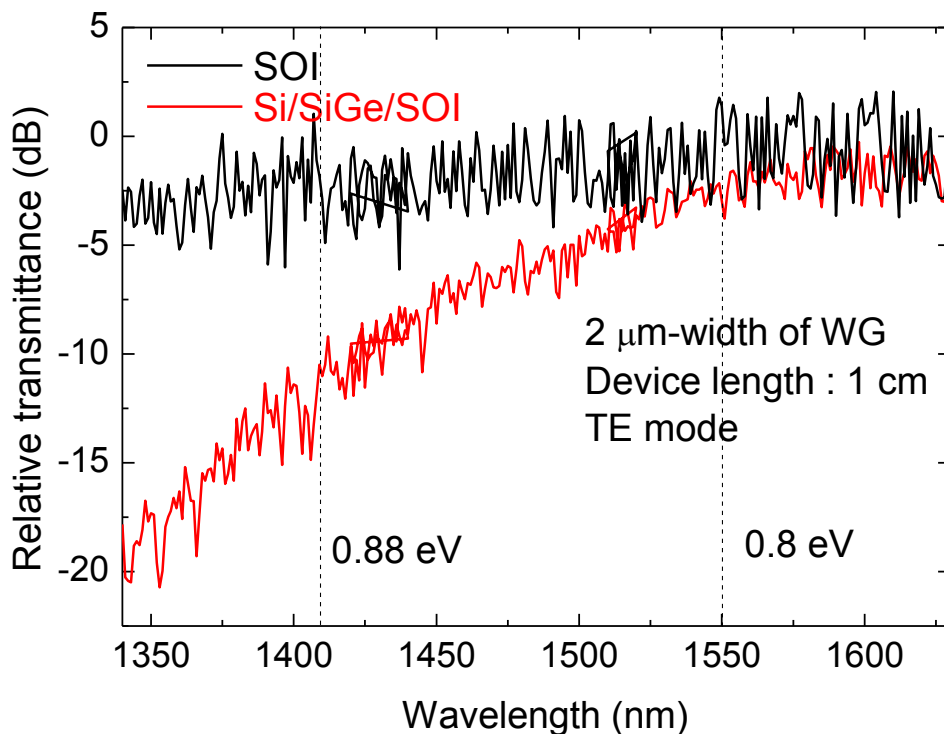


Figure 4.7 Wavelength dependence of propagation loss in 2 μm -width Si and Si/SiGe/Si photonic-wire waveguides. The device length is approximately 1 cm.

The numerical fitting was carried out for the Si and Si/SiGe/Si waveguide with

the model. We found that the increases in the propagation loss with a decrease in waveguide width less than 1 μm are almost same for the Si and Si/SiGe/Si waveguides. In addition, we observed the difference in the propagation loss between the Si and Si/SiGe/Si waveguides with 5- μm width even though the sidewall-roughness-induced loss is almost negligible in case of the large-width waveguide. Therefore, we can conclude that the sidewall-roughness-induced losses for the Si and Si/SiGe/Si waveguide are almost same and the estimation of the band-to-band absorption in the SiGe layer is not affected by the sidewall roughness of the waveguides.

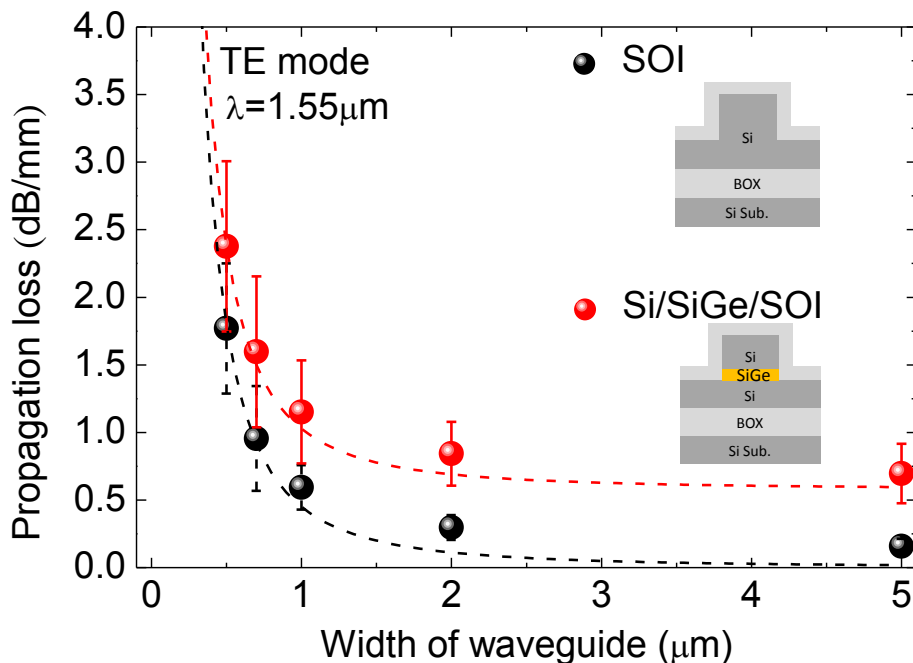


Figure 4.8 Propagation losses of Si and Si/SiGe/Si waveguides as a function of the waveguide width measured by the cut-back method and schematic of the waveguides (inset).

The ratio of σ of between the Si/SiGe_{0.28}/Si and Si waveguides is nearly one, meaning that the surface-roughness-induced losses are almost same. On the other hand, *offset* of Si/SiGe_{0.28}/Si is 0.54 while *offset* of Si is almost 0; we assumed the constant offset loss in the model because the band-to-band absorption in the SiGe layer was not dependent on the waveguide width. Hence, the additional loss caused by the absorption in the compressively strained Si_{0.72}Ge_{0.28} layer is estimated to be 0.54 dB/mm (1.2 cm⁻¹)

at 1.55 μm . Although the propagation loss of the Si/SiGe/Si waveguide is higher than the typical Si waveguides loss of less than 0.3 dB/mm, we can monolithically integrate a Si/SiGe/Si layer for active regions and a Si layer for passive regions by using selective area growth. Thus, we can avoid additional propagation loss in the passive area. In addition, the increase in the propagation loss of the Si/SiGe/Si modulators is not significant because the length of the modulator can be reduced by the enhanced plasma dispersion effect in strained SiGe.

4.4 Conclusion

We have fabricated the Si/SiGe/Si waveguide on an SOI substrate by using MBE. The wavelength and waveguide's width dependences of the propagation loss of the Si/SiGe/Si photonic-wire waveguides reveal that the additional propagation loss related to the narrow bandgap in the fully strained $\text{Si}_{0.72}\text{Ge}_{0.28}$ layer is approximately 0.54 dB/mm at 1.55- μm wavelength, which is negligible for optical modulator applications.

References

- [4.1] A. S. Liu and M. Paniccia, "Advances in silicon photonic devices for silicon-based optoelectronic applications," *Physica E-Low-Dimensional Systems & Nanostructures*, vol. 35, pp. 223-228, Dec 2006.
- [4.2] C. Gunn, "CMOS photonics for high-speed interconnects," *IEEE Micro*, vol. 26, pp. 58-66, Mar-Apr 2006.
- [4.3] G. T. Reed, G. Mashanovich, F. Y. Gardes, and D. J. Thomson, "Silicon optical modulators," *Nature Photonics*, vol. 4, pp. 518-526, Aug 2010.
- [4.4] L. Liao, A. Liu, D. Rubin, J. Basak, Y. Chetrit, H. Nguyen, *et al.*, "40 Gbit/s silicon optical modulator for high-speed applications," *Electronics Letters*, pp. 51-52, Jun 2009.
- [4.5] F. Y. Gardes, D. J. Thomson, N. G. Emerson, and G. T. Reed, "40 Gb/s silicon photonics modulator for TE and TM polarisations," *Opt Express*, vol. 19, pp. 11804-14, Jun 6 2011.
- [4.6] D. J. Thomson, F. Y. Gardes, J. M. Fedeli, S. Zlatanovic, Y. F. Hu, B. P. P. Kuo, *et al.*, "50-Gb/s Silicon Optical Modulator," *IEEE Photonics Technology Letters*, vol. 24, Feb 15 2012.
- [4.7] M. Takenaka and S. Takagi, "Strain Engineering of Plasma Dispersion Effect for SiGe Optical Modulators," *IEEE Journal of Quantum Electronics*, vol. 48, pp. 8-16, Jan 2012.
- [4.8] Y. Kim, M. Takenaka, S. Takagi, San Diego, U.S.A., September 29, 2012, 9th Conf. of Group IV Photonics, Proceedings WP18 (2012) 126.
- [4.9] R. A. Soref and B. R. Bennett, "Electrooptical Effects in Silicon," *IEEE Journal of Quantum Electronics*, vol. 23, pp. 123-129, Jan 1987.
- [4.10] M. V. Fischetti and S. E. Laux, "Band structure, deformation potentials, and carrier mobility in strained Si, Ge, and SiGe alloys," *Journal of Applied Physics*, vol. 80, pp. 2234-2252, Aug 15 1996.
- [4.11] T. Manku, J. M. McGregor, A. Nathan, D. J. Roulston, J. P. Noel, D. C. Houghton, "Drift hole mobility in strained and unstrained doped $\text{Si}_{1-x}\text{Ge}_x$ alloys," *IEEE Transactions on Electron Devices*, vol. 40, pp. 1990-1996, 1993

- [4.12] K. Cheng, A. Khakifirooz, N. Loubet, S. Luning, T. Nagumo, M. Vinet, Q. Liu, A. Reznicek, T. Adam, S. Naczas, P. Hashemi, J. Kuss, J. Li, H. He, L. Edge, J. Gimbert, P. Khare, Y. Zhu, Z. Zhu, A. Madan, N. Klymko, S. Holmes, T. M. Levin, A. Hubbard, R. Johnson, M. Terrizzi, S. Teehan, A. Upham, G. Pfeiffer, T. Wu, A. Inada, F. Allibert, B.-Y. Nguyen, L. Grenouillet, Y. Le Tiec, R. Wacquez, W. Kleemeier, R. Sampson, R. H. Dennard, T. H. Ning, M. Khare, G. Shahidi, and B. Doris., IEEE International Electron Devices Meeting, Conference Proceedings (2012) 18.1.1.
- [4.13] R. Braunstein, A. R. Moore, and F. Herman, "Intrinsic Optical Absorption in Germanium-Silicon Alloys," *Physical Review*, vol. 109, pp. 695-710, 1958.
- [4.14] D. V. Lang, R. People, J. C. Bean, and A. M. Sergent, "Measurement of the Band-Gap of Gexsi1-X/Si Strained-Layer Heterostructures," *Applied Physics Letters*, vol. 47, pp. 1333-1335, 1985.
- [4.15] R. People and J. C. Bean, "Calculation of Critical Layer Thickness Versus Lattice Mismatch for Gexsi1-X/Si Strained-Layer Heterostructures," *Applied Physics Letters*, vol. 47, pp. 322-324, 1985. .
- [4.16] F. Pezzoli, E. Bonera, E. Grilli, M. Guzzi, S. Sanguinetti, D. Chrastina, *et al.*, "Raman spectroscopy determination of composition and strain in Si_{1-x}Gex/Si heterostructures," *Materials Science in Semiconductor Processing*, vol. 11, pp. 279-284, Oct 2008.
- [4.17] K. Hammani, M. A. Ettabib, A. Bogris, A. Kapsalis, D. Syvridis, M. Brun, *et al.*, "Optical properties of silicon germanium waveguides at telecommunication wavelengths," *Optics Express*, vol. 21, pp. 16690-16701, Jul 15 2013. .
- [4.18] J. C. Bean, "Silicon-Based Semiconductor Heterostructures - Column-Iv Bandgap Engineering," *Proceedings of the IEEE*, vol. 80, pp. 571-587, Apr 1992.
- [4.19] F. P. Payne and J. P. R. Lacey, "A Theoretical-Analysis of Scattering Loss from Planar Optical Wave-Guides," *Optical and Quantum Electronics*, vol. 26, pp. 977-986, Oct 1994.

Chapter 5

Demonstration of enhanced free-carrier effect in carrier-injection type SiGe variable optical attenuator

We have experimentally investigated the enhancement of the plasma dispersion effect and free-carrier absorption by strain-induced mass modulation in silicon-germanium (SiGe). The application of compressive strain to SiGe reduces the conductivity effective mass for holes, resulting in the enhanced free-carrier effects. Thus, the strained SiGe-based optical modulator exhibits more than twice modulation efficiency as large as that of the Si modulator. It is the first demonstration of the enhanced free-carrier effects in strained SiGe at the near-infrared telecommunication wavelength. The strain-induced enhancement technology for the free-carrier effects is expected to boost the modulation efficiency of the most Si-based optical modulators thanks to high complementary metal-oxide-semiconductor (CMOS) compatibility.

5.1 Introduction

The plasma dispersion effect and free-carrier absorption are well known physical phenomena to change optical constants: refractive index (n) and absorption coefficient (α) in semiconductors. In particular, these effects are the most promising for silicon (Si) to build-up optical modulators as previously shown in the study by Soref and Bennett [5.1]. Thus, Si optical modulators based on the free-carrier effects have been demonstrated thus far by carrier modulation through injection, depletion and accumulation [5.2], [5.3], [5.4], [5.5], [5.6], [5.7], [5.8], [5.9], [5.10], [5.11], [5.12], [5.13]. In particular, a

depletion-based Mach-Zehnder interferometer (MZI) optical modulator, in which the refractive index of the phase shifters are modulated by carrier depletion, is one of the most promising modulators in terms of modulation speed and optical bandwidth. However, the weak plasma dispersion and free-carrier absorption in Si cause the low modulation efficiency, resulting in a long device length for MZI modulators.

To supplement the weak plasma dispersion effect and free-carrier absorption in Si, the introduction of ring resonators instead of MZIs,^{[5.2], [5.11]} and slow-light structures using photonic crystals^{[5.12], [5.13]} have been investigated, while the optical bandwidth has also been reduced in such structures. Hence, the enhancement of the plasma dispersion effect and free-carrier absorption is indispensable for Si-based optical modulators.

According to the Drude model as discussed in Chapter 2, the plasma dispersion effect and free-carrier absorption are expressed by

$$\Delta n = -(e^2 \lambda^2 / 8\pi^2 c^2 \epsilon_0 n) [\Delta N_e / m_{ce}^* + \Delta N_h / m_{ch}^*] \quad (5.1)$$

$$\Delta \alpha = (e^3 \lambda^2 / 4\pi^2 c^3 \epsilon_0 n) [\Delta N_e / m_{ce}^{*2} \mu_e + \Delta N_h / m_{ch}^{*2} \mu_h], \quad (5.2)$$

where e is the elementary charge, ϵ_0 is the permittivity in vacuum, c is the speed of light in vacuum, λ is the wavelength, n is the unperturbed refractive index, m_{ce}^* and m_{ch}^* are the conductivity effective masses of electrons and holes, and μ_e and μ_h are the mobilities of electrons and holes, respectively. The Drude model describes the changes in the refractive index and absorption coefficient arising from a change in the plasma frequency of free carriers, which is dependent on not only the number of free carriers but also their conductivity effective masses. According to the model, the change in the refractive index induced by the plasma dispersion effect is inversely proportional to the conductivity effective masses of electrons and holes^[5.14]. Therefore, the lighter the conductivity masses become, the greater the plasma dispersion is. In complementary metal-oxide-semiconductor (CMOS) technology, the application of strain to Si has been widely used to achieve lighter conductivity masses and higher mobilities in the channels of transistors, which can overcome the fundamental difficulty in scaling MOS

transistors. Tensile strain and compressive strain are applied to Si n-channel MOS transistors and p-channel MOS transistors, respectively [5.15], [5.16], [5.17]. It was also experimentally observed that the plasma dispersion effect and free-carrier absorption in Si in the far-infrared wavelength range from 5 to 20 μm were modified by uniaxial strain mechanically applied to Si through strain-induced mass modulation [5.18], [5.19], [5.20]. Here, we report the enhancement of the plasma dispersion effect and free-carrier absorption by strain-induced mass modulation in a Si/strained SiGe/Si double-heterostructure waveguide with a lateral *pin* junction for carrier injection in the near-infrared wavelength range from 1.3 to 1.6 μm , which is the most important range of wavelengths for optical fiber communication.

5.2 Experiment

A *pin* injection-type optical modulator was fabricated by the conventional Si CMOS process as shown in Fig. 5.1. A 6-inch Si/SiGe/Si-on-insulator wafer was prepared by epitaxial growth on a commercially available (001) Si-on-insulator (SOI) wafer with a 2- μm -thick buried oxide (BOX) layer. First, a 260-nm-thick SOI layer was thinned to 100 nm by thermal oxidation. Then, a 30-nm-thick pseudomorphic $\text{Si}_{0.77}\text{Ge}_{0.23}$ layer and a 70-nm-thick Si layer were grown by chemical vapor deposition (CVD) as shown in Fig. 5.1(a).

First, a straight rib waveguide with a Si/SiGe/Si core was formed by deep ultraviolet (DUV) lithography and dry etching as shown in Fig. 5.1(b). Then, the ion implantation of boron and phosphorus was carried out to form the p^+ and n^+ regions for the fabrication of a *pin* junction, respectively, which was followed by activation annealing at 1000 °C for 30 min in nitrogen atmosphere, as shown in Fig. 5.2(c). Finally, the contact pads for the p^+ and n^+ regions were formed by the thermal evaporation of aluminum as shown in Fig. 5.1(d).

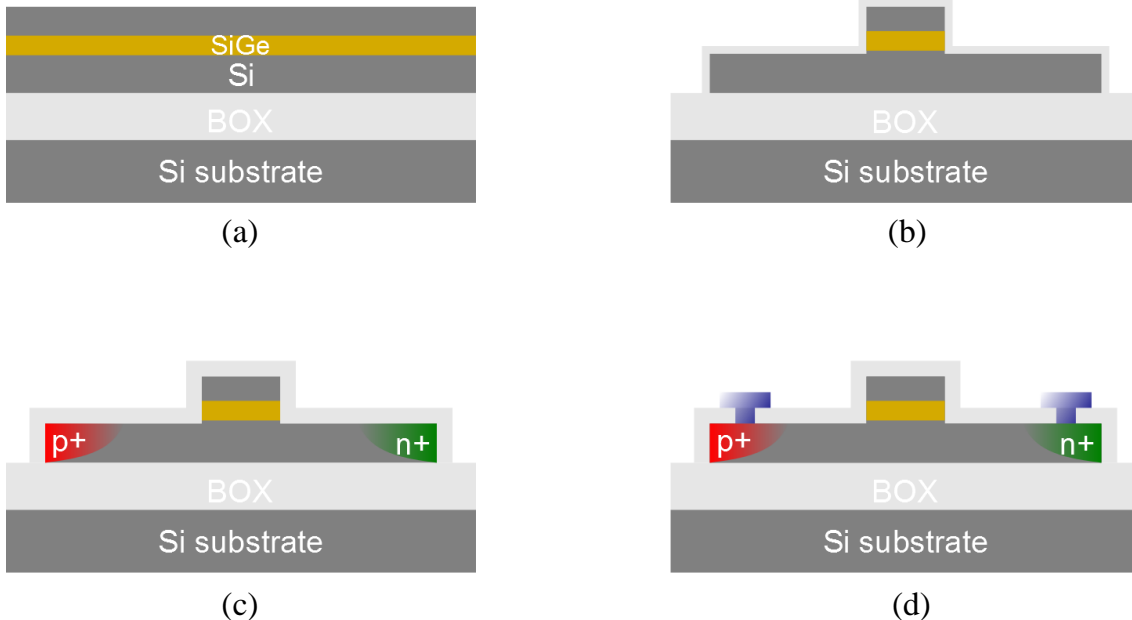


Figure 5.1 Fabrication flow of SiGe VOA (a) Si/SiGe/SOI, (b) Waveguide formation, (c) Lateral pin junction formation by activation followed by ion implantation, and (d) Fabricated device structure with Al contact formation.

Figure 5.2(a) shows a cross-sectional transmission electron microscopy (TEM) image of the Si/SiGe/Si rib waveguide with a 600-nm-wide mesa. The Si/SiGe/Si heterostructure can be clearly observed in Fig. 5.2(b). Also, we show the top-view of fabricated SiGe device observed by optical microscopy as shown in Fig. 5.2(c). A Si-based device without a SiGe well was also fabricated as a control device by the same process.

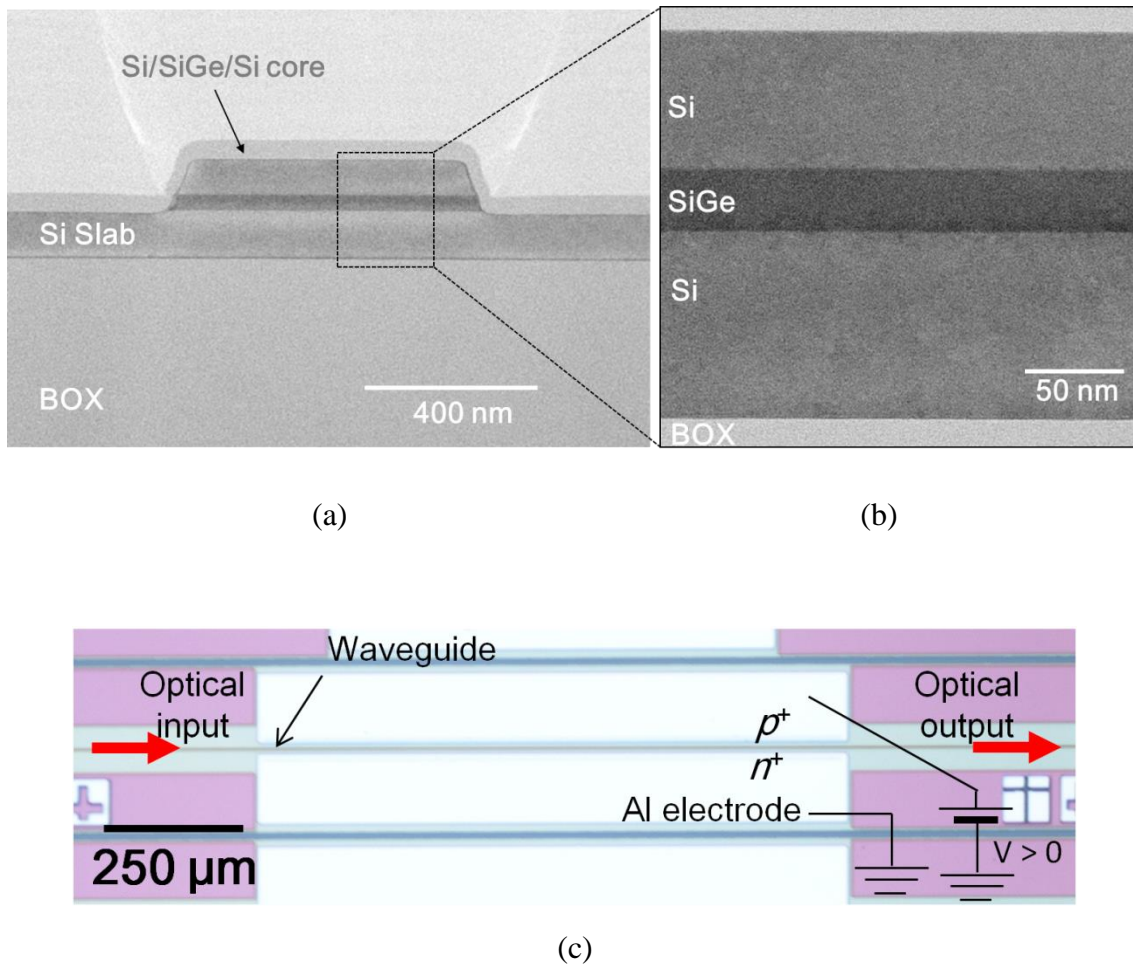


Figure 5.2 (a) Cross-sectional TEM image of the Si/SiGe/Si waveguide, (b) TEM image of the Si/SiGe/Si heterostructure, and (c) Top-view of fabricated SiGe device observed by optical microscopy.

5.3 Result and discussion

The amount of strain in the SiGe layer in the fabricated device was evaluated by Raman spectroscopy. It is well known that the biaxial strain is partially relaxed when a biaxially strained layer is etched into a narrow mesa with submicron width such as optical waveguides. Ge diffusion during high-temperature activation annealing also causes strain relaxation in the SiGe layer. Figure 5.3 shows the amount of strain in SiGe measured before and after dopant activation annealing at 1000 °C for 30 min. The effect

of the waveguide width on strain is also shown in Fig. 5.3 for mesa widths from 600 nm to 1900 nm. The dotted line in Fig. 5.3 shows the ideal strain curve of fully strained SiGe. The wide-mesa SiGe exhibits full strain before annealing, while the amount of strain decreases after annealing because the Ge fraction is reduced by Ge diffusion into the Si layers. The cross-sectional TEM image of the Si/SiGe/Si heterostructure in the inset of Fig. S5 indicates that the thickness of the SiGe layer after annealing is increased to approximately 50 nm. The dry etching of the 600-nm-wide waveguide also causes partial strain relaxation by 15%, as shown in Fig. S5. Thus, the Ge fraction and compressive strain of the SiGe layer in the fabricated device are approximately 14% and 0.48%, respectively, corresponding to 85%-strained $\text{Si}_{0.86}\text{Ge}_{0.14}$.

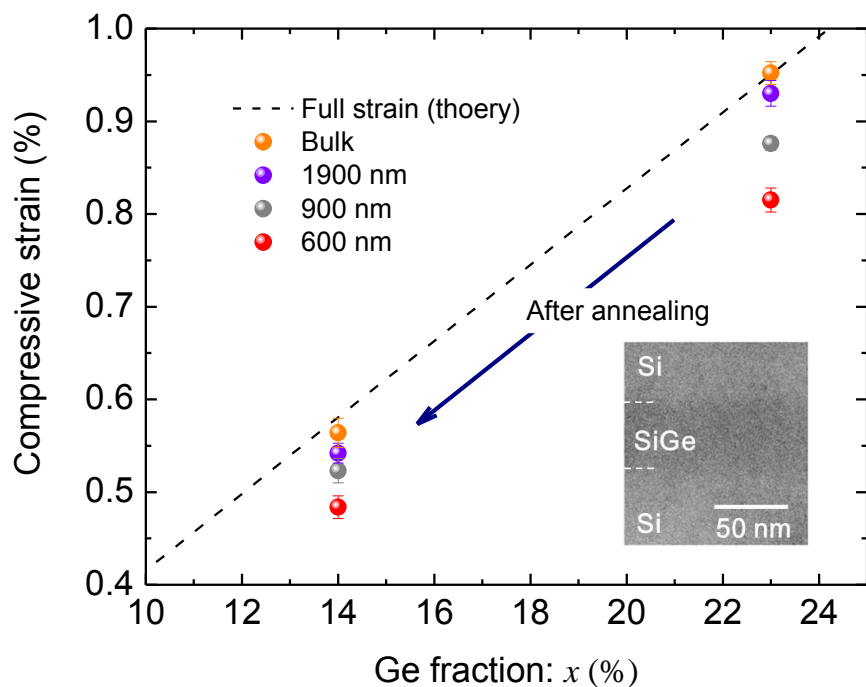


Figure 5.3 Compressive strain as a function of Ge fraction for different waveguide widths and cross-sectional TEM image of Si/SiGe/Si heterostructure after annealing process (inset).

The optical attenuation was measured by injecting current to evaluate the

enhancement of free-carrier absorption in the strained SiGe layer. Continuous-wave (CW) TE-polarized light in the wavelength range from 1.34 to 1.64 μm was coupled to the waveguide through a lensed fiber. Then, the output power was monitored using an InGaAs photodetector while changing the injection current. To calibrate the total coupling loss of approximately -30 dB, the insertion loss without injecting current was subtracted from the loss measured at the various injected currents.

Figure 5.4 shows the measured optical attenuation properties of the SiGe and Si in-line intensity modulators at the wavelength of 1.55 μm . The simulated optical attenuation properties, in which the changes in the Ge fraction and strain after device fabrication are taken into account as shown in Fig. 5.3, are also plotted as solid lines. As shown in Fig. 5.4, the optical attenuation is increased by current injection through the *pin* junction owing to free-carrier absorption; the SiGe modulator exhibits higher attenuation than the Si modulator at the same current density. The experimental results of the SiGe device show fairly good agreement with the simulation results. Therefore, it is clearly shown that strain-induced mass modulation enhances the free-carrier absorption and improves the device performance. The injected current densities required for 20 dB attenuation are approximately 24 and 55 mA/mm for the SiGe and Si modulators, respectively. Thus, the modulation efficiency of the SiGe device is more than twice as large as that of the Si control device. Furthermore, the bias voltages are approximately 1.8 and 2.45 V for the SiGe and Si modulators, respectively. Therefore, the power consumption required for 20-dB attenuation is also reduced from 135 mW to 43 mW by introducing strained SiGe instead of Si.

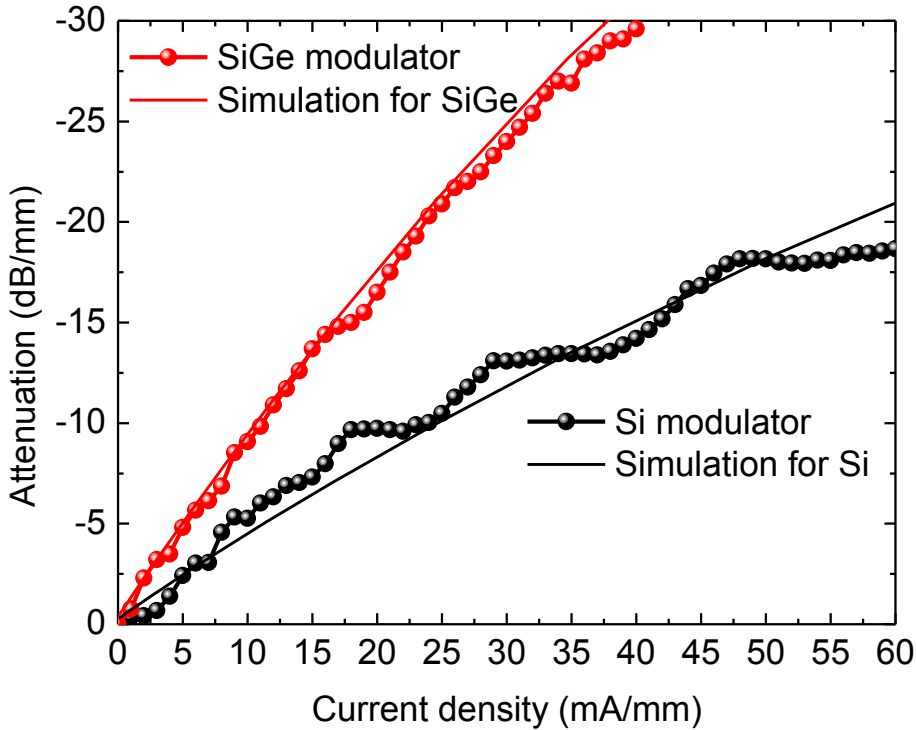


Figure 5.4 Attenuation characteristics of the SiGe and Si modulators. Experimental results are shown by circles and simulated results are shown by lines. The modulation efficiency of the SiGe device is more than twice as large as that of the Si control device.

The wavelength dependence of the optical attenuation of the strained SiGe and Si modulators is analyzed with varied currents in the wavelength range from 1.34 to 1.64 μm . Since the free-carrier effects are proportional to the square of the wavelength according to the Drude model, we plot the optical attenuation measured at injection currents of 20, 30, and 40 mA/mm as a function of the square of the wavelength in Fig. 5.5(a). Linear relationships between the optical attenuation and the square of the wavelength are clearly observed, meaning that the optical attenuation arises from free-carrier absorption. From the wavelength dependences of the optical attenuation characteristics, we calculated the change in the effective refractive index using the Kramers-Kronig relations [5.1].

The Kramers-Kronig relations are the well-known physical relationship between the change in refractive index and absorption coefficient, and is described as follows:

$$\Delta n(\omega) = \frac{c}{\pi} P \int_0^\infty \frac{\Delta \alpha(\omega') d\omega'}{\omega'^2 - \omega^2}, \quad (5.3)$$

where c is the speed of light, ω is the angular frequency, and P is the principal value of the integral. Here, the change in absorption coefficient change is defined as follows:

$$\Delta \alpha(\omega, \Delta N) = \Delta \alpha(\omega, \Delta N) - \Delta \alpha(\omega, 0), \quad (5.4)$$

where ΔN is the change in carrier concentration. Hence, equation (5) can be used to extract the change in the refractive index from the spectrum showing the change in the absorption coefficient. Figures 5.6(a) and (b) show the change in the effective refractive index of the Si and SiGe optical modulators, calculated from the experimentally obtained changes in the absorption coefficient spectra, respectively. As described in equation (3), the calculated changes in the effective refractive index have linear relationship with the square of the wavelength. It is clearly observed in Fig. S6 that the changes for the SiGe device have larger slopes than those for the Si device at all current densities, indicating that the plasma dispersion effect of strained SiGe is larger than that of Si.

Since the measurable wavelength range is limited to from 1.34 to 1.64 μm , corresponding to the photon energy range from 0.756 to 0.925 eV, the free-carrier absorption spectra are extrapolated into the far-infrared wavelength range for the calculation^[5,21]. Figure 4b shows the calculated changes in the effective refractive index at injection currents of 20, 30, and 40 mA/mm as a function of the square of the wavelength, which exhibit a linear relationship.

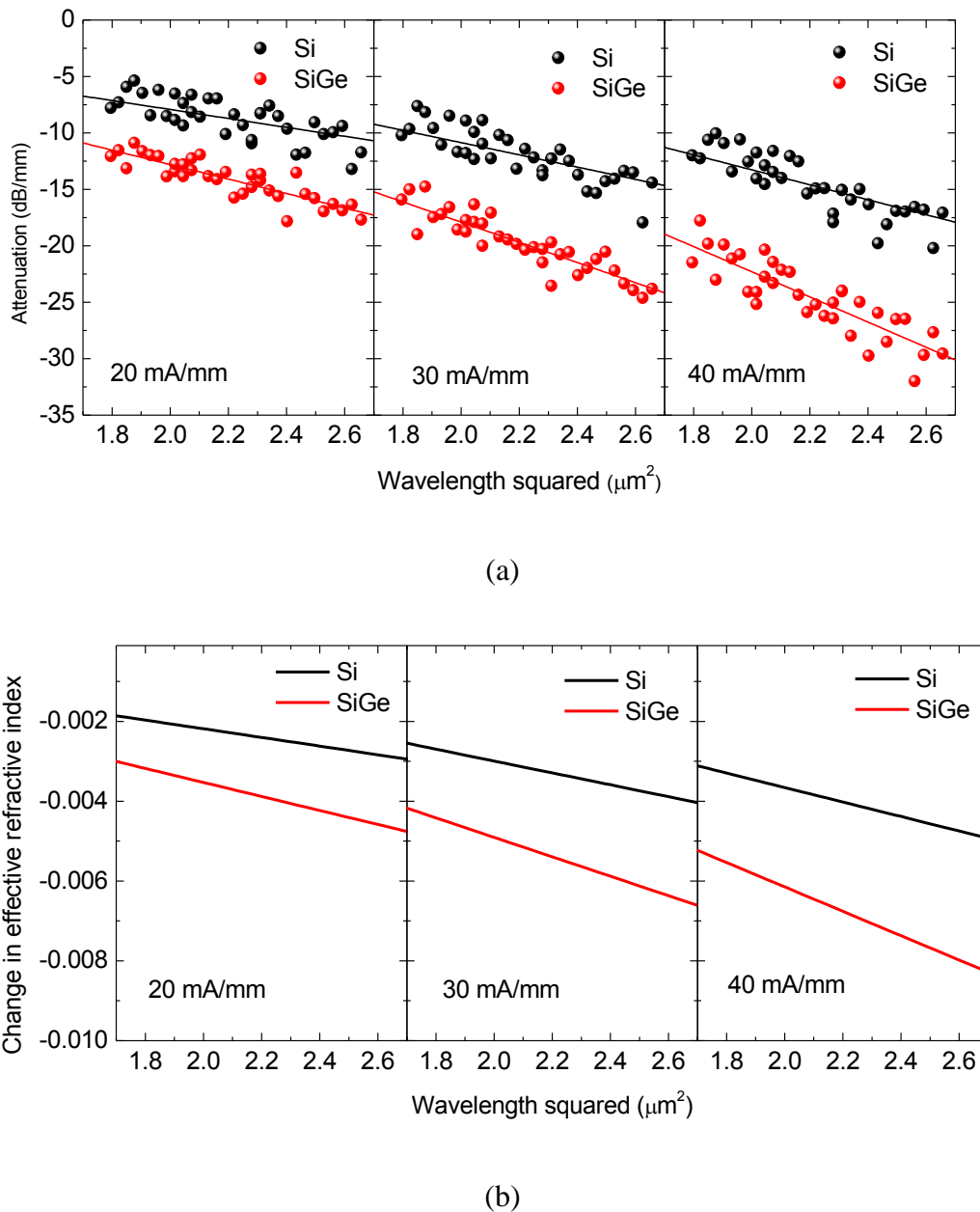


Figure 5.5 Wavelength dependence of modulation characteristics. (a) Measured attenuation of the SiGe and Si modulators with current densities of 20, 30, and 40 mA/mm. (b) Change in the effective refractive index calculated using the Kramers-Kronig relations from the measured wavelength dependence of the attenuation.

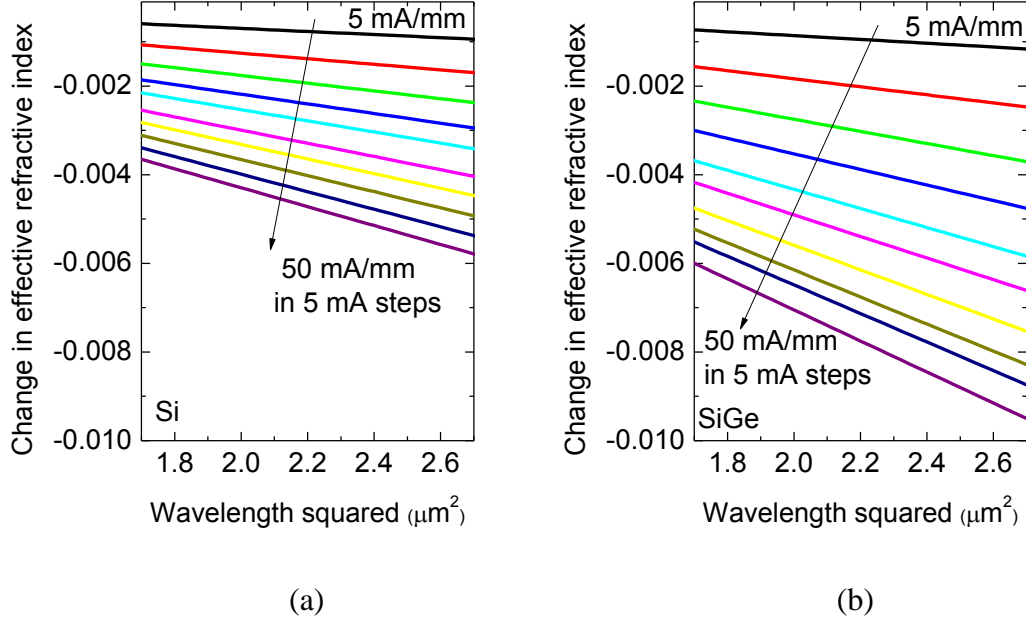


Figure 5.6 Changes in effective refractive index of (a) Si and (b) SiGe optical modulators calculated using the Kramers-Kronig relations from the measured spectra of the change in absorption coefficient with injected current density for current densities of 5 to 50 mA/mm in 5 mA steps.

The changes in the optical constants of the SiGe layer are deduced from the wavelength dependences in Fig. 5.7 by taking into account the optical confinement factor, the strain relaxation during the dopant activation process, and the carrier concentration in the 50-nm-thick SiGe layer through the TCAD simulation. The changes in the optical constants of Si are also deduced in the same way. Figure 5 shows the changes in the refractive index and absorption coefficient change of 85%-strained $\text{Si}_{0.86}\text{Ge}_{0.14}$ and Si as functions of carrier concentration, in which the solid lines show the theoretical values calculated using the Drude model. The fairly good agreement between the experiment results and the theory clearly indicates that the plasma dispersion effect and free-carrier absorption are enhanced by strain-induced mass modulation in strained SiGe. Thus, the enhancement factors of 1.3 for Δn and 1.7 for $\Delta\alpha$ in 85%-strained $\text{Si}_{0.86}\text{Ge}_{0.14}$ have been successfully demonstrated.

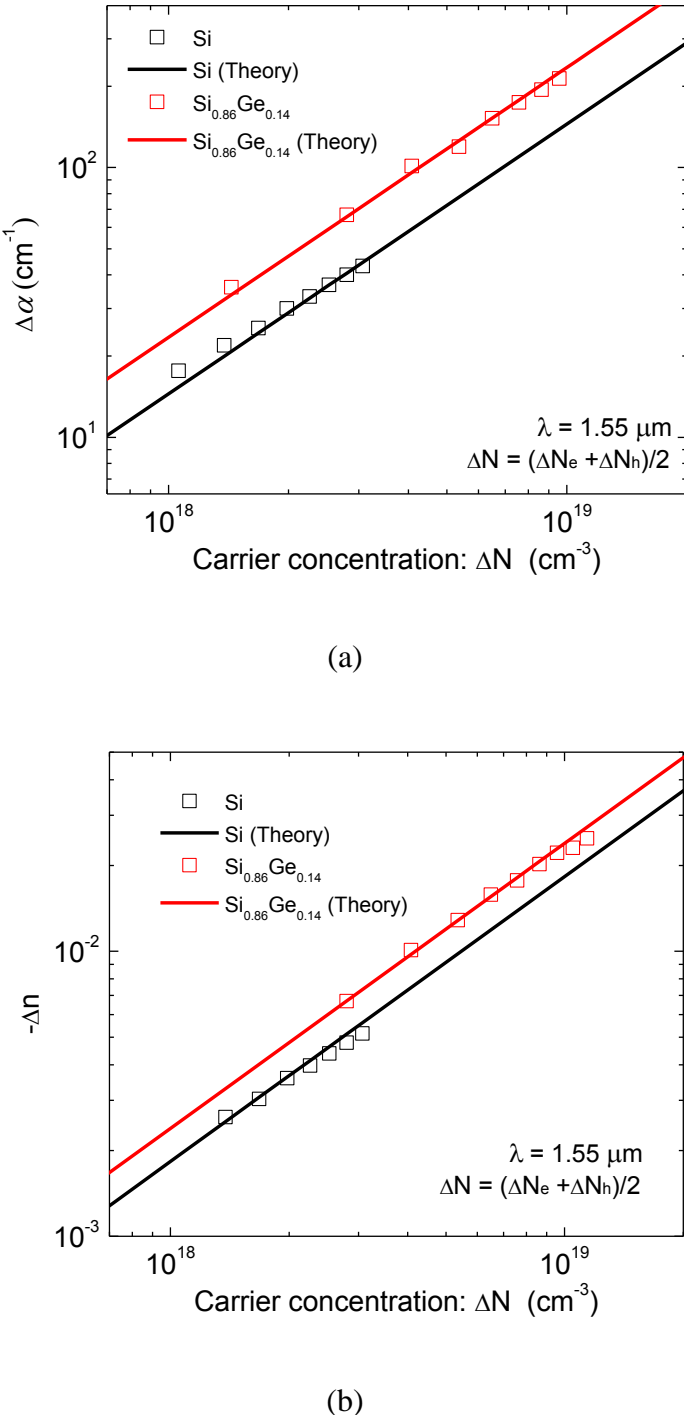


Figure 5.7 Changes in optical constants of $\text{Si}_{0.86}\text{Ge}_{0.14}$ and Si as functions of carrier concentration. (a) Change in absorption coefficient and (b) Change in refractive index. The experimental results and the theoretical values calculated using the Drude model are in good agreement, indicating that the plasma dispersion effect and free-carrier absorption are enhanced by strain-induced mass modulation in strained SiGe.

We have measured the dynamic characteristics of strained SiGe VOA. Figure 5.8(a) shows the switching characteristic when the SiGe VOA is driven by 3 V_{p-p} voltage at 1 MHz. The green line is the driving voltage signal and the yellow line is the modulated optical output signal from the VOA. The clear switching characteristic with the switching time of approximately 500 ns was successfully obtained. The switching time can be much improved by reducing the parasitic resistance. The bit-error rate (BER) test was also carried out to investigate transmission characteristics of the SiGe VOA. The 1.55-μm NRZ 2³¹-1 PRBS optical signal at 12.5 Gb/s generated by a LN modulator with a PPG was injected to the VOA. The output signal was detected by the receiver composed of an EDFA and InGaAs photodetector for analysing the signal by a DCA and a BERT. Figure 5.8(b) shows the BER curves of the back-to-back and output signals of Si and SiGe devices with input power of 16 and 18 dBm, respectively. Although optical nonlinearity has been reported to be enhanced in SiGe [5.22], no significant degradation in BER is observed even when the signal power up to 18 dBm is injected into the SiGe device. The measured eye diagrams of the 12.5 Gb/s output signal also shows clear eye opening as shown in the inset of Fig. 5.8(b).

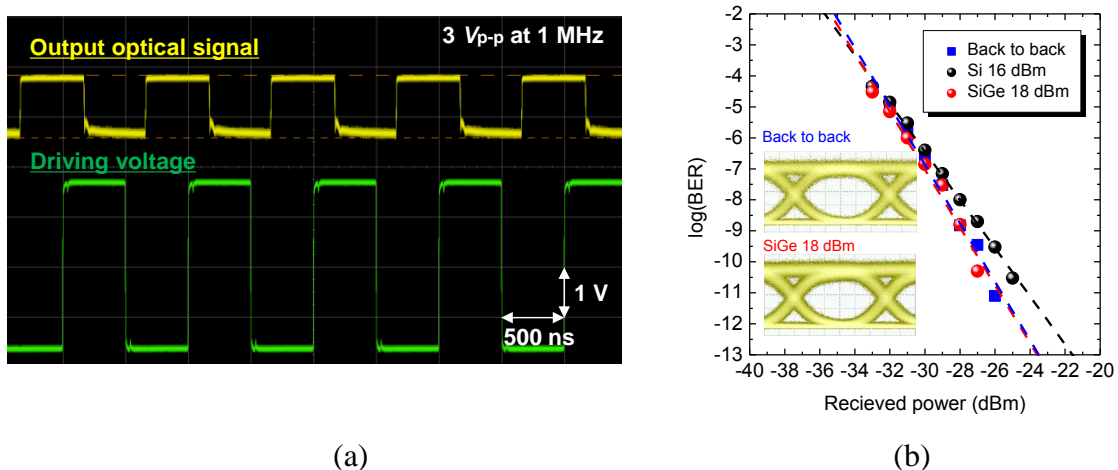


Figure 5.8 (a) Switching characteristic of SiGe VOA using electric signal of 1 MHz and 3 V_{p-p} (b) BER versus received power for Si and SiGe VOA at 12.5 Gb/s signal and eye patterns of back to back and SiGe with 18-dBm input power (inset).

5.4 Conclusion

In conclusion, we have demonstrated that the strain-induced enhancement of the plasma dispersion effect and free-carrier absorption in biaxial compressive strained SiGe is effective for boosting the modulation efficiency of Si-based optical modulators. The optical attenuation of the SiGe-based in-line intensity optical modulator is more than twice as large as that of the Si modulator. This is the first demonstration of enhanced free-carrier absorption in SiGe through strain-induced mass modulation for the telecommunication wavelength range from 1.3 to 1.6 μm .

References

- [5.1] R. A. Soref and B. R. Bennett, "Electrooptical Effects in Silicon," *IEEE Journal of Quantum Electronics*, vol. 23, pp. 123-129, Jan 1987.
- [5.2] Q. F. Xu, B. Schmidt, S. Pradhan, and M. Lipson, "Micrometre-scale silicon electro-optic modulator," *Nature*, vol. 435, pp. 325-327, May 19 2005.
- [5.3] W. M. J. Green, M. J. Rooks, L. Sekaric, and Y. A. Vlasov, "Ultra-compact, low RF power, 10 Gb/s silicon Mach-Zehnder modulator," *Optics Express*, vol. 15, pp. 17106-17113, Dec 10 2007.
- [5.4] S. Sekiguchi, T. Kurahashi, L. Zhu, K. Kawaguchi, and K. Morito, "Compact and low power operation optical switch using silicon-germanium/silicon hetero-structure waveguide," *Optics Express*, vol. 20, pp. 8949-8958, Apr 9 2012.
- [5.5] C. Gunn, "CMOS photonics for high-speed interconnects," *IEEE Micro*, vol. 26, pp. 58-66, Mar-Apr 2006.
- [5.6] L. Liao, A. Liu, D. Rubin, J. Basak, Y. Chetrit, H. Nguyen, *et al.*, "40 Gbit/s silicon optical modulator for high-speed applications," *Electronics Letters*, pp. 51-52, Jun 2009.
- [5.7] F. Y. Gardes, D. J. Thomson, N. G. Emerson, and G. T. Reed, "40 Gb/s silicon photonics modulator for TE and TM polarisations," *Opt Express*, vol. 19, pp. 11804-14, Jun 6 2011.
- [5.8] A. S. Liu, R. Jones, L. Liao, D. Samara-Rubio, D. Rubin, O. Cohen, *et al.*, "A high-speed silicon optical modulator based on a metal-oxide-semiconductor capacitor," *Nature*, vol. 427, pp. 615-618, Feb 12 2004.
- [5.9] H. Xu, X. Xiao, X. Y. Li, Y. T. Hu, Z. Y. Li, T. Chu, *et al.*, "High speed silicon Mach-Zehnder modulator based on interleaved PN junctions," *Optics Express*, vol. 20, pp. 15093-15099, Jul 2 2012.
- [5.10] L. Liao, A. S. Liu, R. Jones, D. Samara-Rubio, O. Cohen, *et al.*, "Phase modulation efficiency and transmission loss of silicon optical phase shifters," *Ieee Journal of Quantum Electronics*, vol. 41, pp. 250-257, Feb 2005.
- [5.11] P. Dong, R. Shafiiha, S. R. Liao, H. Liang, N. N. Feng, D. Z. Feng, *et al.*, "Wavelength-tunable silicon microring modulator," *Optics Express*, vol. 18, pp.

10941-10946, May 24 2010.

- [5.12] H. C. Nguyen, Y. Sakai, M. Shinkawa, N. Ishikura, and T. Baba, "Photonic Crystal Silicon Optical Modulators: Carrier-Injection and Depletion at 10 Gb/s," *IEEE Journal of Quantum Electronics*, vol. 48, pp. 210-220, Feb 2012.
- [5.13] T. Baba, "Slow light in photonic crystals," *Nature Photonics*, vol. 2, pp. 465-473, Aug 2008.
- [5.14] M. Takenaka and S. Takagi, "Strain Engineering of Plasma Dispersion Effect for SiGe Optical Modulators," *IEEE Journal of Quantum Electronics*, vol. 48, pp. 8-16, Jan 2012.
- [5.15] S. Takagi, N. Sugiyama, T. Mizuno, T. Tezuka, and A. Kurobe, "Device structure and electrical characteristics of strained-Si-on-insulator (strained-SOI) MOSFETs," *Materials Science and Engineering B-Solid State Materials for Advanced Technology*, vol. 89, pp. 426-434, Feb 14 2002.
- [5.16] K. Rim, R. Anderson, D. Boyd, F. Cardone, K. Chan, H. Chen, *et al.*, "Strained SiCMOS (SS CMOS) technology: opportunities and challenges," *Solid-State Electronics*, vol. 47, pp. 1133-1139, Jul 2003.
- [5.17] S. E. Thompson, G. Y. Sun, Y. S. Choi, and T. Nishida, "Uniaxial-process-induced strained-Si: Extending the CMOS roadmap," *IEEE Transactions on Electron Devices*, vol. 53, pp. 1010-1020, May 2006.
- [5.18] A. K. Walton, "Infrared Modulation and Energy Band Parameters in Multivalley Semiconductors through Uniaxial Stress Dependence of Free Carrier Contribution to Optical Constants," *Physica Status Solidi B-Basic Research*, vol. 43, pp. 379-386, 1971.
- [5.19] A. K. Walton and S. F. Metcalfe, "Free-Carrier Absorption at Low-Temperatures in Uniaxially Stressed N-Type Ge, Si and Gaas," *Journal of Physics C-Solid State Physics*, vol. 9, pp. 3605-3625, 1976.
- [5.20] A. E. Belyaev, O. P. Gorodnichii, E. V. Pidlisny, Z. A. Demidenko, and P. M. Tomchuk, "Free Carrier Absorption in Uniaxially Stressed N-Si," *Solid State Communications*, vol. 42, pp. 441-445, 1982.
- [5.21] D. K. Schroder, R. N. Thomas, and J. C. Swartz, "Free Carrier Absorption in Silicon," *Ieee Journal of Solid-State Circuits*, vol. 13, pp. 180-187, 1978.

- [5.22] K. Hammani, M. A. Ettabib, A. Bogris, A. Kapsalis, D. Syvridis, M. Brun, *et al.*, "Optical properties of silicon germanium waveguides at telecommunication wavelengths," *Optics Express*, vol. 21, pp. 16690-16701, Jul 15 2013.

Chapter 6

Low temperature Al₂O₃ surface passivation for carrier-injection SiGe optical modulator

Surface passivation by Al₂O₃ deposited by atomic layer deposition (ALD) at 200 °C is examined to suppress surface recombination for carrier-injection SiGe optical modulators. We have investigated the interface trap densities at SiO₂/Si and Al₂O₃/Si interfaces formed by plasma enhanced chemical vapor deposition (PECVD) and ALD, respectively. By evaluating metal-oxide-semiconductor (MOS) capacitors formed on Si surfaces after dry etching, we found that the interface trap density of Al₂O₃ passivated surface is more than one order of magnitude less than that of SiO₂ passivated one. As a result, the modulation efficiency is improved by 1.3 by inserting Al₂O₃ layer prior to SiO₂ deposition by PECVD owing to superior interface between Al₂O₃ and Si. The Al₂O₃ passivated device exhibits comparable modulation efficiency to a thermally-grown SiO₂ passivated one formed by dry oxidation. Hence, the ALD Al₂O₃ passivation is effective to passivate SiGe optical modulators for which low temperature processes are required.

6.1 Introduction

Si-based optical modulators have been attracted much attention as an essential component for on-chip optical interconnect in conjunction with electronics ^[6.1]. The Si optical modulators based on the plasma dispersion effect have been demonstrated ^[6.2] by means of carrier injection^{[6.3], [6.4], [6.5], [6.6]}, depletion^{[6.8], [6.9], [6.10], [6.11], [6.12], [6.13], [6.14]}, and accumulation^[6.15] using *pin* and *pn* junctions, and MOS capacitor. However, the weak free-carrier effects in Si cause the low modulation efficiency, resulting in the longer

device length [6.9]. The plasma dispersion effect and free-carrier absorption are expressed by the Drude model. According to the Drude model, the changes in refractive index and absorption coefficient are described by a change in the plasma frequency of free carriers, and the plasma frequency is dependent on not only the number of free carriers but also their conductivity effective masses. The change in the refractive index induced by the plasma dispersion effect is inversely proportional to the conductivity effective masses of electrons and holes [6.16], [6.17], [6.18]. Therefore, the lighter the conductivity masses become, the greater the plasma dispersion is. In terms of that, we have proposed carrier injection type SiGe modulator in which the plasma dispersion effect is enhanced by introducing a compressively strained SiGe layer as shown in Fig.6.1 [6.19], [6.20].

On the other hand, it is known that the modulation efficiency of the carrier injection type modulators is deteriorated by surface recombination due to interface traps between Si and a passivation layer. When carriers are injected to a waveguide core from p+ and n+ regions by forward bias, the injected carriers are trapped by interface traps, and recombined at dry-etched Si surfaces, decreasing carrier concentrations in the waveguide core where the light interacts with carriers [6.21], [6.22]. A thermally grown SiO₂ layer is one of the best solutions for passivating etched Si surfaces with low interface trap densities; however it requires the high temperature oxidation process above 900 °C, which causes undesirable strain relaxation of strained SiGe [6.23]. Thus, a low temperature surface passivation process is indispensable for the strained SiGe optical modulators. One of the promising passivation layers on crystal Si is an Al₂O₃ layer deposited by atomic layer deposition (ALD). The Al₂O₃ layer is known as the negatively charged layer which fixed negative charges exist in the layer as large as up to 10¹³ cm⁻². This property is applied to surface passivation by a reduction in electron or hole concentration near the surface due to band bending in the c-Si toward the interface. This passivation type is known as field-effect passivation. Therefore, the field-effect passivation using the Al₂O₃ layer has been widely used for solar cell applications [6.24], [6.25], [6.26].

In this paper, we investigate a low temperature passivation process by using Al₂O₃ deposited by ALD to suppress surface recombination by using Si optical modulators. If SiGe modulators were used, we had to take into account the Ge diffusion

impact on the modulation efficiency. Thus, it might be difficult to evaluate the surface passivation effect independently. Since interface traps on the etched Si slab region mainly degrade the efficiency of carrier injection in both cases of Si and SiGe modulators, Si modulators are more preferable to investigate the surface passivation effect between the thermally grown SiO_2 and Al_2O_3 . Evaluation of interface traps by *Capacitance-Voltage (C-V)* measurements of metal-oxide-semiconductor (MOS) capacitors reveals that Al_2O_3 passivation is effective to reduce the interface traps even with 200 °C process temperature. By introducing Al_2O_3 passivation prior to SiO_2 passivation, we demonstrate the improvement in the modulation efficiency of a carrier-injection Si optical modulator.

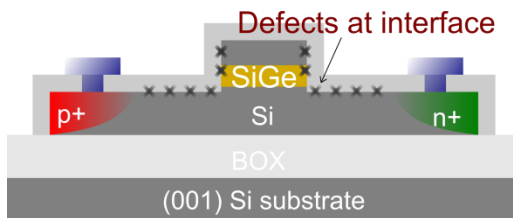


Figure 6.1 Schematic device structure of carrier injection type strained SiGe optical modulator.

6.2 Evaluation of Interface Traps

To evaluate Al_2O_3 passivation effect, we have fabricated Al/ Al_2O_3 /Si MOS capacitors by ALD. A B-doped *p*-Si ($N_A \sim 1 \times 10^{15} \text{ cm}^{-3}$) substrate was used to fabricate the MOS capacitors. We have also fabricated Al/ Al_2O_3 /etched Si MOS capacitors to investigate interface traps generated by reactive ion etching (RIE) of Si surfaces. For comparison, Al/ SiO_2 /Si and etched Si MOS capacitors have also been fabricated by SiO_2 deposition by plasma enhanced chemical vapor deposition (PECVD). The interface trap density (D_{it}) distributions of the MOS capacitors are evaluated by the *C-V* measurements. Figure 6.2 shows the process flow of Al/ Al_2O_3 /etched Si MOS capacitor. First, the Si substrate was etched by RIE with CF_4 gas after organic cleaning. After cleaning Si surfaces by buffered HF, the 5-nm-thick Al_2O_3 was deposited at 200 °C. Then, Al electrode was formed by thermal evaporation. Finally, the forming gas annealing (FGA) was carried out for 30 min at 400 °C. Although a 1-nm thick Al_2O_3 layer is enough for

passivating the Si surface, it is difficult to evaluate *C-V* curves when the Al_2O_3 thickness is less than 3 nm because of gate leakage current through quantum tunneling. Thus, we chose 5-nm thickness in Al_2O_3 to evaluate the interfacial properties by *C-V* measurements. The Al/SiO₂/etched Si MOS capacitor was fabricated by 45-nm-thick SiO₂ deposition at 350 °C instead of Al_2O_3 . Since it is difficult to deposit 5-nm SiO₂ with keeping good uniformity, we chose 45-nm thickness in PECVD SiO₂. The difference in thickness between Al_2O_3 and SiO₂ does not affect the evaluation of interface trap density.

Since there are many interface traps at the PECVD SiO₂/Si interface, an additional annealing for 30 min at 1000 °C in N₂ was carried out after SiO₂ deposition.

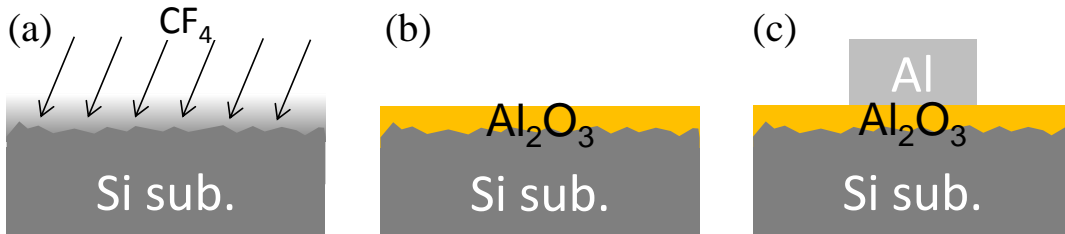


Figure 6.2 Process flow of Al/Al₂O₃/etched Si MOS capacitor. (a) Dry etching, (b) Deposition of 5-nm-thick Al₂O₃ (c) Gate formation by Al electrode.

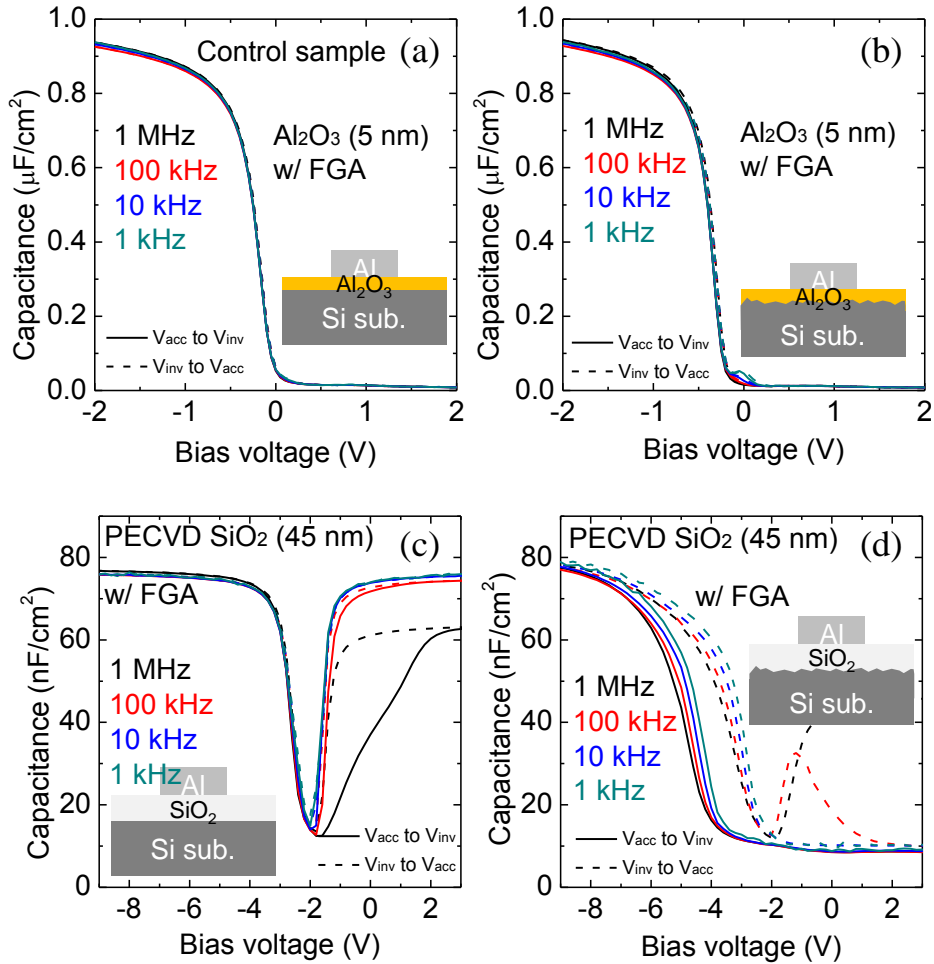


Figure 6.3 C-V characteristics of (a) Al₂O₃/Si, (b) Al₂O₃/etched Si, (c) SiO₂/Si, and (d) SiO₂/etched Si MOS capacitors.

To investigate electrical properties of the MOS interfaces, we measured the C-V curves of the MOS capacitors at 1 kHz to 1 MHz. Figures 6.3 show the C-V characteristics of (a) the Al/Al₂O₃/Si, (b) the Al/Al₂O₃/etched Si, (c) Al/SiO₂/Si, and (d) Al/SiO₂/etched Si MOS capacitors. The solid line and dotted line show the voltage sweep of accumulation (V_{acc}) to inversion (V_{inv}) and inversion to accumulation, respectively. The C-V curves of the Al/Al₂O₃/Si MOS capacitor shows a well-behaved characteristic with no frequency dispersion, meaning that ALD Al₂O₃ can passivate Si surfaces well. It is found in Fig. 6.3(b) that the etched Si surface is also well passivated by Al₂O₃. On the other hand, Figs. 6.3(c) and (d) reveal that PECVD SiO₂ cannot passivate the etched Si surface because the Al/SiO₂/etched Si MOS capacitor exhibits stretch-out C-V curves with large frequency dispersion and hysteresis due to interface

traps. Hence, it is shown that Al_2O_3 passivation is more effective to minimize etching damage of the Si surface than PECVD SiO_2 passivation. For the quantitative estimation, the energy distributions of D_{it} evaluated by the conductance method^[6,27] are shown in Fig. 6.4. Although the etched Si samples exhibits higher D_{it} than the bulk Si sample, the ALD Al_2O_3 passivated surface shows D_{it} of less than $2 \times 10^{11} \text{ cm}^{-2} \text{ eV}^{-1}$. On the other hand, the PECVD SiO_2 passivated surface has D_{it} of larger than $10^{12} \text{ cm}^{-2} \text{ eV}^{-1}$. Hence, the Al_2O_3 passivation is more effective to suppress surface recombination due to low interface traps.

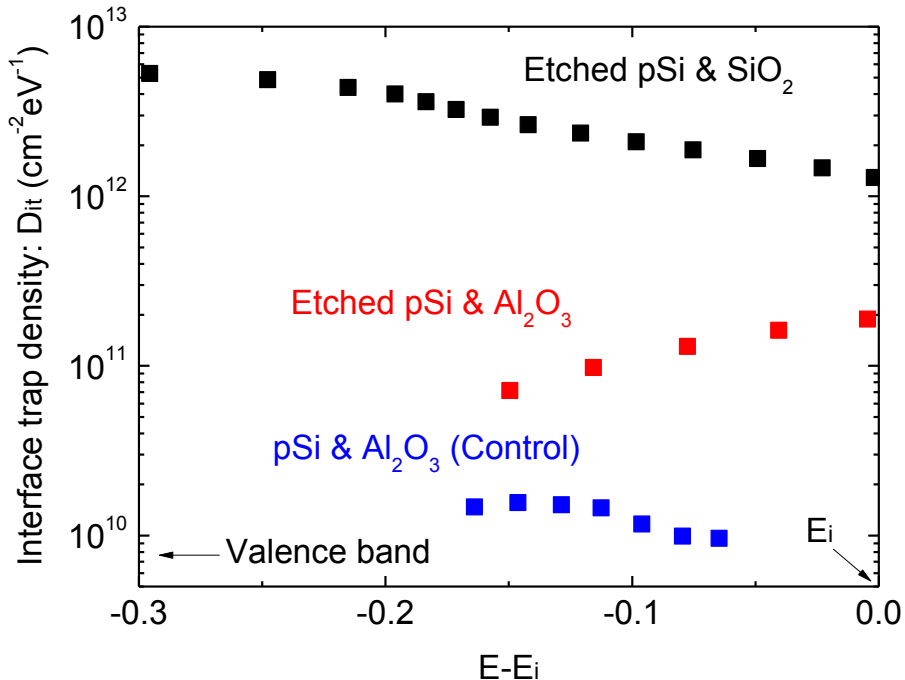


Figure 6.4 Interface trap density distributions of the SiO_2 /etched Si, the Al_2O_3 /etched Si, and the Al_2O_3 /Si MOS interfaces.

6.3 Device Fabrication and Characterization

To evaluate the effect of surface passivation on the modulation characteristics, the pin-junction-based in-line optical modulators with the Al_2O_3 or SiO_2 passivation were fabricated by using a 220-nm-thick silicon-on-insulator (SOI) with N_A of $\sim 1 \times 10^{15} \text{ cm}^{-3}$ wafer as shown in Fig. 6.5. To estimate carrier injection efficiency precisely, it is

necessary to evaluate the modulator characteristic in the wide range of injection current. However, it is not easy to precisely estimate the carrier injection efficiency from refractive index change in a Mach-Zehnder interferometer (MZI) due to the unavoidable free-carrier absorption in an MZI's arm which degrades interference properties. In the case of an in-line modulator, there is not such a problem to evaluate attenuation properties in the wide range of injection current. Therefore, an in-line modulator based on straight waveguide was used for the attenuation characteristics. First, the straight rib waveguide was formed by deep ultraviolet lithography and dry etching by reactive ion etching with CF_4 gas, followed by 20-nm-thick SiO_2 deposition by PECVD as a hard mask in Fig. 6.5(a). The width and mesa of waveguide is 2 μm and 120 nm, respectively. We chose the width of waveguides for obtaining enough optical output power in the experiments. Since we fabricated the waveguide by using contact photolithography, the propagation loss is large when the waveguide width is less than 1 μm due to the large sidewall roughness. In addition, the coupling loss is increased by narrowing waveguide width due to end coupling. The 2- μm -wide waveguide has theoretically high-order optical modes. However, we have tried to couple the light to the fundamental mode of the 2- μm -wide waveguide as much as possible by monitoring the output image through InGaAs camera. Thus, the 2- μm -wide waveguide does not have significant impact on evaluating the attenuation properties. Although the waveguide width should be scaled down to 500 nm for high speed operation, we have focused on carrier injection efficiency which is affected by interface traps on the Si surfaces. Therefore, it is not a significant matter to use the 2- μm -wide waveguide for evaluating the static characteristics of output power by carrier injection in this paper. Then, ion implantations of boron and phosphorus (dose: $1 \times 10^{15} \text{ cm}^{-2}$, energy: 10 keV and 30 keV, respectively) were carried out to make the p+ and n+ regions to form a lateral pin-junction, followed by activation annealing at 1000 °C for 30 min in N_2 atmosphere in Fig. 6.5(b). Here, the distance between implanted regions and waveguide edge is approximately 2 μm . Then, the contact pads for the p+ and n+ regions were formed by thermal evaporation of aluminum. The final structure of a SiO_2 -passivated device is shown in Fig. 6.4(c). In the case of the Al_2O_3 -passivated device, the SiO_2 passivation layer was removed by wet etching using BHF after activating the implanted dopants. Then, a 1-nm-thick Al_2O_3

layer was deposited on Si as a passivation layer by ALD at 200 °C and a 280-nm-thick SiO₂ layer was deposited on Al₂O₃ layer by PECVD as shown in Fig. 6.5(e). Finally, the contact pads regions were formed. The final structure of a Al₂O₃ passivated device is shown in Fig 6.5(f). Forming gas annealing was implemented for all devices to decrease the contact resistance, which is for 30 min at 400 °C. Figure 6.6 shows a top-view of the fabricated device passivated by Al₂O₃. The structure of in-line modulator has been used to estimate the optical attenuation occurred by free-carrier absorption.

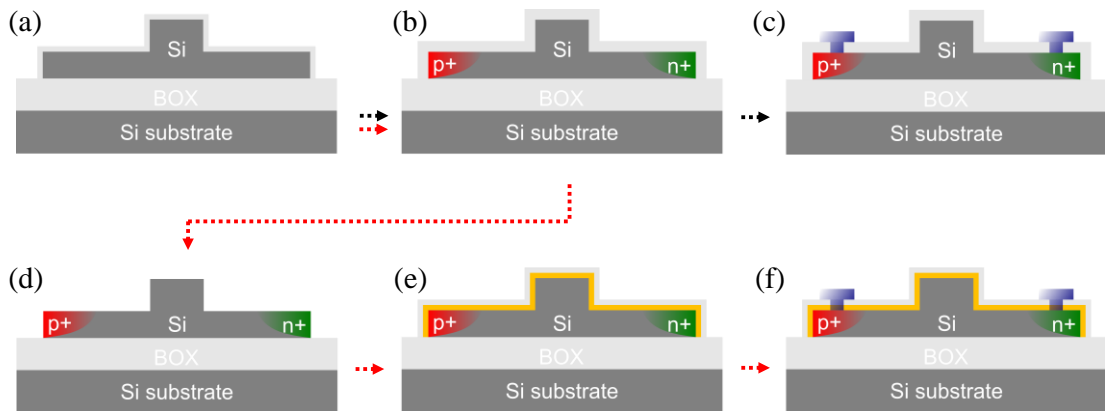


Figure 6.5 Process flow of carrier-injection type Si in-line optical modulator. (a) Waveguide formation (b) p+ and n+ region formation by ion implantation and activation. (c) Final structure of SiO₂-passivated device after Al electrode formation, (d) Removal of SiO₂ passivation layer by wet etching (e) Al₂O₃ and SiO₂ passivation , and (f) Final structure of Al₂O₃-passivated device after Al electrode formation

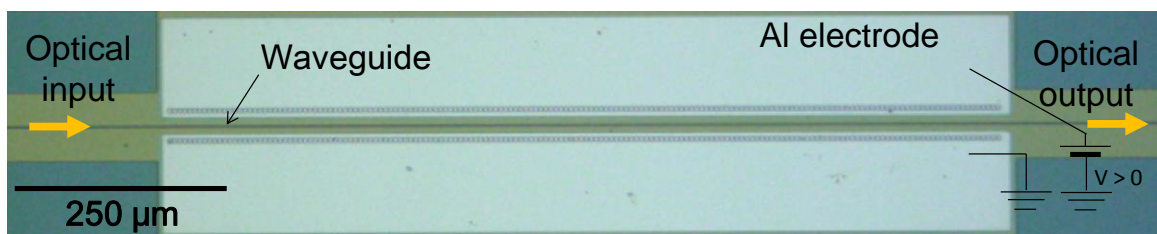


Figure 6.6 Top-view of Al₂O₃-passivated device observed by optical microscopy.

Figure 6.7 shows the measured optical attenuation properties of the Si in-line intensity modulators with and without the Al₂O₃ layer as a function of injected current.

The optical attenuation was measured by injecting current to evaluate the effect of Al₂O₃ passivation. Since we have not focused on high-speed operation, the static characteristics of attenuation are measured to evaluate the carrier injection efficiency. Continuous-wave (CW) TE-polarized light with a wavelength of 1550 nm was coupled to the waveguide through a lensed fiber. Then, the output power was monitored using an InGaAs photodetector while changing the injection current. The length of the phase-shifters is 1 mm. It can be seen that the attenuation of the Al₂O₃-passivated modulator is larger than that of the SiO₂-passivated modulator. As a result, the injection current required for the 20-dB attenuation can be reduced from 64 mA/mm to 47 mA/mm owing to the reduction in the interface trap density using the Al₂O₃ passivation layer. Also, we have fabricated the Si in-line intensity modulator passivated by the thermally oxidized SiO₂ at 1000 °C. It is worth noting that the performance of the Al₂O₃-passivated device is comparable to the SiO₂ passivated device formed by dry oxidation, indicating that Al₂O₃ passivation is as good as SiO₂ passivation by dry oxidation in terms of surface recombination. We can estimate the modulation efficiency in V_πL from the attenuation results. Since the voltage necessary for 20-dB attenuation is reduced from 2.2 V to 1.8 V by using Al₂O₃ passivation as compared with PECVD SiO₂ passivation, V_πL of the Al₂O₂-passivated device is expected to be improved by approximately 20%, which is comparable to the thermally grown SiO₂ passivation. We have also found no significant impact of the passivation layers on the propagation loss. Thus, the total insertion loss is not changed even in the Al₂O₃-passivated device.

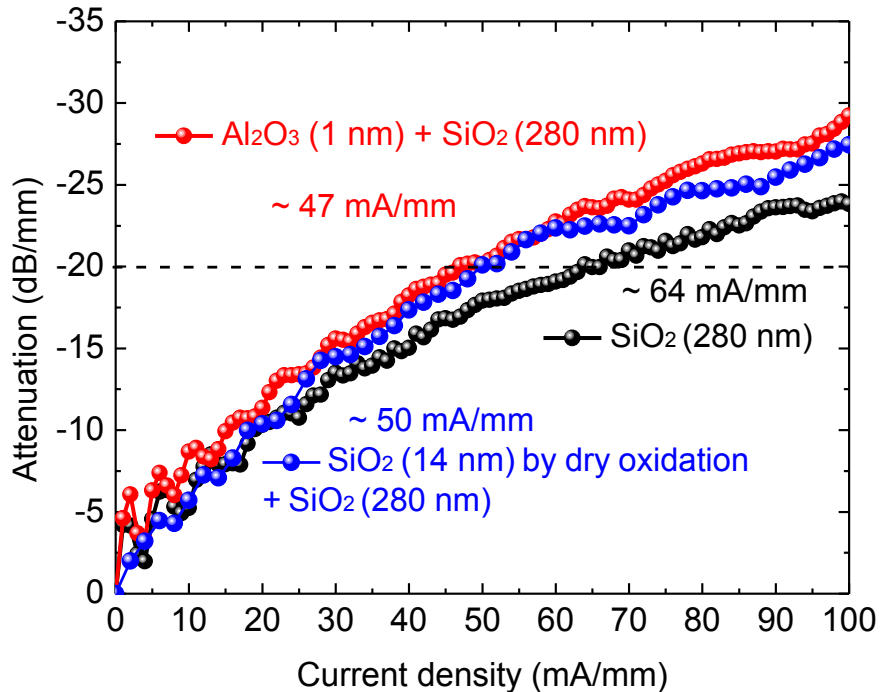


Figure 6.7 Attenuation characteristics of Si modulators passivated by PECVD SiO_2 (black), dry-oxidized SiO_2 (blue), and Al_2O_3 (red).

6.4 Conclusion

We have investigated the low-temperature surface passivation, which is especially necessary for carrier-injection SiGe optical modulators due to the restriction of thermal budge, for suppressing surface recombination. We found that Al_2O_3 passivation formed by ALD at 200 °C is effective to decrease interface traps on the etched Si surfaces at low temperature as compared with PECVD SiO_2 passivation. The interface trap density of the Al_2O_3 -passivated etched Si surface is less than $2 \times 10^{11} \text{ cm}^{-2}\text{eV}^{-2}$, which is one order magnitude lower than that of the PECVD SiO_2 -passivated surface. The modulation efficiency has been also improved by introducing the Al_2O_3 passivation layer prior to SiO_2 deposition. The injection current density for 20-dB attenuation has been improved by approximately 40%, which is comparable to the thermally grown SiO_2 -passivated device. Thus, ALD Al_2O_3 is promising for passivating the strained SiGe optical modulator at low temperature.

References

- [6.1] G. T. Reed, G. Mashanovich, F. Y. Gardes, and D. J. Thomson, "Silicon optical modulators," *Nature Photonics*, vol. 4, pp. 518-526, Aug 2010.
- [6.2] R. A. Soref and B. R. Bennett, "Electrooptical Effects in Silicon," *Ieee Journal of Quantum Electronics*, vol. 23, pp. 123-129, Jan 1987.
- [6.3] Q. F. Xu, B. Schmidt, S. Pradhan, and M. Lipson, "Micrometre-scale silicon electro-optic modulator," *Nature*, vol. 435, pp. 325-327, May 19 2005.
- [6.4] Q. Xu, S. Manipatruni, B. Schmidt, J. Shakya, and M. Lipson, "12.5 Gbit/s carrier-injection-based silicon micro-ring silicon modulators," *Opt Express*, vol. 15, pp. 430-6, Jan 22 2007.
- [6.5] W. M. J. Green, M. J. Rooks, L. Sekaric, and Y. A. Vlasov, "Ultra-compact, low RF power, 10 gb/s silicon Mach-Zehnder modulator," *Optics Express*, vol. 15, pp. 17106-17113, Dec 10 2007.
- [6.6] S. Akiyama, T. Baba, M. Imai, T. Akagawa, M. Takahashi, N. Hirayama, *et al.*, "12.5-Gb/s operation with 0.29-V.cm V pi L using silicon Mach-Zehnder modulator based-on forward-biased pin diode," *Optics Express*, vol. 20, pp. 2911-2923, Jan 30 2012.
- [6.7] L. Liao, A. Liu, D. Rubin, J. Basak, Y. Chetrit, H. Nguyen, *et al.*, "40 Gbit/s silicon optical modulator for high-speed applications," *Electronics Letters*, pp. 51-52, Jun 2009.
- [6.8] D. J. Thomson, F. Y. Gardes, Y. Hu, G. Mashanovich, M. Fournier, P. Grosse, *et al.*, "High contrast 40Gbit/s optical modulation in silicon," *Opt Express*, vol. 19, pp. 11507-16, Jun 6 2011.
- [6.9] F. Y. Gardes, D. J. Thomson, N. G. Emerson, and G. T. Reed, "40 Gb/s silicon photonics modulator for TE and TM polarisations," *Opt Express*, vol. 19, pp. 11804-14, Jun 6 2011.
- [6.10] T. Baehr-Jones, R. Ding, Y. Liu, A. Ayazi, T. Pinguet, N. C. Harris, *et al.*, "Ultralow drive voltage silicon traveling-wave modulator," *Optics Express*, vol. 20, pp. 12014-12020, May 21 2012.

- [6.11] J. F. Ding, R. Q. Ji, L. Zhang, and L. Yang, "Electro-Optical Response Analysis of a 40 Gb/s Silicon Mach-Zehnder Optical Modulator," *Journal of Lightwave Technology*, vol. 31, pp. 2434-2440, Jul 15 2013.
- [6.12] M. Streshinsky, A. Ayazi, Z. Xuan, A. E. J. Lim, G. Q. Lo, T. Baehr-Jones, *et al.*, "Highly linear silicon traveling wave Mach-Zehnder carrier depletion modulator based on differential drive," *Optics Express*, vol. 21, pp. 3818-3825, Feb 11 2013.
- [6.13] M. Streshinsky, R. Ding, Y. Liu, A. Novack, Y. S. Yang, Y. J. Ma, *et al.*, "Low power 50 Gb/s silicon traveling wave Mach-Zehnder modulator near 1300 nm," *Optics Express*, vol. 21, pp. 30350-30357, Dec 16 2013.
- [6.14] L. Yang and J. F. Ding, "High-Speed Silicon Mach-Zehnder Optical Modulator With Large Optical Bandwidth," *Journal of Lightwave Technology*, vol. 32, pp. 966-970, Mar 1 2014.
- [6.15] A. S. Liu, R. Jones, L. Liao, D. Samara-Rubio, D. Rubin, O. Cohen, *et al.*, *A high-speed silicon optical modulator based on a metal-oxide-semiconductor capacitor* vol. 427, 2004.
- [6.16] M. Takenaka and S. Takagi, "Strain Engineering of Plasma Dispersion Effect for SiGe Optical Modulators," *IEEE Journal of Quantum Electronics*, vol. 48, pp. 8-16, Jan 2012.
- [6.17] J. Han, R. Zhang, T. Osada, M. Hata, M. Takenaka, and S. Takagi, "Improvement of SiGe MOS interfaces by plasma post-nitridation for SiGe high-k MOS optical modulators," 2012 IEEE International Conference on Group IV Photonics.
- [6.18] Y. Kim, M. Yokoyama, N. Taoka, M. Takenaka, and S. Takagi, "Ge-rich SiGe-on-insulator for waveguide optical modulator application fabricated by Ge condensation and SiGe regrowth," *Opt Express*, vol. 21, pp. 19615-23, Aug 26 2013.
- [6.19] Y. Kim, M. Takenaka and S. Takagi, "Numerical analysis of strained SiGe-based carrier-injection optical modulators," 2012 IEEE International Conference on Group IV Photonics.

- [6.20] Y. Kim, M. Takenaka, T. Osada, M. Hata, and S. Takagi, "Strain-induced enhancement of plasma dispersion effect and free-carrier absorption in SiGe optical modulators," *Sci Rep*, vol. 4, p. 4683, 2014.
- [6.21] G. R. Zhou, M. W. Geis, S. J. Spector, F. Gan, M. E. Grein, R. T. Schulein, *et al.*, "Effect of carrier lifetime on forward-biased silicon Mach-Zehnder modulators," *Opt Express*, vol. 16, pp. 5218-26, Apr 14 2008.
- [6.22] S. Park, K. Yamada, T. Tsuchizawa, T. Watanabe, H. Shinojima, H. Nishi, *et al.*, "Influence of carrier lifetime on performance of silicon p-i-n variable optical attenuators fabricated on submicrometer rib waveguides," *Opt Express*, vol. 18, pp. 11282-91, May 24 2010.
- [6.23] R. Hull, J. C. Bean, D. J. Werder, and R. E. Leibenguth, "In situ observations of misfit dislocation propagation in $\text{Ge}_{x}\text{Si}_{1-x}/\text{Si}(100)$ heterostructures," *Applied Physics Letters*, vol. 52, p. 1605, 1988.
- [6.24] G. Agostinelli, A. Delabie, P. Vitanov, Z. Alexieva, H. F. W. Dekkers, S. De Wolf, *et al.*, "Very low surface recombination velocities on p-type silicon wafers passivated with a dielectric with fixed negative charge," *Solar Energy Materials and Solar Cells*, vol. 90, pp. 3438-3443, Nov 23 2006.
- [6.25] B. Hoex, J. J. H. Gielis, M. C. M. V. de Sanden, and W. M. M. Kessels, "On the c-Si surface passivation mechanism by the negative-charge-dielectric Al_2O_3 ," *Journal of Applied Physics*, vol. 104, Dec 1 2008.
- [6.26] F. Werner, B. Veith, D. Zielke, L. Kuhnemund, C. Tegenkamp, M. Seibt, *et al.*, "Electronic and chemical properties of the c-Si/ Al_2O_3 interface," *Journal of Applied Physics*, vol. 109, Jun 1 2011.
- [6.27] Nicollia.Eh and Goetzber.A, "Si-SiO₂ Interface - Electrical Properties as Determined by Metal-Insulator-Silicon Conductance Technique," *Bell System Technical Journal*, vol. 46, pp. 1055-&, 1967.

Chapter 7

Optimization of distance between pin junctions for high carrier-injection efficiency

We demonstrate a strained SiGe variable optical attenuator (VOA) with a lateral *pin* junction which has record-low injection-current by applying enhanced free-carrier absorption in compressively strained SiGe. We have optimized the distance between highly doped regions of p+ and n+ alongside a waveguide core to effectively inject electrons and holes, taking into account the attenuator loss. The strained SiGe VOA with optimized lateral *pin* junction represents 20-dB attenuation by 20-mA/mm injection current, which is 1.5 times lower current density than that of the Si VOA. For dynamic characteristics, the SiGe VOA shows the higher small-signal response than the Si VOA. Furthermore, 2-GHz switching and error-free transmission of 50-Gbps WDM signal have been also achieved.

7.1 Introduction

For the burgeoning internet data centers and high-performance computing systems, electronic-photonic-integrated circuits (EPICs) for optical communications has been considered as a promising solution to satisfy the demands on broad bandwidth and low power consumption [7.1]. For the EPICs, Si photonics is a key technology, which has been dramatically developed in the past ten years [7.2], [7.3], [7.4]. Si-based variable optical attenuators (VOAs) are necessary components for controlling optical power level in EPICs. Si VOAs based on the free-carrier absorption have been mostly investigated and demonstrated using carrier injection by forward bias through a lateral *pin* junction [7.5], [7.6], [7.7], [7.8], [7.9], [7.10], [7.11]. However, the efficiency in absorption modulation is still low

due to the small free-carrier absorption in Si, resulting in high injection current and large power consumption. Therefore, it is indispensable to enhance the free-carrier effect for high-performance VOA to achieve low injection current and power consumption. In terms of the enhancement, we have proposed the strain-induced enhancement of the plasma dispersion effect and free-carrier absorption in SiGe for the device applications such as SiGe optical modulators, switches, and VOAs. The enhancement of the free-carrier effects, the plasma dispersion effect and the free-carrier absorption, is expected by reduction in the conductivity effective mass of holes in strained SiGe^{[7,12], [7,13]}. Recently, we have demonstrated strain-induced enhancements in the plasma dispersion effect and free-carrier absorption for optical modulator and VOA applications by using the carrier-injection type strained SiGe waveguide device with a lateral *pin* junction^[7,14]. However, the first demonstration of the SiGe VOA in^[7,14] was not fully optimized, regarding to the distance between heavily doped p+ and n+ regions, resulting in the low carrier injection efficiency.

In this paper, we demonstrate strained SiGe VOAs with high carrier injection efficiency through the optimization of the distance between the highly doped regions, taking into account the tradeoff between attenuator loss and carrier-injection efficiency, as shown in Fig. 7.1. As a result, we have achieved the record-low injection current of 20 mA for 20-dB attenuation in the SiGe VOA. Furthermore, we have obtained 2-GHz switching and error-free transmission of 50-Gbps WDM signal.

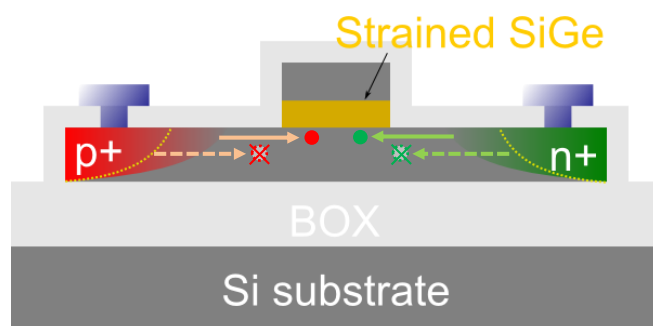


Figure 7.1 Schematic of strained SiGe VOA with optimized lateral *pin* junction.

7.2 Optimization of distance between highly doped p+ and n+ region

To effectively inject carriers into a waveguide core, it is necessary to make the distance between highly doped p+ and n+ regions short due to the limited diffusion length of carriers by recombination. However, the loss inevitably increases as the distance is reduced owing to free-carrier absorption by highly doped regions.

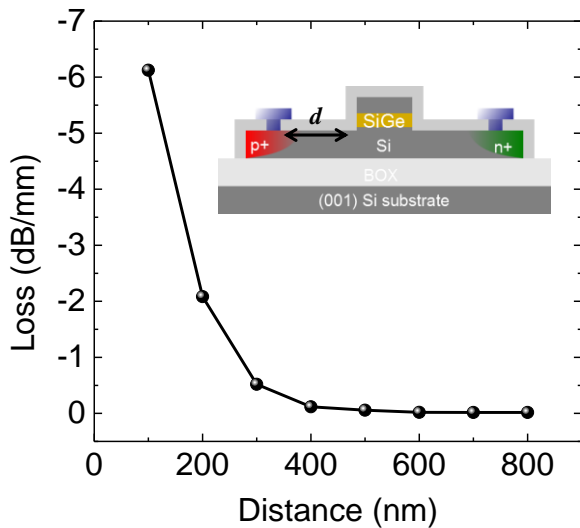


Figure 7.2 Attenuator loss as a function of distance.

We have investigated the attenuation loss in terms of the distance between the edges of the waveguide core and designed implantation area by the method of numerical analysis using by technology computer-aided design (TCAD) simulation and finite-difference optical mode analysis^{[7.13], [7.14]}. The attenuator loss is calculated by the overlap between carrier distribution of highly doped regions with 0V bias and the fundamental transverse electric (TE) mode of a rib waveguide. Figure 7.2 shows the simulation result of attenuator loss as a function of the distance. As the distance becomes short, the loss dramatically increases due to free-carrier absorption by heavily doped regions. As shown in Fig. 7.2, the loss can be ignored when the distance is larger than 500 nm. In this study, we however chose the 650-nm-distance, considering the process margin of EB lithography.

7.3 Device fabrication

We have fabricated strained SiGe VOAs using a (001) Si-on-insulator (SOI) wafer with a 250-nm-thick top Si layer and 2- μm -thick buried oxide (BOX) layer. To obtain the designed structure of Si/SiGe/SOI as shown in Fig. 7.3(a), we thinned the SOI layer down to 95 nm by thermal oxidation, then a 30-nm-thick fully strained $\text{Si}_{0.77}\text{Ge}_{0.23}$ layer and a 75-nm-thick Si layer were grown by chemical vapor deposition (CVD). The 600-nm-wide waveguide mesa was formed by EB lithography and dry etching as shown in Fig. 7.3(b). To form a lateral *pin* junction, we implemented the ion implantation of boron and phosphorus for highly doped regions of p+ and n+, respectively and the activation annealing in nitrogen atmosphere was carried out at 1000 °C. We designed the distance between the highly doped regions by EB lithography and the rib waveguide edge to be 650 nm to effectively inject electrons and holes. Finally, the Al contact pads for the p+ and n+ regions were formed by thermal evaporation, followed by forming gas annealing at 400 °C to decrease contact resistances. Si VOAs are also fabricated at the same time.

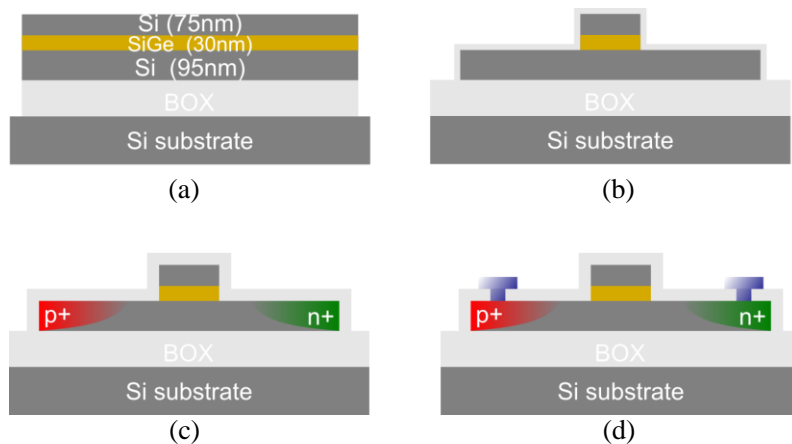


Figure 7.3 Process flow of strained SiGe VOA with optimized lateral *pin* junction. (a) Si/SiGe/SOI substrate, (b) waveguide formation (c) *pin* junction formation by ion implantation, and (d) fabricated device after Al contact formation.

We observed the fabricated SiGe device by scanning electron microscopy (SEM). The tilted SEM image in Fig. 7.2 shows the well-defined Si/SiGe/Si waveguide and Al electrodes formed by EB lithography.

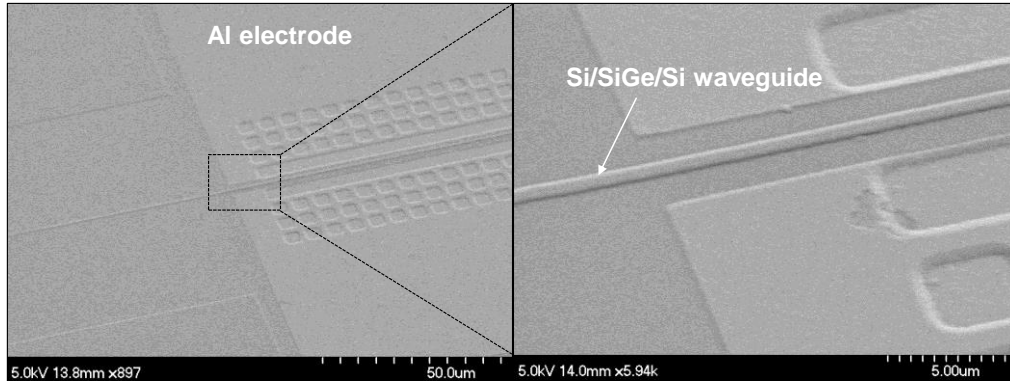


Figure 7.4 SEM image of fabricated strained SiGe VOA.

7.4 Static characteristics

We measured the optical attenuation by injecting current to evaluate the device performance of SiGe VOAs, including Si VOAs as reference devices. Continuous-wave (CW) light which is polarized to TE-like mode by a polarization controller was coupled to the waveguide through a lensed fiber, which is in the wavelength range from 1.34 to 1.64 μm . Then, the output power in dBm was monitored using an InGaAs photodetector while changing the injection current through a *pin* junction.

Figure 7.3(a) shows the measured optical attenuation versus the injected current density of the 1-mm-long SiGe and Si VOAs at a wavelength of 1.55 μm . As increasing injection current by forward-bias voltage, the optical attenuation increases due to the free-carrier absorption. The higher attenuation is shown for the SiGe VOA than the Si VOA at the same current density due to the enhanced free-carrier absorption in strained SiGe [7,14]. By optimizing the lateral *pin* junction structure, the injection current for 20-dB attenuation in the Si device as well as the SiGe device is reduced. For SiGe VOA, the injection current density is as low as 20 mA/mm for 20-dB attenuation. The benchmark of injection current for 20-dB attenuation as a function of the distance between the p+ and n+ regions in the lateral *pin* junction is shown in Fig. 7.3(b). It is

notable that the current required for 20-dB attenuation decreases with decreasing the distance due to improved carrier injection efficiency. Therefore, the optical attenuation property is improved by shortening the distance between p+ and n+ regions. Thus, we achieved record-low injection current of 20 mA/mm for 20-dB attenuation thanks to the optimization as compared with Si VOAs reported so far^{[7.9], [7.10]}.

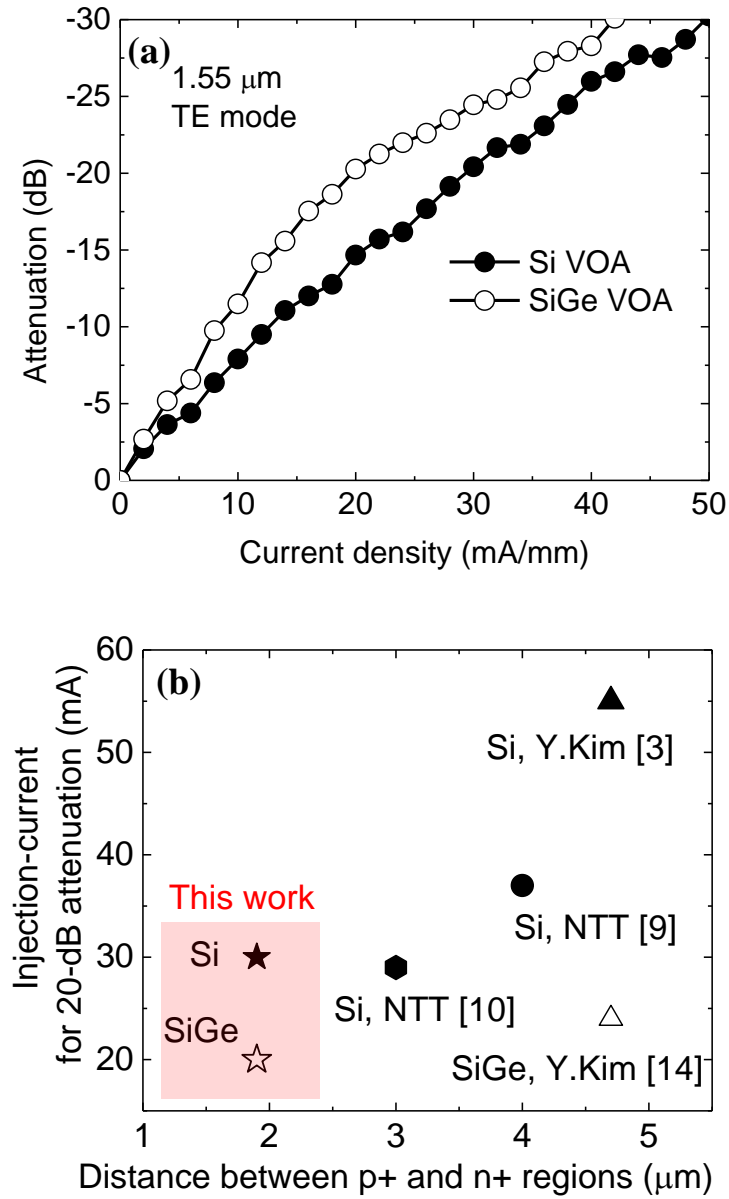


Figure 7.5 (a) Attenuation characteristics as a function of current density for Si and SiGe VOAs and (b) benchmark of Si and SiGe VOAs.

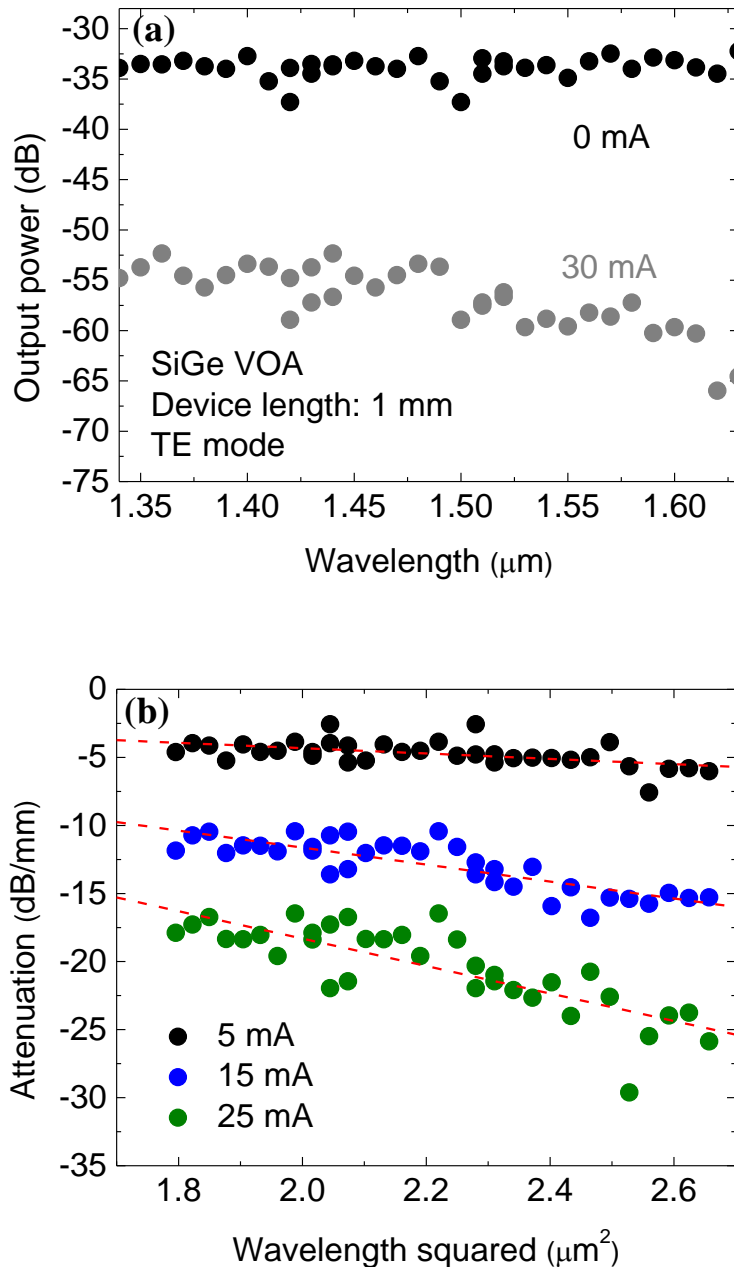


Figure 7.6 Wavelength dependence of (a) transmission and (b) attenuation of SiGe VOA.

We show the wavelength dependence of devices in Fig. 7.4. Figure 7.4(a) shows the transmission spectra of the SiGe VOA from 1.34 to 1.64 μm with 0 and 30 mA/mm. We achieved the wide optical bandwidth despite bandgap shrinkage in strained SiGe^{[7.13], [7.14]}. Figure 7.4(b) shows the optical attenuation at injection currents of 5, 15, and 25 mA/mm as a function of the square of the wavelength. It is shown that the attenuation and the square of the wavelength have clear linear relationship, indicating

the optical attenuation is from the free-carrier absorption.

Figure 7.5 shows current density vs. voltage (I-V) characteristics of the lateral *pin* junctions in the SiGe and Si VOAs. It is found that the threshold voltage of the SiGe VOA is smaller than that of the Si VOA due to the reduction in built-in potential by strained SiGe. It is interesting to note that the reduction in the threshold voltage can contribute low-power operation especially for optical modulators and switches. In terms of the power consumption between the SiGe and Si VOAs, the SiGe and Si VOAs have approximately 22 mW and 36 mW for 20-dB attenuation, respectively. The power consumption of the SiGe device is reduced by an half of the reported value^[7,14] due to the *pin* junction optimization for the distance.

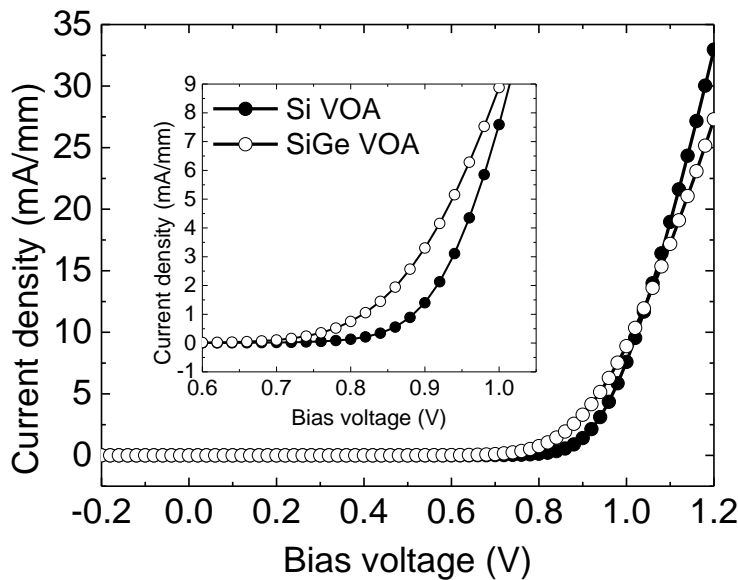


Figure 7.7 (a) I-V characteristics of *pin* junctions of Si and SiGe VOAs.

7.5 Dynamic characteristics

We carried out the RF measurement for the dynamic characteristics. We investigated the small-signal frequency response of Si and SiGe VOAs as shown in Fig. 7.6(a). Although the response is limited by minority carrier lifetime in case of forward-biased *pin* junctions^[7,9], the SiGe VOA shows the better frequency response than the Si VOA. The 3-dB bandwidth in the SiGe VOA is approximately improved by 1.5 times. Also,

we have obtained 2-GHz switching operation at a bias voltage of 0.77 V with the pre-emphasis method^[7,17] as shown in Fig. 7.6(b).

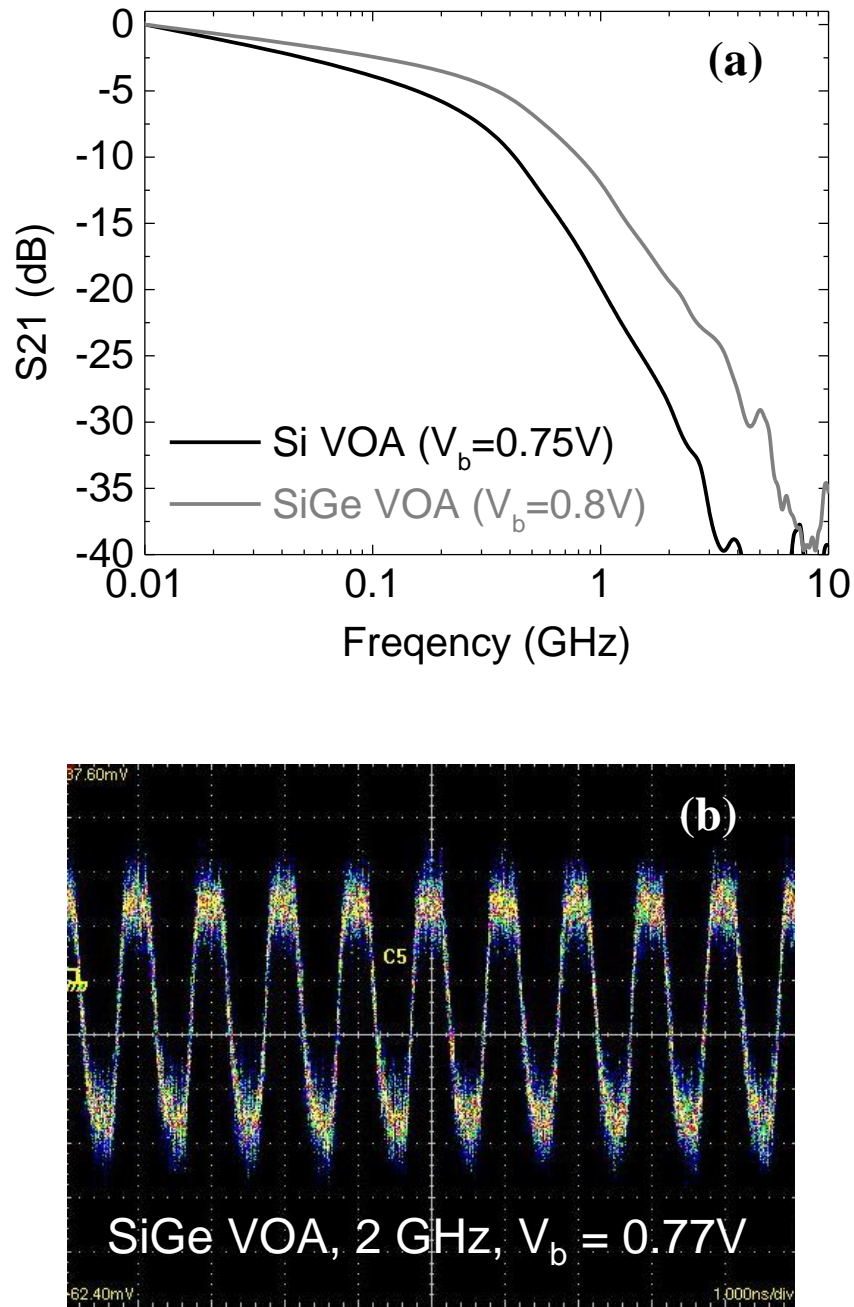


Figure 7.8 (a) Frequency response and (b) sine-wave response at 2 GHz of SiGe VOA.

To clarify higher RF response of the SiGe VOA, we have numerically analyzed the effective lifetime using technology computer-aided design (TCAD) simulation and

finite-difference optical mode analysis^[7.14]. To reproduce the experimentally obtained attenuation characteristics by the simulation, we used the fitting parameters of SRH recombination, τ_{Si} for Si layers and τ_{SiGe} for SiGe layer^[7.18]. First, the attenuation result of the Si VOA is fitted by choosing 2.8 ns of τ_{Si} as shown in Fig. 7.7(a). Then, we simulated the attenuation characteristics of the SiGe VOA with the same parameter of 2.8 ns in Si and SiGe layers. However, it is shown that the simulation result for the SiGe VOA is not in agreement with the experiment result as shown in Fig. 7.7(a). The simulated attenuation is larger than the experimental result, indicating the injected carriers are lower than expected due to recombination. Assuming the SiGe layer has higher recombination by defects, we used τ_{SiGe} to fit the simulation result. As shown in Fig. 7.7(a), the simulation result of 2.0-ns- τ_{SiGe} and 2.8-ns- τ_{Si} is in good agreement with the experiment result of the SiGe VOA. From the simulation results, we calculated the effective lifetime of carriers^[7.6] as shown in Fig. 7.7(b). As increasing bias voltage, the effective lifetime decrease. The SRH recombination and auger recombination mainly affect the lifetime less than and more than around 1 V, respectively. Therefore, the SiGe of 2.8 ns in Si and SiGe layers show almost the same effective lifetime less than 1 V, but the effective lifetime in SiGe become much shorter than that in Si above 1 V due to the larger auger recombination in SiGe layer. Namely, the auger recombination has no effects on the higher RF response of the SiGe VOA due to the responses measured around 0.8 V. In the case of SiGe with 2.0-ns- τ_{SiGe} and 2.8-ns- τ_{Si} , it is found that the effective lifetime of SiGe is shorter than that of Si. At the bias voltage of 0.8 V, the effective lifetime of Si and SiGe is 6.4 ns and 4.6 ns, respectively. As a result, the 1.5 times higher RF response of SiGe VOA can be explained by 1.4 times shorter effective lifetime. Even though the higher RF response of the SiGe VOA is occurred by the degenerated attenuation property, the attenuation is still larger than the Si VOA. Therefore, it is notable that the SiGe VOA can be used to control the tradeoff between attenuation and device speed in conformity to demands on applications.

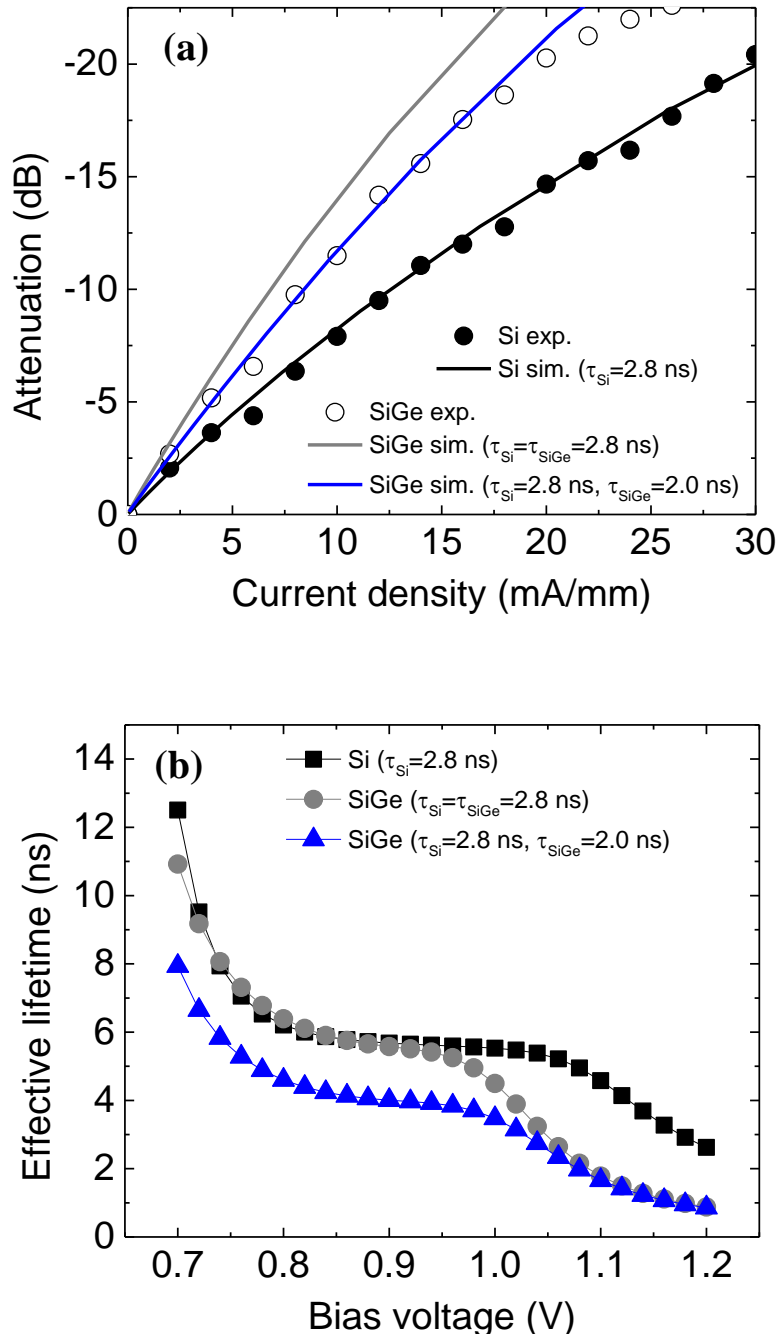


Figure 7.9 (a) Attenuation vs. current density with experiment and simulation results (b) Effective lifetime for Si and SiGe.

The transmission characteristics for 50 Gb/s wavelength division multiplexing (WDM) signal were also evaluated under the measurement setup as shown in Fig. 7.8. 4×12.5 Gb/s non-return-to-zero (NRZ) $2^{31}-1$ Pseudo Random Bit Sequence (PRBS) optical

signals was fed into the SiGe VOA. The total input power is approximately 18 dBm. The output signal was demultiplexed and evaluated by the bit-error tester. Figure 7.9 shows the bit error rate (BER) curves of all the wavelength channels. Although Ch. 40 exhibits relatively large power penalty which might be attributable to the nonlinear crosstalk in SiGe^[7,19], error-free transmission for all the channels with clear eye openings were successfully obtained.

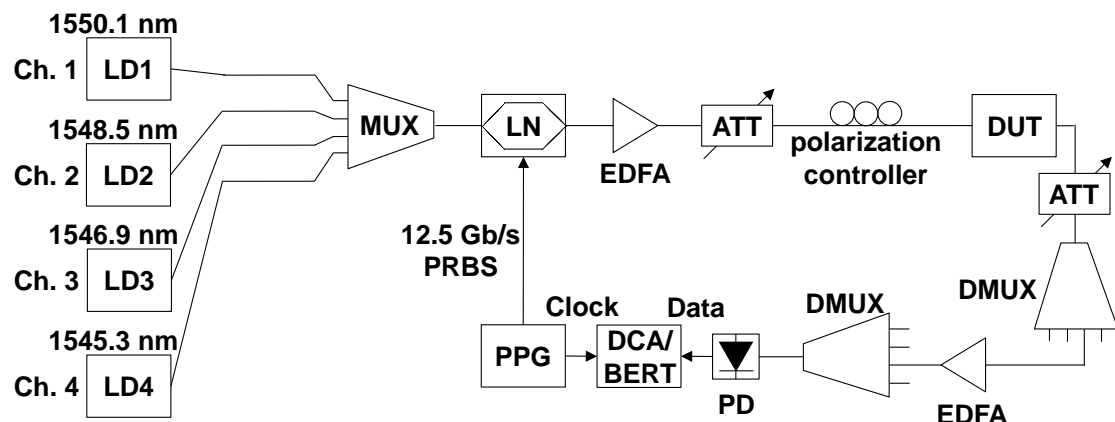


Figure 7.10 Experimental setup for optical transmission test of 12.5 Gb/s PRBS signal.

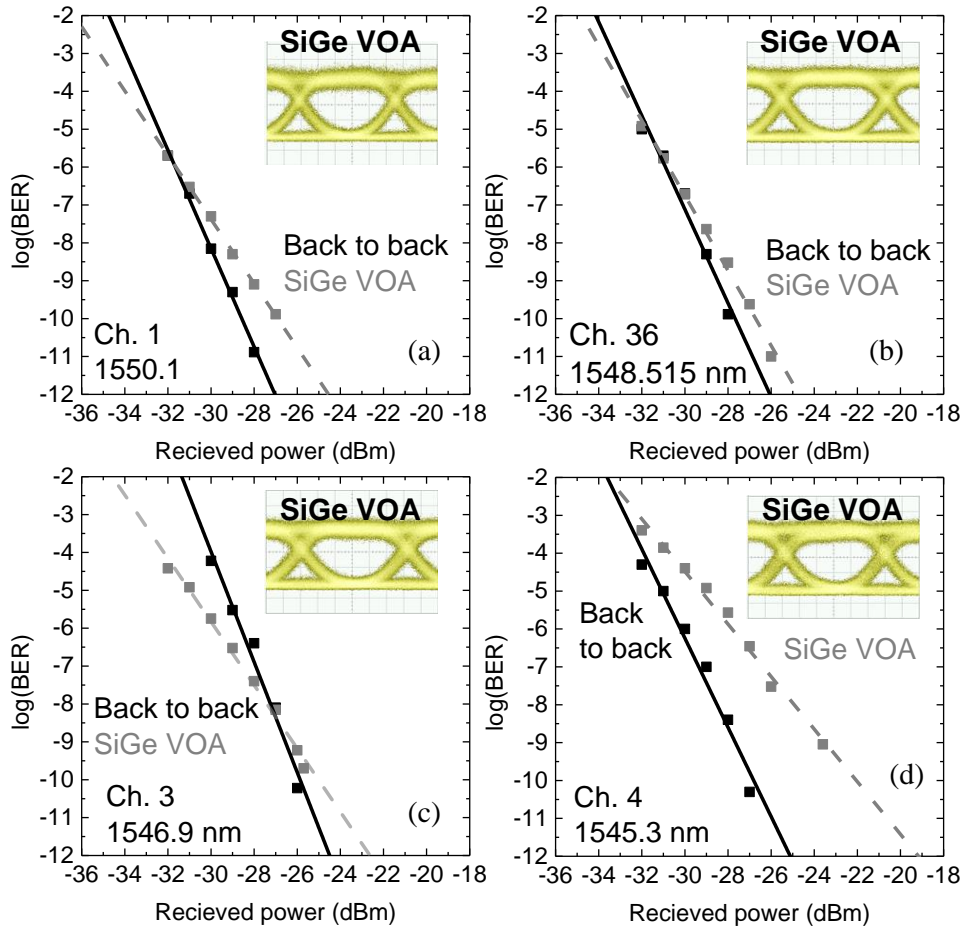


Figure 7.11 BER after transmission of 4×12.5 Gb/s WDM signal through SiGe VOA.

7.6 Conclusion

We have demonstrated record-low injection-current strained SiGe VOAs by optimizing the distance between the p+ and n+ regions in the lateral *pin* junction. The injection current for 20-dB attenuation of the SiGe VOA is as low as 20 mA/mm thanks to the optimization and strain-induced enhancement. We have also found 1.5 times improvement in the RF response of the SiGe VOA comparing to the Si VOA, and 2-GHz switching was achieved. Error-free transmission of 4×12.5 Gb/s WDM signal was also demonstrated.

References

- [7.1] Y. A. Vlasov, "Silicon CMOS-Integrated Nano-Photonics for Computer and Data Communications Beyond 100G," *IEEE Communications Magazine*, vol. 50, pp. S67-S72, Feb 2012.
- [7.2] G. T. Reed, G. Mashanovich, F. Y. Gardes, and D. J. Thomson, "Silicon optical modulators," *Nature Photonics*, vol. 4, pp. 518-526, Aug 2010.
- [7.3] D. Liang and J. E. Bowers, "Recent progress in lasers on silicon," *Nature Photonics*, vol. 4, pp. 511-517, Aug 2010.
- [7.4] J. Michel, J. F. Liu, and L. C. Kimerling, "High-performance Ge-on-Si photodetectors," *Nature Photonics*, vol. 4, pp. 527-534, Aug 2010.
- [7.5] D. W. Zheng, B. T. Smith, and M. Asghari, "Improved efficiency Si-photonic attenuator," *Optics Express*, vol. 16, pp. 16754-16765, Oct 13 2008.
- [7.6] D. W. Zheng, B. T. Smith, J. Dong, and M. Asghari, "On the effective carrier lifetime of a silicon p-i-n diode optical modulator," *Semiconductor Science and Technology*, vol. 23, Jun 2008.
- [7.7] P. Dong, S. R. Liao, H. Liang, R. Shafiiha, D. Z. Feng, G. L. Li, *et al.*, "Submilliwatt, ultrafast and broadband electro-optic silicon switches," *Optics Express*, vol. 18, pp. 25225-25231, Nov 22 2010.
- [7.8] H. Nishi, T. Tsuchizawa, T. Watanabe, H. Shinojima, K. Yamada, and S. Itabashi, "Compact and Polarization-Independent Variable Optical Attenuator Based on a Silicon Wire Waveguide with a Carrier Injection Structure," *Japanese Journal of Applied Physics*, vol. 49, 2010.
- [7.9] S. Park, K. Yamada, T. Tsuchizawa, T. Watanabe, H. Shinojima, H. Nishi, *et al.*, "Influence of carrier lifetime on performance of silicon p-i-n variable optical attenuators fabricated on submicrometer rib waveguides," *Opt Express*, vol. 18, pp. 11282-91, May 24 2010.
- [7.10] T. Tsuchizawa, K. Yamada, T. Watanabe, S. Park, H. Nishi, R. Kou, *et al.*, "Monolithic Integration of Silicon-, Germanium-, and Silica-Based Optical Devices

- for Telecommunications Applications," *IEEE Journal of Selected Topics in Quantum Electronics*, vol. 17, pp. 516-525, May-Jun 2011.
- [7.11] Y. Kim, J. Han, M. Takenaka, and S. Takagi, "Low temperature Al₂O₃ surface passivation for carrier-injection SiGe optical modulator," *Optics Express*, vol. 22, pp. 7458-7464, Apr 7 2014.
- [7.12] R. A. Soref and B. R. Bennett, "Electrooptical Effects in Silicon," *IEEE Journal of Quantum Electronics*, vol. 23, pp. 123-129, Jan 1987.
- [7.13] M. Takenaka and S. Takagi, "Strain Engineering of Plasma Dispersion Effect for SiGe Optical Modulators," *IEEE Journal of Quantum Electronics*, vol. 48, pp. 8-16, Jan 2012.
- [7.14] Y. Kim, M. Takenaka, T. Osada, M. Hata, and S. Takagi, "Strain-induced enhancement of plasma dispersion effect and free-carrier absorption in SiGe optical modulators," *Sci Rep*, vol. 4, p. 4683, 2014.
- [7.15] R. Braunstein, A. R. Moore, and F. Herman, "Intrinsic Optical Absorption in Germanium-Silicon Alloys," *Physical Review*, vol. 109, pp. 695-710, 1958.
- [7.16] D. V. Lang, R. People, J. C. Bean, and A. M. Sergent, "Measurement of the Band-Gap of Ge_xSi_{1-x}/Si Strained-Layer Heterostructures," *Applied Physics Letters*, vol. 47, pp. 1333-1335, 1985.
- [7.17] Q. Xu, S. Manipatruni, B. Schmidt, J. Shakya, and M. Lipson, "12.5 Gbit/s carrier-injection-based silicon micro-ring silicon modulators," *Optics Express*, vol. 15, pp. 430-6, Jan 22 2007.
- [7.18] G. R. Zhou, M. W. Geis, S. J. Spector, F. Gan, M. E. Grein, R. T. Schulein, *et al.*, "Effect of carrier lifetime on forward-biased silicon Mach-Zehnder modulators," *Optics Express*, vol. 16, pp. 5218-5226, Apr 14 2008.
- [7.19] K. Hammani, M. A. Ettabib, A. Bogris, A. Kapsalis, D. Syvridis, M. Brun, *et al.*, "Optical properties of silicon germanium waveguides at telecommunication wavelengths," *Optics Express*, vol. 21, pp. 16690-16701, Jul 15 2013.

Chapter 8

SiGe-based carrier-injection Mach-Zehnder modulator with enhanced plasma dispersion effect in strained SiGe

In this chapter, we demonstrate strained SiGe-based carrier-injection MZ optical modulator with low driving current of 1.47 mA owing to the enhanced plasma dispersion effect in SiGe. The 10 Gbps modulation with clear eye opening is also obtained.

8.1 Introduction

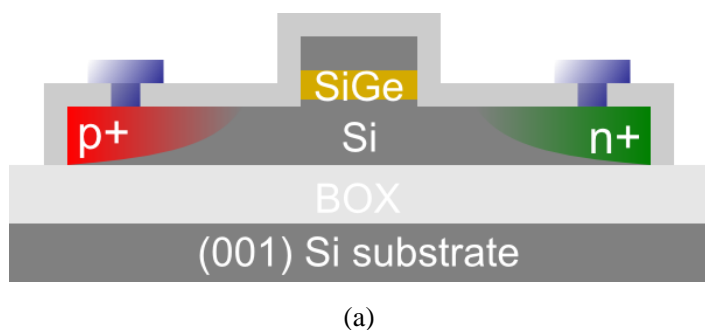
Si optical modulators are expected to play an important role in high-speed and low-power optical interconnections especially for datacenter networks^[8.1]. Among various Si optical modulators demonstrated so far, the Si Mach-Zehnder (MZ) optical modulators based on the plasma dispersion effect have been mostly reported for high-speed modulation and broad-wavelength operation. However, the carrier-depletion Si modulators need relatively long phase-shifter or high driving voltage because of the weak plasma dispersion effect in Si, which are not favorable for large-scale integration. For further improvement in modulation efficiency, we have proposed strained SiGe modulators to enhance the plasma dispersion effect by reducing effective mass of holes in SiGe because the effect is inversely proportional to the effective mass^[8.2]. We have experimentally demonstrated the enhanced free-carrier absorption in strained SiGe^[8.3],^[8.4], and low-power SiGe variable optical attenuators^[8.5]. However, the SiGe MZ

optical modulators based on the enhanced plasma dispersion effect have not been demonstrated yet.

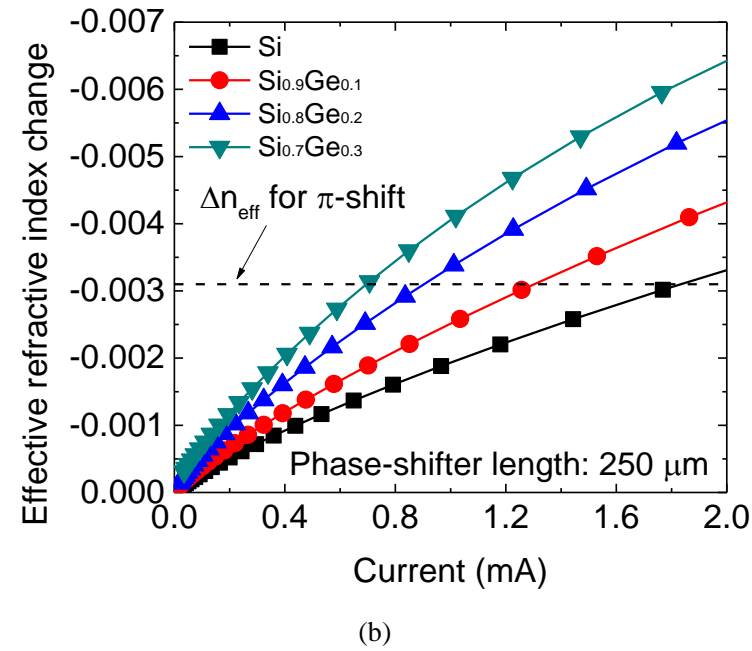
In this paper, we present the strained SiGe-based optical modulator, which exhibits higher modulation efficiency than the Si modulator due to the enhanced plasma dispersion effect in strained SiGe for the first time. We successfully demonstrate 10-Gbps modulation with clear eye opening by carrier injection with pre-emphasis driving.

8.2 Numerical analysis of strained SiGe MZ modulator

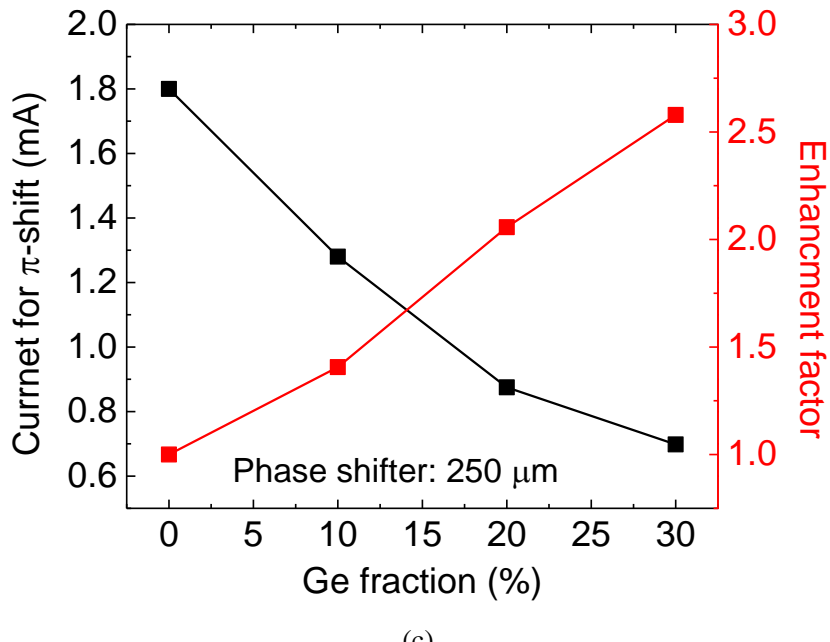
To estimate the improvement of modulation efficiency by strain-induced enhancement of the plasma dispersion effect in SiGe, we numerically analyzed the carrier-injection strained SiGe MZ modulator with a lateral p-i-n junction using technology computer-aided design simulation and finite-difference optical mode analysis^[8,4]. Figure 1(a) shows the cross-sectional device structure of the phase shifter in the SiGe modulator, which consists of 40-nm-thick SiGe in the waveguide core. Figure 1(b) shows the change in effective refractive index as a function of injected carrier density with varied Ge fractions in SiGe from 0.0 to 0.3. As increasing injection current, the effective index change increases due to the plasma dispersion effect. When the Ge fraction increases, the effective index change is enhanced thanks to the enhanced plasma dispersion effect in strained SiGe. It is expected that the injection current required for π phase shift decreases with increasing Ge fraction as shown in Fig. 1(c). It is worth noting that the injection current can be as low as 0.7 mA using $\text{Si}_{0.7}\text{Ge}_{0.3}$ in the case of 250- μm -long phase-shifter, approximately 2.5 times lower current than that of the Si device.



(a)



(b)

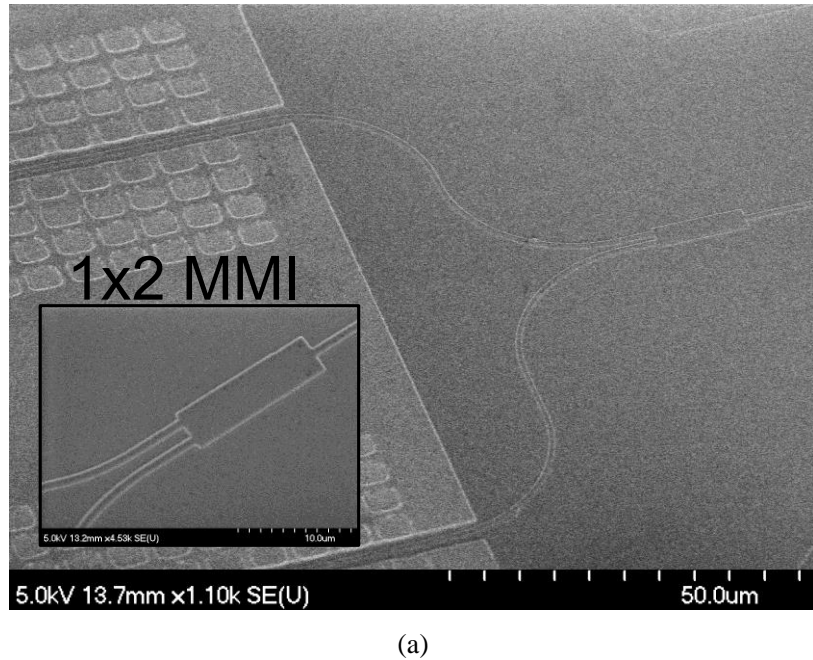


(c)

Figure 8.1 (a) A cross-sectional schematic of the phase shifter in the carrier-injection SiGe modulator, (b) Simulation result of change in effective refractive index as a function of injected current density with Ge fractions from 0.0 to 0.3 when the phase shifter length is 250 μm , and (c) Current density required for π phase shift (left axis) and its enhancement factor (right axis) as a function of Ge fraction.

8.3 Fabrication of strained SiGe MZ modulator

We have fabricated the SiGe asymmetric MZ modulator as follow. A 45-nm-thick pseudomorphic $\text{Si}_{0.76}\text{Ge}_{0.14}$ layer and a 75-nm-thick Si layer were grown on the 105-nm-thick silicon-on-insulator (SOI) by chemical vapor deposition (CVD). The waveguides with a Si/SiGe/Si core were formed by electron beam lithography and RIE etching with CF_4 . Then, the ion implantation of boron and phosphorus was carried out to form the *pin* junctions. Although the Ge fraction of the SiGe layer was changed to 9% from 14% due to the Ge diffusion during the activation annealing, the strain in the SiGe has been almost maintained. We have also fabricated the Si asymmetric MZ modulator using a 220-nm-thick SOI as a reference device. Figure 2(a) shows a tilted SEM image of the fabricated device. The well-defined 1×2 MMI coupler is also shown in the inset of Fig. 2(a). Figure 2(b) shows the top-view of the SiGe asymmetric MZ modulator, which consists of two 1×2 MMI couplers and 250- μm -long phase shifters in the two MZ interferometer arms.



(a)

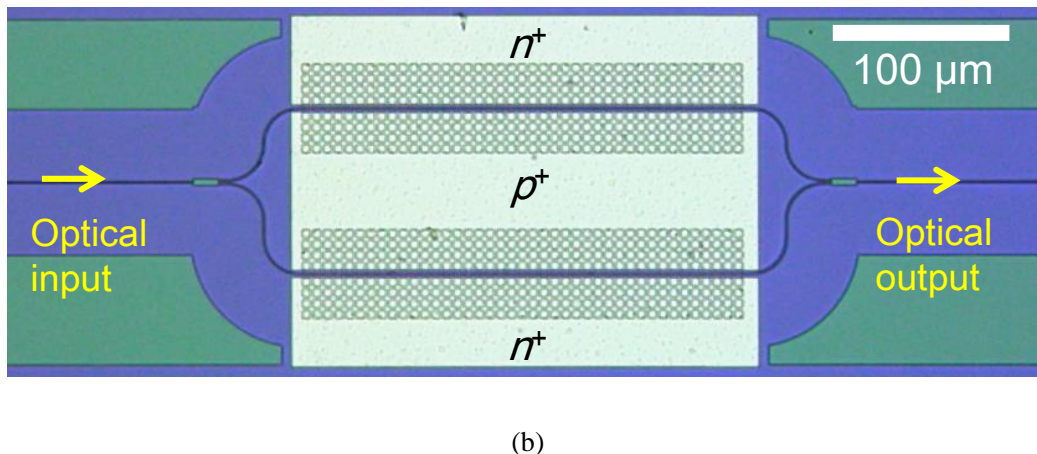
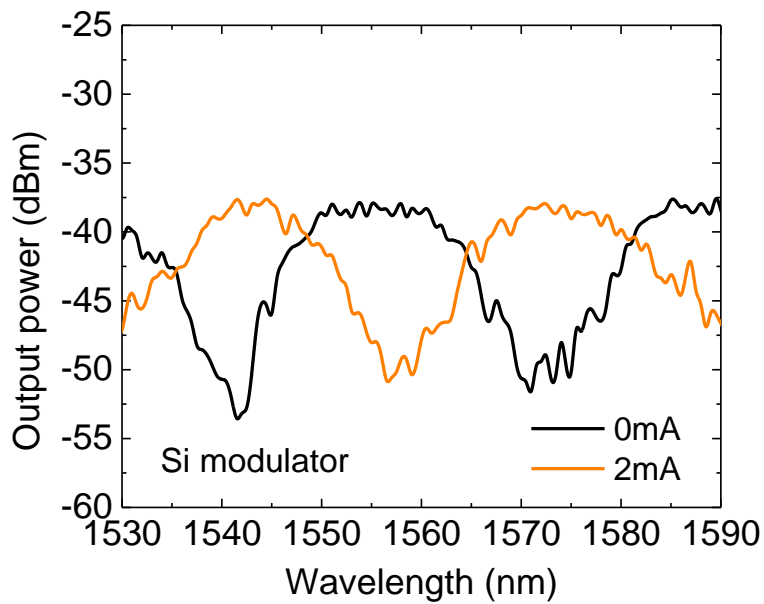


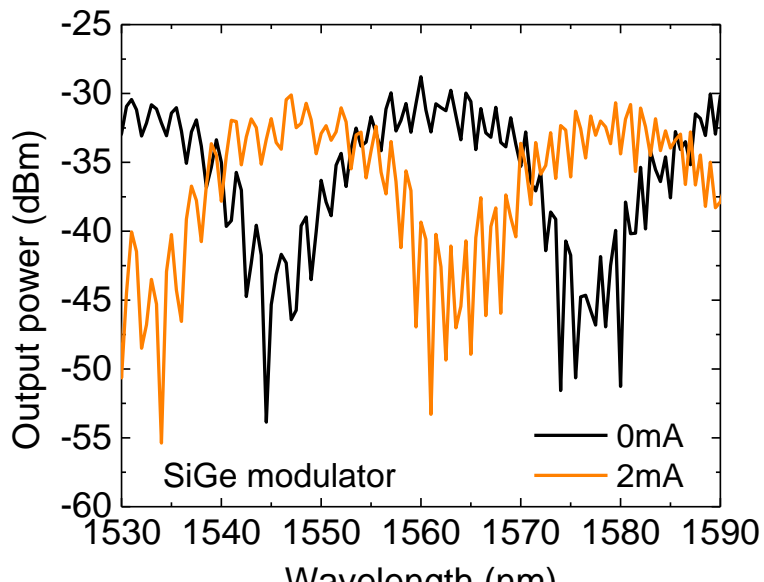
Figure 8.2 (a) Tilted SEM image and (b) Optical microscopy image of the fabricated device.

8.4 Static characteristics of strained SiGe asymmetric MZ modulator

The values of the phase shift in the SiGe and Si MZ modulators were evaluated by measuring the wavelength spectrum change when the injection current was increased. The free spectrum range in the asymmetric MZ interferometer was designed to be approximately 30 nm, according to the 20- μm difference in the length between the two MZI arms. Figures 3(a) and 3(b) show the transmission spectra of the Si and SiGe modulators with the injection current of 0 mA and 2 mA, respectively. The wavelength spectra are shifted by the increase in the optical phase difference between the two MZI arms due to the plasma dispersion effect. From those spectrum shifts, the values of the phase shift were extracted.



(a)

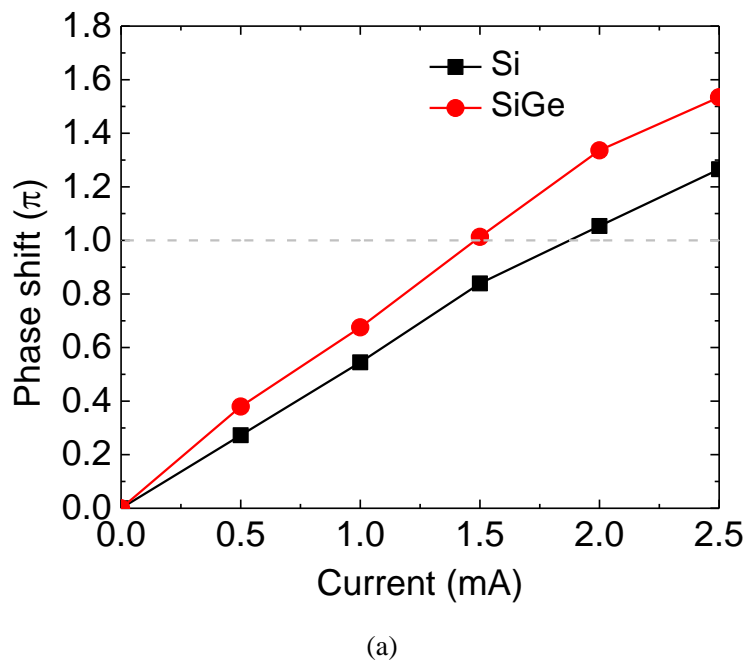


(b)

Figure 8.3 Measured transmission spectra with injection currents of 0 mA and 2 mA for (a) Si and (b) SiGe asymmetric MZ modulators.

Figure 4(a) shows the optical phase shift of the Si and SiGe asymmetric modulators as a function of the injected current, obtained by the wavelength spectrum at each injected currents. The optical phase shift is increased by increasing injection

current due to the plasma dispersion effect. The SiGe modulator exhibits higher optical phase shift than the Si modulator at the same injection current, indicating the modulation efficiency is improved by the enhancement of the plasma dispersion effect in strained SiGe. The injection currents for π phase shift are 1.47 mA for SiGe modulator and 1.87 mA for Si modulator, respectively. Figure 4(b) shows a benchmark of the injection current required for π phase shift in the carrier-injection phase shifter as a function of the phase shifter length. The injection current is more required to obtain π phase shift when the phase shift length is reduced^[8,6]. Among the Si modulators reported so far^{[8,6], [8,7], [8,8]}, the Si modulator in this work exhibits one of the lowest injection current in the case of the 250- μm -long phase shifter, which may be attributable to the optimized fabrication procedure of the pin junction. As shown in Fig. 4(b), further reduction in the injection current is achieved by using the SiGe optical modulator. The open circles in Fig. 4(b) show the simulated injection currents for π phase shift for the Ge fraction from 0 to 0.3. It is found that the experimental results of the Si and SiGe modulator show relatively good agreement with the simulation results. Thus, it is expected that the injection current for π phase shift can be reduced to be less than 1 mA by using higher strain and Ge fraction.



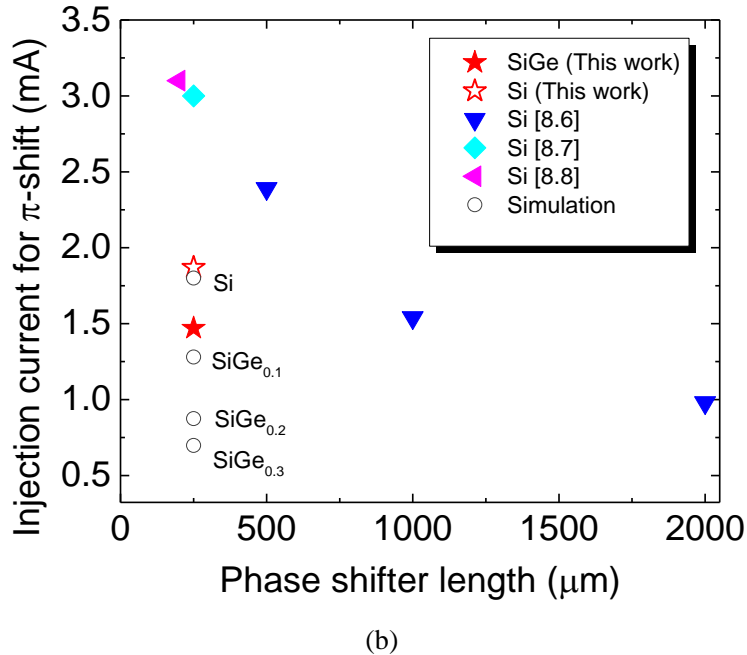


Figure 8.4 (a) Extracted phase shift as a function of injection current for Si and SiGe asymmetric MZ modulator. (b) Benchmark of injection current for π phase shift as a function of phase shifter length.

8.5 Dynamic characteristics of strained SiGe asymmetric MZI modulator

We have performed the dynamic measurement of the SiGe asymmetric MZ modulator by using the measurement setup in Fig. 5(a). A 10 Gbps non-return-to-zero (NRZ) $2^7 - 1$ pseudo random bit sequence (PRBS) electrical signals are converted to the pre-emphasis signals by using the differentiators^[8,9]. Then, the electrical signals of $2.1 \text{ V}_{\text{p-p}}$ with $-0.78 \text{ V}_{\text{DC}}$ are applied to both arms of the SiGe modulator for the push-pull operation. As shown in Fig. 5(b), the clear eye opening at 10 Gbps was successfully obtained at the wavelength of 1541 nm which is the balance point of -3 dB .

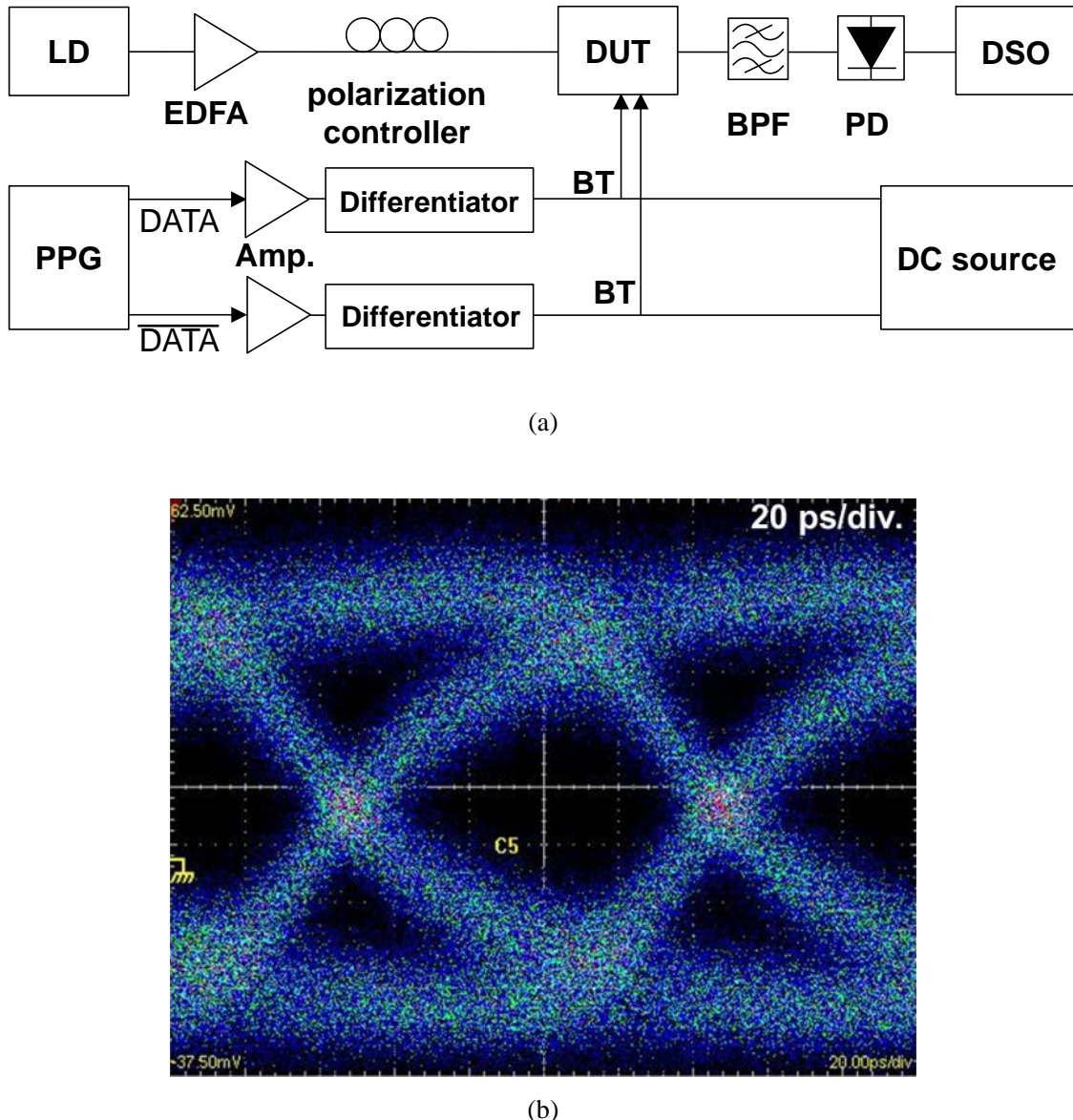
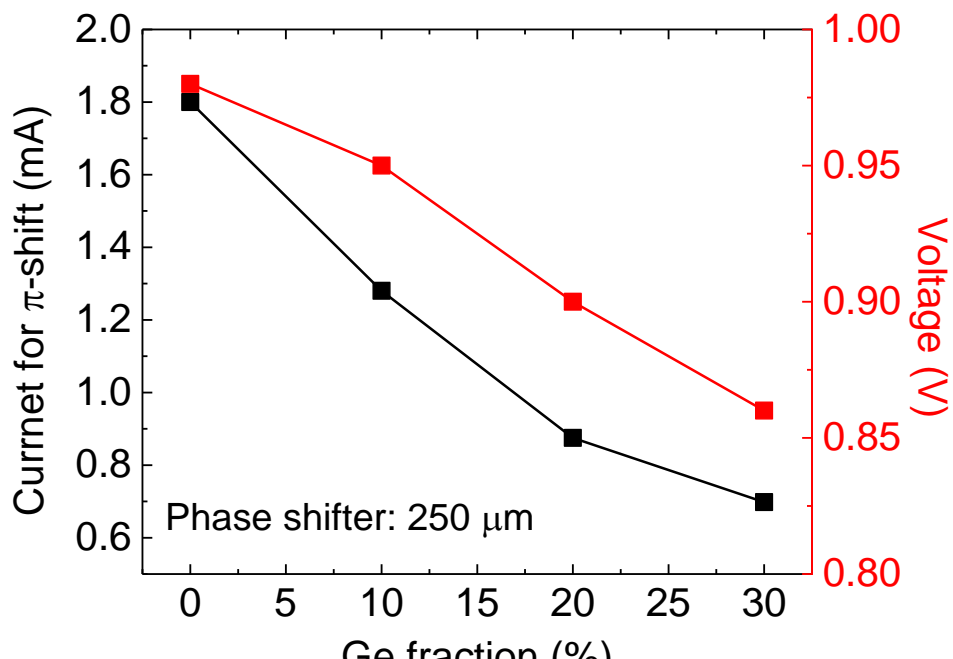


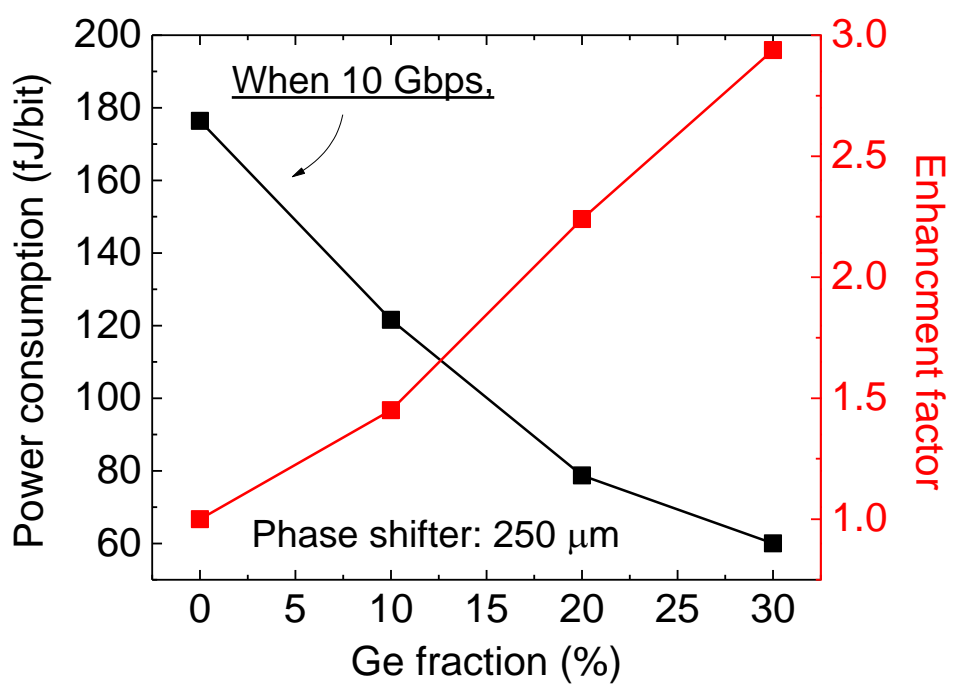
Figure 8.5 (a) Measurement setup for dynamic characteristics of SiGe modulator. (b) Eye pattern of SiGe MZ modulator at 10 Gbps.

8.6 Power consumption of SiGe Mach-Zhender modulator

As we described about power consumption in Chapter 1.4, it is the most important parameter for the system of optical interconnect. The requirement for power consumption of optical modulators should be less than 100 fJ/bit. To realize that, we have developed the strain-induced enhancement of the plasma dispersion effect to improve the conventional Si-based optical modulators.



(a)



(b)

Figure 8.6 (a) Current and voltage for π phase shift as a function of Ge fraction by numerical analysis, (b) power consumption and its enhancement factor as a function of Ge fraction.

Figure 8.6 shows the current and voltage for π phase shift as a function of Ge fraction, and power consumption and its enhancement factor as a function of Ge fraction. The current and voltage are the results by numerical analysis based on Sentaurus in conjunction with FDM mode analysis. The current and voltage for π phase shift decreases as increasing Ge fraction by strain effect in SiGe. It is notable that the decrease in voltage has two effects of decrease in current by strain effect and threshold voltage by bandgap narrowed SiGe. By the product of the current and voltage, we have estimated power consumption based on DC results, given 10-Gbps operation. Here, we have also estimated the power consumption based on DC result in reference^[8,10] to know difference between the estimations based on DC and AC. The power consumptions of DC and AC are 3 pJ/bit and 5 pJ/bit^[8,10], respectively, meaning the DC based estimation can be reliable. We show the power consumption and its enhancement factor as a function of Ge fraction. The power consumption decreases as increasing Ge fraction, and the enhancement factor reaches three times at 30% Ge fraction of SiGe. Even the Si modulator has much less power consumption of 180 fJ/bit than the reference. Thanks to three times enhancement by strained Si_{0.7}Ge_{0.3}, it is expected that the power consumption is less than 100 fJ/bit.

8.7 Conclusion

We have successfully demonstrated the strained SiGe-based MZ optical modulator. The enhanced plasma dispersion in strained SiGe is experimentally observed for the first time. Thus, the injection current required for π phase shift is reduced to 1.47 mA from 1.87 mA as compared with the Si modulator. It is also expected that the modulation efficiency can be further improved by using higher strain and Ge fraction, enabling the operation at the injection current less than 1 mA. The 10 Gbps of clear eye pattern has also been successfully obtained by the pre-emphasis method. Therefore, strained SiGe is a highly promising material as a technology booster for Si-based optical modulators.

References

- [8.1] G. T. Reed, G. Mashanovich, F. Y. Gardes, and D. J. Thomson, "Silicon optical modulators," *Nature Photonics*, vol. 4, pp. 518-526, Aug 2010.
- [8.2] M. Takenaka and S. Takagi, "Strain Engineering of Plasma Dispersion Effect for SiGe Optical Modulators," *IEEE Journal of Quantum Electronics*, vol. 48, pp. 8-16, Jan 2012.
- [8.3] Y. Kim, M. Takenaka, T. Osada, M. Hata and S. Takagi, "Strain-induced enhancement of free-carrier effects in SiGe for optical modulator and VOA applications," Proceeding of Optical Fiber Communication Conference, Th1C.4., San Francisco, 2014.
- [8.4] Y. Kim, M. Takenaka, T. Osada, M. Hata, and S. Takagi, "Strain-induced enhancement of plasma dispersion effect and free-carrier absorption in SiGe optical modulators," *Sci Rep*, vol. 4, p. 4683, 2014.
- [8.5] Y. Kim, J. Fujikata, S. Takahashi, M. Takenaka, and S. Takagi, "Record-low injection-current strained SiGe variable optical attenuator with optimized lateral PIN junction," Proceeding of European Conference on Optical Communications, P.2.6, Cannes, 2014.
- [8.6] P. Dong, S. R. Liao, H. Liang, R. Shafiiha, D. Z. Feng, G. L. Li, *et al.*, "Submilliwatt, ultrafast and broadband electro-optic silicon switches," *Optics Express*, vol. 18, pp. 25225-25231, Nov 22 2010.
- [8.7] G. R. Zhou, M. W. Geis, S. J. Spector, F. Gan, M. E. Grein, R. T. Schulein, *et al.*, "Effect of carrier lifetime on forward-biased silicon Mach-Zehnder modulators," *Optics Express*, vol. 16, pp. 5218-5226, Apr 14 2008.
- [8.8] J. Van Campenhout, W. M. J. Green, S. Assefa, and Y. A. Vlasov, "Low-power, 2x2 silicon electro-optic switch with 110-nm bandwidth for broadband reconfigurable optical networks," *Optics Express*, vol. 17, pp. 24020-24029, Dec 21 2009.
- [8.9] Q. Xu, S. Manipatruni, B. Schmidt, J. Shakya, and M. Lipson, "12.5 Gbit/s carrier-injection-based silicon micro-ring silicon modulators," *Opt Express*, vol. 15, pp. 430-6, Jan 22 2007.

- [8.10] W. M. J. Green, M. J. Rooks, L. Sekaric, and Y. A. Vlasov, "Ultra-compact, low RF power, 10 gb/s silicon Mach-Zehnder modulator," *Optics Express*, vol. 15, pp. 17106-17113, Dec 10 2007.

Chapter 9

High Ge fraction SiGe optical modulator by considering Ge diffusion at high temperature process

In this chapter, we propose the novel method to achieve a high Ge fraction SiGe optical modulator by taking Ge diffusion at high temperature into account. The numerical analysis of the SiGe optical modulator is carried out by technology computer-aided design (TCAD) simulation and finite-difference optical mode analysis. The results show that sub-mA for π -shift injection-current can be achieved using 20-nm-thick $\text{Si}_{0.7}\text{Ge}_{0.3}$ thanks to stronger carrier confinement in the thinner SiGe layer of SiGe even though modulation efficiency decrease with a decrease in the thickness.

9.1 Introduction

Si-based optical modulators are one of the fundamental building blocks for on-chip optical interconnections to meet the increasing bandwidth and power consumption challenges of Si LSIs beyond the current copper interconnect technology^[10.1]. The Si optical modulators are mainly based on the free carrier plasma dispersion effect^[10.2], however, the device footprints of the Mach-Zehnder interferometer (MZI) based modulators are still large^[10.3] because the plasma dispersion effect is not strong enough. The device footprints are expected to be reduced by enhancing the plasma dispersion effect by means of strain-induced mass modulation^[10.4]. We have successfully demonstrated the enhancement of free-carrier effects using strained SiGe for optical modulators/VOAs/switches applications. For further improved device performance, it is

required to obtain high Ge fraction and strain in SiGe. However, the high Ge fraction SiGe devices have not been demonstrated yet. The Ge fraction of SiGe, demonstrated in previous works, are lower than 20% due to high thermal process causing Ge diffusion as shown in Fig. 9.1 [10,5].

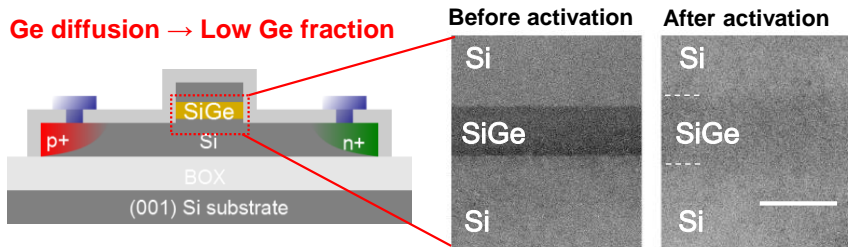


Figure 9.1 Current issue on a decrease in Ge fraction by Ge diffusion during activation process.

In this chapter, we propose a novel method to achieve high Ge fraction SiGe, approximately 30%, taking into account Ge diffusion after high-temperature activation process. Numerical analysis shows that sub-mA for π -shift can be achieved even 20-nm-thick $\text{Si}_{0.7}\text{Ge}_{0.3}$. We also estimate the prepared high SiGe wafer in terms of layer thickness, Ge fraction, and strain relaxation.

9.2 Design for SiGe layer of high Ge fraction with consideration of Ge diffusion

As mentioned above, the high Ge fraction and strain are required for high-performance devices. From the previous work, we found that the Ge fraction in SiGe and strain decreases after activation annealing. However, the percentage of strain at the SiGe of the reduced Ge fraction is also almost strained. As shown in Fig. 9.2., the strain value at 14% Ge fraction is slightly under the theoretical strain, indicating the SiGe layer is almost strained. Therefore, it is expected that the high Ge fraction and strained SiGe layer after annealing can be obtained by using the higher Ge fraction and strained SiGe layer. Even though the higher Ge fraction SiGe should be thinner due to critical thickness, the thickness becomes thicker as much as Ge diffuses as shown in Fig.9.3.

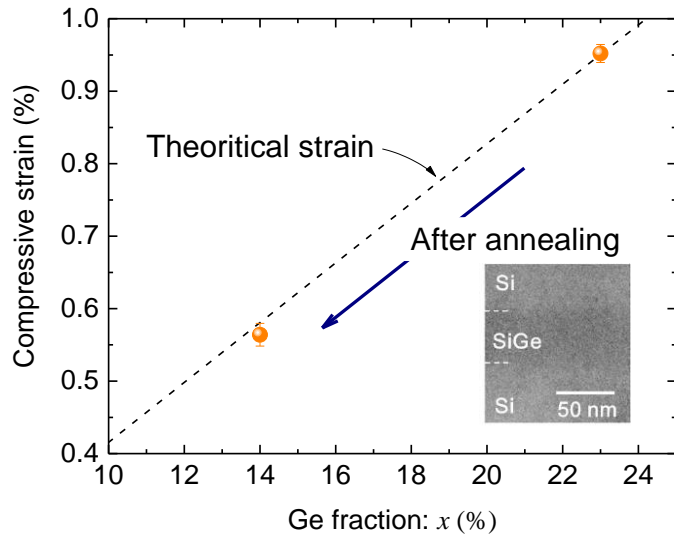


Figure 9.2 Strain versus Ge fraction with before and after activation process.

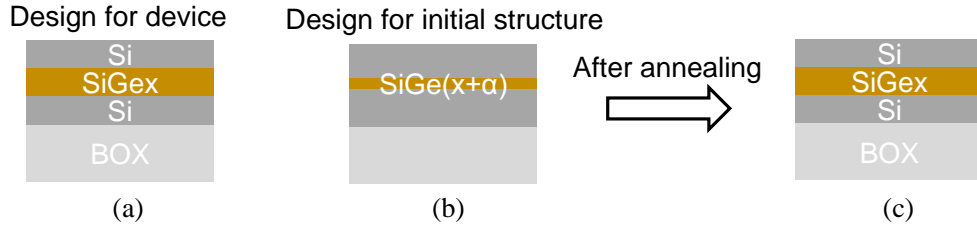


Figure 9.3 Epitaxial Si/SiGe/SOI structure for (a) Design for device, (b) Design for initial structure, and (c) Structure after annealing process.

9.3 Numerical analysis on dependence of SiGe layer thickness in SiGe modulator

To obtain high Ge fraction SiGe layer after device fabrication, the higher Ge fraction SiGe is required. However, the critical thickness exponentially decreases as shown in Fig. 2.4. Therefore, it is difficult to obtain 40-nm-thick $\text{Si}_{0.7}\text{Ge}_{0.3}$ because the metastable critical thickness of $\text{Si}_{0.4}\text{Ge}_{0.6}$ is approximately 10 nm. In terms of that, it is important to know the thickness dependence of SiGe layer. Hence, in this section, we show the numerical analysis on dependence of $\text{Si}_{0.7}\text{Ge}_{0.3}$ layer thickness in SiGe optical modulators.

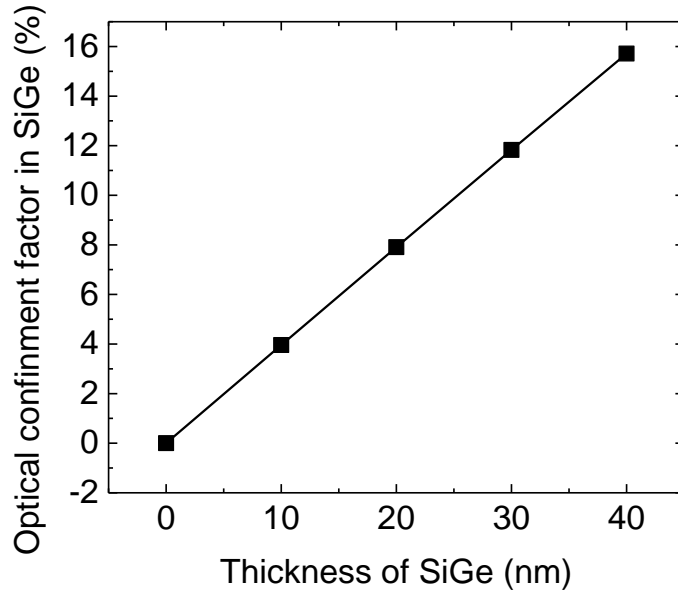


Figure 9.4 Calculated optical confinement factor in SiGe as a function of thickness of SiGe layer.

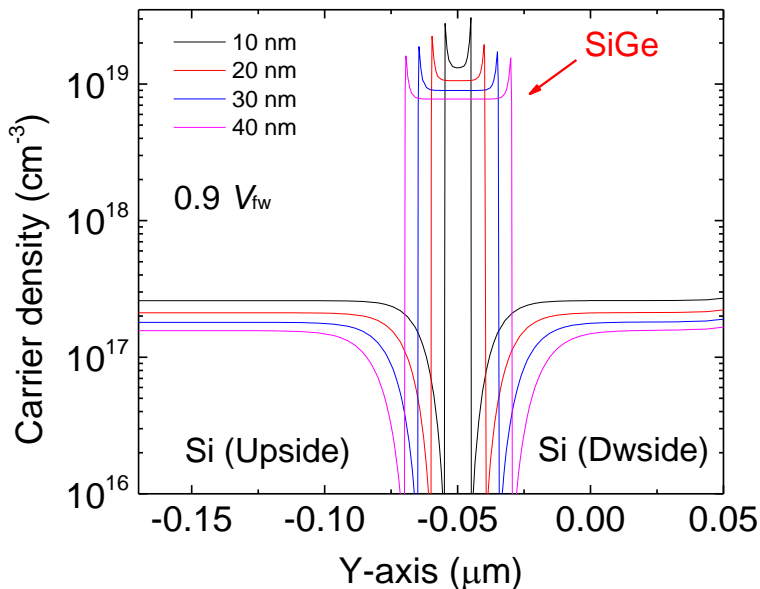
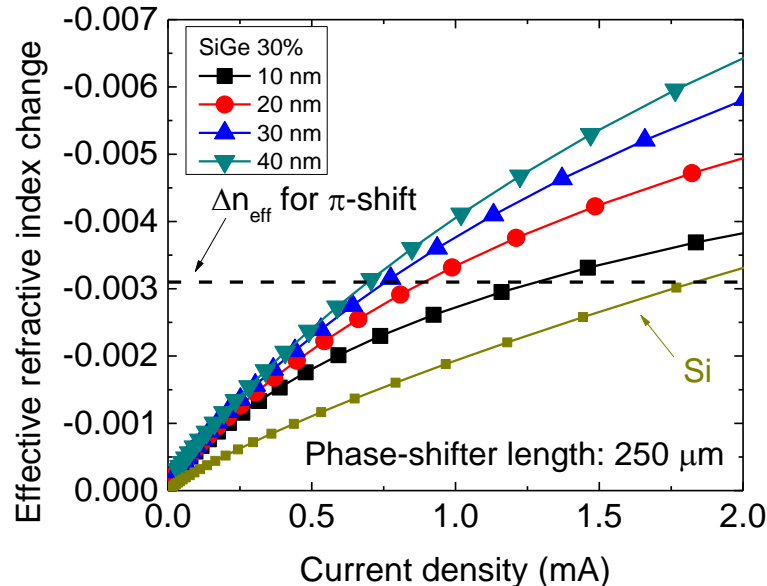


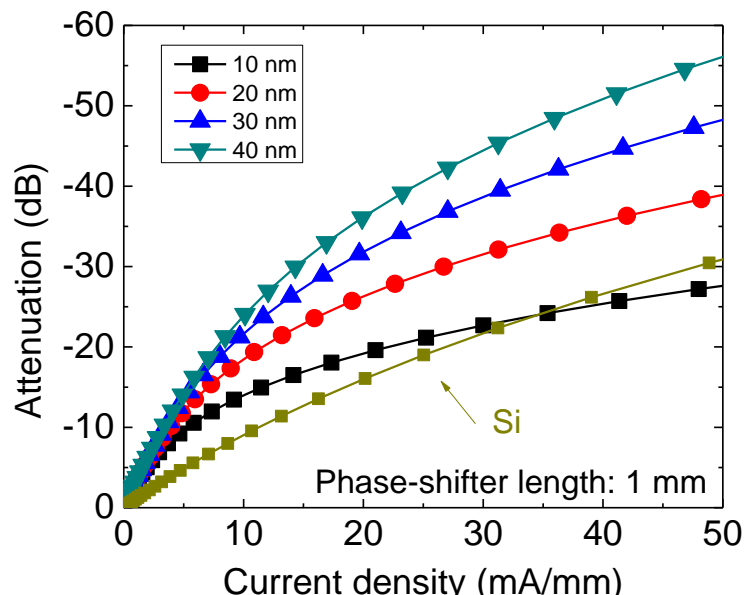
Figure 9.5 Carrier densities in horizontal direction with various thickness of SiGe layers when 0.9V-forward bias is applied.

It is important to know the tradeoff between optical confinement factor in SiGe and carrier confinement in SiGe in terms of the optimization of SiGe thickness. Figure 9.4 shows Calculated optical confinement factor in SiGe as a function of thickness of SiGe layer. It indicates that the optical confinement factor in SiGe increases as

increasing SiGe thickness. On the other hand, the carrier concentration in SiGe decreases as increasing SiGe thickness. Therefore, the numerical analysis is needed since optical characteristics cannot simply be anticipated.



(a)



(b)

Figure 9.5 Simulation result of (a) change in effective refractive index change and (b) attenuation as a function of injected current density with various SiGe thickness.

Figure 9.5 shows the simulation results of change in effective refractive index change and attenuation as a function of injected current density with various SiGe thickness. As decreasing SiGe thickness, change in refractive index and attenuation decreases. It is important to notice that the initial rise in low level injection current less than 5 mA is steep, indicating that thin SiGe layer can be applicable for modulator applications. In terms of the attenuation property, it might not be preferable to use too thin SiGe since carrier density is limited by strong Auger recombination in thin SiGe layer.

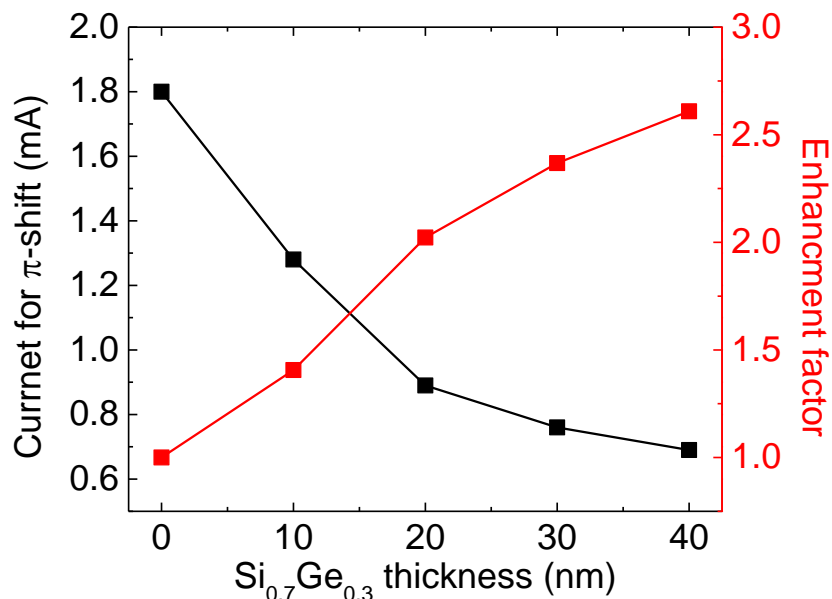


Figure 9.6 Current density required for π phase shift (left axis) and its enhancement factor (right axis) as a SiGe thickness.

Figure 9.6 show injection current for π -phase shift and its enhancement factor comparing to Si modulator as a function of SiGe thickness. It is interesting to know that Sub-mA for π -phase shift can be achieved even 20-nm-thick $\text{Si}_{0.7}\text{Ge}_{0.3}$ with 2-times enhancement factor, which can be obtained by 10-nm-thick $\text{Si}_{0.4}\text{Ge}_{0.6}$ less than critical thickness.

9.4 Estimation of higher Ge fraction SiGe layer in Si/SiGe/SOI

We have prepared the higher Ge fraction SiGe substrates for high Ge fraction SiGe optical modulators as shown in Fig. 9.7. Ge fractions is as high as 50% and 60%, and SiGe thickness is 20, 15, and 10 nm for 50%, and 20, 15, 10, and 5 nm for 60%.

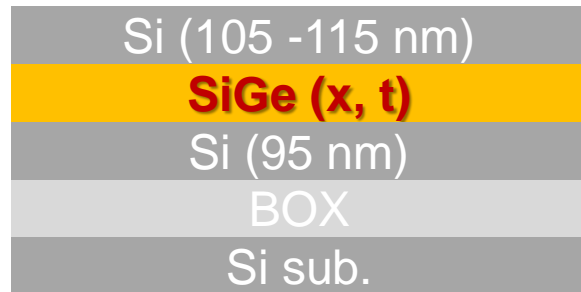


Figure 9.7 Si/SiGe/SOI substrates for SiGe optical modulator

Surface morphology is observed by optical microscopy as shown in Fig. 9.8. In the cases of 20-nm-thick and 15-nm-thick $\text{Si}_{0.4}\text{Ge}_{0.6}$, the cracks are observed on the surface, indicating strain relaxation. In terms of that, Raman spectrums of samples with cracks vary widely, on the other hand, almost no variations in spectrums of 10- and 5-nm $\text{Si}_{0.4}\text{Ge}_{0.6}$ samples in Fig. 9.9. Also, no variations are observed in $\text{Si}_{0.5}\text{Ge}_{0.5}$ samples in Fig. 9.10. Therefore, except the two samples, they can be used for device fabrication. In particular, 20-nm $\text{Si}_{0.7}\text{Ge}_{0.3}$ device can be achieved by 10-nm $\text{Si}_{0.4}\text{Ge}_{0.6}$.

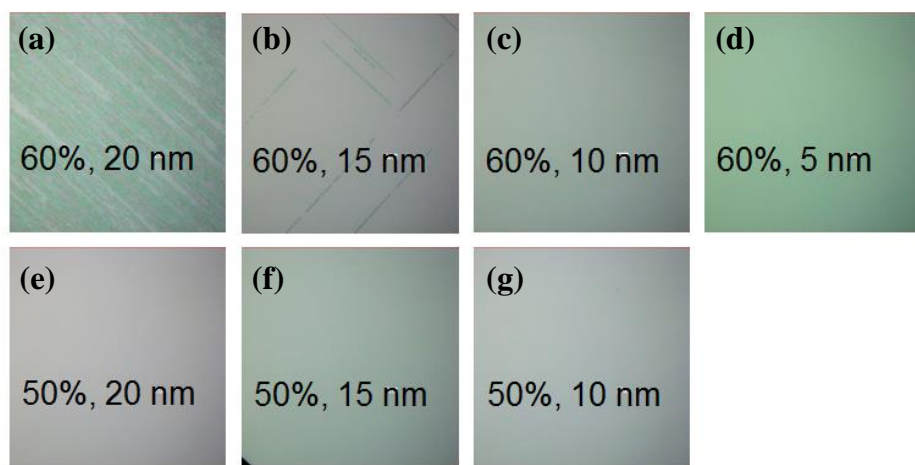


Figure 9.8 Image observed by optical microscopy with 50 times magnification

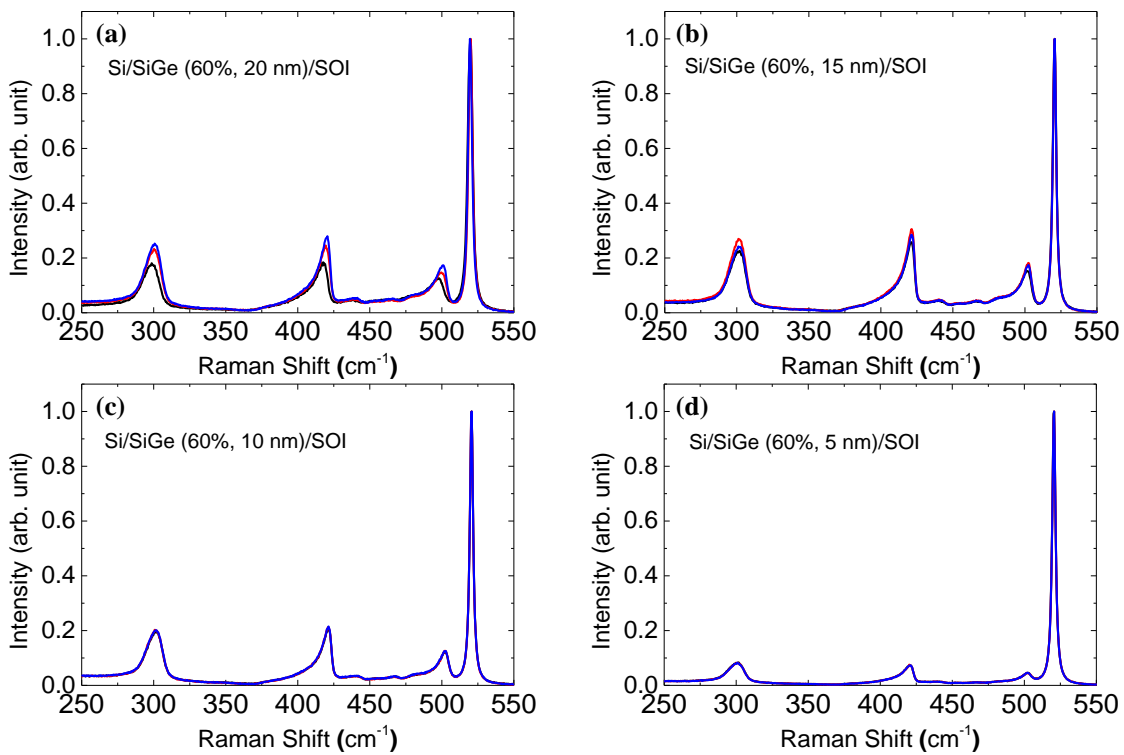


Figure 9.9 Raman spectroscopy of $\text{Si}_{0.4}\text{Ge}_{0.6}$ samples (a) 20 nm, (b) 15 nm, (c) 10 nm, and (d) 5 nm

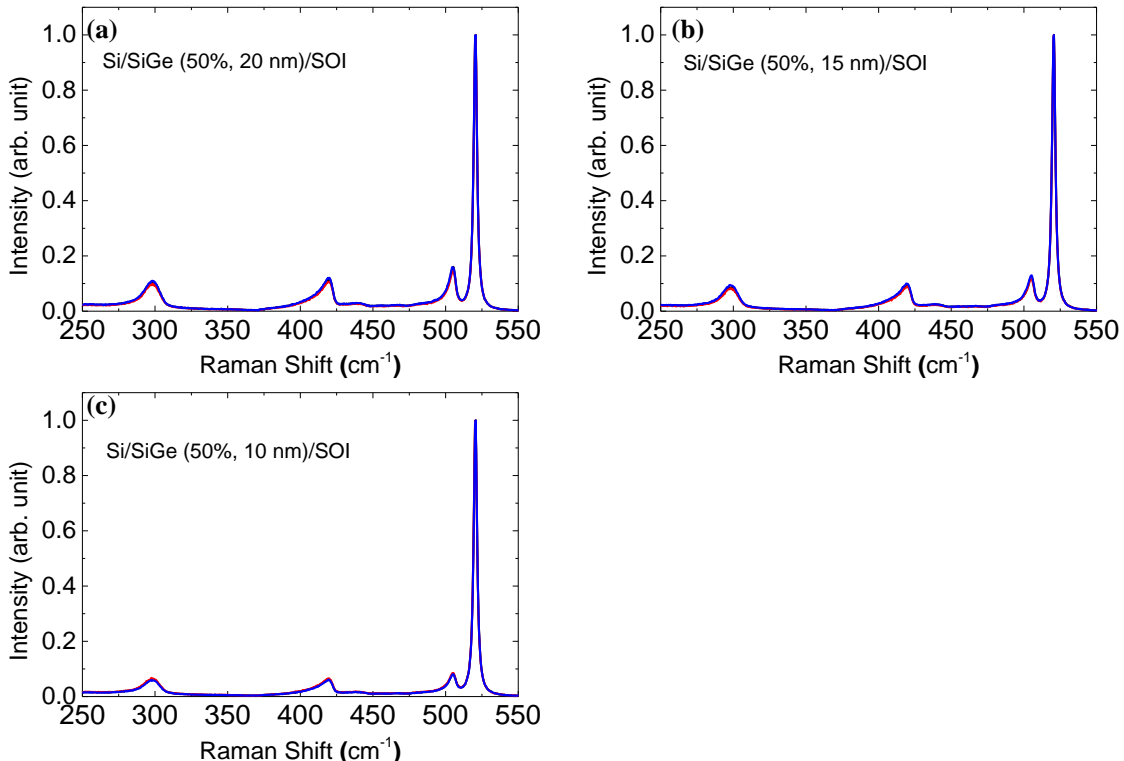


Figure 9.10 Raman spectroscopy of $\text{Si}_{0.5}\text{Ge}_{0.5}$ samples (a) 20 nm, (b) 15 nm, and (c) 10 nm

9.5 Conclusion

We have proposed a novel method to achieve high Ge fraction SiGe optical modulator taking into account Ge diffusion. The thickness dependence of $\text{Si}_{0.7}\text{Ge}_{0.3}$ optical modulator has been estimated. Sub-mA for π -shift can be achieved even 20-nm-thick $\text{Si}_{0.7}\text{Ge}_{0.3}$ with 2-times enhancement factor. Higher Ge fraction SiGe wafers are prepared for high Ge fraction SiGe optical modulator. 20- and 15-nm-thick $\text{Si}_{0.4}\text{Ge}_{0.6}$ show cracks, indicating strain relaxation. 10-nm-thick $\text{Si}_{0.4}\text{Ge}_{0.6}$ is promising for 20-nm-thick $\text{Si}_{0.7}\text{Ge}_{0.3}$ optical modulator.

References

- [10.1] A. S. Liu and M. Paniccia, "Advances in silicon photonic devices for silicon-based optoelectronic applications," *Physica E-Low-Dimensional Systems & Nanostructures*, vol. 35, pp. 223-228, Dec 2006.
- [10.2] R. A. Soref and B. R. Bennett, "Electrooptical Effects in Silicon," *Ieee Journal of Quantum Electronics*, vol. 23, pp. 123-129, Jan 1987.
- [10.3] L. Liao, A. Liu, D. Rubin, J. Basak, Y. Chetrit, H. Nguyen, *et al.*, "40 Gbit/s silicon optical modulator for high-speed applications," *Electronics Letters*, pp. 51-52, Jun 2009.
- [10.4] M. Takenaka and S. Takagi, "Strain Engineering of Plasma Dispersion Effect for SiGe Optical Modulators," *IEEE Journal of Quantum Electronics*, vol. 48, pp. 8-16, Jan 2012.
- [10.5] Y. Kim, M. Takenaka, T. Osada, M. Hata, and S. Takagi, "Strain-induced enhancement of plasma dispersion effect and free-carrier absorption in SiGe optical modulators," *Sci Rep*, vol. 4, p. 4683, 2014.

Chapter 10

Numerical Analysis of Carrier-Depletion Strained SiGe Optical Modulators with Vertical P-N Junction

The modulation characteristics of carrier-depletion strained SiGe optical modulators with a vertical *p-n* junction are numerically analyzed by technology computer-aided design (TCAD) simulation and finite-difference optical mode analysis. In addition to the strong optical confinement in the vertical direction for the fundamental transverse electric field (TE) mode, the vertical *p-n* junction effectively depletes the strained SiGe layer in which the plasma dispersion effect is enhanced owing to the mass modulation of holes by strain. We predict that an $\text{Si}_{0.7}\text{Ge}_{0.3}$ optical modulator exhibits $V_{\pi}L$ at 1.55 μm of as small as 0.31 V·cm at a bias voltage of -2 V, which is approximately 1.8 times smaller than that of a Si optical modulator. The product of $V_{\pi}L$ and the phase-shifter loss ($\alpha V_{\pi}L$) is also expected to be as low as 18.3 V·dB at -2 V, enabling optical modulation with a 5dB extinction ratio in a symmetric Mach-Zehnder modulator.

10.1 Introduction

Si based optical modulators have been intensely developed in the past ten years as one of the important building blocks for optical interconnects^[10.1]. Many types of Si-based optical modulators based on free-carrier effects^{[10.2], [10.3], [10.4], [10.5], [10.6]} and electric-field effects^{[10.7], [10.8], [10.9]} have been demonstrated so far. Among them, depletion-type Si optical Mach-Zehnder interferometer (MZI) modulators with a *p-n* junction based on the plasma dispersion effect have been mostly reported because of the

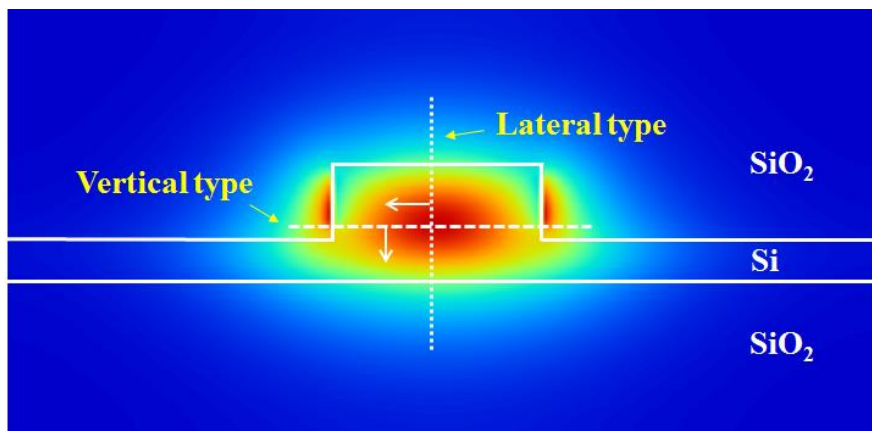
high modulation speed over a broad wavelength range. High-speed modulation of up to 50 Gbps has been demonstrated by taking advantage of the fast response of majority carriers in carrier depletion^{[10.10], [10.11]}. However, the modulation efficiency $V_{\pi}L$ of Si optical modulators with a lateral *p-n* junction is typically 1 to 4 V-cm because of the weak plasma dispersion effect in Si, where $V_{\pi}L$ is defined as the product of the driving voltage and the phase-shifter length required for a π phase shift. As a result, a long phase-shifter length or a high driving voltage is necessary in MZI modulators^{[10.12], [10.13]}. Although it is possible to reduce $V_{\pi}L$ for carrier-depletion-type Si MZI modulators by increasing the doping concentration of the *p-n* junction in the waveguide core, an increase in the insertion loss of the phase shifter is unavoidable because of the increase in the free-carrier absorption. To take into account the phase-shifter loss, the product of $V_{\pi}L$ and the phase-shifter loss ($\alpha V_{\pi}L$) has been recently suggested as a new figure of merit^[10.14]. $V_{\pi}L \times$ loss is generally higher in the case of highly doped modulators designed to have a low $V_{\pi}L$. Therefore, it is important to reduce $\alpha V_{\pi}L$ in addition to reducing $V_{\pi}L$ ^[10.15]. For this purpose, we have proposed compressively strained SiGe-based optical modulators, in which the enhancement of the plasma dispersion effect is expected by reducing the effective mass of holes in strained SiGe^[10.16]. Recently, we have experimentally demonstrated the enhanced plasma dispersion effect and free-carrier absorption in a carrier-injection strained SiGe modulator^[10.17]. Owing to the enhanced plasma dispersion effect, the reduction of $\alpha V_{\pi}L$ is expected in a carrier-depletion strained SiGe modulator as compared with that in a Si modulator.

In this chapter, we numerically analyze the modulation characteristics at 1.55 μm of carrier-depletion strained SiGe optical modulators with a vertical *p-n* junction by technology computer-aided design (TCAD) simulation and finite-difference optical mode analysis. Since the optical confinement in the vertical direction is stronger than that in the lateral direction in a conventional rib waveguide on a silicon-on-insulator (SOI) substrate, the vertical *p-n* junction modulator exhibits better modulation efficiency than a lateral *p-n* junction modulator. The vertical *p-n* junction can also effectively deplete the strained SiGe layer, making it suitable for obtaining high modulation efficiency. It is predicted that a $\text{Si}_{0.7}\text{Ge}_{0.3}$ optical modulator exhibits $V_{\pi}L$ of as small as 0.31 V-cm at -2 V bias voltage, which is approximately 1.8 times smaller

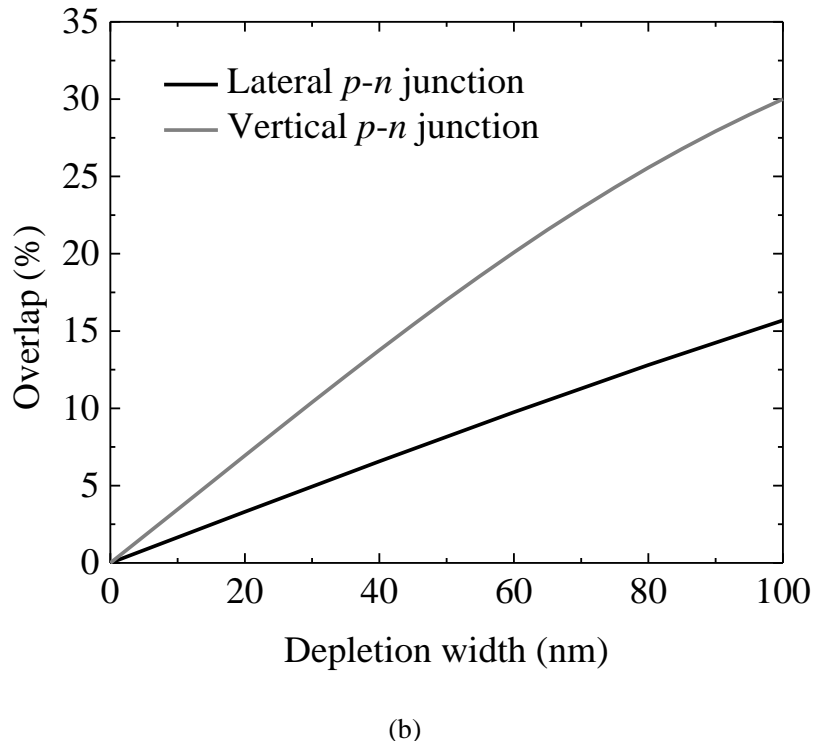
than that of Si optical modulator. Simultaneously, $\alpha V_{\pi} L$ can be maintained as low as 18.3 V-dB owing to the enhanced plasma dispersion effect in the strained SiGe layer.

10.2 Comparison of lateral and vertical pn junctions for carrier-depletion modulators

We first compare the modulation efficiencies of carrier-depletion optical modulators between lateral and vertical *p-n* junctions by calculating the overlap between a depletion layer and the fundamental transverse electric field (TE) mode of a rib waveguide on an SOI substrate as shown in Fig. 10.1(a). The fundamental TE field mode is calculated by finite-difference optical mode analysis using a rib waveguide with a 500-nm-wide and 170-nm-high mesa, assumed to be fabricated on a 220-nm-thick SOI wafer. The depletion layer is assumed to be depleted vertically or laterally from the center of the waveguide where the optical intensity is greatest. The vertical depletion modulator has an approximately two times larger overlap between the depletion layer and the optical field than the lateral depletion modulator owing to the difference between the width and height of the waveguide core as shown in Fig. 10.1(b). Since the modulation efficiency increases as the overlap increases, the carrier-depletion optical modulator with a vertical *p-n* junction is expected to show greater modulation efficiency than a modulator with a lateral *p-n* junction.



(a)



(b)

Figure 10.1 (a) Fundamental TE mode of a rib waveguide on an SOI substrate and (b) overlap between depletion layer and TE mode in lateral- and vertical-depletion optical modulators as a function of depletion width.

10.3 Carrier-depletion strained SiGe optical modulator with vertical p-n junction

In Section II, we showed that a vertical *p-n* junction is approximately two times more effective than a lateral *p-n* junction. To utilize strained SiGe in conjunction with a vertical *p-n* junction, we propose a strained SiGe optical modulator with a vertical *p-n* junction as shown in Fig. 10.2. In this section, the modulation characteristics of the vertical *p-n* junction SiGe optical modulator will be discussed.

10.3.1 Device structure

Figure 10.2 shows a schematic of the strained SiGe optical modulator with a vertical *p-n* junction. It consists of a 220-nm-thick and a 600-nm-wide waveguide rib. The slab thickness is assumed to be 50 nm in this study.

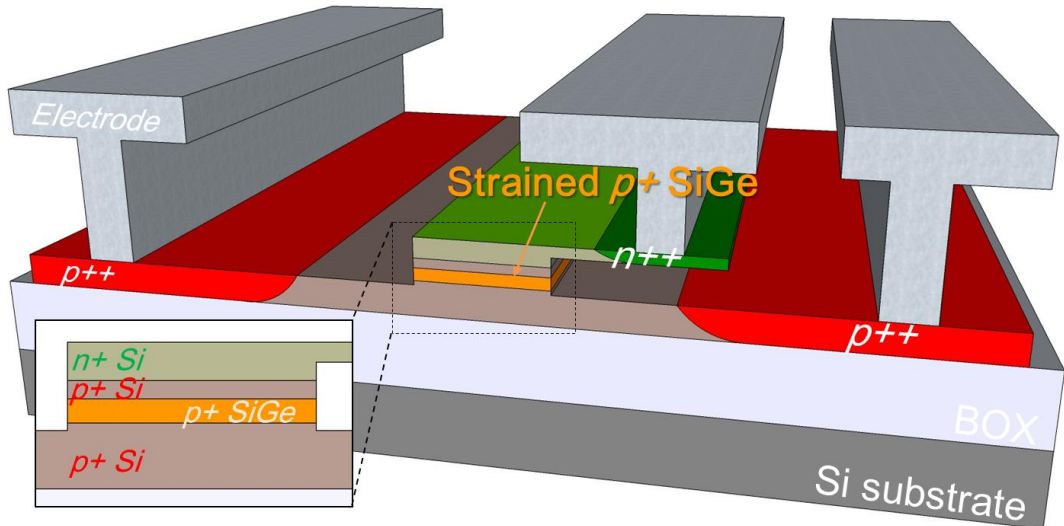


Figure 10.2 Schematic of carrier-depletion strained SiGe optical modulator with vertical $p-n$ junction.

In the waveguide core, a 40-nm-thick strained $\text{Si}_{1-x}\text{Ge}_x$ layer is embedded, which can be coherently grown on Si (001) without defect-related losses when the Ge fraction is less than 0.3^{[10.18], [10.19], [10.20]}. Even though the bandgap shrinkage by strain induces optical loss when a photon energy at an operating wavelength is close to the narrowed bandgap energy, the optical loss of SiGe with approximately 30 % Ge fraction is negligible for an optical modulator application^[10.21].

In the mesa, the thickness of the top n^+ Si layer is 60 nm and the total thickness of the p^+ Si/SiGe/Si layers is 110 nm including the 40-nm-thick SiGe. The thicknesses of p^+ Si layer will be discussed when describing the SiGe modulator.

The process of the proposed vertical type SiGe modulator is more complex than the lateral type modulator. However, strained SiGe itself has been already used in commercially available CMOS circuits. Thus, through CMOS-compatible process, the vertical layer structure in the phase shifter can be formed by buried regrowth with in-situ doping as like Ge photodetectors reported in reference^[10.22]. Although carrier-accumulation modulators exhibit higher modulation efficiency, a larger capacitance in accumulation devices results in higher power consumption and lower speed operation than carrier-depletion devices. Therefore, the carrier-depletion type SiGe modulator with vertical $p-n$ junction is more promising than a carrier-accumulation

modulator in terms of simple process, low power and high speed.

To simulate the optical characteristics of modulators, Synopsys TCAD Sentaurus to calculate the carrier concentration in conjunction with a finite-difference mode solver for optical waveguides was used. The carrier concentration was calculated as a function of the applied DC reverse-bias between the p^{++} and n^{++} contact regions. We assume ohmic contact to the p^{++} and n^{++} regions with a doping concentration of 10^{20} cm^{-3} for boron and phosphorus, respectively. The electron density at the top of the n^+ region is assumed to be $5 \times 10^{18} \text{ cm}^{-3}$, which is designed to decrease toward the boundary of the $p-n$ junction as shown in Fig. 10.3 [10.23]. The electron density in the n^+ region at the $p-n$ boundary is assumed to be the same as the hole density in the p^+ region. We assume that each p^+ region is uniformly doped. The electron density in the n^+ region is higher than the hole density in the p^+ region so that the depletion region mostly extends toward the p^+ region which includes the p^+ Si/SiGe/Si layers.

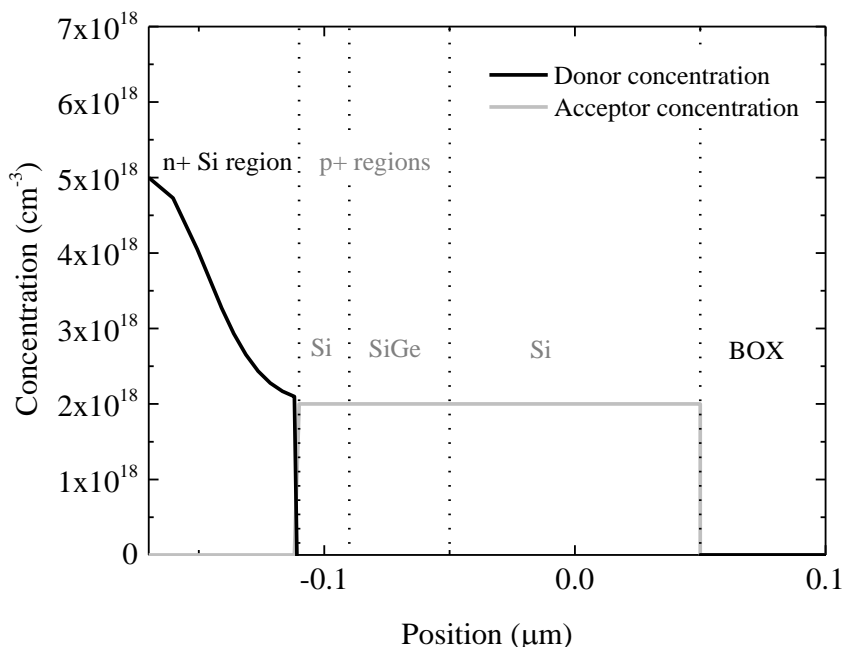


Figure 10.3 Doping profile in [001] direction at the center of the waveguide for a hole density of $2.0 \times 10^{18} \text{ cm}^{-3}$.

To evaluate the optical characteristics, the changes in the refractive index and

absorption coefficient of SiGe and Si are calculated using Soref's equations^[10,24] by taking into account the enhanced free-carrier effects in strained SiGe^{[10,16], [10,17]}. The changes in the effective refractive index and absorption coefficient in the modulators are extracted by calculating the overlap between the carrier distributions and the optical field.

10.3.2 Optimization of carrier-depletion Si optical modulator with vertical p-n junction

First, we optimized the hole density of the p+ region in the Si modulator with the vertical *p-n* junction, which has the greatest effect on the device performances. Here, we assume that the Ge fraction of the SiGe layer is 0 and all the p⁺ regions are composed of p+Si with the same doping concentration. To optimize the hole density of the p⁺ region, the modulation characteristics were investigated for hole densities ranging from 1.5×10^{17} to $3 \times 10^{18} \text{ cm}^{-3}$ in the p⁺ region, which is less than the electron density in the n⁺ region. Figure 10.4 shows the calculated change in the effective refractive index for various hole densities in the p⁺ region as a function of reverse bias voltage. As the hole density increases, the effective refractive index increases due to the large change in the carrier density caused by depletion. When the hole density is $1.5 \times 10^{17} \text{ cm}^{-3}$, saturation of the change in the effective refractive index is observed at -4 V because the depletion region reaches the bottom of the Si slab.

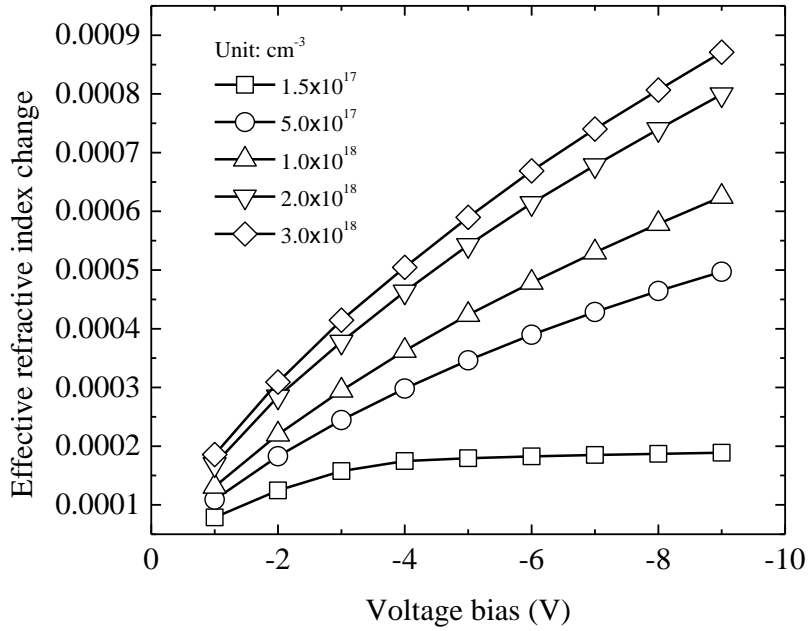


Figure 10.4 Calculated change in the effective refractive index for various hole densities in the p^+ region as a function of reverse bias voltage.

Figure 10.5 shows $V_\pi L$ as a function of reverse bias voltage. $V_\pi L$ also decreases with increasing hole density. When the hole density is larger than $1 \times 10^{18} \text{ cm}^{-3}$, $V_\pi L$ of less than 1.0 V-cm is achievable with a reverse bias voltage of larger than -3 V. On the other hand, the phase-shifter loss at 0 V also increases with increasing hole density owing to free-carrier absorption as shown in Fig. 10.6. The phase-shifter loss at 0 V is as large as -5.6 dB/mm at a hole density of $3 \times 10^{18} \text{ cm}^{-3}$. The trade-off between the modulation efficiency and the phase-shifter loss in terms of the doping concentration is an important issue to be carefully considered. Also, the change in the phase-shifter loss becomes large with increasing hole density. For MZI modulators, a change in the phase-shifter loss affects the extinction ratio of modulation. Therefore, we also analyzed the extinction ratio of a symmetric MZI modulator, as shown in Fig. 10.7, which was calculated by the transfer-matrix method^[10.25] with the assumption of the same phase-shifter loss at 0 V in both arms owing to the same doping density. The length of the phase shifter is assumed to be 1000 μm . A difference between the loss in the two arms is induced when a reverse bias voltage is applied to one arm. However, an

extinction ratio of larger than 5 dB is still expected even when the hole density is as high as $2 \times 10^{18} \text{ cm}^{-3}$ at -5 V. As discussed here, we can achieve high modulation efficiency by using a doping concentration of $2 - 3 \times 10^{18} \text{ cm}^{-3}$. However, the insertion loss increases simultaneously as shown in Fig. 10.6. Hence, the enhancement of the plasma dispersion effect itself is essential to achieve high modulation efficiency and low insertion loss simultaneously.

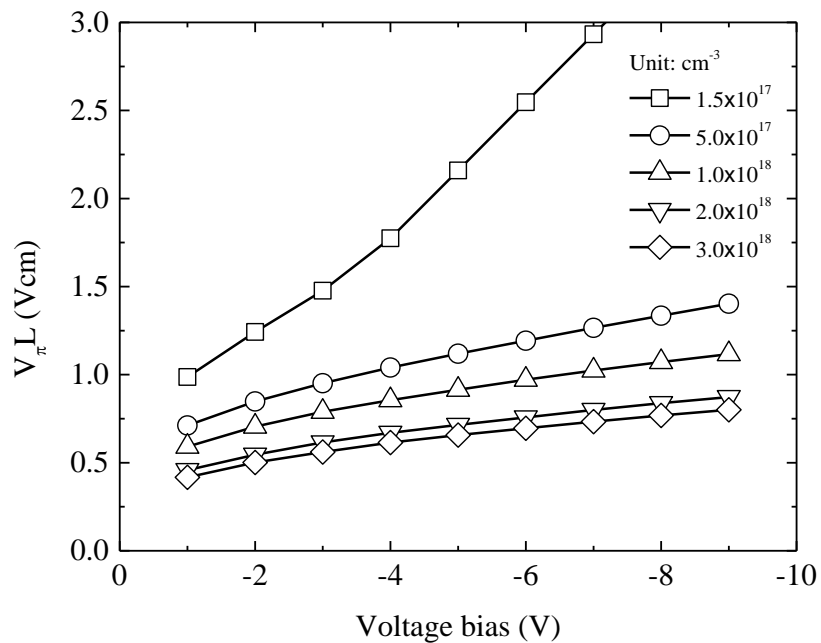


Figure 10.5 $V_{\pi}L$ as a function of reversed bias voltage.

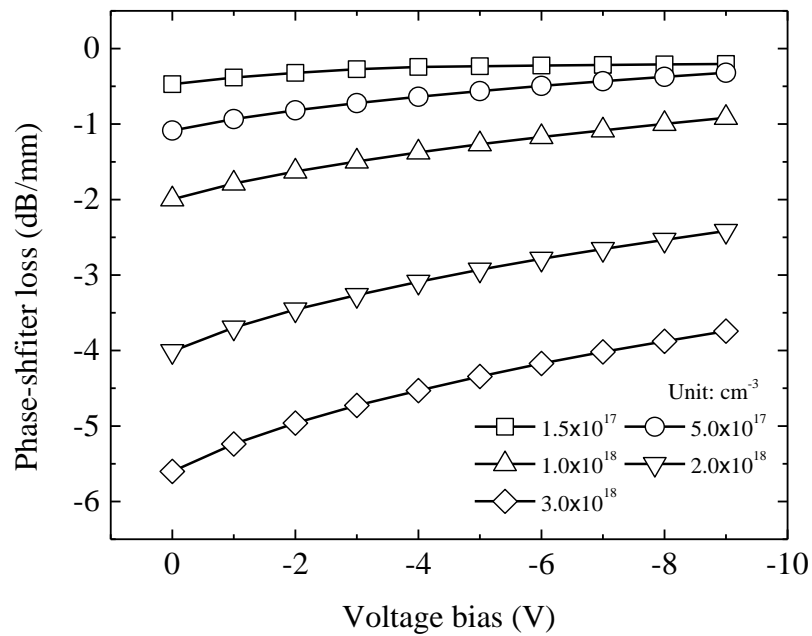


Figure 10.6 Phase-shifter loss at 0 V for various hole densities as a function of reverse bias voltage.

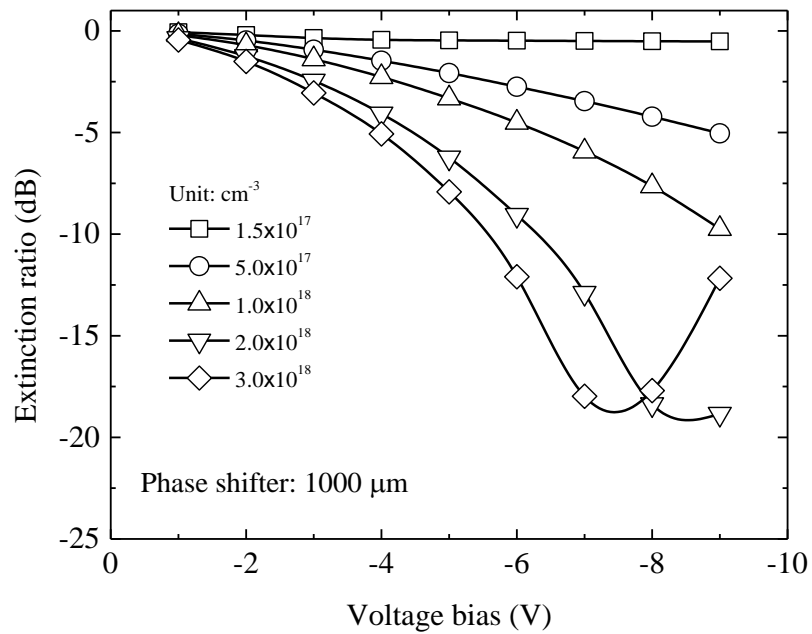


Figure 10.7 Extinction ratio of symmetric MZI modulator as a function of reverse bias voltage.

10.3.3 Carrier-depletion SiGe optical modulator with vertical p-n junction

By considering the optimized structure of the Si optical modulator, we attempt to optimize the design of the carrier-depletion SiGe optical modulator with the vertical *p-n* junction. For the SiGe optical modulator, it is expected that the loss in the modulator will increase further as a result of the enhanced free-carrier absorption. Therefore, in the following analyses, a hole density of $2 \times 10^{18} \text{ cm}^{-3}$ is adopted to achieve a $V_\pi L \times \text{loss}$ value of approximately 18 V-dB, which is comparable to that for a low-doped Si modulator^[10,14] as discussed later.

The proposed SiGe optical modulator has the Si/SiGe heterostructures in the waveguide core. The bandgap of strained SiGe is smaller than that of Si, resulting in the large band offset in the valence band. Therefore, the band alignment should be carefully considered since it affects carrier distribution and modulation efficiency. Figure 8 shows band structure and carrier distribution in [001] direction at the center of waveguide. The *p-n* junction is formed between *n*-Si and *p*-Si, showing the large band bending and the low carrier concentrations due to depletion as shown in Fig. 10.8 (a) and (b), respectively. It is worthy to note that holes are confined in the edges of SiGe because of the band offset in the valence band between SiGe and Si. It indicates that the modulation efficiency is expected to be further enhanced by confining more holes in the strained SiGe layer where the plasma dispersion is greater than Si layers.

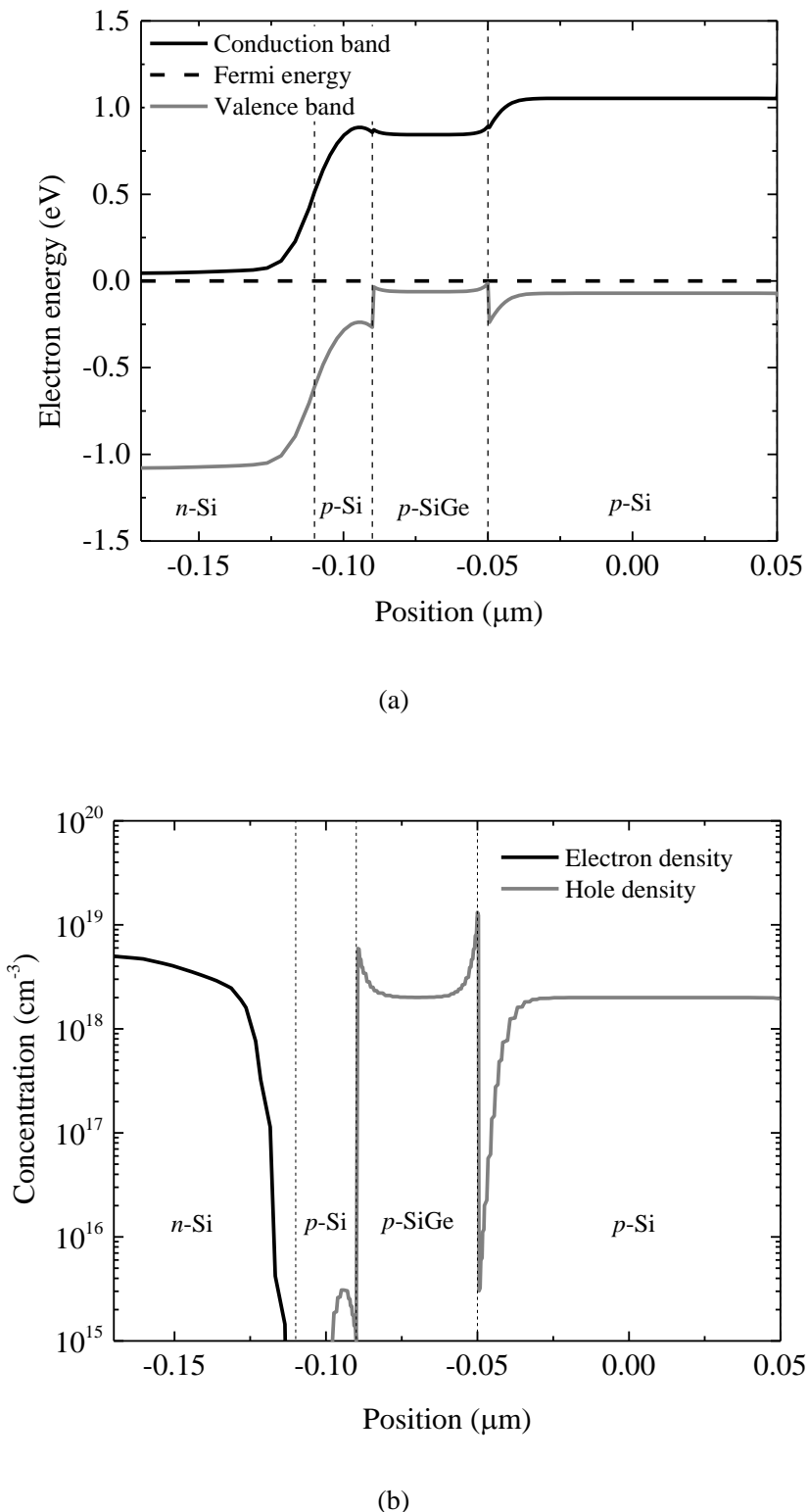


Figure 10.8 (a) Band structure and (b) carrier distribution in [001] direction at the center of the waveguide with a hole doping density of $2.0 \times 10^{18} \text{ cm}^{-3}$.

First we optimize the thickness of the p⁺ Si layer between the n⁺ Si and p⁺ SiGe layers. Even with no bias voltage, there is an initial depletion region at the junction. Thus, an appropriate thickness of the p⁺ Si layer above the p⁺ SiGe layer is important to ensure that depletion starts from the p⁺ SiGe layer when a reverse bias voltage is applied. Figure 10.9 shows the change in the effective refractive index of the Si_{0.7}Ge_{0.3} optical modulator for various p⁺ Si thicknesses as a function of reverse bias voltage. When the reverse bias voltage increases, the change in the effective refractive index increases due to the extension of the depletion layer. As shown in Fig. 10.9, the largest change in the effective refractive index is obtained when the thickness of the p⁺ Si layer ranges from 10 to 20 nm. There is no significant difference in the changes in the effective refractive index between 10-nm-thick and 20-nm-thick p⁺ Si structures when the bias voltage is below - 5 V. However, the change in the effective refractive index slightly degrades below a bias voltage of - 6 V in the 10-nm-thick p⁺ Si device because of the full depletion of the SiGe layer. Therefore, a 20-nm-thick p+ Si layer is chosen for the SiGe optical modulator.

Figure 10.10 shows the dependence of the effective refractive index on the Ge fraction of the SiGe optical modulator. As the Ge fraction increases, the change in the effective refractive index increases thanks to the enhancement of the plasma dispersion effect in strained SiGe.

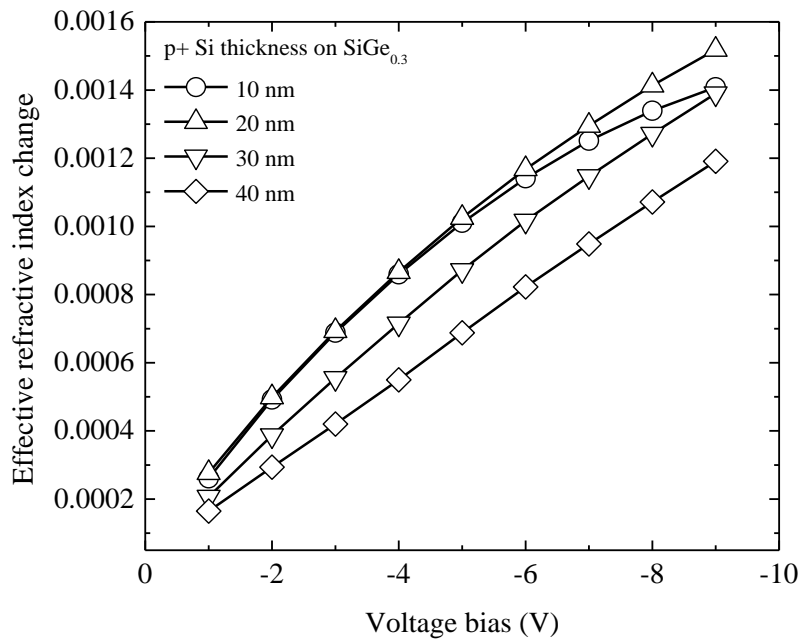


Figure 10.9 Calculated change in effective refractive index of strained SiGe optical modulator for various p^+ Si thicknesses as a function of reverse bias voltage.

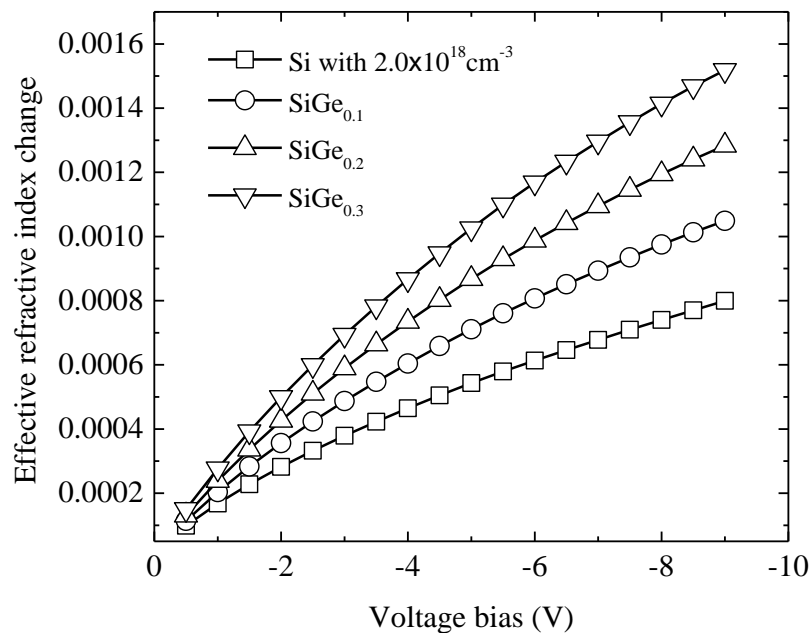


Figure 10.10 Calculated change in effective refractive index of strained SiGe optical modulator for various Ge fractions in SiGe alloy as a function of reverse bias voltage.

Figure 10.11 shows $V_{\pi}L$ for the SiGe optical modulator with various Ge fractions as a function of reverse bias voltage. $V_{\pi}L$ decreases with increasing Ge fraction due to the enhanced plasma dispersion effect. $V_{\pi}L$ is as low as 0.31 V-cm at -2 V when the Ge fraction is 0.3, which is approximately 1.8 times smaller than that of the Si modulator, as shown in Fig. 10.12.

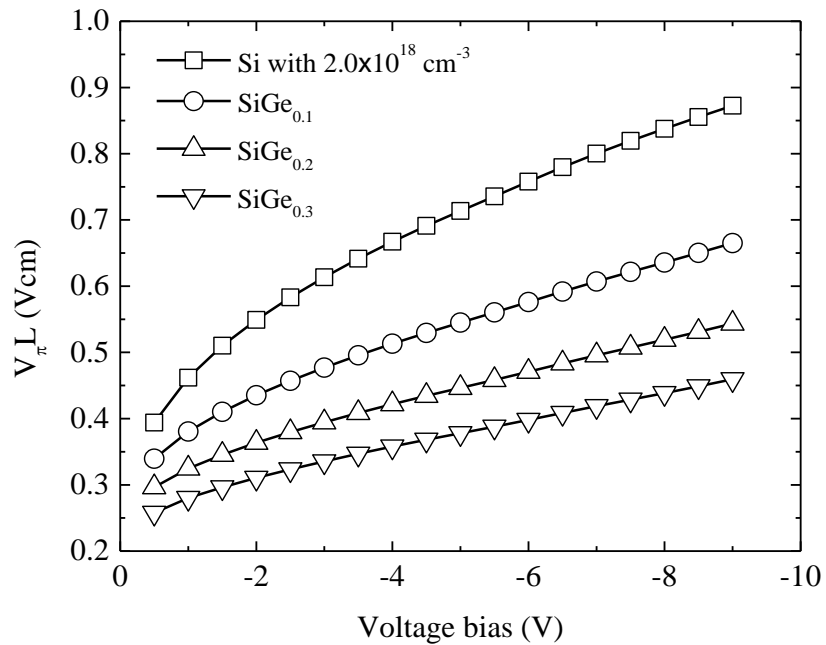


Figure 10.11 $V_{\pi}L$ for strained SiGe optical modulator with different Ge fractions in SiGe alloy as a function of reverse bias voltage.

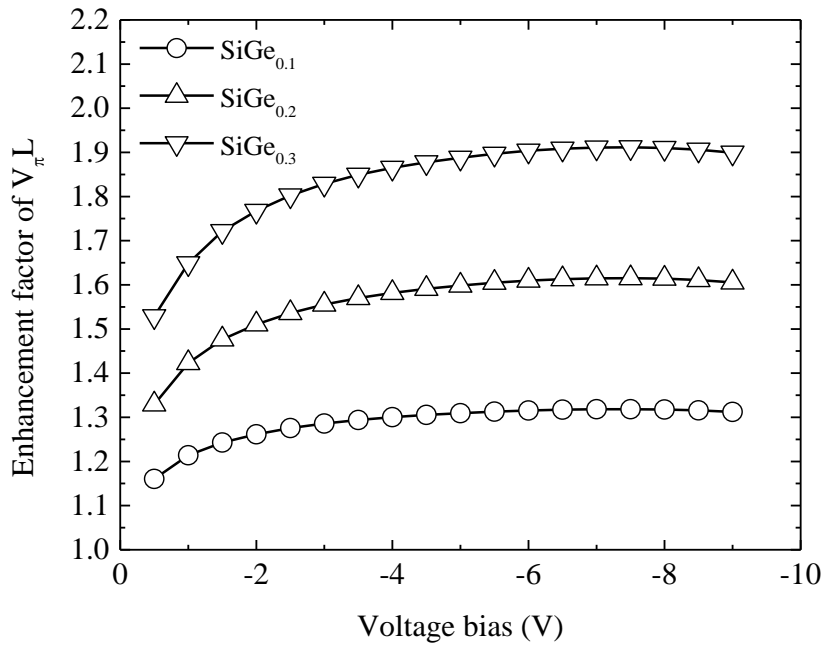


Figure 10.12 Enhancement factor of $V_{\pi}L$ for strained SiGe optical modulator with various Ge fractions in SiGe alloy as a function of reverse bias voltage.

In addition to the enhancement of the modulation efficiency, the insertion loss per unit length simultaneously increases with increasing Ge fraction as a result of the enhanced free-carrier absorption. Figure 10.13 shows the Ge fraction dependence of the insertion loss of the 1-mm-long phase shifter. The insertion loss of the phase shifter increases by approximately 2 dB/mm as the Ge fraction increases from 0 to 0.3, which is not significant because the modulation efficiency also increases, enabling a shorter phase shifter. To clarify the improvement of the carrier-depletion optical modulator for strained SiGe, we show the enhancement factor for the change in effective refractive index divided by insertion loss at 0 V for each Ge fractions of SiGe in Fig. 10.14, taking into account the both enhanced plasma dispersion effect and free-carrier absorption in strained SiGe. It is shown that the enhancement is still expected even considering the increased loss by strained SiGe, indicating strained SiGe is effective in terms of the modulation efficiency and the insertion loss.

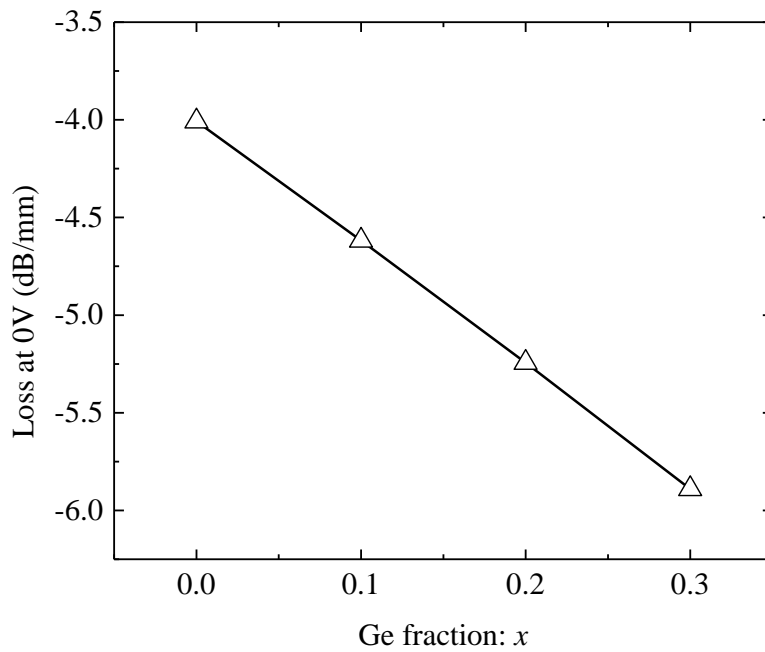


Figure 10.13 Phase-shifter loss of strained SiGe optical modulator at 0 V as a function of Ge fraction in SiGe alloy.

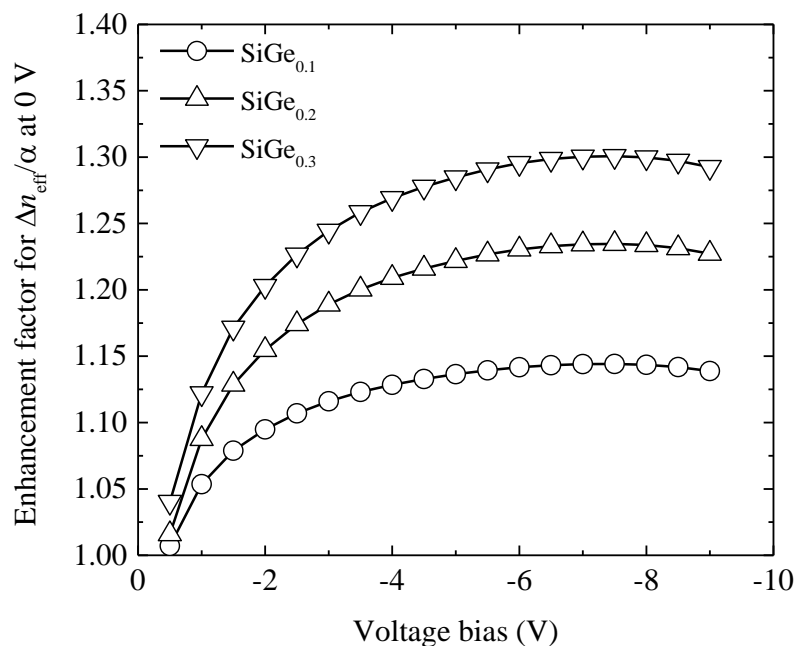


Figure 10.14 Enhancement factor for change in effective refractive index divided by insertion loss at 0 V.

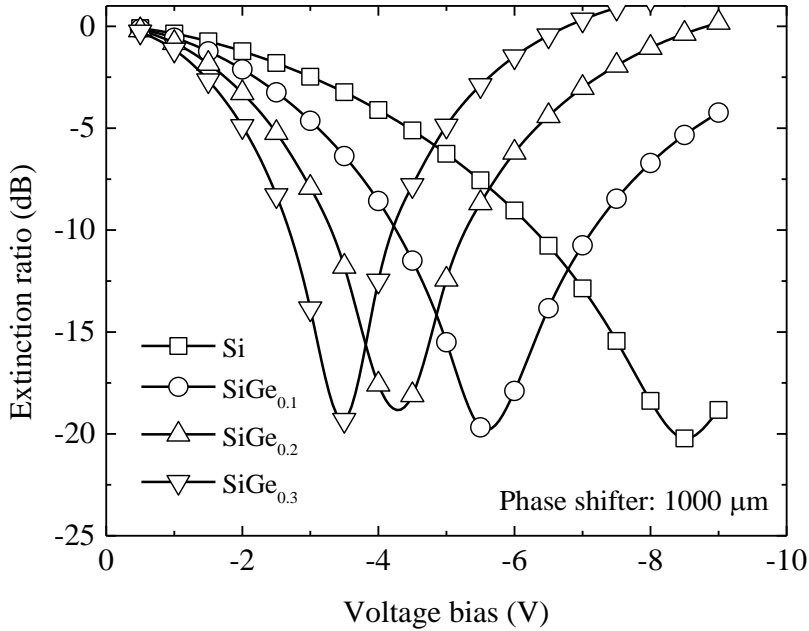


Figure 10.15 Extinction ratio of vertical *p-n* junction carrier-depletion strained SiGe optical modulator with different Ge fractions in SiGe alloy as a function of reverse bias voltage.

In conjunction with the changes in the effective refractive index changes in Fig. 10.9, we calculate the transfer characteristics of symmetric SiGe MZI modulators by the transfer-matrix method as shown in Fig. 10.15. Modulation with an extinction ratio larger than -5 dB can be obtained in a symmetric $\text{Si}_{0.7}\text{Ge}_{0.3}$ MZI modulator with a 1-mm-long phase shifter when the reverse bias voltage is -2 V.

Figure 10.16 shows the reverse bias voltage required for a 5dB extinction ratio of the SiGe modulator as a function of the Ge fraction when the phase shifter length is 1000 μm . Using $\text{Si}_{0.7}\text{Ge}_{0.3}$, the driving voltage required for a 5dB extinction ratio can be reduced to less than half of that for a Si modulator. To discuss the device performance taking the loss of the phase shifter into account, $V_{\pi}L$ at -2 V as a function of the phase-shifter loss is shown in Fig. 10.17. In general, $V_{\pi}L$ can be reduced by increasing a hole density. However, the value of $V_{\pi}L \times$ loss increases since the increase in the phase-shifter loss is greater than the decrease in $V_{\pi}L$. Although the highly doped Si modulator in ^[10.26] can exhibit a low $V_{\pi}L$, the value of $V_{\pi}L \times$ loss is increased to approximately 25.4 V-dB higher than that for the lightly doped Si modulator in ^[10.14].

Because the Si modulator with a vertical *p-n* junction exhibits a high modulation efficiency; the value of $V_{\pi}L \times \text{loss}$ is under the 25.4 V-dB line in Fig. 10.17 for the strained SiGe modulator, it is worth noting that the value of $V_{\pi}L \times \text{loss}$ is even lower further owing to the enhanced plasma dispersion effect in strained SiGe. Thus, we can achieve a low $V_{\pi}L$ with maintaining $V_{\pi}L \times \text{loss}$ at a value comparable to that of a lightly doped Si modulator when the Ge fraction is 0.3.

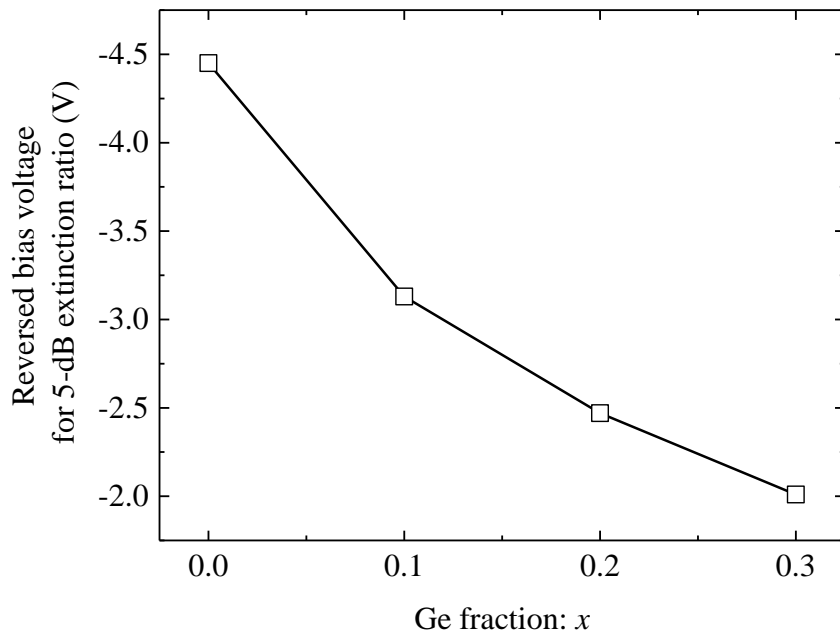


Figure 10.16 Reverse bias voltage required for 5dB extinction ratio as a function of Ge fraction in SiGe alloy.

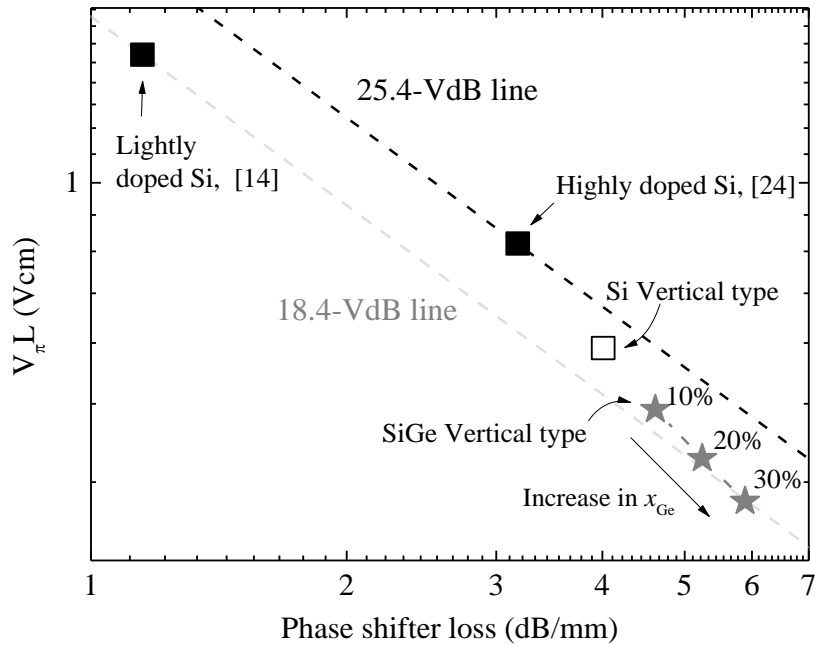


Figure 10.17 $V_{\pi}L$ as a function of phase-shifter loss in Si and SiGe modulators.

In terms of modulation speed, SiGe is expected to be effective for faster RF response due to the short minority lifetime in SiGe in the case of the carrier-injection modulator^[10,27]. However, it is not expected for the carrier-depletion modulator based on majority carriers. We expect that the crystal quality of SiGe is high enough for depletion modulators because the SiGe thickness considered in this paper is less than its critical thickness. Although the dielectric constant of the $\text{Si}_{0.7}\text{Ge}_{0.3}$ is slightly higher than Si, the increase in the depletion capacitance is negligible for the modulation speed. Thus, we expect that the introduction of SiGe has no negative impact of the modulation speed in terms of the material quality of SiGe. When the $V_{\pi}L$ of the SiGe modulator is designed to the same as the Si modulator, we can reduce the depletion capacitance of the SiGe modulator because of the enhanced plasma dispersion effect in SiGe. This means that the SiGe modulator can operate at higher modulation speed than Si modulators.

10.4 Conclusion

We have numerically analyzed a carrier-depletion strained SiGe modulator with a vertical *p-n* junction. We have found that a vertical *p-n* junction shows approximately two times higher modulation efficiency than a lateral *p-n* junction, which is suitable for utilizing strained SiGe. By optimizing the doping concentration of the *p-n* junction, it was predicted that a strained Si_{0.7}Ge_{0.3} optical modulator exhibits a modulation efficiency, $V_{\pi}L$ at 1.55 μm, of 0.31 V·cm at -2 V, which is approximately 1.8 times smaller than that of a Si optical modulator owing to the enhanced plasma dispersion effect in strained SiGe. Despite the high doping concentration of the *p-n* junction to obtain a low value of $V_{\pi}L$ design, the low $V_{\pi}L \times$ loss of 18.3 VdB, which is comparable to that for a lightly doped Si modulator, can be simultaneously obtained. Hence, the strained SiGe modulator based on carrier depletion can fundamentally improve the performance of Si-based optical modulators in terms of modulation efficiency and insertion loss.

References

- [10.1] D. G. T. Reed, G. Mashanovich, F. Y. Gardes, and D. J. Thomson, "Silicon optical modulators," *Nature Photonics*, vol. 4, pp. 518–526, Jul., 2010.
- [10.2] Q. F. Xu, B. Schmidt, S. Pradhan, and M. Lipson, "Micrometre-scale silicon electro-optic modulator," *Nature*, vol. 435, pp. 325–327, May, 2005.
- [10.3] L. Liao, A. Liu, D. Rubin, J. Basak, Y. Chetrit, H. Nguyen, *et al.*, "40 Gbit/s silicon optical modulator for high-speed applications," *Electronics Letters*, vol. 43, no. 22, pp. 1196–1197, Oct., 2007.
- [10.4] A. S. Liu, L. Liao, D. Rubin, H. Nguyen, B. Ciftcioglu, Y. Chetrit, *et al.*, "High-speed optical modulation based on carrier depletion in a silicon waveguide," *Optics Express*, vol. 15, pp. 660–668, Jan., 2007.
- [10.5] A. S. Liu, R. Jones, L. Liao, D. Samara-Rubio, D. Rubin, O. Cohen, *et al.*, "A high-speed silicon optical modulator based on a metal-oxide-semiconductor capacitor," *Nature*, vol. 427, pp. 615–618, Feb., 2004.
- [10.6] F. Y. Gardes, D. J. Thomson, N. G. Emerson, and G. T. Reed, "40 Gb/s silicon photonics modulator for TE and TM polarisations," *Optics Express*, vol. 19, pp. 11804–11814, Jun., 2011.
- [10.7] Y. H. Kuo, Y. K. Lee, Y. S. Ge, S. Ren, J. E. Roth, T. I. Kamins, *et al.*, "Strong quantum-confined Stark effect in germanium quantum-well structures on silicon," *Nature*, vol. 437, pp. 1334–1336, Oct., 2005.
- [10.8] J. Liu, M. Beals, A. Pomerene, S. Bernardis, R. Sun, J. Cheng, *et al.*, "Waveguide-integrated, ultralow-energy GeSi electro-absorption modulators," *Nature Photonics*, vol. 2, pp. 433–437, Jul., 2008.
- [10.9] R. S. Jacobsen, K. N. Andersen, P. I. Borel, J. Fage-Pedersen, L. H. Frandsen, O. Hansen, *et al.*, "Strained silicon as a new electro-optic material," *Nature*, vol. 441, pp. 199–202, May, 2006.
- [10.10] D. J. Thomson, F. Y. Gardes, J. M. Fedeli, S. Zlatanovic, Y. F. Hu, B. P. P. Kuo, *et al.*, "50-Gb/s silicon optical modulator," *IEEE Photonics Technology Letters*, vol. 24, Feb., 2012.

- [10.11] X. G. Tu, T. Y. Liow, J. F. Song, X. S. Luo, Q. Fang, M. B. Yu, *et al.*, "50-Gb/s silicon optical modulator with traveling-wave electrodes," *Optics Express*, vol. 21, pp. 12776–12782, May, 2013.
- [10.12] J. F. Ding, R. Q. Ji, L. Zhang, and L. Yang, "Electro-optical response analysis of a 40 Gb/s silicon Mach-Zehnder optical modulator," *Journal of Lightwave Technology*, vol. 31, pp. 2434–2440, Jul., 2013.
- [10.13] T. Baehr-Jones, R. Ding, Y. Liu, A. Ayazi, T. Pinguet, N. C. Harris, *et al.*, "Ultralow drive voltage silicon traveling-wave modulator," *Optics Express*, vol. 20, pp. 12014–12020, May, 2012.
- [10.14] D. M. Gill, W. M. J. Green, S. Assefa, J. C. Rosenberg, T. Barwicz, S. M. Shank, H. Pan, and Y. A. Vlasov, "A figure of merit based transmitter link penalty calculation for CMOS-compatible plasma-dispersion electro-optic Mach-Zehnder modulators," <http://arxiv.org/abs/1211.2419>, 2012
- [10.15] I. Goykhman, B. Desiatov, S. Ben-Ezra, J. Shappir, and U. Levy, "Optimization of efficiency-loss figure of merit in carrier-depletion silicon Mach-Zehnder optical modulator," *Optics Express*, vol. 21, pp. 19518–19529, Aug., 2013.
- [10.16] M. Takenaka and S. Takagi, "Strain engineering of plasma dispersion effect for SiGe optical modulators," *IEEE Journal of Quantum Electronics*, vol. 48, pp. 8–16, Jan., 2012.
- [10.17] Y. Kim, M. Takenaka, T. Osada, M. Hata, and S. Takagi, "Strain-induced enhancement of plasma dispersion effect and free-carrier absorption in SiGe optical modulators," *Scientific Reports*, vol. 4, p. 4683, 2014.
- [10.18] R. People and J. C. Bean, "Calculation of critical layer thickness versus lattice mismatch for $\text{Ge}_x\text{Si}_{1-x}/\text{Si}$ strained-layer heterostructures," *Applied Physics Letters*, vol. 47, pp. 322–324, 1985.
- [10.19] R. People and J. C. Bean, "Erratum: Calculation of critical layer thickness versus lattice mismatch for $\text{Ge}_x\text{Si}_{1-x}/\text{Si}$ strained-layer heterostructures [Appl. Phys. Lett. 47, 322 (1985)]," *Applied Physics Letters*, vol. 49, p. 229, 1986.
- [10.20] P. Majhi, P. Kalra, R. Harris, K. J. Choi, D. Heh, J. Oh, *et al.*, "Demonstration of high-performance PMOSFETs using Si-Si_xGe_{1-x}-Si quantum wells with

- high- κ /metal-gate stacks," *IEEE Electron Device Letters*, vol. 29, pp. 99–101, Jan., 2008.
- [10.21] Y. Kim, M. Takenaka, T. Osada, M. Hata, and S. Takagi, "Fabrication and evaluation of propagation loss of Si/SiGe/Si photonic-wire waveguides for Si based optical modulator," *Thin Solid Films*, vol. 557, pp. 342-345, Apr 30 2014
- [10.22] M. Miura, J. Fujikata, M. Noguchi, and Y. Arakawa, "Ultra-Small Butt-Joint Ge Photodetector Featuring Self-Aligned In-situ Doping and CMP-Free Novel CVD Process," in *Proc. Collocated Nat. Fiber Opt. Eng. Conf. Opt. Fiber Commu.*, San Francisco, CA, 2014.
- [10.23] A. S. Liu, L. Liao, D. Rubin, H. Nguyen, B. Ciftcioglu, Y. Chetrit, N. Izhaky, and M. Paniccia, "High-speed optical modulation based on carrier depletion in a silicon waveguide," *Optics Express*, **15**, 660–668 (2007).
- [10.24] R. A. Soref and B. R. Bennett, "Electrooptical effects in silicon," *IEEE Journal of Quantum Electronics*, vol. 23, pp. 123–129, Jan., 1987.
- [10.25] J. Van Campenhout, W. M. J. Green, and Y. A. Vlasov, "Design of a digital, ultra-broadband electro-optic switch for reconfigurable optical networks-on-chip," *Optics Express*, vol. 17, pp. 23793–23808, Dec., 2009.
- [10.26] J. C. Rosenberg, W. M. J. Green, S. Assefa, D. M. Gill, T. Barwicz, M. Yang, *et al.*, "A 25 Gbps silicon microring modulator based on an interleaved junction," *Optics Express*, vol. 20, pp. 26411–26423, Nov., 2012.
- [10.27] Y. Kim, J. Fujikata, S. Takahashi, M. Takenaka, and S. Takagi, "Record-low injection-current strained SiGe variable optical attenuator with optimized lateral PIN junction," Proceeding of European Conference on Optical Communications, P.2.6, Cannes, 2014.

Chapter 11

Conclusion

The most important thing in this thesis is that we have successfully demonstrated strain-induced enhancement free-carrier effects in SiGe and optical modulators and variable optical attenuators using strained SiGe with the enhancement. In this chapter, we conclude each chapter and we discuss the future works and prospect with regard to strained SiGe technology for optical modulators.

11.1 Conclusion

In this thesis we have focused on the experimental demonstration of strain-induced enhancement of the plasma dispersion effect and free-carrier absorption in SiGe in near infrared wavelengths. The demonstration of strain-induced enhancement has been achieved with the physical understanding of mass-modulation^[11.1]. Furthermore, we have been demonstrated the record-low carrier-injection SiGe VOA^[11.2] and SiGe MZ optical modulators^[11.3], which show the improved device performance comparing to Si devices. The theory, numerical analysis, passive device, and surface passivation technology as well as the improved device performance with regard to strained SiGe technology are studied in this thesis. In particular, we have shown that the strained SiGe engineering for optical modulator application is highly promising for improving modulation efficiency, which enables low power consumption less than 100 fJ/bit. In this part, we conclude the each chapter.

In chapter 1, the necessity of Si photonics technology has been introduced. Then, state-of-the-art Si-based optical modulators have been reviewed. It has been clearly discussed why the strain-induced enhancement of the plasma dispersion effect and free-carrier absorption is indispensable for Si-based optical modulators.

In chapter 2, the physical properties of SiGe were briefly introduced. In

particular, the strain-induced mass modulation was analyzed for the theory of strain-induced enhancement of free-carrier effects in SiGe. We estimated the enhancement of the plasma dispersion effect and free-carrier effect based on Drude model. The enhancement factors of changes in refractive index (Δn) and absorption coefficient ($\Delta \alpha$) increase with an increase in Ge fraction. The average enhancement factors for carrier-injection type of Δn and $\Delta \alpha$ still increase with increasing Ge fraction and are expected to be approximately 1.6 for Δn and 2.1 for $\Delta \alpha$ in $\text{Si}_{0.7}\text{Ge}_{0.3}$.

In chapter 3, the numerical analysis on SiGe-based modulator/attenuator comparing with the Si modulator has been carried out for obtaining the high modulation efficiency. By taking into account the enhancement in the plasma dispersion effect and free-carrier absorption in the SiGe layer, the modulation characteristics of SiGe-based optical modulators and variable optical attenuator were analyzed. The current-injection $\text{Si}_{0.7}\text{Ge}_{0.3}$ -based VOA exhibits the current density of approximately 15 mA/mm for 20 dB-attenuation, which is 3 times as small as that of the Si-based optical modulator. Also, the injection current for π -shift is expected to be reduced by 1/3 using strained $\text{Si}_{0.7}\text{Ge}_{0.3}$.

In chapter 4, we have fabricated the Si/SiGe/Si waveguide on an SOI substrate by using MBE. The wavelength and waveguide's width dependences of the propagation loss of the Si/SiGe/Si rib waveguides reveal that the additional propagation loss related to the narrow bandgap in the fully strained $\text{Si}_{0.72}\text{Ge}_{0.28}$ layer is approximately 0.54 dB/mm at 1.55- μm wavelength, which is negligible for optical modulator applications.

In chapter 5, we have demonstrated that the strain-induced enhancement of the plasma dispersion effect and free-carrier absorption in biaxial compressive strained SiGe is effective for boosting the modulation efficiency of Si-based optical modulators. The optical attenuation of the SiGe-based in-line intensity optical modulator is more than twice as large as that of the Si modulator. This is the first demonstration of enhanced free-carrier absorption in SiGe through strain-induced mass modulation for the telecommunication wavelength range from 1.3 to 1.6 μm .

In chapter 6, we have investigated the low-temperature surface passivation, which is especially necessary for carrier-injection SiGe optical modulators due to the restriction of thermal budge, for suppressing surface recombination. We found that

Al_2O_3 passivation formed by ALD at 200 °C is effective to decrease interface traps on the etched Si surfaces at low temperature as compared with PECVD SiO_2 passivation. The interface trap density of the Al_2O_3 -passivated etched Si surface is less than $2 \times 10^{11} \text{ cm}^{-2}\text{eV}^2$, which is one order magnitude lower than that of the PECVD SiO_2 -passivated surface. The modulation efficiency has been also improved by introducing the Al_2O_3 passivation layer prior to SiO_2 deposition. The injection current density for 20-dB attenuation has been improved by approximately 40%, which is comparable to the thermally grown SiO_2 -passivated device. Thus, ALD Al_2O_3 is promising for passivating the strained SiGe optical modulator at low temperature.

In chapter 7, we have demonstrated record-low injection-current strained SiGe VOAs by optimizing the distance between the p+ and n+ regions in the lateral *pin* junction. The injection current for 20-dB attenuation of the SiGe VOA is as low as 20 mA/mm thanks to the optimization and strain-induced enhancement. We have also found 1.5 times improvement in the RF response of the SiGe VOA comparing to the Si VOA, and 2-GHz switching was achieved. Error-free transmission of $4 \times 12.5 \text{ Gb/s}$ WDM signal was also demonstrated.

In chapter 8, we have successfully demonstrated the strained SiGe-based MZ optical modulator. The enhanced plasma dispersion in strained SiGe is experimentally observed for the first time. Thus, the injection current required for π phase shift is reduced to 1.47 mA from 1.87 mA as compared with the Si modulator. It is also expected that the modulation efficiency can be further improved by using higher strain and Ge fraction, enabling the operation at the injection current less than 1 mA. The 10 Gbps of clear eye pattern has also been successfully obtained by the pre-emphasis method. Therefore, strained SiGe is a highly promising material as a technology booster for Si-based optical modulators.

In chapter 9, we have proposed a novel method to achieve high Ge fraction SiGe optical modulator taking into account Ge diffusion. The thickness dependence of $\text{Si}_{0.7}\text{Ge}_{0.3}$ optical modulator has been estimated. Sub-mA for π -shift can be achieved even 20-nm-thick $\text{Si}_{0.7}\text{Ge}_{0.3}$ with 2-times enhancement factor. Higher Ge fraction SiGe wafers are prepared for high Ge fraction SiGe optical modulator. 20- and 15-nm-thick $\text{Si}_{0.4}\text{Ge}_{0.6}$ show cracks, indicating strain relaxation. 10-nm-thick $\text{Si}_{0.4}\text{Ge}_{0.6}$ is promising

for 20-nm-thick $\text{Si}_{0.7}\text{Ge}_{0.3}$ optical modulator.

In chapter 10, we have numerically analyzed a carrier-depletion strained SiGe modulator with a vertical *p-n* junction. By optimizing the doping concentration of the *p-n* junction, it was predicted that a strained $\text{Si}_{0.7}\text{Ge}_{0.3}$ optical modulator exhibits a modulation efficiency, $V_{\pi}L$, of 0.31 V-cm at -2 V, which is approximately 1.8 times smaller than that of a Si optical modulator owing to the enhanced plasma dispersion effect in strained SiGe. Despite the high doping concentration of the *p-n* junction to obtain a the low value of $V_{\pi}L$ design, the low $V_{\pi}L \times$ loss of 18.3 VdB, which is comparable to that for a lightly doped Si modulator, can be simultaneously obtained. Hence, the strained SiGe modulator based on carrier depletion can fundamentally improve the performance of Si-based optical modulators in terms of modulation efficiency and insertion loss.

In conclusion, we have shown not only the experimental demonstration of strain-induced enhancement of the plasma dispersion effect and free-carrier absorption but also the demonstrations of optical modulators and variable optical attenuators taking advantage of strained SiGe technology.

11.2 Future work and prospect

For the carrier-injection type SiGe modulator, we expect that the introduction of greater strain by increasing the Ge fraction in SiGe will enable the further enhancement of the plasma dispersion effect and free-carrier absorption. Additionally, the Si/SiGe multi-wells in a waveguide core can be used to increase optical confinement factor of SiGe layers without any strain relaxation. Furthermore, if Si layers are thin enough to show quantum effect, the carriers are more confined in SiGe layers which enhance the plasma dispersion in strained SiGe, so boost the modulation efficiency.

Although the modulation speed based on carrier-injection is relatively slower than those based on carrier-depletion and carrier-accumulation due to the slow minority carrier response time, we can expect a modulation speed above 10 Gbps by the pre-emphasis method [11.5], [11.6] for the strained SiGe optical modulator in a similar manner to the Si optical modulators. Even the high-speed operation of 50 Gbps of the Si optical modulator has been already demonstrated using a lateral pin junction with

forward bias^[11.7].

Furthermore, it is worth noting that the strain-induced enhancement of the free-carrier effects by strained SiGe is also applicable for accumulation^[11.8] or depletion^[11.9] type modulators to achieve further high speed modulation without pre-emphasis method.

Finally, the CMOS compatibility of SiGe technology is very important to introduce it into Si photonics technology. On the other hand, Ge for photodetectors has been introduced even in the some foundry services for Si photonic chips. SiGe is not yet for it. However, since SiGe has already been introduced into CMOS production by Intel^[11.4], the SiGe-based optical modulator presented here is highly CMOS-compatible. Thus, strained SiGe technology is easily applicable to most Si optical modulators based on the plasma dispersion effect and free-carrier absorption. Hence, the strain-induced enhancement of the plasma dispersion effect and free-carrier absorption is one of the most promising technologies for boosting the performance of Si-based optical modulators.

References

- [11.1] Y. Kim, M. Takenaka, T. Osada, M. Hata, and S. Takagi, "Strain-induced enhancement of plasma dispersion effect and free-carrier absorption in SiGe optical modulators," *Sci Rep*, vol. 4, p. 4683, 2014.
- [11.2] Y. Kim, J. Fujikata, S. Takahashi, M. Takenaka, and S. Takagi, "Record-low injection-current strained SiGe variable optical attenuator with optimized lateral PIN junction," Proceeding of European Conference on Optical Communications, P.2.6, Cannes, 2014.
- [11.3] Y. Kim, J. Fujikata, S. Takahashi, M. Takenaka, and S. Takagi. "SiGe-based carrier-injection Mach-Zehnder modulator with enhanced plasma dispersion effect in strained SiGe," Proceeding of Optical Fiber Communication Conference, Tu2A.7, San Francisco, 2015, Los Angeles.
- [11.4] T. Ghani *et al.* "A 90nm high volume manufacturing logic technology featuring novel 45nm gate length strained silicon CMOS transistors," *Tech. Dig. Int. Electron Devices Meet.*, (Washington, D.C., 2003).
- [11.5] Q. F. Xu, S. Manipatruni, B. Schmidt, J. Shakya, and M. Lipson, "12.5 Gbit/s carrier-injection-based silicon micro-ring silicon modulators," *Optics Express*, vol. 15, pp. 430-436, Jan 22 2007.
- [11.6] S. Akiyama, T. Baba, M. Imai, T. Akagawa, M. Takahashi, N. Hirayama, *et al.*, "12.5-Gb/s operation with 0.29-V.cm V pi L using silicon Mach-Zehnder modulator based-on forward-biased pin diode," *Optics Express*, vol. 20, pp. 2911-2923, Jan 30 2012.
- [11.7] S. Akiyama, T. Baba, T. Akagawa, M. Noguchi, E. Saito, Y. Noguchi, N. Hirayama, T. Horikawa, T. Usuki "50-Gb/s Silicon Modulator Using 250- μ m-Long Phase Shifter Based-on Forward-Biased Pin Diodes" Group IV Photonics (GFP), 2012 IEEE 9th International Conference on, ThC2.
- [11.8] M. Takenaka and S. Takagi, "Strain Engineering of Plasma Dispersion Effect for SiGe Optical Modulators," *IEEE Journal of Quantum Electronics*, vol. 48, pp. 8-16, Jan 2012.

- [11.9] Y. Kim, M. Takenaka and S. Takagi, "Simulation of carrier-depletion strained SiGe optical modulators with vertical p-n junction," Proceeding of Group IV Photonics, ThP.5, Paris, 2014.

First Author Only

● *Journal*

1. **Younghyun Kim**, Mitsuji Takenaka, Takenori Osada, Masahiko Hata, and Shinichi Takagi, “Strain-induced enhancement of plasma dispersion effect and free-carrier absorption in SiGe optical modulators”, *Scientific Reports* **4**, no.4683 (2014).
2. **Younghyun Kim**, Jaehoon Han, Mitsuji Takenaka, and Shinichi Takagi, “Low temperature Al₂O₃ surface passivation for carrier-injection SiGe optical modulator,” *Optics Express*, Vol. 22, No. 7, p.7458 (2014)
3. **Younghyun Kim**, Mitsuji Takenaka, Takenori Osada, Masahiko Hata, and Shinichi Takagi, “Fabrication and evaluation of propagation loss of Si/SiGe/Si photonic-wire waveguides for Si based optical modulator”, *Thin Solid Films* **557**, pp. 342-345(2014).
4. **Younghyun Kim**, Masafumi Yokoyama, Noriyuki Taoka, Mitsuji Takenaka, and Shinichi Takagi, “Ge-rich SiGe-on-insulator for waveguide optical modulator application fabricated by Ge condensation and SiGe regrowth,” *Optics Express*, Vol. 21, Iss. 17, pp. 19615-19623 (2013).

● *International Conference*

1. **Younghyun Kim**, Junichi Fujikata, Shigeki Takahashi, Mitsuji Takenaka, and Shinichi Takagi, “SiGe-based carrier-injection Mach-Zehnder modulator with enhanced plasma dispersion effect in strained SiGe”, OFC2015 at Los Angeles, Tu2A.7. 24th Mar 2015.
2. **Younghyun Kim**, Junichi Fujikata, Shigeki Takahashi, Mitsuji Takenaka, and Shinichi Takagi, “Low Injection-current Variable Optical Attenuator by using strained SiGe with Optimized Lateral PIN junction”, *ISPEC*, 18th Nov. 2014.
3. **Younghyun Kim**, Junichi Fujikata, Shigeki Takahashi, Mitsuji Takenaka, and Shinichi Takagi, “Record-low Injection-current Strained SiGe Variable Optical Attenuator with Optimized Lateral PIN junction”, Proc. ECOC, P.2.6, Cannes (2014).
4. **Younghyun Kim**, Mitsuji Takenaka, and Shinichi Takagi, “Simulation of carrier-depletion strained SiGe optical modulators with vertical p-n junction”, Proc. GFP, ThP.5, Paris (2014).
5. **Younghyun Kim**, Mitsuji Takenaka, Takenori Osada, Masahiko Hata, and Shinichi Takagi, “Strain-induced enhancement of free-carrier effects in SiGe for optical modulator and VOA applications”, OFC2014 at San Francisco, Th1C.4. 13th Mar 2014.
6. **Younghyun Kim**, Jaehoon Han, Mitsuji Takenaka, Shinichi Takagi, “Low temperature Al₂O₃ surface passivation for carrier injection type Si/strained SiGe/Si waveguide modulator”, *ISPEC*, Nov. 2013.
7. **Younghyun Kim**, Jaehoon Han, Mitsuji Takenaka, Shinichi Takagi, “Low temperature surface passivation for carrier injection type SiGe optical modulator,” 10th International Conf.

of Group IV Photonics at Seoul, 29th Aug 2013.

8. **Younghyun Kim**, Takenori Osada, Masahiko Hata, Mitsuru Takenaka, Shinichi Takagi, “Evaluation of propagation loss of Si/SiGe/Si photonic-wire waveguides for Si based optical modulator,” P1-34, ICSI-8, Fukuoka, 4th Jun 2013.
9. **Younghyun Kim**, Mitsuru Takenaka, and Shinichi Takagi, “Simulation of Si/SiGe/Si double heterostructure based carrier-injection modulator”, *ISPEC*, Nov. 2012.
10. **Younghyun Kim**, Mitsuru Takenaka, Shinichi Takagi, “Numerical analysis of strained SiGe-based carrier-injection optical modulators,” 9th International Conf. of Group IV Photonics at San Diego, ThD4, Aug. 2012.
11. **Younghyun Kim**, Masafumi Yokoyama, Noriyuki Taoka, Mitsuru Takenaka, and Shinichi Takagi, “Fabrication of Ge-rich SiGe-On-Insulator by Ge Condensation and Regrowth Technique for Optical Modulator,” *ISPEC*, 14th Nov 2011.
12. **Younghyun Kim**, Masafumi Yokoyama, Noriyuki Taoka, Mitsuru Takenaka, and Shinichi Takagi, “Fabrication of Ge-rich SiGe-on-Insulator waveguide for Optical Modulator”, *IEEE Photonics Conference*, Oct. 2011.

● *Domestic Conference*

1. **Younghyun Kim**, Takenori Osada, Masahiko Hata, Mitsuru Takenaka, and Shinichi Takagi: “Strain-induced enhancement of free-carrier effects in strained SiGe modulator”, Spring meeting of Japan Society Applied Physics, 2014. 3 [In Japanese]
2. **Younghyun Kim**, Jaehoon Han, Mitsuru Takenaka, and Shinichi Takagi, “Low temperature surface passivation for strained SiGe optical modulator”, Autumn meeting of Japan Society Applied Physics, 2013. 9 [In Japanese]
3. **Younghyun Kim**, Takenori Osada, Masahiko Hata, Mitsuru Takenaka, and Shinichi Takagi, “Fabrication of waveguide with Si/SiGe/Si core for SiGe optical modulator”, Spring meeting of Japan Society Applied Physics, 2013. 3 [In Japanese]
4. **Younghyun Kim**, Masafumi Yokoyama, Noriyuki Taoka, Mitsuru Takenaka, and Shinichi Takagi, “TCAD simulations of carrier -injection strained SiGe optical modulator”, Autumn meeting of Japan Society Applied Physics, 2012. 9 [In Japanese]
5. **Younghyun Kim**, Masafumi Yokoyama, Noriyuki Taoka, Mitsuru Takenaka, and Shinichi Takagi, “Fabrication of Ge-rich SiGe-on-Insulator waveguide for Optical Modulator”, Spring meeting of Japan Society Applied Physics, 2011. 3 [In Japanese]

Co-author

● *Journal*

1. Minsoo Kim, **Younghyun Kim**, Masafumi Yokoyama, Ryosho Nakane, SangHyeon Kim, Mitsuru Takenaka, and Shinichi Takagi, “Tunnel field-effect transistors with germanium/strained-silicon hetero-junctions for low power applications”, *Thin Solid Films* 557, pp. 298-301 (2014).

● *International Conference*

1. WuKang Kim, Yufei Kin, **Younghyun Kim**, SangHyeon Kim, Takenori Osada, Masahiko Hata, Mitsuru Takenka, and Shinichi Takagi, “Sb-diffused Source/Drain Ultra-thin Body Ge-On Insulator nMOSFETs Fabricated by Ge Condensation,” D-6-5L, SSDM, Fukuoka, 2013.
2. Minsoo Kim, **Younghyun Kim**, Masafumi Yokoyama, Ryosho Nakane, SangHyeon Kim, Mitsuru Takenaka and Shinichi Takagi, “Tunnel Field-Effect Transistors with Germanium/Strained-Silicon Hetero-junctions for Low Power Applications,” P1-26, ICSI-8, Fukuoka, 4th Jun 2013.

● *Domestic Conference*

1. WuKang Kim, **Younghyun Kim**, SangHyeon Kim, Takenori Osada, Masahiko Hata, Mitsuru Takenka, and Shinichi Takagi, “Ultra-thin body Ge-on insulator nMOSFETs by Ge condensation and Sb-diffused source/drain,” 18p-PA12-5, Spring meeting of Japan Society Applied Physics, 2014. 3 [In Japanese]
2. WuKang Kim, **Younghyun Kim**, SangHyeon Kim, Takenori Osada, Masahiko Hata, Mitsuru Takenka, and Shinichi Takagi, “Ultra-thin body Ge-on insulator nMOSFETs fabricated by Ge condensation and Sb diffusion,” 18p-P10-2, Autumn meeting of Japan Society Applied Physics, 2013. 9 [In Japanese]
3. Yufei Xin, **Younghyun Kim**, Rui Zhang, Takenori Osada, Masahiko Hata, Masafumi Yokoyama, Mitsuru Takenaka, and Shinichi Takagi, “Effects of thinning Ge-On-Insulator layers formed by Germanium condensation technique on hole mobility in MOS channels,” 27p-PB5-3, Spring meeting of Japan Society Applied Physics, 2013. 3 [In Japanese]
4. K. Kuroda, S. Dissanayake, J. Suh, **Y. Kim**, M. Yokoyama, N. Taoka, M. Takenaka, and S. Takagi: “Improvement of Ge-On-Insulator fabricated by Ge condensation technique for Ge photodetector application,” 24p-KB-4, Spring meeting of Japan Society Applied Physics, 2011. 3 [In Japanese]